ELECTRIC FIELD DEPENDENT SPECTROSCOPY OF SINGLE NANOCRYSTAL SYSTEMS

by

Sharonda L. Johnson LeBlanc

A dissertation submitted to the faculty of
The University of North Carolina at Charlotte
in partial fulfillment of the requirements
for the degree of Doctor of Philosophy in
Nanoscale Science

Charlotte

2012

Approved by:

Dr. Patrick Moyer

Dr. Marcus Jones

Dr. Tsing-Hua Her

Dr. Thomas Schmedake

Dr. Howard Godfrey

ABSTRACT

SHARONDA L. JOHNSON LEBLANC. Electric field dependent spectroscopy of single nanocrystal systems. (Under the direction of DR. MARCUS JONES and DR. PATRICK MOYER)

A suite of single molecule spectroscopic techniques and data analysis methods were implemented to explore the complex role of electric fields in single semiconductor nanocrystal photophysics. This dissertation spans the synthesis, characterization, biological applications, and photophysics of semiconductor nanocrystals. The core single molecule techniques employed in the current work include time-resolved fluorescence, time-correlated single photon counting, single molecule spectroscopy, and photon correlation spectroscopy. Various electrode devices were patterned to investigate the optical properties of single nanocrystal systems under an applied electric field. Electric field dependent spectroscopy and data analysis have revealed distributed kinetics and multiple charging of nanocrystals. In addition, interactions of nanocrystal excited states with plasmonic gold films have revealed strong enhancement of multiple exciton emission from single nanocrystals, and control by an applied electric field. The broader implications of this work can be extended to bioimaging, light harvesting, electro-optics, and lasing technologies.

DEDICATION

I dedicate this dissertation to my husband, Morris. I could not have completed this without his constant love and unwavering support over the years.

I would also like to acknowledge my parents, Ronald and Shirbey, and grandparents for instilling strong values of education. I am descended from a family of architects, war veterans, caretakers, and educators whose hard work has inspired my love of wisdom. Without the strong support system provided by my family and friends, this would not have been possible.

ACKNOWLEDGEMENTS

I would like to acknowledge the support and expertise of my advisors, Dr. Marcus Jones (Assistant Professor, Department of Chemistry) and Dr. Patrick Moyer (Professor, Department of Physics and Optical Science). In addition, I would like to thank the other members of my committee, Dr. Tom Schmedake, (Chemistry) Dr. Tsing-Hua Her (Physics and Optical Science), and Dr. Howard Godfrey (Accounting). I thank the National Science Foundation Graduate Research Fellowship Program, the Lucille P. and Edward C. Giles Foundation Dissertation Year Fellowship offered by the Graduate School at UNC Charlotte, and the Nanoscale Science PhD Program at UNC Charlotte for funding. Portions of this research were also supported by the Department of Defense and The University of North Carolina at Chapel Hill via the project entitled "Collaborative Initiative in Biomedical Imaging to Study Complex Diseases." I also acknowledge the help of my group members, past and present. From the Moyer group: Wesley Parker and Ryan Hefti. From the Jones group: Dr. Kevin Major, Danielle Woodall, Gaurav Singh, Michael Guericke, Andrew Tobias, Edward Williams, and Jose Castaneda. I would like to acknowledge Dr. Gloria Elliot and members of her research group, especially Dr. Katherine Weaver, Dr. Hye Jin Kim, and Regina Vrikkis. I would like to thank my summer students Mason McClanahan, Tully Moyer, and Michael Pope for all of their hard work. I also thank UNC Charlotte's Department of Chemistry, especially the following faculty and staff members: Dr. Bernadette Donovan-Merkert (Chair and Director of the Nanoscale Science PhD Program), Dr. Jordan Poler, Dr. Michael Walter,

Dr. Banita Brown, Dr. Jon Merkert, Dr. Cliff Carlin, Dr. Sherine Obare, Susan Michael, Dan Deadwyler, Vladimir Kubalik, Dewey Williams, Paul Bainbridge, Caroline Kennedy, Robin Burns, Linda Spurrier, and Lisa Carlin. In addition, I thank the named faculty and staff from the following UNC Charlotte Departments. Department of Physics and Optical Science: Dr. Ed Stokes, Dr. Robert Hudgins, Dr. Lou Deguzman, Dr. Ana Jofre, Dr. Tim Gutu, Scott Williams, Alec Martin, Margaret Williams, Liz Butler, Mark Clayton, Wendy Ramirez, and Fran Paluso. College of Engineering: Dr. Robin Coger, and Dr. Stuart Smith. Biology: Dr. Amy Ringwood. Graduate School: Dr. Susan Sell, and Amelia Perez.

TABLE OF CONTENTS

LIST OF TABLES

LIST OF FIGURES

LIST OF ABBREVIATIONS

APD	avalanche photodiode
CCD	charge coupled device
CdSe	cadmium selenide
EDX	energy dispersive x-ray spectroscopy
EM	electromagnetic
ET	electron transfer
HDA	hexadecyl amine
IRF	instrument response function
LSCM	laser scanning confocal microscopy
NA	numerical aperture
NC	nanocrystal
PL	photoluminescence
PMMA	poly-(methyl methacrylate)
PSF	point spread function
QCSE	quantum-confined Stark effect
QD	quantum dot
SEM	scanning electron microscopy
SNR	signal-to-noise ratio
SPAD	single photon avalanche photodiode

SPCM	single photon-counting module
TCSPC	time correlated single photon counting
TDPA	tetradecylphosphonic acid
TEM	transmission electron microscopy
TOP	trioctylphosphine
TOPO	trioctylphosphine oxide
TRPL	time-resolved photoluminescence

CHAPTER 1: INTRODUCTION

Nanoscale materials offer intriguing chemical, electrical, optical, and mechanical properties, which arise as a result of the physically reduced dimensions of the material, and lead to a completely new horizon of science and engineering possibilities. Utilizing new classes of functional nanoscale materials relies on the ability to synthesize or fabricate them reproducibly and have an in-depth understanding of their properties. Specific to our studies, ultrasmall nanoparticles (2-10 nm) called semiconductor nanocrystals (NCs) or quantum dots (QDs) are currently being investigated for use in a variety of applications spanning from solar energy harvesting[1] to fluorescent probes in biological systems.[2, 3]

The purpose of the bulk of this research is to gain an in-depth understanding of the fundamental physical properties of semiconductor nanocrystals for the aforementioned applications. More specifically, we developed a range of single molecule spectroscopic techniques and data analysis tools for investigation of the fluorescence emission properties of single QDs under various conditions. Novel outcomes of the work include enhancement of multiphoton emission using plasmon fields, control of multiphoton to single photon emission ratio with an applied electric field, control of

multiphoton to single photon emission with an applied electric field, and a statistical analysis of single QD emission characteristics under the influence of an applied electric field.

Current solar cell technologies remain too expensive and/or inefficient to compete with non-renewable energy sources such as coal and oil. Thus, the need for affordable and efficient energy sources is apparent. Of particular interest in the current work are nanocrystals that can be produced via inexpensive wet chemical methods, which could lead to a decrease in the cost of a solar cell. A device that incorporates semiconductor NCs will utilize their broad absorption spectrum and spectral tunability to capture a range of the solar spectrum, and generate free charge carriers to flow through an external circuit to power an electronic component.

Biological applications of semiconductor NCs take advantage of their bright, narrow emission, and resistance to photobleaching. Compared to traditional fluorescent probes, which lose their fluorescence over the course of an experiment, semiconductor NCs are more robust. For example, by linking biological molecules to nanocrystals, one can track a single biomolecule through a cellular environment for long periods of time. This type of single molecule tracking has revealed new and interesting kinetic and structural information about biomolecules such as protein folding kinetics, and motion of molecular motors, affording the opportunity to observe rare events that can be obscured in many-particle measurements. One can imagine ultimate sensitivity in detecting a

single copy of a protein or gene that is indicative of disease. For many diseases, early detection means the difference between life and death for a patient.

The nanocrystals explored in the current work are fluorescent semiconductor materials made of cadmium selenide, CdSe, which exhibit size-dependent properties. The size of an NC can easily be controlled during the synthetic process and the resultant size determines the narrow emission spectrum of the nanocrystal upon excitation by a laser. These semiconductor materials exhibit enhanced properties over their bulk counterparts as a result of quantum confinement. While the material properties of NCs are intriguing and controllable, they are also rich in complexity. Since each nanocrystal within a chemically synthesized sample is not exactly the same, these systems are naturally inhomogeneous, in direct contrast to molecular systems. In addition, nanocrystals have a well-defined surface, which becomes extremely important due to the large surface area to volume ratio of NCs. In order to fully appreciate and utilize NCs we must characterize them in detail with complex experimental methods.

We use photoluminescence (PL), or fluorescence, to study the excited state dynamics of nanocrystal systems. When a semiconductor material is excited with sufficient energy above the bandgap, an energetic electron-hole pair, or exciton, is created. These charge carriers (electrons and holes) move about the material for a short time and de-excite by recombining to emit a photon (fluorescence). The motivation for the current work is to understand the role of electric fields in the movement and

recombination of charge carriers in nanocrystals. We accomplish this by applying an external electric field. Using the quantum-confined Stark effect (QCSE), it may also be possible to control the optical properties of nanocrystals, which will be widely applicable in devices and biological systems. We use advanced microscopic and time-resolved spectroscopic techniques to study dynamics at the single molecule level, with Time-Correlated Single Photon Counting (TCSPC) as a cornerstone.

Previous experiments by other groups have revealed random spectral diffusion[4, 5] and fluorescence intermittency[6] in single nanocrystals, but there is no clear consensus on the root cause of these observed dynamics. The most common explanation of spectral diffusion and fluorescence intermittency in nanocrystals (NCs) is biexciton annihilation via an Auger ionization process.[6] In this charge-separated state, one electron or hole carrier is trapped on or near the surface while the other remains in the core, leading to a non-emissive state. The effect of the electric field generated by this charge-separated state has been implicated in a number of studies as the cause of observed dynamics, but remains scarcely explored.[7, 8] A few reports suggest that a single trapped carrier cannot account for a completely non-emissive state and suggest multiple trapped charges are the cause.[9, 10] We characterize fluorescence dynamics including fluorescence vs. time trajectories, fluorescence decays, and spectroscopy simultaneously under the influence of an applied electric field in an effort understand the electric field effect on the excited state dynamics of the NCs and its role in their optical properties.

We have designed experiments, which aim to control the local electric field of the nanocrystal. CdSe nanocrystals are patterned onto a glass-mounted gold electrode. An electric field is applied using a function generator. Using our homebuilt confocal microscope, we can locate individual nanocrystals, and simultaneously collect fluorescence trajectories, lifetime decays, and spectra. This dissertation research will explore the analysis of field-dependent dynamic information about a range of nanocrystal systems. Utilizing the above-mentioned single nanocrystal techniques, we can access dynamics on a range of timescales, from picoseconds to several minutes. Extracting rates of radiative and nonradiative processes from time-resolved photoluminescence spectroscopy and connecting those dynamics with spectral and intensity fluctuations enable an in-depth understanding of dynamic processes in nanocrystal systems, comparable to molecular systems. These experimental results and modeling of the charge transfer and relaxation dynamics of confined excitons will advance nanostructure applications.

Ultimately, a fundamental understanding and control of these dynamic processes will lead to rational design of materials that either reduce or enhance specific NC properties. These nanoscale materials with desired properties may be integrated into devices for solar energy harvesting or utilized in biological applications.

This dissertation is outlined as follows: the results of synthesis and biological applications of quantum dots is discussed, followed by a transition to the photophysics of

quantum dots in an overview of spectroscopy and electronic structure of QDs. Chapter 4 gives an in-depth explanation of single molecule spectroscopic techniques, and the suite of techniques implemented in the current work. Chapter 5 is an extensive literature review of relevant topics, followed by an overview of analytical techniques used in the current work. Lastly, the results of electric field dependent studies are presented in Chapter 7, the major contributions of which are summarized in figure 1.1, followed by conclusions.

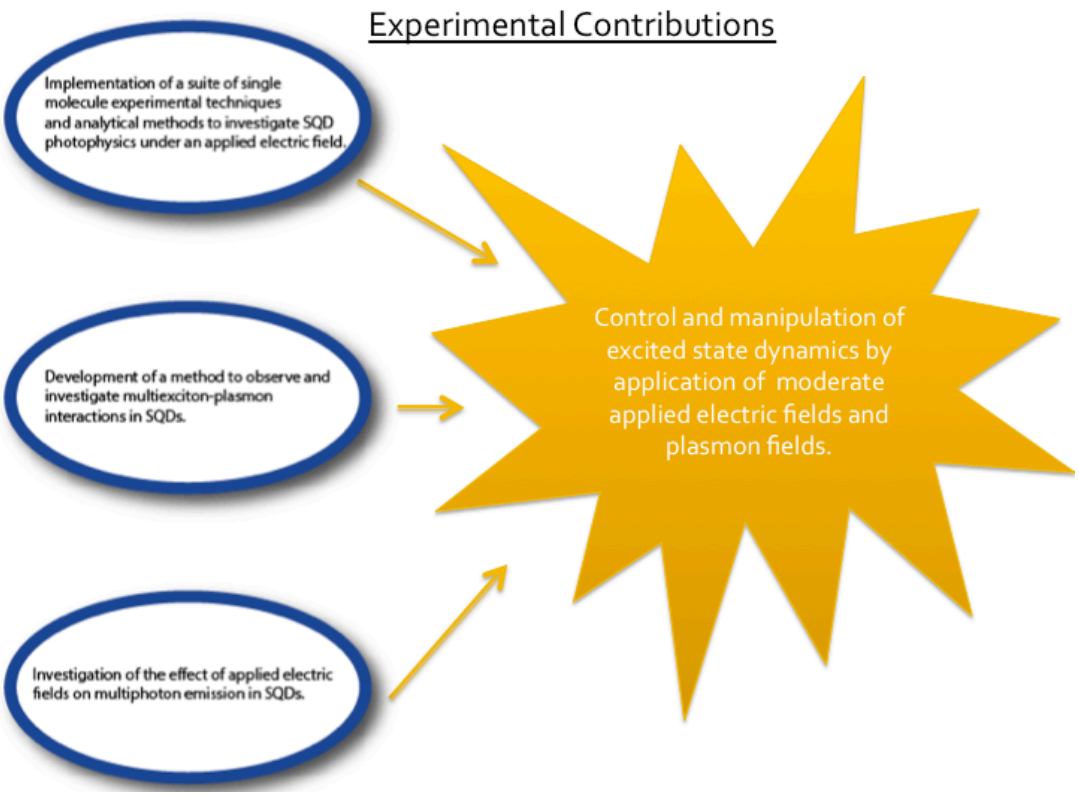

FIGURE 1.1: Experimental contributions of this dissertation research.

CHAPTER 2: SYNTHESIS, CHARACTERIZATION, AND BIOLOGICAL APPLICATIONS OF SEMICONDUCTOR NANOCRYSTALS

2.1 Introduction

Synthesis and fabrication of nanomaterials is an important part of nanoscale research. Top-down (etching) and bottom-up (gas-phase or solution-phase) are two ways that nanomaterials can be made, with solution-based chemical methods being the most common and least expensive. Critical to the current work is a reliable source of high-quality nanocrystals, specifically quantum dots. Cadmium selenide (CdSe) quantum dots (QDs) have served as a model system due to their relative ease of fabrication and reproducible optical properties.

Since quantum dots are not discrete molecules, each one is not exactly the same. Thus, there is a need to produce high quality, nearly monodisperse quantum dots via inexpensive methods. The first solution-based growth of cadmium sulfide (CdS) quantum dots in inverse micelles was reported in the early 1980's.[11-13] The Bawendi group made a major advance in chemical synthesis of QDs in 1993.[14] Using dimethylcadmium ($CdMe_2$) and trioctylphosphine selenide (TOP:Se) as precursors, they synthesized highly crystalline cadmium selenide (CdSe) quantum dots with narrow size distributions and high quantum yields. This synthesis relies on rapid injection of $CdMe_2$

and TOP:Se into hot (280-300°C) trioctylphosphine oxide (TOPO). The organometallic precursors undergo pyrolysis, leading to nucleation of nanocrystals. The TOPO acts not only as a solvent for the reaction, but also as a strong coordinating ligand. As-synthesized QDs are coated and stabilized by a TOPO layer as shown in figure 2.1.

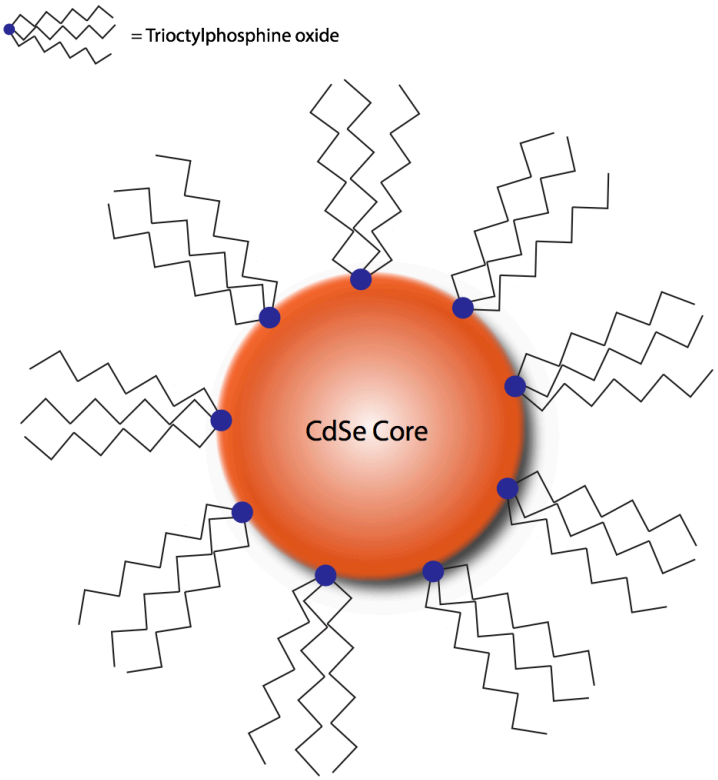

FIGURE 2.1: Schematic of cadmium selenide quantum dot, stabilized by coordinating ligand, trioctylphosphine oxide (TOPO).

Variations of the Bawendi synthesis of quantum dots are still employed today. Many have replaced the extremely volatile and pyrophoric $CdMe_2$ precursor with other sources such as cadmium oxide (CdO), cadmium acetate [$Cd(Ac)_2$], and cadmium acetylacetonate ($Cd(acac)_2$).[15, 16] Numerous methods still use the TOPO/TOP system, but other coordinating ligands have been introduced such as fatty acids, phosphonic acids, and amines.[16-18] These methods produce highly crystalline quantum dots with narrow size distributions.

The quantum yield of TOPO-capped CdSe QDs can be increased by growing a shell of wider bandgap material over the core.[19] The most common material is zinc sulfide (ZnS), although others such as cadmium sulfide have been employed.[18] This shell, which may be several monolayers thick, serves to passivate unbonded atoms on the QD surface, thereby reducing nonradiative relaxation pathways and increasing quantum yield. However, there is some leakage of the exciton into the shell and a small red-shift is observed for shelled QDs. In a typical synthesis, the zinc precursor is diethylzinc and the sulfur source is bis(trimethylsilyl) sulfide [$(TMS)_2S$]. Diethylzinc is very air and water sensitive, so other sources of zinc are desirable. With the wide variety of well-studied synthetic methods available, CdSe-ZnS core-shell quantum dots have become the quintessential quantum dot system. In this chapter, methods and results of CdSe QD synthesis and shell addition via solution phase methods are discussed. Quantum dots are synthesized based on the methods outlined in the literature.[18, 20, 21] As-synthesized

quantum dots are characterized using UV-Vis Spectroscopy, Fluorescence Spectroscopy, Transmission Electron Microscopy, and Energy Dispersive X-Ray Spectroscopy. Lastly, applications of quantum dots are discussed which utilize commercial quantum dots to label living cells and image them with confocal microscopy, toward biological tracking applications.

2.2 Synthesis

2.2.1 Core Synthesis

Cadmium acetate hydrate (99.99%) was dried overnight at 100°C on a hotplate with stirring. In a glove box, a 0.17 M solution of cadmium in trioctyl phosphine (TOP, Sigma-Aldrich) and a 1.0 M solution of selenium powder (as-received) in TOP were prepared in a vessel containing a stir bar. Solutions were allowed to stir until clear and colorless. The resulting solutions are referred to as TOP:Cd and TOP:Se respectively.

The following steps were carried out using standard Schlenk techniques for air-free synthesis. To a 3-neck round bottom flask fitted with a thermometer and flow adapter, 8 grams of trioctyl phosphine oxide (TOPO, Alfa Aesar) was dried and degassed under 50 mTorr vacuum at 160 °C for 1 hour with stirring at 100 rpm. The reaction temperature was reduced to 80°C. To the reaction mixture, 5 grams of hexadecylamine (HDA) and 0.15 g tetradecylphosphonic acid (TDPA) were added. The flask was heated to 110°C under vacuum for 20 minutes. The Schlenk line was then switched to argon atmosphere. 2 mL of the TOP:Se was added to the solution and heated to 300°C. When

at temperature, 3 mL of the TOP:Cd solution was rapidly injected. Instant nucleation of nanocrystals was observed by an immediate color change. The solution cooled, and was maintained at a growth temperature of 260°C. Samples of the solution were taken at time intervals using a glass syringe. The reaction flask was allowed to cool to room temperature, and 15 mL of chloroform was added. The raw growth solution was filtered with a 0.2 μm PTFE syringe filter. Methanol was added as a non-solvent to precipitate the quantum dots. The crude product was isolated by decanting the liquid and re-suspending the solid in chloroform. The results of the synthesis are shown in figure 2.2. Under ambient illumination, it is clear that the growth solution deepens in color over the course of the experiment. Under ultraviolet illumination, shifting to redder emission with time is indicative of an increasing core size. This size-tunability is due to quantum confinement, which is discussed in Chapter 3. The UV-Vis and fluorescence spectra are shown in figure 2.3. The evolution of absorption and emission wavelengths is clearly observed. The full width at half maximum (FWHM) of the emission spectra is ~29 nm, which is indicative of a monodisperse sample. Spectroscopy basics are also discussed in Chapter 3.

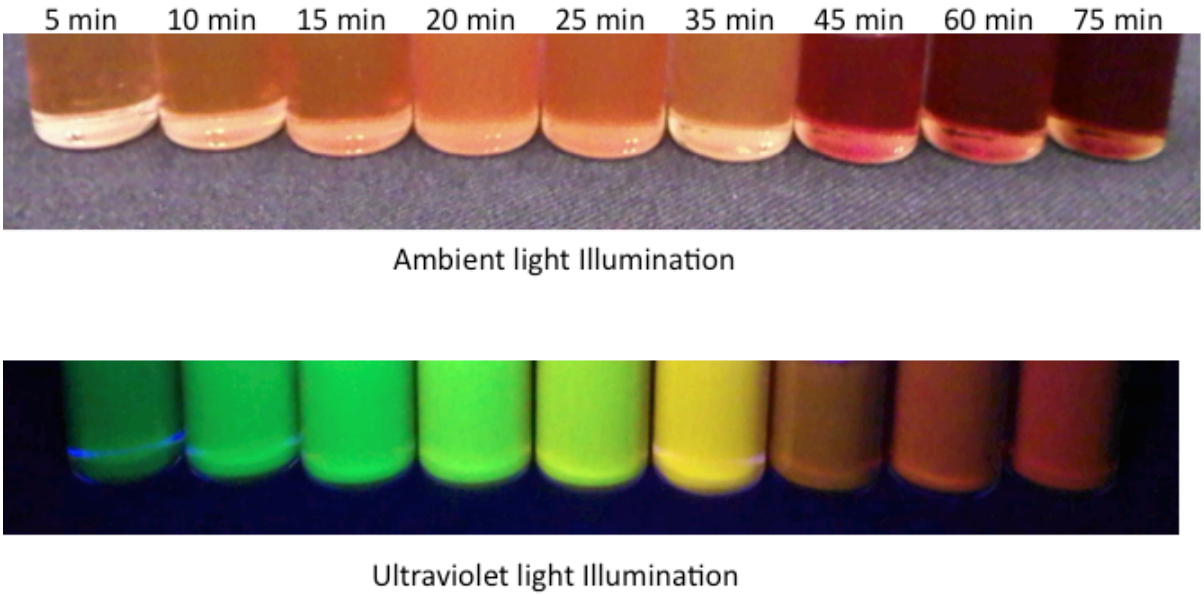

FIGURE 2.2: Aliquots of cadmium selenide quantum dots taken at various times during growth, as indicated. Top- ambient light illumination; Bottom- ultraviolet light illumination.

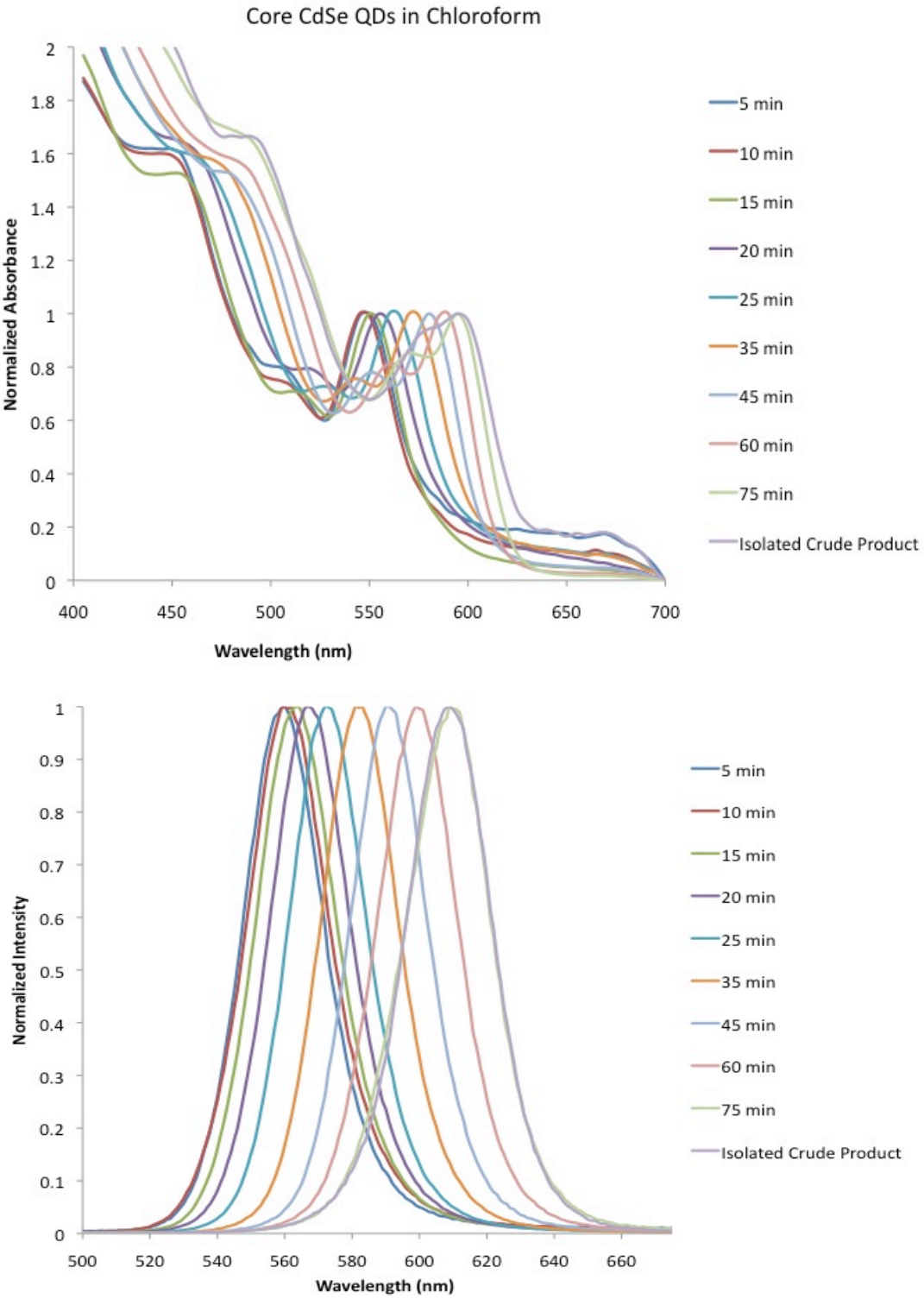

FIGURE 2.3: Steady state spectroscopy of cadmium selenide quantum dot solutions in figure 2.2, taken at various times during growth as indicated. Top- UV-Vis Absorbance; Bottom- Fluorescence Emission.

2.2.2 Shell Addition

As mentioned previously, growing a shell of wider bandgap material over the CdSe core can improve its optical properties. The crude precipitated product obtained from core synthesis described in the previous section was carried over to the shell addition step.

To a three-neck round bottom flask fitted with a thermometer and flow adapter, 3 g of TOPO, 2 mL TOP, and crude CdSe product was added along with a stirbar. The flask was brought into a glovebox. In the glovebox, 40 μL diethyl zinc, 82 μL hexmethyldisilathiane, and 3 mL TOP were mixed in an addition funnel. The amounts of precursor were calculated based on the desired number of monolayers. This is referred to as the Zn/S:TOP solution. The addition funnel was placed in the middle neck of the round bottom flask (stopped), and other fittings (adapter and thermometer) were attached and sealed before removing from the glovebox.

Using a Schlenk line, the solution was heated at 100°C with stirring for 5 minutes under vacuum, after which the line was switched to argon gas flow. The solution was heated to 200°C. When at temperature, the dropwise addition of Zn/S:TOP solution was started. After complete addition (several minutes), the solution was cooled to 90°C and allowed to stir for 3 hours. The solution was cooled to room temperature after 3 hours and the product was isolated as described before. The result is a CdSe core quantum dot surrounded by a ~1.5 monolayer shell of ZnS and coordinating ligands as shown in figure

2.4. The UV-Vis and fluorescence spectra are also shown in figure 2.5. A small shift in both spectra is clearly seen, which is indicative of a quantum dot that is effectively larger than the original core. Using the fluorescence spectroscopy, the average diameter of the quantum dots are estimated at 4.8 nm according to the literature.[22]

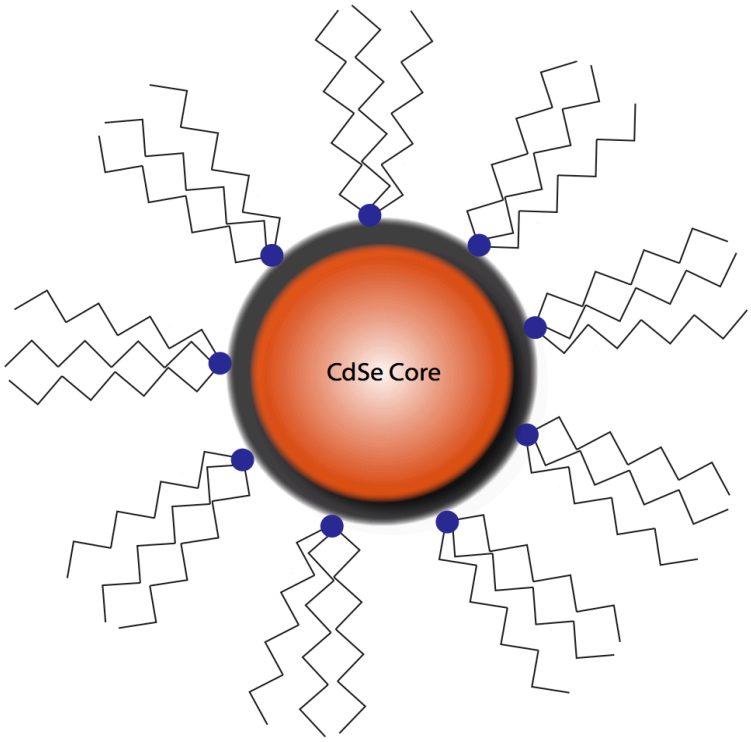

FIGURE 2.4: Schematic of cadmium selenide quantum dot with a shell of wider bandgap semiconductor material grown around it, stabilized by TOPO.

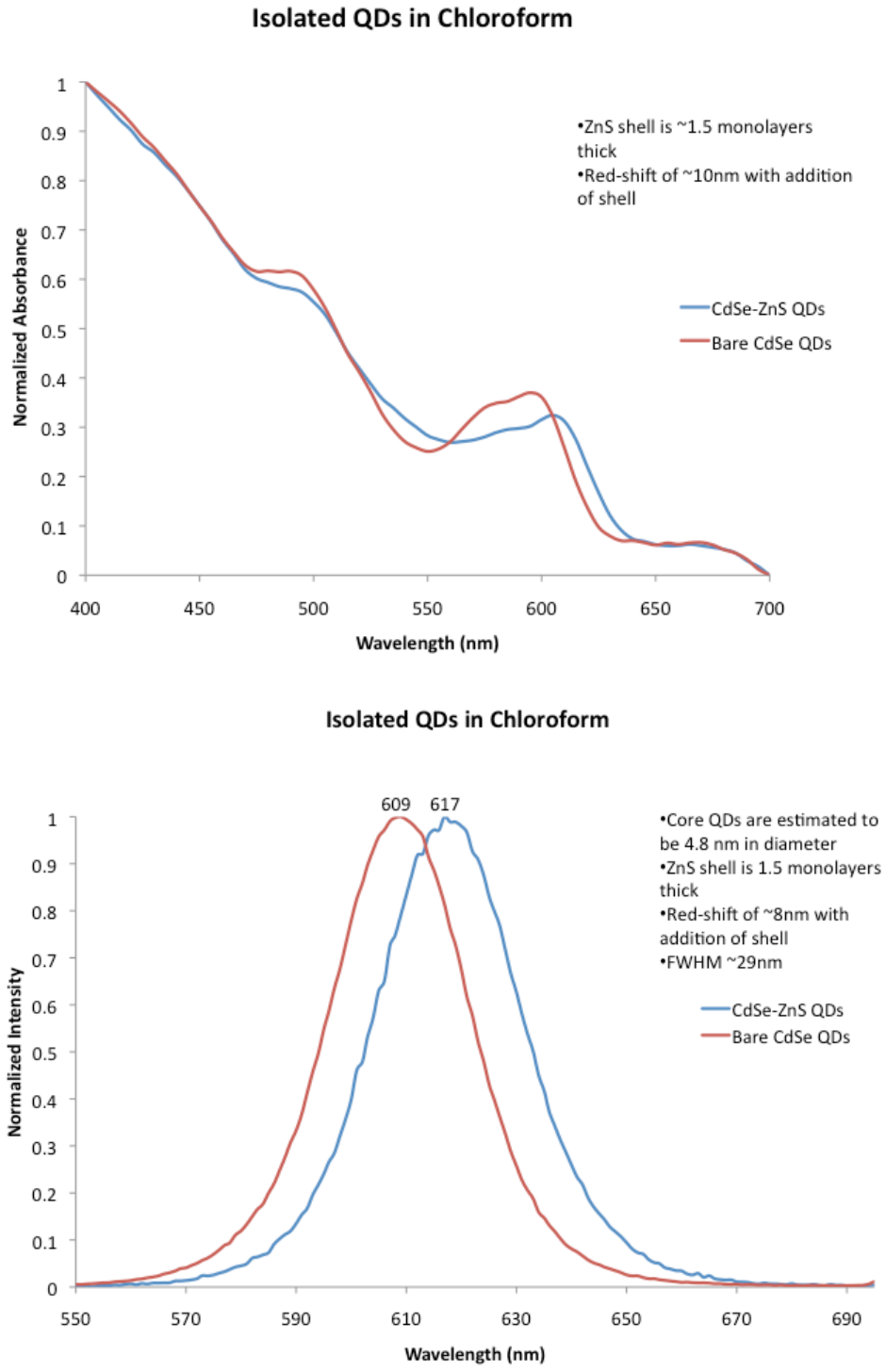

FIGURE 2.5: Steady state spectroscopy of cadmium selenide (CdSe) quantum dots after a shell of zinc sulfide was overgrown. Top- UV-Vis Absorbance; Bottom- Fluorescence Intensity. Red- Core CdSe; Blue- Core-Shell CdSe/ZnS quantum dots.

2.3 Characterization

2.3.1 Transmission Electron Microscopy (TEM)

Transmission Electron Microscopy is an instrument for structural characterization of nanoscale materials. The principle of TEM involves an accelerated beam of electrons, which interacts with the sample as it is transmitted through the thin grid containing the sample. Typically, the beam is generated by a tungsten filament, which is focused through an evacuated chamber to a small spot size using electric and magnetic fields. The transmitted electrons form an image, which provides atomic-level information about the sample. This high resolution, as compared to optical microscopy, is due to the wave nature of electrons in which the *de Broglie* wavelength is many orders of magnitude shorter than optical wavelengths. Resolution limits in optical microscopy are discussed extensively in Chapter 4.

Figure 2.6 shows a TEM image of the CdSe/ZnS quantum dots synthesized in the previous section. The sample was prepared by drop-casting a dilute solution of quantum dots onto a copper mesh grid, and evaporating excess solvent in a cool vacuum oven overnight. Planes of atoms are clearly observed in the image, confirming the crystallinity of the product. In addition, the particle diameters are measured to be ~4nm, consistent with spectroscopic data. It should be noted that the 1.5 nm ZnS shell cannot be distinguished from the CdSe core due to their similar electron density. A highly crystalline and size-monodisperse product is confirmed by TEM.

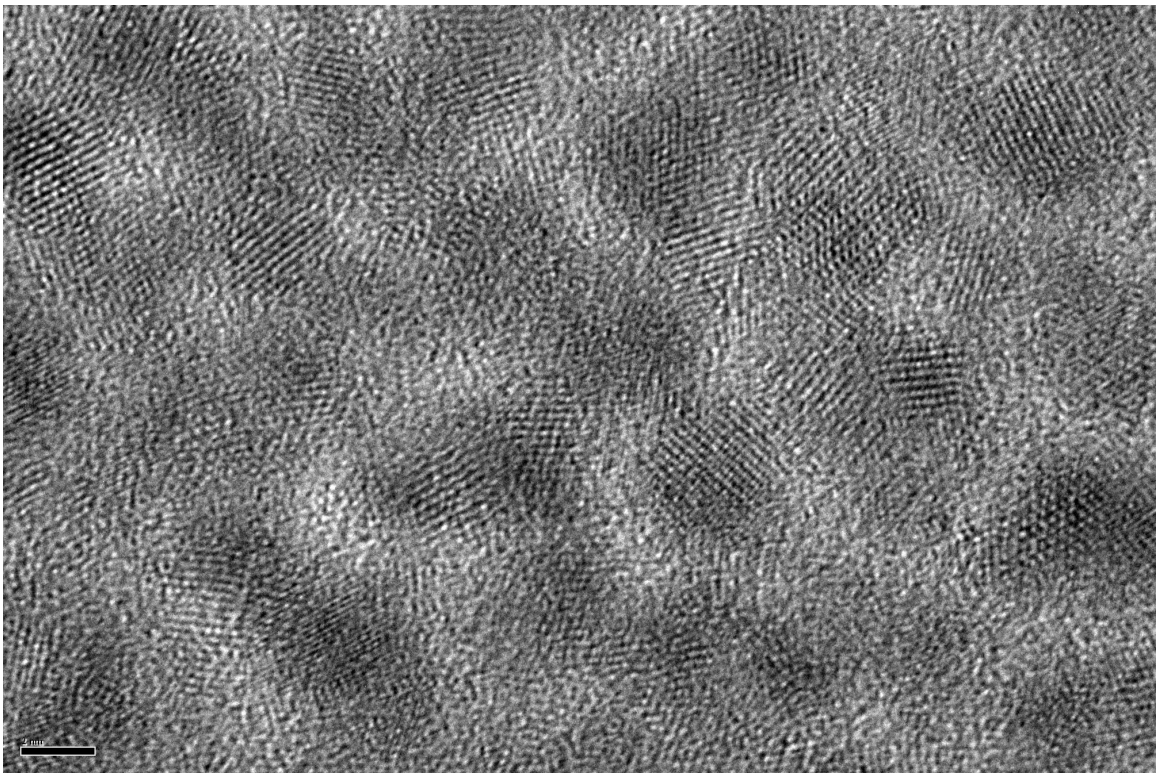

FIGURE 2.6: TEM of synthesized CdSe/ZnS quantum dots. 600,000x magnification. Scalebar is 2 nanometers.

2.3.2 Energy Dispersive X-Ray Spectroscopy (EDX)

Energy Dispersive X-Ray Spectroscopy is utilized in a TEM system for elemental analysis. As the sample is bombarded with high-energy electrons, some core electrons in the material are ejected, leaving behind holes in the core. Electrons in higher energy levels relax to fill the holes, emitting high-energy X-Rays. The spectrum of emitted X-Rays contains signatures of the elements that are contained in the sample. The spectra are stored in a database and matched to the collected data.

Figure 2.7 shows the EDX spectrum of the CdSe/ZnS quantum dots synthesized in the previous section. The elements cadmium (Cd), selenium (Se), zinc (Zn), and sulfur

(S) are identified in the spectrum as components of the quantum dot. In addition, copper (Cu) originates from the sample grid, and oxygen (O) and silicon (Si) presumably originate from the sulfur source used in shell addition, hexmethyldisilathiane. Table 2.1 shows the relative atomic percentages of the constituent elements. The Cd:Se ratio is ~ 2:1, while the Zn:S ratio is ~ 1:1. Thus, the core is cadmium-enriched, which may play an important role in carrier dynamics. EDX has revealed useful elemental information about the sample.

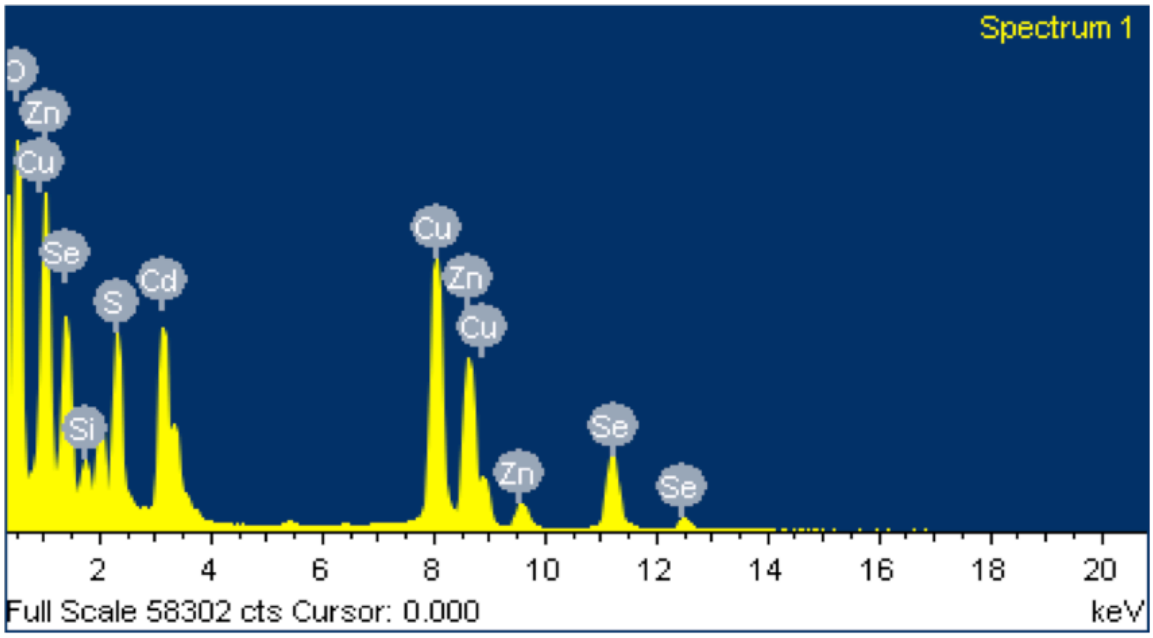

FIGURE 2.7: EDX of synthesized CdSe/ZnS quantum dots.

TABLE 2.1: Elemental analysis from EDX measurements.

Element	Weight%	Atomic%
O K	25.24	58.16
Si K	1.83	2.40
S K	7.26	8.34
Cu K	20.02	11.61
Zn K	13.87	7.82
Se K	8.91	4.16
Cd L	22.88	7.50
Totals	100.00	

2.3.3 Confocal Imaging and Fluorescence Intermittency ("Blinking")

Confocal Fluorescence Microscopy provides a method to observe the fluorescence of single quantum dots. Single molecule techniques are discussed extensively in Chapter 4. Observation of quantum dots at the single particle level has revealed fluorescence intermittency or blinking as introduced in Chapter 1. Figure 2.8 shows a confocal fluorescence image of the CdSe/ZnS quantum dots synthesized in the previous section. Blinking, characterized by on-off behavior of single quantum dots is clearly observed in the image. Figure 2.9 shows a fluorescence intensity versus time trace collected using time-correlated single photon counting when parked over a single quantum dot for 60 seconds. The intermittent emission behavior is clearly observed in

the trace as well. Fluorescence intermittency is problematic for applications such as single biomolecule tracking, and is discussed extensively in Chapter 5 as a central phenomenon studied in this dissertation research. This blinking phenomenon is just one of the many unresolved emission characteristics of QDs that make the study of excited state photophysics a challenging scientific problem.

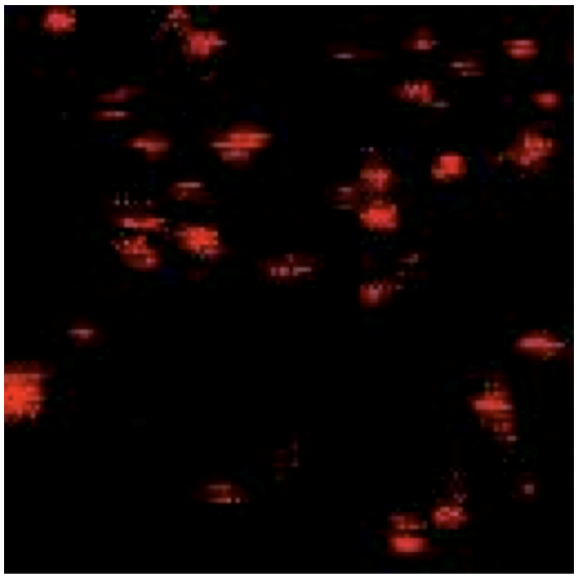

FIGURE 2.8: 12x12 μm confocal fluorescence microscope scan of synthesized CdSe/ZnS core-shell QDs

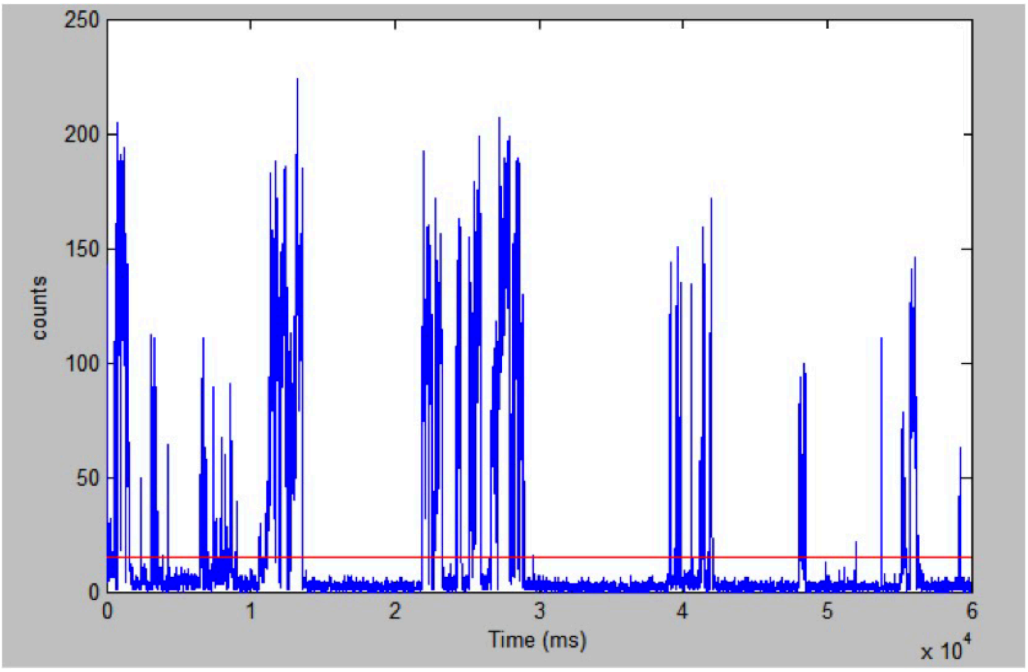

FIGURE 2.9: Fluorescence intensity vs. time trace of synthesized CdSe/Zns core-shell quantum dots.

2.4 Biological Applications

2.4.1 Introduction

The unique properties of quantum dots make them ideal probes in molecular biology. Bright and photostable fluorophores with broad absorption spectra and narrow emission spectra are beneficial for many biological applications.[2, 3, 23-27] For example, by conjugating the bright emitters to single biomolecules, one can track the motion of individual particles, gaining valuable information not previously observed using organic fluorophores.[28] One can observe dynamic processes one molecule at a time.

QDs synthesized by the methods described above yield nanocrystals that are highly soluble in organic solvents such as chloroform, toluene, and hexanes. In order to

conjugate to biomolecules such as proteins, nucleic acids, and carbohydrates they must first be rendered water-soluble. Water-soluble quantum dots can then be conjugated to a variety of biomolecules for specific applications by reaction of surface functional groups.[23, 25, 26, 29-35] The first reports of water-soluble quantum dots appeared in the literature in 1998.[23, 24] Since, QDs have been employed in a variety of biological applications such as specific targeting,[34-36] energy transfer-based sensing,[31, 37-40] and tracking of organelles and biomolecules.[32, 33, 36, 41-43]

Two categories for water-solubilizing nanocrystals include ligand exchange and encapsulation. In the former instance, the native hydrophobic ligands of CdSe/ZnS QDs are replaced with bifunctional ligands that contain different functional groups on either end. For example, a ligand that presents a thiol (-SH) group on one end and a carboxylic acid (-COOH) on the other end. The thiol group contains sulfur with a lone pair of electrons that has a strong affinity for the zinc metal atoms on the QD surface, forming a dative bond. The carboxyl group assumes a negatively charged carboxylate ($-COO^-$) in neutral to basic solutions, rendering the QD soluble in water and buffered solutions. Early procedures used simple thiols such as mercaptoacetic acid, mercaptopropionic, and mercaptoundecanoic acid.[29] However, these solutions have only shown solubility over a narrow range of pHs, and poor stability over time in solution, leading to aggregation.[44] The aggregation is thought to result from desorption of ligands over time and subsequent oxidation of the CdSe QD surface.[45] Alternatives to simple ligands are bidentate thiols

such as dihydrolipoic acid (DHLA), which have been shown to exhibit greater stability over time and over a wider range of pH values.[30, 37, 46] Incorporating polyethylene glycol (PEG), a biocompatible and bioinert polymer, has been shown to enhance stability and reduce nonspecific attachment to biomolecules.[47, 48] Specific attachment is vital for intracellular drug delivery and tracking applications.

Ligand exchange produces QDs with a small final diameter (close to the as-synthesized diameter). This can be important in live cell studies where the size of the QD may either impede the natural function of an attached biomolecule or crowd the already packed intracellular environment.[49] One drawback of the exchange method is typically a reduced quantum yield, resulting in weakly emitting QDs. This is a result of perturbing the original ligands, which may introduce surface defects and new pathways for nonradiative recombination.

An alternative method of encapsulation involves essentially covering up the native hydrophobic ligands. This can be accomplished with an amphiphilic molecule that has both a hydrophilic and a hydrophobic end. For this method, the hydrophobic ends of the molecule can interdigitate between the long octyl groups of TOPO, leaving the hydrophilic ends pointed to the outside. One such example is the encapsulation of QDs in phospholipid micelles.[50] A drawback is that the micelles have a fixed inner-diameter that can only incorporate a small range of QD sizes. The overwhelming advantage of encapsulation over ligand exchange is preservation of photoluminescence properties.

The original ligands remain intact, thus no new defects are introduced. However, the nanocrystals will usually have a large final diameter due to an added layer of ligands, which may limit its use in some biological applications. Ligand exchange methods were explored in the current work due to the ultimate goal of single molecule tracking.

2.4.2 Ligand Exchange for Biological Applications

The quantum dots synthesized in section 2.2 were rendered soluble in aqueous solution via methods outlined in the literature.[20, 29, 44] CdSe/ZnS quantum dots were synthesized as described previously. The as-synthesized QDs were dispersed in a small amount of chloroform and added to a 50 mL 3-neck round bottom flask. The chloroform was evaporated using Schlenk technique. An excess (1g, depends on amount of QD product) of mercaptoundecanoic acid (MUA, 95%, Sigma Aldrich) was added to the QDs along with a stir bar. The solution was reacted for 2 hours at 60°C under nitrogen. The solution was transferred to a 50 mL centrifuge tube. A 2-fold molar excess (compared to MUA) of potassium tert-butoxide in dimethylformamide (DMF) (2wt% solution) was added to the tube containing the QDs. The solid formed was dissolved in water, and DMF added until the solution turned clear. The QDs were collected via centrifuge and washed twice with DMF. The crude product was dissolved in distilled water. The UV-Vis absorbance and fluorescence spectroscopy are shown in figure 2.10. The water-soluble quantum dots are compared to the core CdSe and core-shell CdSe/ZnS.

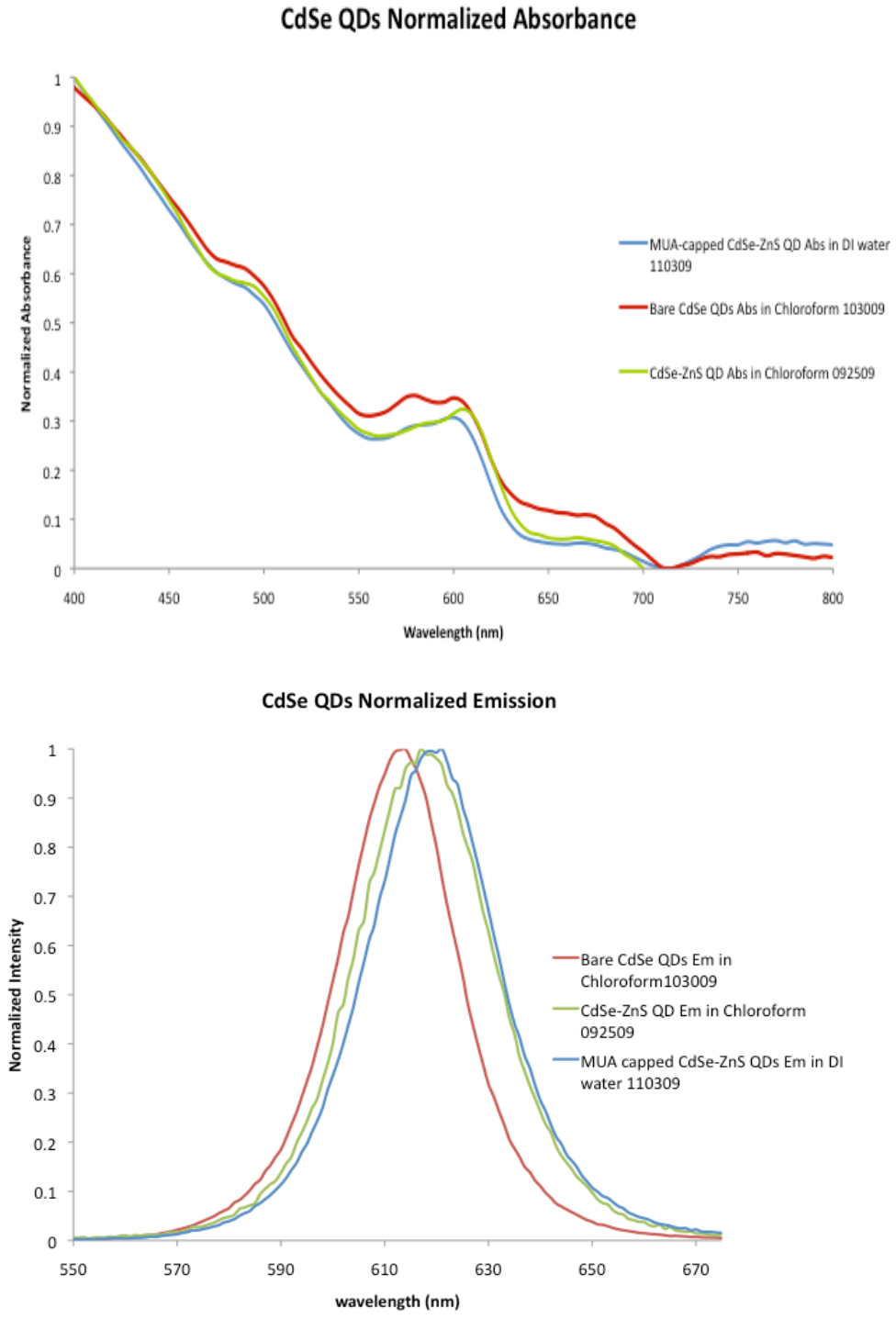

FIGURE 2.10: Steady state spectroscopy of cadmium selenide (CdSe) quantum dots after a shell of zinc sulfide was overgrown and native TOPO ligands were exchanged for water solubilization. Top- UV-Vis Absorbance; Bottom- Fluorescence Intensity. Red- Core CdSe; Green- Core-Shell CdSe/ZnS; Blue MUA-CdSe/ZnS quantum dots.

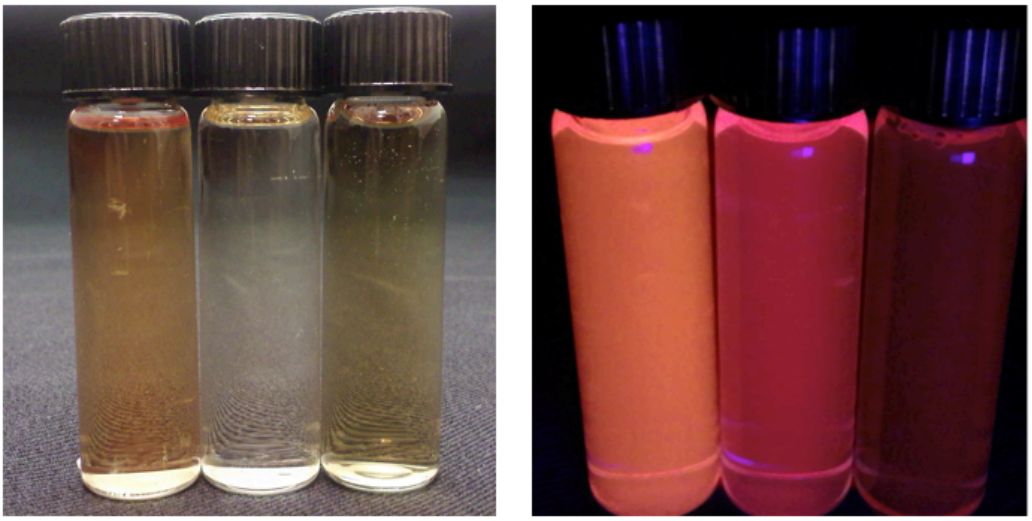

FIGURE 2.11: Images of cadmium selenide quantum dot solutions. From left to right: Core CdSe, CdSe/ZnS, MUA-CdSe/ZnS.

2.4.3 Cell Culture and Labeling

As mentioned previously, tracking of single biomolecules would provide a wealth of knowledge about the behavior of biomolecules in their native environment. The goal of this part of the project was to observe single quantum dots in living cells. J774 mouse macrophage cells were cultured in Dr. Gloria Elliot's lab (Mechanical Engineering). They were cultured in full compliment media containing fetal bovine serum (FBS), Dulbecco's Modified Eagle Medium (DMEM, 1X), and antibiotics. The cells were attached to a glass substrate for optical imaging, and labeled with an organic fluorophore (pyranine, HPTS) and/or carboxyl quantum dots (Invitrogen QDot® 605 ITK™).

For optical imaging, 5 mL of cells were taken from culture and centrifuged for 5 minutes at 1000 rpm. The old media was decanted and the cells re-dispersed in 1 mL of

fresh media to concentrate the solution. 20 μL of the cell solution was pipetted onto a glass coverslip (Note: a small circle was drawn in the middle of the coverslip to mark the location of the droplet). The coverslip was incubated for 15 minutes at 37°C to attach the cells to the glass. To label the cells with HPTS and/or quantum dots, the medium was removed, and a ~10^{-7}- 10^{-12} M solution of HPTS and/or quantum dots in phosphate buffered saline (PBS, 1X) was pipetted onto the cells. The cells were incubated with the fluorophore at 37°C for 15 minutes. The fluorophore solution was removed and the cells were washed several times with 100 μL aliquots of warmed (37°C) PBS solution to remove excess fluorophore.

The samples were imaged using either an epifluorescence microscope or a confocal microscope. Figure 2.12 shows a bright field image of the J774 mouse macrophage cells (left) and a fluorescence image of the cells labeled with HPTS. The fluorophore has been taken into the interior of the cells via endocytosis. For quantum dot labeling, the synthesized MUA-CdSe/ZnS quantum dots were incubated with the cells as described. Figure 2.13 shows the result. It appears that the fluorophore has not been taken into the interior of the cells, as shown with the HPTS fluorophore. The fact that the image indicates fluorescence at the edge of the cell leads to the conclusion that the QDs attach to the outside of the cell, thus appearing as a 'donut' type image since the microscope images a plane of the relatively thick cell. This result is not surprising and can be attributed to incomplete ligand exchange, which results in a quantum dot that is

not entirely biocompatible. Thus, experiments with quantum dots were conducted using commercially available quantum dots. Observation of single fluorophores is not possible with conventional microscopy, so further experiments were conducted using confocal microscopy as described in the next section.

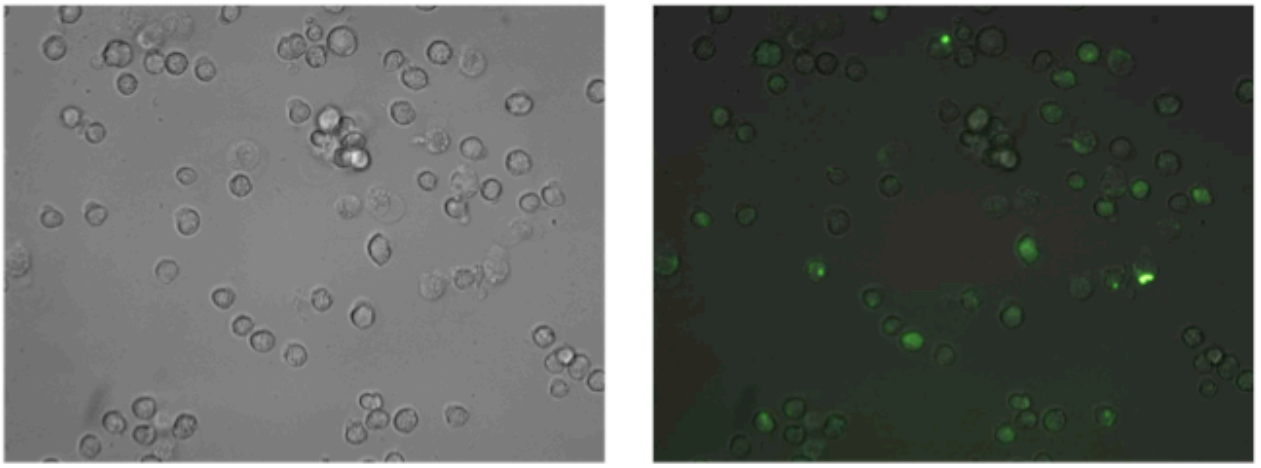

FIGURE 2.12: Optical microscopy of live J774 mouse macrophage cells. Left- bright field illumination; Right- fluorescence image of cells labeled with HPTS.

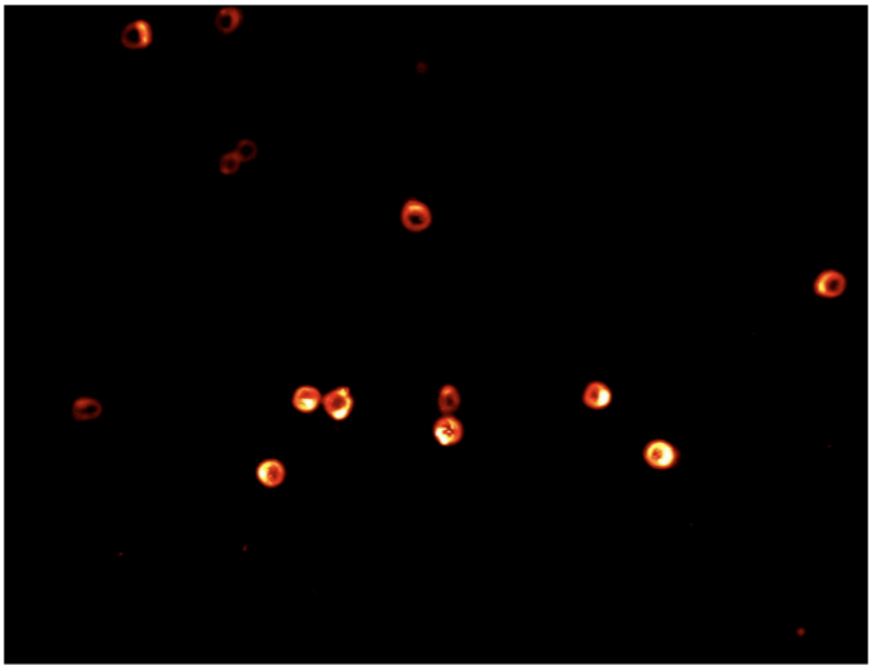

FIGURE 2.13: Optical microscopy of live J774 mouse macrophage cells labeled with synthesized MUA-CdSe/ZnS quantum dots.

2.4.4 Confocal Microscopy

Confocal Fluorescence Microscopy was introduced in section 2.3.3 as a method to observe the fluorescence of single quantum dots. In an effort to image single quantum dots in a live biological environment, J774 mouse macrophage cells were co-labeled with HPTS and carboxyl quantum dots. We used bandpass filters to discriminate between the HPTS and QD fluorescence. A bandpass filter transmits only a selected "band" of wavelengths, or colors. A bandpass filter is described by its center wavelength, and the width of bands emitted. Thus, a 535/45 bandpass filter will transmit 512.5-557.5 nm.

The spectra of the QDs and HPTS are shown in figure 2.14. The QDs emit at 609 nm (blue curve), and are clearly blocked when the HPTS filter (535/45) is used (red

curve). The HPTS emission peaks at 525 nm (red curve), and is blocked when the QD filter (620/35) is used (green curve). Figure 2.15 shows the results of changing filters while imaging a cell. The top left image shows the fluorescence of carboxyl QDs loaded into the J774 cell with the 620/35 filter in place. The top right shows the fluorescence of HPTS loaded into the same J774 cell. The bottom image is an overlay of the two fluorescence images. It is clear that there is some co-localization of the fluorophores. The quantum dot image indicates that the QDs are ingested into the cell via endocytosis, but remain localized in endocytotic vesicles. This is due in part to QD aggregation in solution, and non-specific attachment. This is problematic for single biomolecule tracking applications, and specific targeting using bioconjugation methods mentioned in section 2.4.1 is necessary. Further efforts to decrease the concentration of QDs for observation of single particles were unsuccessful.

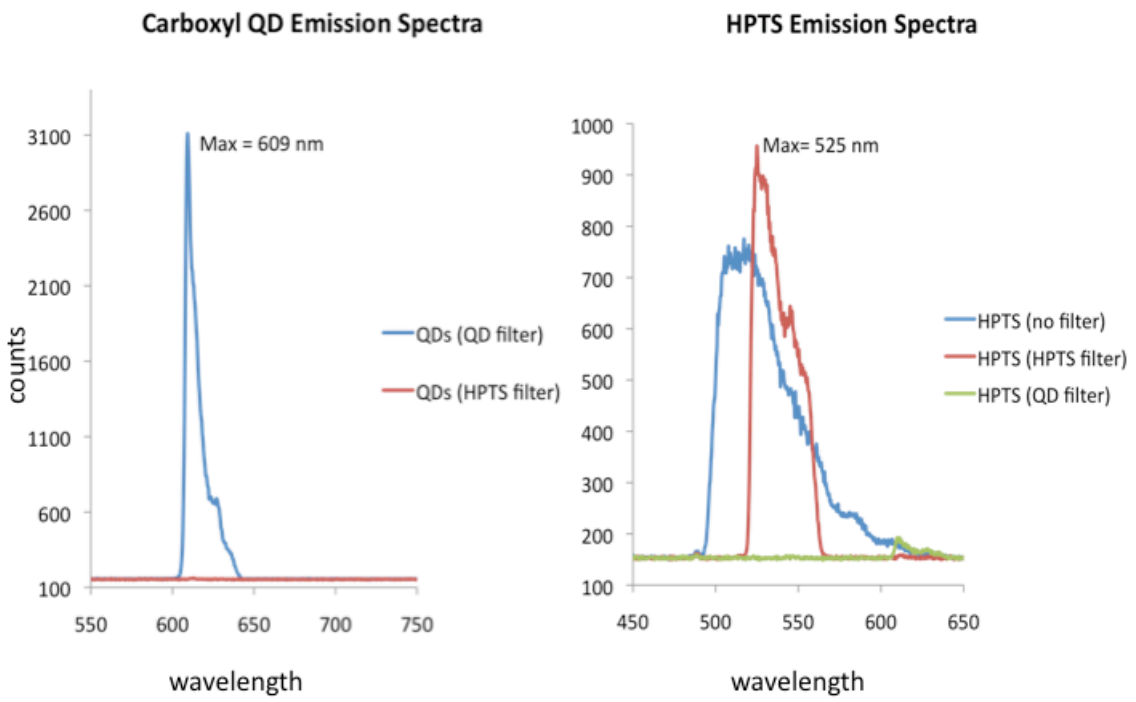

FIGURE 2.14: Emission spectra of carboxyl quantum dots and HPTS in phosphate buffered saline solution. Left- QD fluorescence is blocked by a 535/45 bandpass filter. Right- HPTS fluorescence is blocked by a 620/35 bandpass filter.

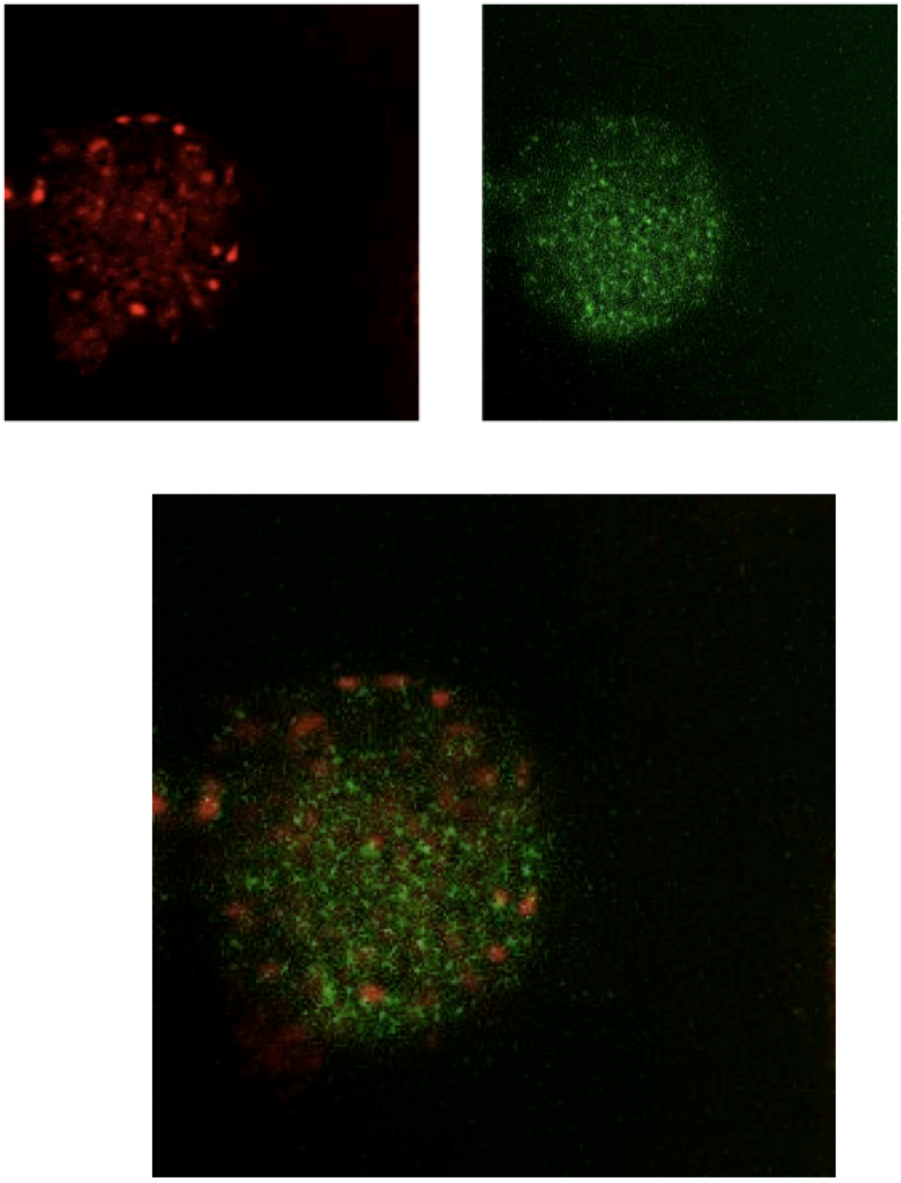

FIGURE 2.15: Confocal microscopy of a live J774 mouse macrophage cell labeled with quantum dots and HPTS. Top left- quantum dot fluorescence; Top right- HPTS fluorescence; Bottom- Overlay of both fluorescence images.

2.5 Conclusions

A size series of CdSe quantum dots was successfully synthesized via solution phase methods. A shell of wider bandgap material was grown around the quantum dots. UV-Vis and fluorescence spectroscopy of both samples clearly show evolution of size with growth time and a characteristic red shift in emission upon shell growth. Additionally, the CdSe/ZnS core-shell quantum dots were characterized structurally and elementally using Transmission Electron Microscopy (TEM) and Energy Dispersive X-Ray Spectroscopy (EDX) respectively. Confocal imaging and time-correlated single photon counting revealed intermittent emissive behavior as expected for single quantum dots.

Steps toward biological applications of quantum dots were also explored. A J774 mouse macrophage cell line was cultured and maintained. As synthesized CdSe/ZnS quantum dots were rendered water soluble using mercaptoundecanoic acid in a ligand exchange process. This was confirmed by solubility in distilled water. Upon labeling of live mouse macrophage cells, the quantum dots appeared not to uptake into the cells very efficiently. This can be attributed to incomplete ligand exchange, leading to instability in buffered solutions.

Commercially available carboxyl-functionalized quantum dots in conjunction with pyranine (HPTS) were used to label live mouse macrophage cells. Confocal microscropy was utilized, revealing some colocalization of both fluorophores, although

again the QDs were not efficiently transferred to the intracellular cytoplasm as desired. Observation of single quantum dots inside of living cells was not achieved. The nature of endocytosis and quantum dot aggregation makes this observation difficult. Although biological applications of quantum dots are a promising area of research, practical experiment requires extensive knowledge and training in which our group has insufficient expertise. The remainder of this dissertation focuses on elucidating the fundamental physics of quantum dots. The dynamics of lifetime decay fluctuations, fluorescence intermittency, spectral diffusion, and multiple excitons are explored in detail. Ultimately a clear understanding of elementary charge carrier processes in QDs will advance their applications.

CHAPTER 3: SPECTROSCOPY AND ELECTRONIC STRUCTURE OF SEMICONDUCTOR NANOCRYSTALS

3.1 Introduction

Central to the remainder of this research is the study of the optical properties of nanoscale materials. We seek to answer the central question: how do the materials under study respond to light when placed in different environments? To investigate optical properties, we use spectroscopy. In general, optical spectroscopy refers to a study of the interaction of light (electromagnetic radiation) with a material sample ("matter"), which yields a spectrum. This spectrum represents the response of the material as a function of the wavelength or frequency of the incident light. The wavelength or frequency translates directly to the relative energy between the recombining electron and hole in a nanocrystal energy manifold. This energy manifold is an extremely complicated and dynamic entity whose heterogeneity from one QD to another is significant, as we will discover in the current research.

Spectroscopic methods differ mainly in the type of light source that interacts with the sample, and the type of system used for detection. A variety of methods are available depending on the type of information one seeks to gain from the measurement. Table 3.1 shows a summary of different spectroscopies, the type of light source utilized, and the information probed in the experiment. Absorbance and fluorescence spectra of CdSe

quantum dots were presented in Chapter 2; refer to figure 2.3. An in-depth discussion of single molecule spectroscopy (method 9) appears in Chapter 4.

TABLE 3.1: Types of Spectroscopy

Spectroscopy Method	**Light Source**	**Probe**
1. Absorption	Ultraviolet-Visible lamp	Light absorption from electronic transitions
2. Fluorescence/Photoluminescence (PL)	Lamp/LED/Laser	Light emission from electronic transitions
3. Infrared (IR)	Infrared lamp	Light absorption of vibrational states
4. Raman	Laser	Vibrational states from scattered light
5. Photoluminescence Excitation (PLE)	LED/tunable Laser	Light absorption
6. Fluorescence Line Narrowing (FLN)	Laser	Light emission
7. Time-resolved (PL, Transient Absorption)	Laser	Excited state dynamics
8. Nonlinear	Laser	Various
9. Single Molecule	Laser	Light emission or scattering

3.2 Spectroscopy of Materials

Spectra obtained from spectroscopy experiments contain valuable information about the electronic structure of the material. The electronic energy levels of a material can be calculated using quantum mechanics, and the results supported by spectroscopic methods. Quantum mechanics is a mathematical formalism that allows one to calculate the energetic states in a material based on knowledge of its physical structure using the Schrödinger equation. These states are comprised of translational, vibrational, and rotational energy of electrons and atomic nuclei. A *wavefunction*, Ψ, associated with each energy state contains all of the dynamical information about that state, most notably movement of electrons. Using the Born interpretation of the wavefunction, the probability of finding an electron in a particular energy state, is proportional to $|\Psi|^2 = \Psi^*\Psi$ (Ψ^* if Ψ is a complex function). It is the transitions of electrons between energy states that lead to absorption and emission of light in material, and thus its optical properties if these transitions originate from absorption and emission of photons. Figure 3.1 shows a Jablonski diagram, which is a schematic representation of the energy level manifold, normally including electronic and vibrational states in a material. Each horizontal line represents states of increasing energy from the ground state to the excited state. Arrows indicate specific absorption and emission transitions. A photon of light is represented by a wavy line and its energy, $h\nu$, where h is the Planck constant, and ν is the frequency of the electromagnetic wave. The absorption event shown in the figure

illustrates an electron being excited into a higher energy state, leaving behind a hole in the ground state.

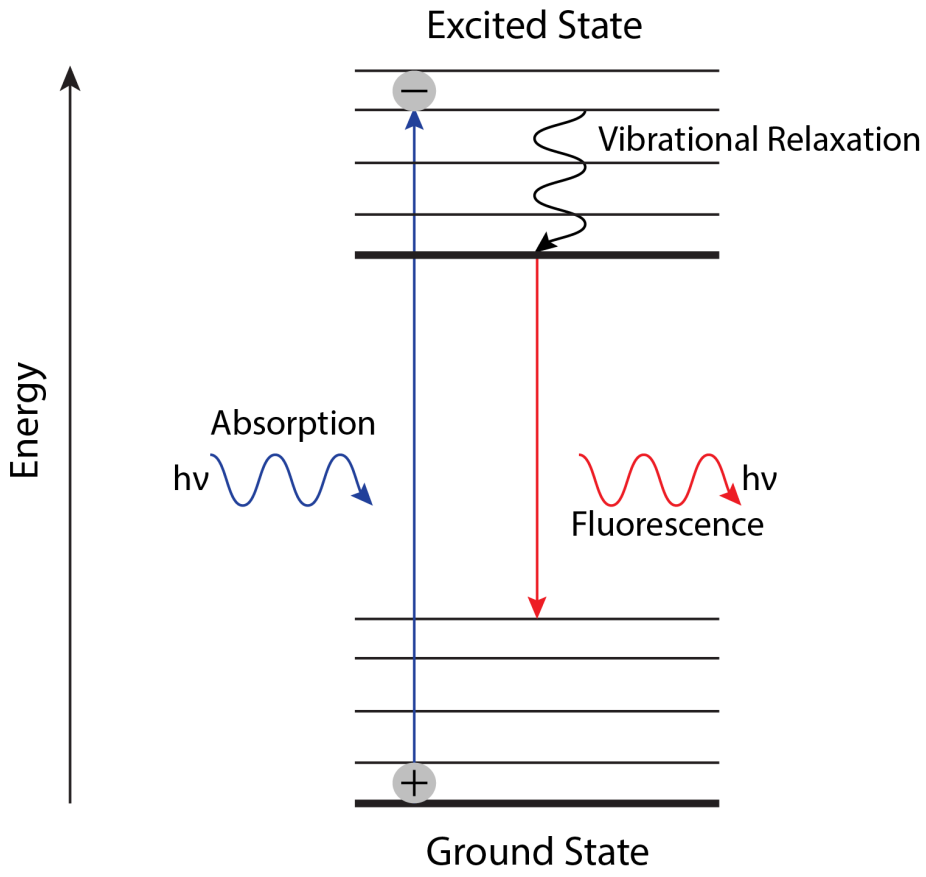

FIGURE 3.1: A simplified energy level diagram of a system, termed a Jablonski diagram, which shows transitions between levels and the corresponding process.

Understanding spectra and the underlying electronic structure is important for the utility of nanomaterials, as it provides insight into the material properties. The radiative electronic transitions that give rise to spectral features are determined by the initial state electronic wavefunction (Ψ_i), final state electronic wavefunction (Ψ_f), electrical dipole

moment operator ($\boldsymbol{\mu}$), and their interaction with an electromagnetic field. The likelihood of particular transitions is governed by spectroscopic selection rules. This electronic transition probability is shown by the matrix element below as an integral over all space and dimensions and in bracket notation:

$$\int \Psi_f^* \mu \Psi_i d\tau = \langle \Psi_f \mid \mu \mid \Psi_i \rangle \quad (3\text{-}1)$$

Evaluating the integral for an initial and final state, one can determine the strength of an electronic transition, which is proportional to the square of the calculated integral. A zero value means the transition is disallowed, and will not result in a spectral feature. Such calculations are used to predict the form of a spectrum for a particular system. Theoretical calculations of electronic structure are very accurate for systems composed of single atoms with few electrons, but become more complicated for molecular systems, and thus are approximated using atomic solutions. Atomic spectra exhibit extremely narrow spectral peaks due to transitions between discrete energy levels. The picture becomes considerably more complicated for semiconductor nanocrystal quantum dots, which are comprised of many thousand atoms. Due to quantum confinement, discrete atomic-like energy levels are predicted, but spectral features are strongly influenced by carrier-carrier interactions and interactions of the nanocrystal surface with its local environment. This picture is further complicated considering that equation 3-1 is time-dependent as well. The time-dependent dynamics are a major part of the discussions in our experimental data analysis sections.

3.3 Electronic Structure of Quantum Dots

A complete understanding of the optical properties of spherical nanocrystals can be achieved by having a clear picture their electronic structure. Theory and spectroscopy of nanocrystals has revealed elements of the complex nature of this electronic structure. [51] The manifold of charge carrier states dictates the observed optical properties that arise from transitions of electrons and holes between quantum-confined energy levels. The absorption and photoluminescence (PL) spectra depend strongly on the nanocrystal radius due to the quantum confinement effect in which a reduction in the size of the particle in one or more dimensions results in constraints on the allowed wavefunctions, and therefore its energetic states. The energy levels of electrons and holes ($E_{e,h}$) confined in a three-dimensional sphere surrounded by infinite potential barrier is given by the following equation:

$$E_{l,n}^{e,h} = \frac{\hbar^2 \phi_{l,n}^2}{2m_{e,h}a^2}, \qquad (3\text{-}2)$$

where l is the angular momentum quantum number, n is the principle quantum number, $\hbar$ is the reduced Plank's constant, $\phi_{l,n}$ is the spherical Bessel function of order l, $m_{e,h}$ are the effective masses of electron and hole, and a is the nanocrystal radius. Clearly, the confinement energy ($E_{e,h}$) increases with decreasing particle radius, such that smaller nanocrystals have larger bandgaps (E_g). It is important to recognize that the allowed energy levels of a semiconductor nanocrystal can be tuned and controlled with a behavior whose dependence is inversely proportional to the square of the radius of the nanoparticle.

Equation 3-2 describes the special case of a perfectly spherical zero-dimensional particle, with electron and hole confined in all three directions (x,y, and z in Cartesian coordinates). The actual energy levels may differ slightly due to deviations from a perfectly spherical shape. Higher dimensional nanoparticles exhibiting less quantum confinement are also possible including quantum wires (1-D), and quantum wells (2-D), until the bulk (3-D) electronic structure is reached. We can now consider three confinement regimes of zero-dimensional structures.

When a nanocrystal interacts with light of energy greater than or equal to its bandgap energy (E_g), an electron can be excited into a higher energy state in the conduction band, leaving behind a hole in the valence band. This pair, called an exciton, resides for a short time in the quantum-confined electron and hole energy levels described above. We can define a quantity called the exciton Bohr radius (a_B), which describes the most probable distance between electron and hole in the excited state as:

$$a_B = \frac{\hbar^2 \varepsilon}{\mu e^2} \quad (3\text{-}3),$$

where ε is the dielectric constant of the semiconductor, μ is the exciton reduced mass, and e is the elementary charge of an electron. Considering the relationship between the nanocrystal radius, a, and the exciton Bohr radius, a_B, three regimes are possible: $a >> a_B$ (weak confinement), $a \sim a_B$ (intermediate confinement), and $a << a_B$ (strong confinement). The CdSe nanocrystals in the current work fall into the strong confinement regime, which will only be considered here. Due to the respective negative and positive charge of

electron and hole, a Coulomb attraction proportional to $e^2/\varepsilon a$ must also be considered. The $1/a^2$ dependence of the confinement energy compared to the 1/a dependence of the Coulomb energy lead to a very small correction to the transition energy in the strong confinement regime. The lowest energy transition is given by the following equation:

$$\hbar\omega = E_g + \frac{\hbar^2\pi^2}{2m_h a^2} + \frac{\hbar^2\pi^2}{2m_e a^2} - 1.8\frac{e^2}{\varepsilon a}$$, where $\phi_{0,0} = \pi$. (3-4)

Considering the bulk semiconductor bandstructure, and solving the electron and hole levels for different sizes of CdSe nanocrystals, one can obtain the following picture of size-dependent energy levels shown in figure 3.2. The energy levels are labeled by their principle quantum number (1,2, or 3), orbital angular momentum (S, P, or D), and subscript *e* for electron states, and total angular momentum for hole states.

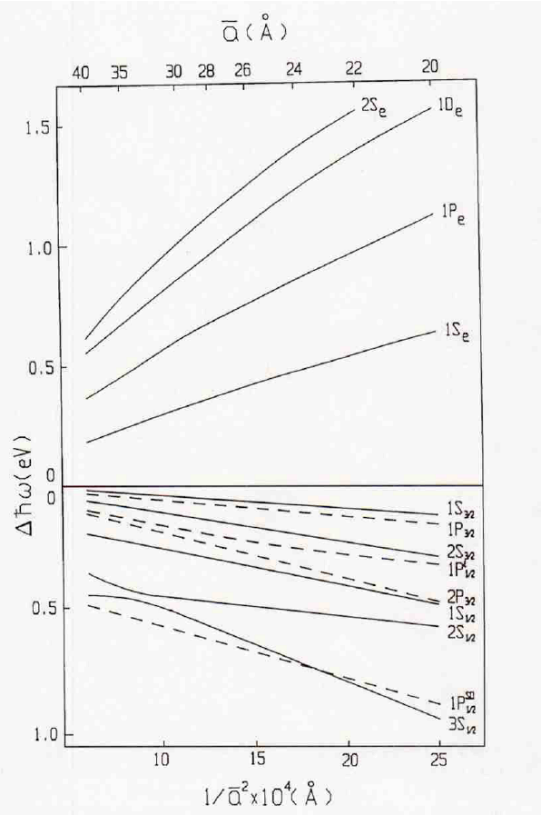

FIGURE 3.2: Size dependent electron and hole energy levels in CdSe nanocrystals. Taken with permission from the literature.[51]

The effective mass model with the parabolic band approximation predicts an 8-fold degenerate lowest excited state ($1S_{3/2}$-$1S_e$) (electron + hole levels) for spherical nanocrystals. In NCs, splitting due to the internal crystal structure, particle morphology, and the electron-hole exchange interaction divide this degeneracy into five states, ±2, ±1L, 0L, ±1U, 0U, which are each labeled by the total exciton angular momentum projection (L and U denote lower and upper levels, respectively). Figure 3.3 shows the calculated band-edge exciton structure for slightly elliptical NCs. The solid lines

represent optically active levels, while the dashed lines represent optically forbidden levels.

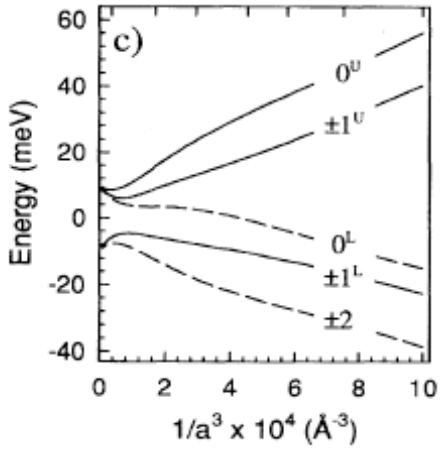

FIGURE 3.3: Calculated band-edge exciton fine structure for slightly elliptical CdSe NC. Taken with permission from the literature.[52]

To support the theoretically predicted band-edge exciton fine structure shown in figure 3.3, the emitting state of a nanocrystal was probed at low temperature (~2 K) using an applied magnetic field.[52] Excitation at the red-edge of the absorption spectrum in fluorescence line narrowing spectroscopy (FLN) reveals absorption into the lowest optically active state (±1L) and Stokes-shifted fluorescence emission from the "dark" band-edge (±2L) state (figure 3.4a). The Stokes shift plotted versus NC radius agrees well with the size-dependent calculations of splitting between the states (figure 3.4b). Under increasing applied magnetic fields, the PL lifetime decreases while the quantum yield remains the same, indicating an enhancement of the radiative rate. This effect is due to the shifting of excitonic spin states due to the magnetic field, comparable to the

molecular Zeeman effect, and analogous to the Stark effect caused by an electric field perturbation. This link with Stark effects is important as they play an important role in nanocrystal emission behavior, as is explored in the current work. Stark effects are discussed extensively in Chapter 5. The presence of an optically passive band-edge state strongly affects the electron-hole recombination as evidenced in the PL decay analysis. In the magnetic field dependent FLN spectra (figure 3.5), the zero-phonon line (ZPL) increases in intensity. This is due to the fact that recombination from the ±2L state is a phonon-assisted process. As the transition becomes more allowed with increasing field strength, there is less need for phonon assistance, thus the ZPL increases relative to the higher-order phonon replicas. These results indicate that the band-edge emission from NCs can be well understood by the intrinsic physics of the particle, but the authors acknowledge that surface effects may still play an important role in nonradiative processes. The effective mass model was further confirmed experimentally by size dependent studies of CdSe NCs using low-temperature (10K) photoluminescence excitation (PLE) and FLN spectroscopies.[53]

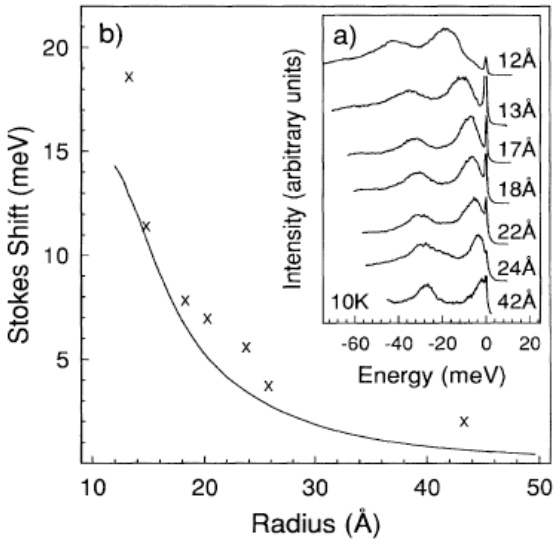

FIGURE 3.4: Fluorescence line narrowing spectroscopy of CdSe NCs. Taken with permission from the literature.[52]

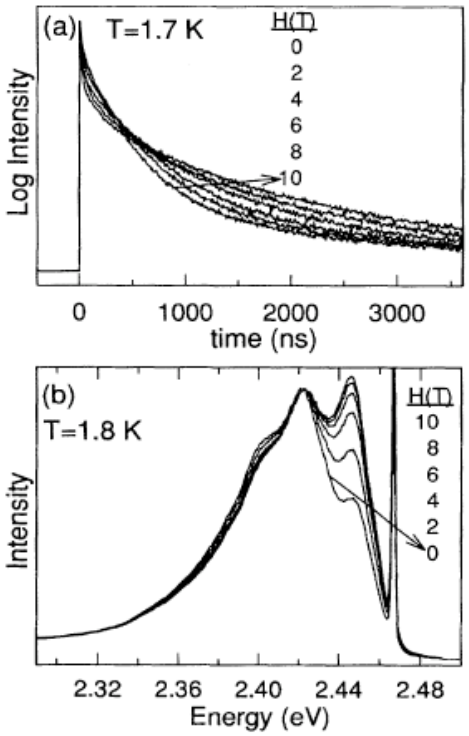

FIGURE 3.5: Fluorescence decays (a) and fluorescence line narrowing spectroscopy (b) of CdSe NCs under and applied magnetic field. Taken with permission from the literature.[52]

Theory predicts the electronic structure of individual nanocrystals. Conventional absorbance and PL spectroscopy of nanocrystals has confirmed many of the predictions of the intrinsic electronic structure by conducting experiments on ensembles of NCs. However, spectroscopy of ensemble measurements yields an average response of the entire sample to the excitation source. This is attributed in part to inhomogenous broadening due to the size distributions within a sample. Single molecule microscopy and spectroscopy eliminates this effect and helps elucidate the photophysics of individual molecules or nanocrystals without ensemble averaging. Spectroscopy of single nanocrystals has lead to the observation of spontaneous spectral diffusion[4, 5, 54] and fluorescence intermittency or "blinking"[6] dynamics.[6] The origins of these phenomena remain an active area of research, and are explored in this dissertation work.

CHAPTER 4: EXPERIMENTAL METHODS

4.1 Single Molecule Microscopy

4.1.1 Introduction

Light-matter interactions are at the heart of optical phenomena. Electromagnetic waves at optical frequencies ("light") can be used to interrogate a sample as shown in figure 4.1. Depending upon the material properties determined by its electronic structure, the electromagnetic waves incident upon the sample could be scattered, reflected, transmitted, absorbed, luminescent, or a combination of all five. The electromagnetic waves emanating from the sample may be collected by a system of optical components, and information about the physical properties of the matter observed or inferred. This is the basis for optical microscopy and spectroscopy. In the present research, these methods are used as an extremely powerful and non-invasive technique for material characterization.

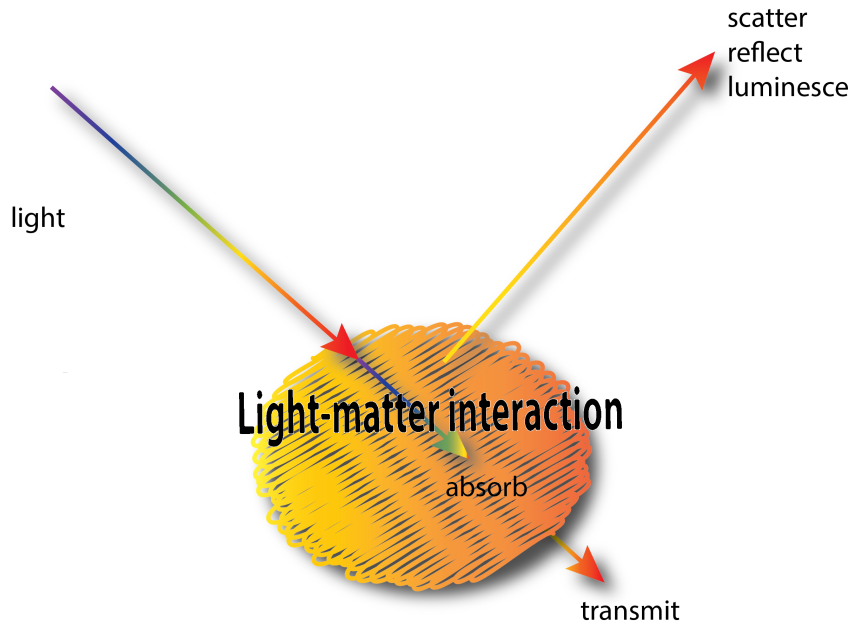

FIGURE 4.1: The possible outcomes of a light-matter interaction.

The utility of nanomaterials depends on our ability to understand their properties. Optical microscopy techniques are attractive because they can be used to image a variety of samples in different environments. In addition, visible light is not harmful to most sample types. However, the sheer nature of light presents a lower bound to the spatial resolution that can be obtained with conventional instrumentation.[55] This places a limit on 1) the size of the object that can be imaged, and 2) the minimum lateral separation needed to resolve two distinct objects. This barrier, known as the diffraction limit, along with advances in nanofabrication has stimulated the development of new forms of microscopy. The advent of single molecule techniques more than fifty years ago has enabled us to investigate optical properties at the nanoscale. Modern nano-optics

continues to push the limits of diffraction as optical microscopy and spectroscopy methods become more and more sensitive to nano-sized objects.

4.1.2 The Diffraction Limit

Conventional optical microscopy is restricted by the so-called diffraction limit in which light can only be focused to a spot size of ~λ/2, or ~200 nm, where λ is wavelength.[56] One might imagine that detecting the interactions of light with features much smaller than 200 nm is nearly impossible. The emerging field of nano-optics offers new approaches for circumventing the diffraction limit including confocal microscopy, and near-field microscopy. We will first explore how this fundamental limit arises, and discuss methods of overcoming the diffraction limit. Confocal microscopy is primarily discussed, as it is the central tool in the current research. What follows in sections 4.1.2-4.1.5 is a summary from Novotny and Hecht.[56]

We can define the propagation of a photon of light in free space in terms of its wavevector **k**, where $k = \sqrt{k_x^{\,2} + k_y^{\,2} + k_z^{\,2}} = 2\pi / \lambda$. The wavevector **k**, with units of inverse wavelength, has components $\mathbf{k}_x$, $\mathbf{k}_y$, and $\mathbf{k}_z$ in Cartesian coordinates as shown in figure 4.2. A light field originating from a particular source can be thought of in the quantum sense as a collection of photons, each with a different value of **k**. Alternatively, in the classical sense, the field can be represented by a superposition of plane waves of the form: $A_0 cos(\mathbf{k}_x x + \mathbf{k}_y y + \mathbf{k}_z z)$, where A_0 is the wave amplitude, each traveling at

different angles. Spatial confinement of this light field is related to the spread in magnitude of the wavevector components in each direction x, y, and z.

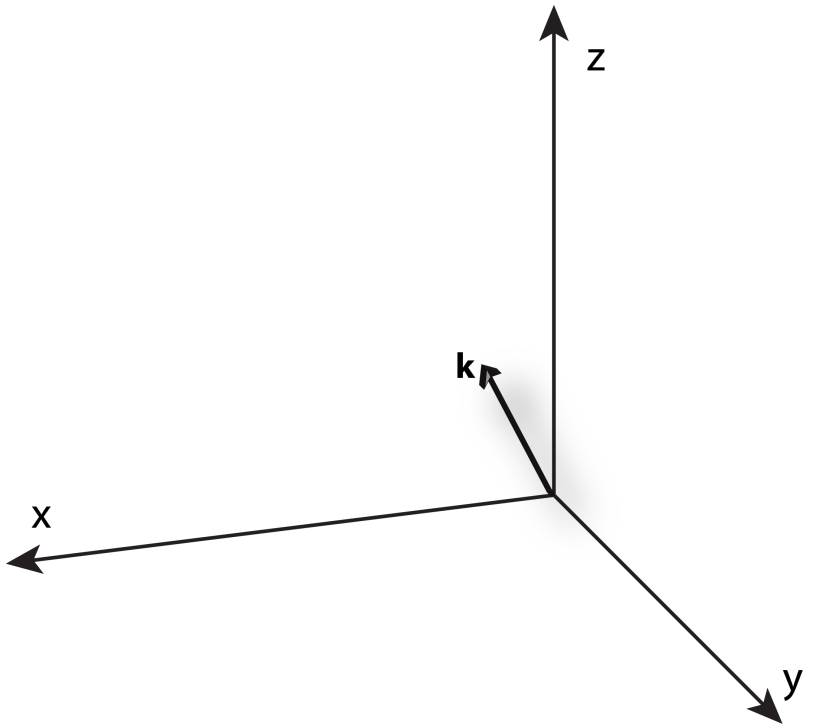

FIGURE 4.2: A wavevector, **k**, on a Cartesian coordinate system. The components of the wavevector are $\mathbf{k}_x$, $\mathbf{k}_y$, and $\mathbf{k}_z$. The wavevector points in the direction of propagation of the wave.

Applying the Heisenberg uncertainty principle, the product of the uncertainty in spatial position of a microscopic particle (i.e. a photon) in a certain direction and the uncertainty in that component of its momentum cannot be smaller than ħ/2, where ħ is the reduced Planck constant. Therefore, in the x direction, $\Delta\hbar k_x \cdot \Delta x \geq \hbar/2$, where

$\hbar k_x = p_x$, the momentum in the x direction, and Δx is the uncertainty in the x component of the position of the particle. This relation can be rewritten as:

$$\Delta x \geq \frac{1}{2\Delta k_x}.$$

Thus, if the range of $\mathbf{k}_x$ values becomes very large, the light field can be maximally confined to a particular location. In free space, the maximum possible value of $\mathbf{k}_x$ is the total wavevector $\mathbf{k}=2\pi/\lambda$. This leads to the expression for the Rayleigh diffraction limit:

$$\Delta x \geq \frac{\lambda}{4\pi}.$$

The methods of nano-optics aim to increase the range of values of one or more components of the wavevector in order to overcome the diffraction limit.

4.1.3 Light Confinement

Consider a space in which there are two perpendicular directions, *x* and *z*, for simplicity as shown in figure 4.3A. Mathematically speaking, if we increase the *x* wavevector component, $\mathbf{k}_x$, to values greater than **k**, while the perpendicular component, $\mathbf{k}_z$, becomes purely imaginary, we can maintain the required $k = \sqrt{k_x^{\,2} + k_y^{\,2} + k_z^{\,2}} = 2\pi/\lambda$ condition as shown in figure 4.3B. Increasing $\mathbf{k}_x$ will raise the possible range of wavevector values, $\Delta\mathbf{k}_x$, decreasing Δx according to the Rayleigh limit, and thereby going beyond as desired. However, the imaginary component, $\mathbf{k}_z$, requires further consideration.

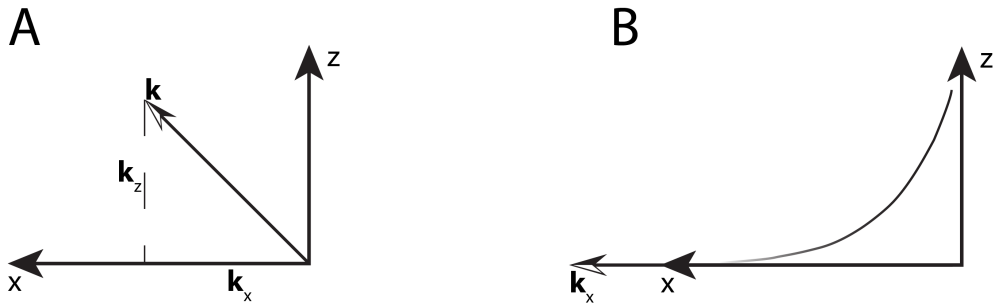

FIGURE 4.3: A) A wavevector, **k**, in an x-z plane, with components $\mathbf{k_x}$ and $\mathbf{k_z}$.
B) The component $\mathbf{k_x}$ increases to a value greater than **k**, while the $\mathbf{k_z}$ component becomes purely imaginary, indicated by the exponential.

Light fields can be described in the classical sense by plane waves of the complex exponential form $e^{i\mathbf{kr}}$, where **k** is the wavevector and **r** is the position vector (a point in space with components x and z in this case). The condition of an imaginary component in the z direction leads to the solution of an exponentially decaying light field in one direction, and an impractical exponentially increasing field in the other. The exponentially decaying component is an evanescent field represented by $e^{-|\mathbf{k}|\mathbf{r}}$ from the expression for a plane wave, which is a non-propagating light field. Thus, the Rayleigh limit is only valid in infinite free space. Instead, confinement of light fields beyond this limit can be achieved in inhomogeneous media, which describes light-matter interactions at interfaces and boundaries. One can tune the behavior of light fields by introducing these interfaces and boundaries, which equate to combining materials with different optical properties. By fulfilling boundary conditions for the behavior of electromagnetic

fields at interfaces according to Maxwell's equations, one can create a state in which the exponentially decaying evanescent field can exist without its exponentially increasing counterpart.

The presence of both real and imaginary field components leads to a field described by plane waves ($e^{i\mathbf{kr}}$) and evanescent waves ($e^{-|\mathbf{k}|\mathbf{r}}$). A central goal of nano-optical methods is to retain the exponentially decaying evanescent components of a light field upon detection. This can be achieved with near field detection, in the case of Near-Field Scanning Optical Microscopy (NSOM), or far field detection, as in Confocal Microscopy. The details of Confocal Microscopy are reserved for section 4.1.6.

4.1.4 Lasers

Laser beams are an obvious choice in applications that require strongly confined light as their electromagnetic fields propagate mainly along a single direction. This means that as the beam propagates longitudinally, there is little propagation, or spreading, in the transverse direction. In this case, the wavevectors, $\mathbf{k}=(\mathbf{k}_x, \mathbf{k}_y, \mathbf{k}_z)$, are almost parallel to the direction of travel, with $\mathbf{k}_x$ and $\mathbf{k}_y$ much smaller than $\mathbf{k}$. As a result, laser beams can be strongly focused using objective lenses as shown in figure 4.4. The result is a paraxial Gaussian beam, for which the electric field distribution along the transverse plane is shown in the inset. This is the case for a single mode laser beam that has either originated from a high quality laser cavity or one that has been spatially filtered with a pinhole or a single mode fiber. We utilize a single mode fiber in our experiment to

generate a single mode beam with the lateral spatial profile shown in the inset of figure 4.4. As we will see later, the beam profile is not exactly Gaussian, but can be very accurately approximated with a Gaussian profile.

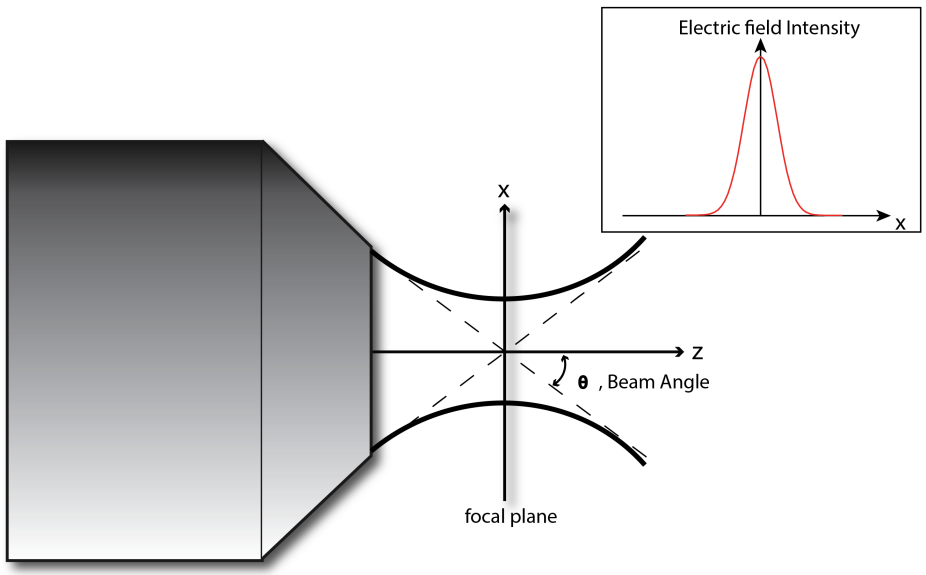

FIGURE 4.4: Focusing of laser beam by objective lens. The inset shows the electric field distribution along the transverse (x) plane, which has a nearly Gaussian profile.

Figure 4.4 shows a laser beam propagating in the z direction whose light field is focused to a small beam waist at some distance from the objective, with the beam diverging again away from this focal point. The ability of the lens to collect and focus light is reflected in its numerical aperture (NA= $n \sin \theta$), where n is the refractive index of the medium, and θ is the beam angle shown in figure 4.4. Specialized lenses are

designed for water or oil immersion, which have a higher refractive index than air, thus increasing NA, and the focusing power of the lens. Generating a narrow beam waist and therefore spot size is critical for confocal microscopy. It is a defining factor in determining the resolution of a system.

4.1.5 Spatial Resolution

Spatial resolution is a central concept in optical microscopy. Specifically, what is the minimum separation of two point-like objects in a plane at which they can still be distinguished from a single object? The Abbe diffraction limit defines this distance rather arbitrarily as:[56]

$$Min = 0.6098\frac{\lambda}{NA}$$

We will find that this is not an insurmountable limit. Nano-optical methods are capable of achieving higher spatial resolution.

Consider a single emitter such as an individual fluorescent molecule in an object plane as shown in figure 4.5. This small molecule can be regarded as occupying a single point in space, or a delta function. A Gaussian laser beam from our earlier discussion excites this molecule. The fluorescence from the molecule is collected by an objective lens and directed by additional optics to a detector ~1 meter away at the image plane. The wavevectors, $\mathbf{k}=(\mathbf{k}_x, \mathbf{k}_y, \mathbf{k}_z)$, of the fluorescence photons carry all of the optical information about the object. During propagation from object plane to image plane, some components of the wavevectors are lost, and we are not able to accurately

reconstruct the original point source. The lost components of the wavevectors include all of the evanescent components, and some of the plane wave components. Thus the detected image of the point will have a finite size due to this uncertainty, which is termed the point spread function (PSF). This is regarded as a measure of the resolving power of an optical system. The more narrow the PSF, the better the resolution of an optical system.

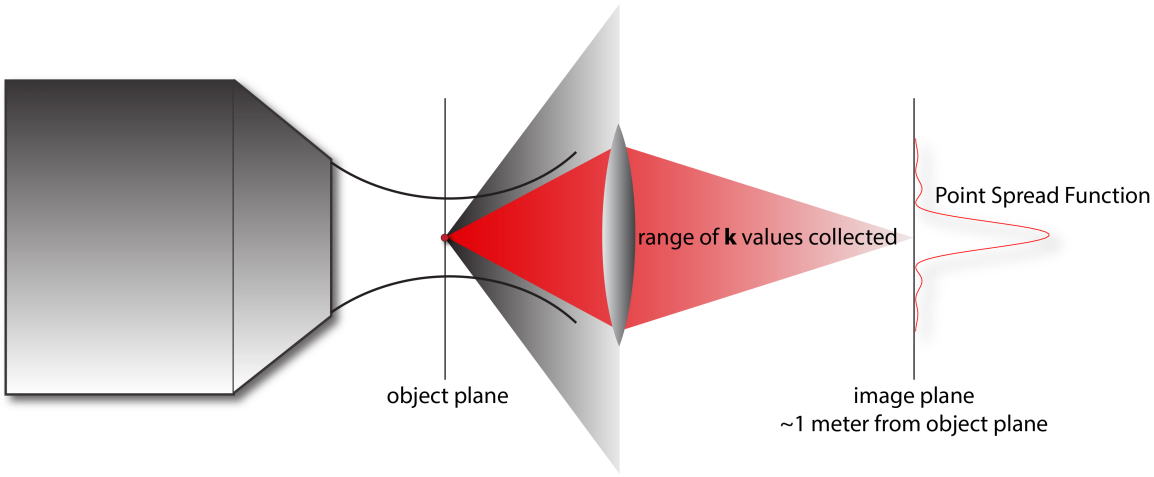

FIGURE 4.5: Propagation of signal from single fluorescent molecule from object plane to image plane. Loss of wave vector components leads to a point spread function, which reflects an uncertainty in the measurement.

The single molecule emitter in the above example can be approximated as an electric dipole, which represents the smallest radiating electromagnetic unit. The PSF of an electric dipole is an *Airy function*, as shown in figure 4.6. It closely resembles a Gaussian function, and is often approximated as such. Considering two radiating dipoles

close together, each with their own PSF, Abbe described the distance at which the maximum of one PSF coincides with the first minimum of a second PSF as the resolution limit, shown in the figure 4.6. This calculation is based on the special case of two parallel dipoles oriented parallel to the optical axis. It is clear that this does not place a hard limit on the resolution of an optical system since the PSF depends on the orientation of the dipole, and the lateral distance defined is arbitrary. Knowledge of the PSF of a system is a nano-optical method used in confocal microscopy to overcome the diffraction limit.

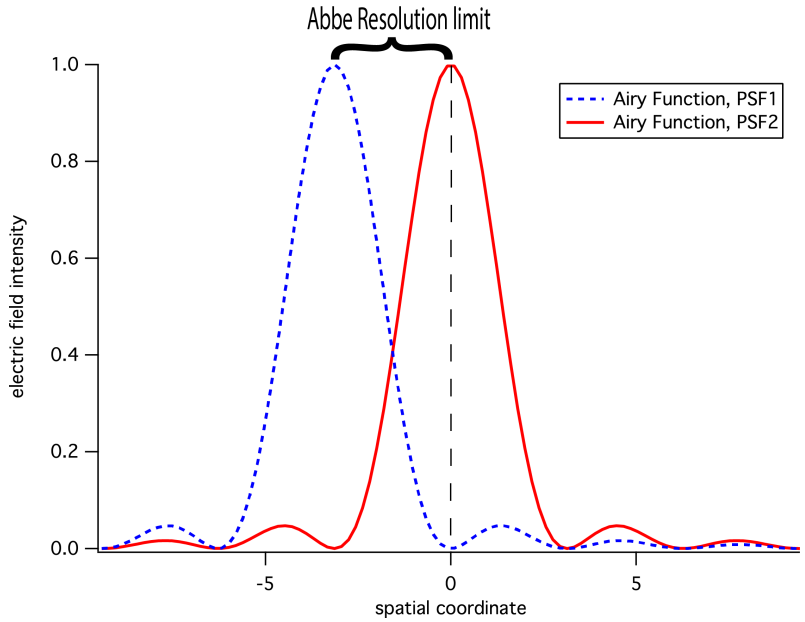

FIGURE 4.6: Point spread function (PSF) of two nearby single molecules, or radiating dipoles, each represented by an Airy function. The Abbe resolution limit as described in the text is labeled on the graph.

4.1.6 Confocal Microscopy

Laser scanning confocal microscopy (LSCM) takes advantage of the point spread function in two ways: 1) it uses for excitation a laser beam whose transverse spatial profile is very nearly Gaussian, which is its own PSF and 2) the detection of a point source (single emitter) is also a PSF. Thus we take advantage of the PSF twice and the total PSF is the excitation PSF multiplied by the detection PSF, which is a narrower function as shown in figure 4.7. Measurement of the PSF of an optical set-up enables accurate reconstruction of the original point source by mathematical deconvolution. A

detailed mathematical implementation of deconvolution is beyond the scope of this dissertation.

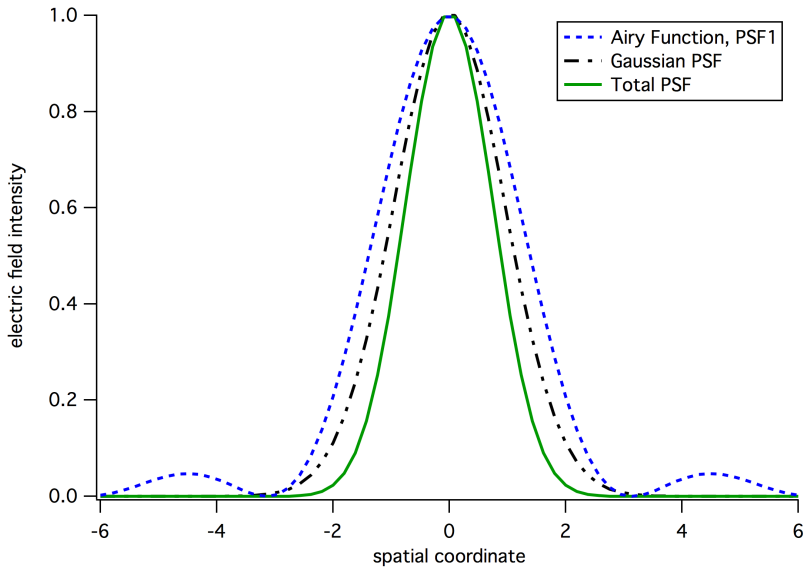

FIGURE 4.7: Two point spread functions (PSF) used in confocal microscopy. The total PSF is narrowest, indicative of high spatial resolution.

To collect an image, the Gaussian beam is scanned over a small sample area in the object plane, collecting information as it moves along, which is detected at the image plane. The type of information collected depends on the light-matter interaction, which may be fluorescence or scattering for example. On the detection side, a pinhole may be used to reject out-of-focus signal. Thus, the object and image planes are confocal. Scanning confocal microscopy offers the advantage of high spatial resolution and a high signal-to-noise ratio (SNR) over wide-field techniques due to illumination of a small

sample area and rejection of out-of-focus signal. LSCM has found applications in disciplines from physics to biology due to its versatility and advantages.

Materials studied in the present research are fluorescent nanoscale semiconductors. Optical characterization involves exciting the material with a visible laser, which the sample absorbs temporarily. After some time, which is characteristic of the material, the absorbed energy is released in the form of fluorescence. We detect the fluorescence using a confocal microscope system as described above. The specific components of our system are discussed in section 4.3.

4.2 Time-Correlated Single Photon Counting

4.2.1 Introduction

While confocal microscopy is a powerful tool for imaging, we are often after additional information from the sample. For the fluorescent nanoscale semiconductors, or quantum dots, in the current research, we are interested in time-resolved fluorescence. Time-dependent spectroscopies yield dynamical information about the excited state of quantum dots. Using a pulsed laser source, one can generate a temporary excited state in the quantum dot. Some time after excitation, a fluorescence photon may be emitted as the excited state decays. In-depth characterization of the decay of an excited state provides invaluable information about the charge carrier dynamics in nanocrystal systems. This can be accomplished using single photon counting detectors in conjunction with a real-time signal processing card.

Time-correlated single photon counting (TCSPC) detection systems sense the arrival of individual photons at the detector and send electrical pulses to the card for processing. Each detected photon is converted to an electrical signal by the detector and is sent to the TCSPC card. Correspondingly, a separate electrical signal is sent to the card each time the laser sends out a pulse. The rate at which the laser pulses can be controlled in the experiment. Each signal receives a time stamp upon arrival, as shown in figure 4.8. This gives rise to a synchronized timing system and a histogram, which is stored in real time. The figure shows an excitation, and subsequent emission of a photon. The length of time between excitation and emission is termed the *microtime*. The TCSPC card generates a histogram of the photon arrivals from many excitation-emission cylces, which represents the decay of the excited state. In an alternate timing mode, the fluorescence photon is also given an absolute time tag, relative to the start of data collection, which is called the *macrotime*. Analysis of the decays generated from the microtimes, and trajectories produced from the macrotimes yields dynamic information about the quantum dots across many decades of time.

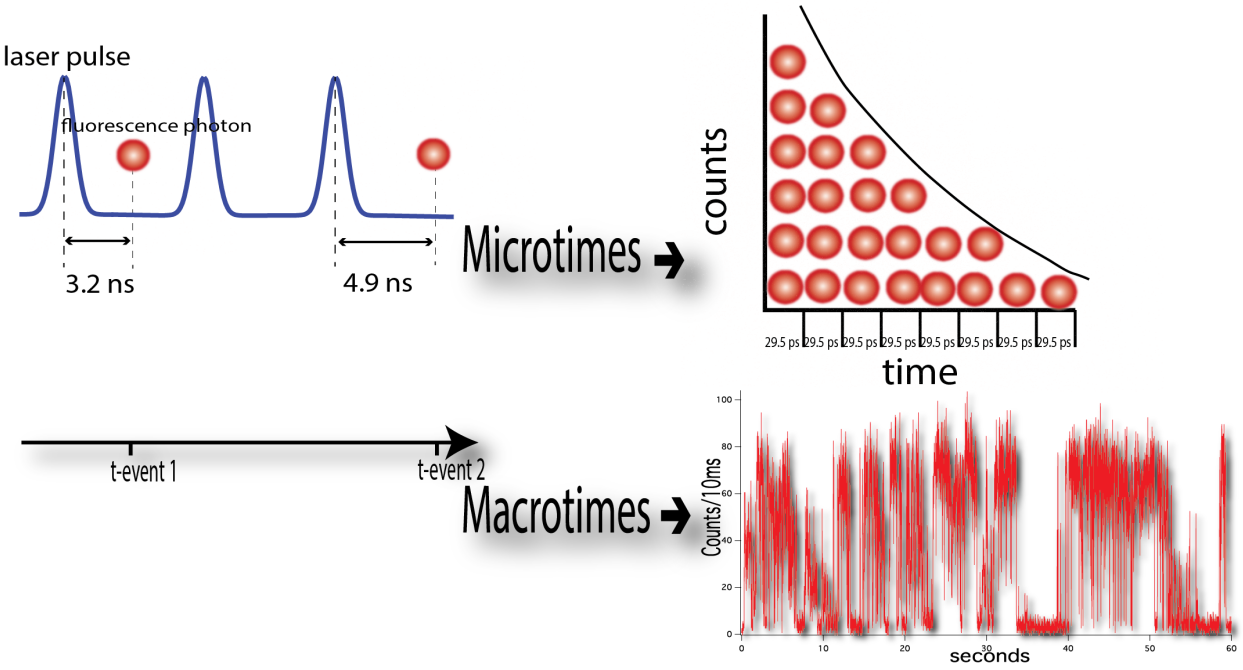

FIGURE 4.8: Principle of Time-Correlated Single Photon Counting (TCSPC).

4.2.2 Measurement Modes

TCSPC enables correlation of photon arrival events 1) relative to the excitation and 2) relative to the start of the experiment. For mode 1, each detected photon is given a time stamp relative to the excitation pulse (microtime). Essentially, each photon is stored in a bin, which has a predetermined time width as shown in figure 4.8. The result is a histogram, which represents the decay of an excited state. Since fluorescence decays of most molecules and quantum dots are hundreds of picoseconds to hundreds of nanoseconds, high-resolution timing is needed. Thus, the time widths should be on the order of tens of picoseconds to measure the shortest decays. For mode 2, each detected photon is given a time tag relative to the start of data acquisition (macrotime). The result

is a quasi-continuous record of each photon arrival, which can be processed further for data analysis.

4.2.3 Instrument Response Function

The resolution of a TCSPC experiment is measured by its instrument response function (IRF). This is the temporal analogue of the spatial point spread function discussed previously for the optical system. Similarly, the more narrow the IRF, the more precise the timing. The width of an IRF depends on the laser pulse width, detector response, and signaling electronics. Thus, the measured fluorescence decay is actually a convolution of the IRF and the true decay behavior, which can be extracted using mathematical deconvolution.

An instrument response is recorded by measuring the response of the system to an instantaneous process, namely scattering. A scattering medium is placed in the path of the excitation source, and directed to the detector. Common scattering solutions include diluted milk, non-dairy creamer, or polystyrene beads in solution. A sample instrument response from our system is shown in figure 4.9. It was obtained by placing a thin glass coverslip in the sample holder with immersion oil, without any additional scattering medium. A 470 nm pulsed laser is scattered off of the glass, and detected. The FWHM is ~ 300 ps.

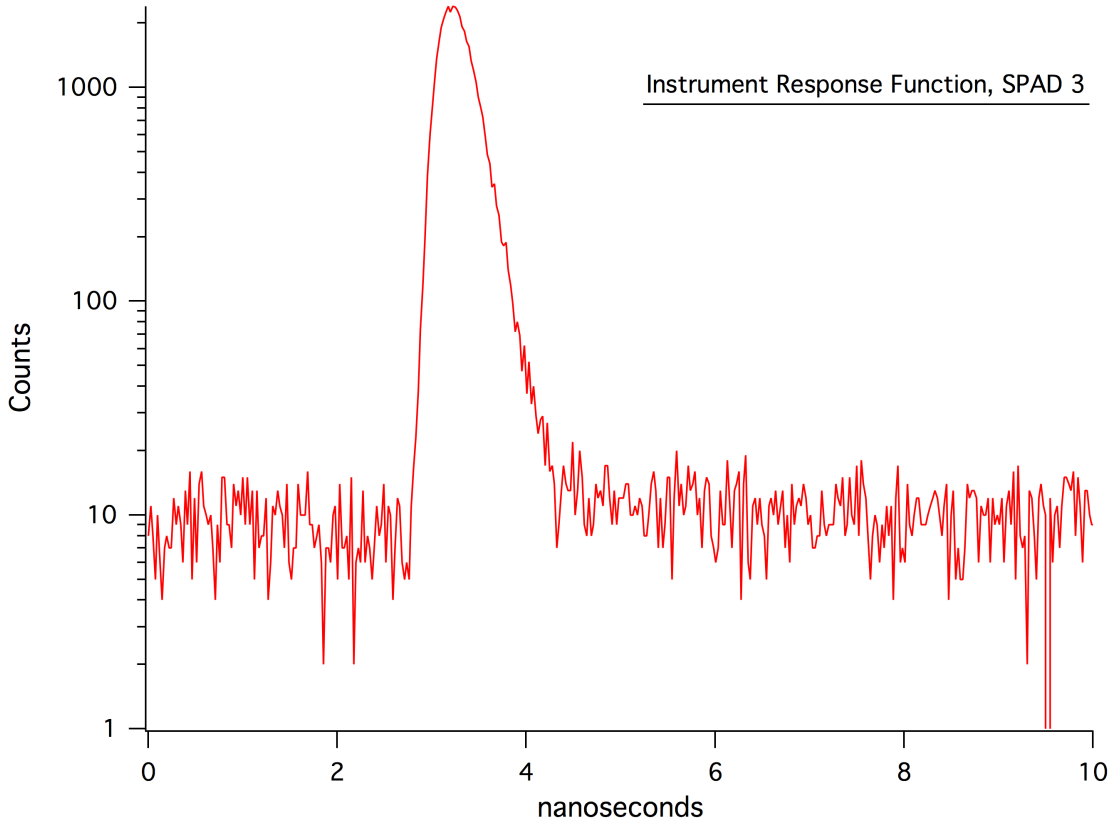

FIGURE 4.9: Instrument Response Function collected in our lab for single photon avalanche photodiode (SPAD) 3 (see figure 4.10).

4.2.4 Detectors

The particular method by which single photons are detected depends on the type of detector. The two most common types are photo multiplier tubes (PMT) and single photon avalanche photodiodes (SPAD) (or simply avalanche photodiode (APD)).[57] A PMT relies on the photoelectric effect for photon detection. It consists of a photocathode, or a light sensitive electrode material, which emits an electron upon absorption of a photon. Since the current generated from a single photon is insufficient signal, the emitted photon is amplified through a secondary electron emission gain process before

reaching the anode as an output pulse. A drawback of PMTs is that photoelectrons are emitted in all directions, which limits the quantum efficiency. Conversely, SPADs rely on semiconductor materials that generate an electron-hole pair upon absorption of a photon. An electric field is needed to separate the electron and hole. Similar to PMTs, a gain process amplifies the signal before output. This is called the avalanche effect in which new electron-hole pairs are generated in a material by acceleration of free charge carriers leading to impact ionization. Compared to PMTs, SPADs have smaller active areas that make alignment of the optical system more difficult, and exhibit smaller gains, which reduces the output signal.

The detector contributes to the width of an IRF in its conversion of a photon to an electrical signal on the order of hundreds of picoseconds.[58] Additionally, there is some dead time after detecting a photon in which the detector cannot register another photon, typically on the order of tens of nanoseconds. Detectors vary in sensitivity, size of active area, dark counts (noise), dead time, and photon detection (quantum) efficiency. Thus, the choice in detector depends on the particular needs in an application. The components of our system are outlined in the following section.

4.3 Experimental Setup

For single nanocrystal spectroscopy, our apparatus is a homebuilt confocal microscope. The schematic is shown in figure 4.10. Each component is described in what follows.

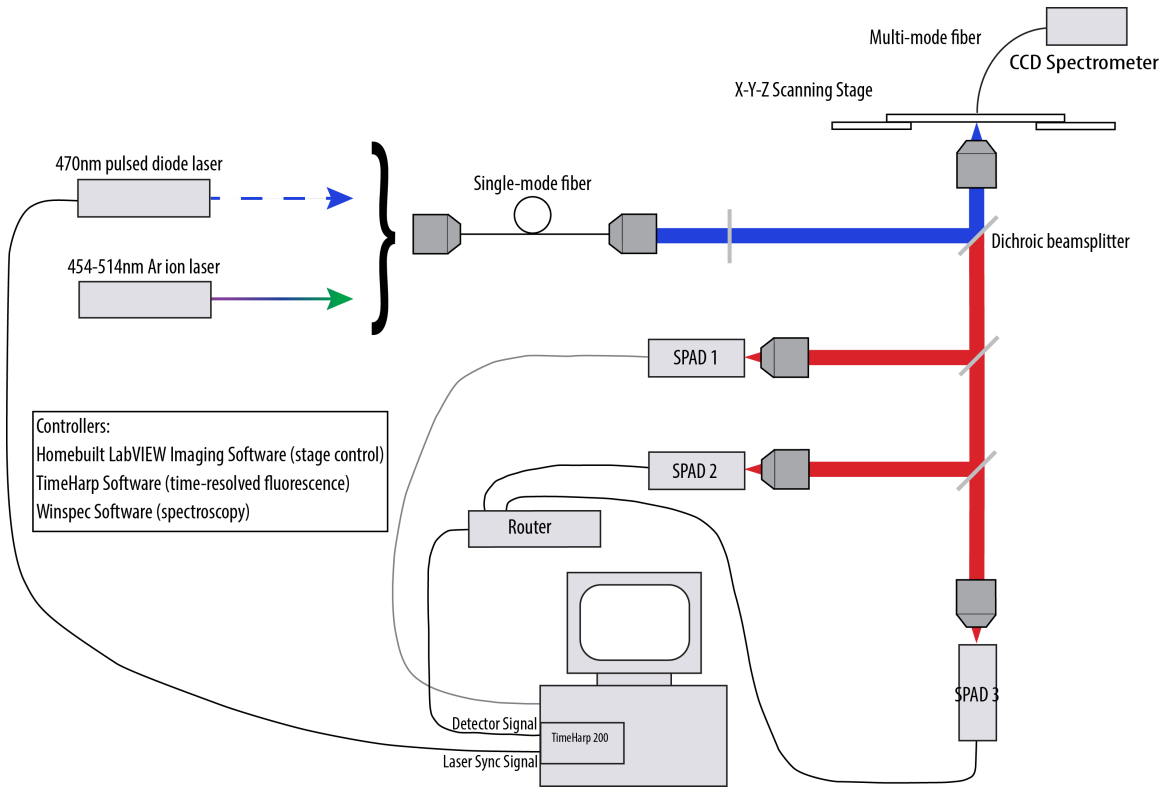

FIGURE 4.10: Schematic of homebuilt confocal microscopy system.

Excitation Source:

The excitation source is pulsed diode laser (PDL 800-B, PicoQuant), with the choice of 405 nm and 470 nm laser heads (LDH Series). The pulse repetition frequency of the laser may be controlled from 2.5 MHz to 40 MHz. The pulse FWHM is ~90 ps. Detailed specifications of the PicoQuant lasers can be found at www.picoquant.com. The option of a continuous tunable argon-ion laser (454-514 nm) is available, however fluorescence decays are not possible with that source.

Objective Lens/Single Mode Fiber:

The objective lens (10x, Nikon) focuses and collimates the laser beam, and directs it to a single mode optical fiber. This fiber picks out the fundamental mode of the laser, which is roughly Gaussian in its spatial distribution. This beam is used for excitation and imaging. An additional objective lens (10x, Nikon) further focuses and collimates the beam before it reaches the dichroic beamsplitter.

Dichroic Beamsplitter (DBS):

The DBS is a semi-transparent mirror that is designed to transmit and reflect wavelengths above and below a certain cut-off. Depending upon the set-up, we can choose from 430, 500, 550, 585, and 630 nm cut-offs.

Mirror:

A familiar optical element, which reflects incident light.

Sample Objective:

The objective is a Zeiss, 1.25 NA, oil immersion lens. It focuses the excitation beam on the sample in an inverted geometry (from below the sample). It also collects the fluorescence from the sample and directs it back to the mirror and through the dichroic beamsplitter.

X-Y-Z Piezoelectric Scanner:

A Mad City Labs, Inc. three dimensional nano-positioning system with 75 x 75μm (x,y) and 10 μm (z) scan range is used to scan the sample, while the objective remains in a fixed position. The scanner moves a precise amount in the given dimension when a voltage is applied. A voided aluminum plate is used as the sample holder. Samples are prepared on 25 x 25 mm glass coverslips (Ted Pella), which are adhered to the plate.

Detectors:

Single photon avalanche photodiodes (SPAD, PDM Series, PicoQuant) are used for detection. The specifications are as follows in table 4.1. In our system, the detector serves as a pinhole.

TABLE 4.1: Specifications of Detectors

Specification	**Value**
Active Area	50 μm
Timing Resolution	< 50 ps
Quantum Efficiency	49% at 550 nm
Dark counts	~75 counts per second
Dead time	70 ns
IRF	~56 ps FWHM @ 470 nm

Imaging Software:

The interface for imaging is a homebuilt LabVIEW program. It controls the movement of the piezoelectric x-y-z scanning stage by controlling the applied voltage in each direction. It is capable of scanning at various speeds and image pixel resolutions. Figure 4.11 shows a screen shot of the imaging interface. The lower left panel (Channel 0) is a single molecule image with a line scan along the X (vertical) axis shown above. The number of pixels per line can be controlled from 64 to 1024 to change the image resolution (middle center). In addition, the zoom feature (bottom center) allows us to zoom in on a single NC. Using Channel 1 on the right panel enables simultaneous two-channel imaging if two detectors are used. The impingent signal can be split between the two detectors by a dichroic, polarizing, or 50/50 beamsplitter for various applications.

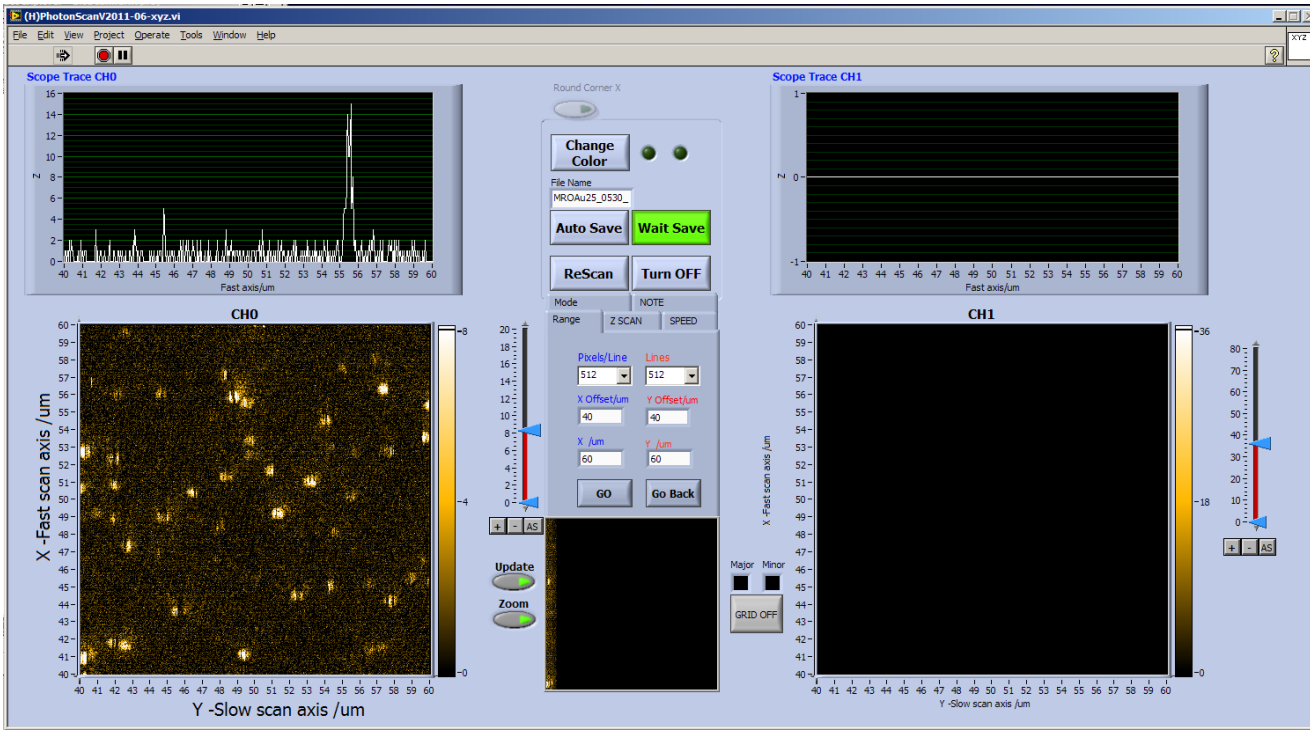

FIGURE 4.11: Screen shot of imaging interface.

TCSPC Card/TimeHarp Software:

The TimeHarp 200 (PCI Board for Time-Correlated Single Photon Counting) is used for processing single photon signals. The TimeHarp 200 enables time tagging of each detected photon i) relative to the laser excitation pulse and ii) relative to the start of the experiment. For histogramming of microtimes, the minimum bin resolution is 29.5 picoseconds, which is used for all experiments. The interface for time-resolved fluorescence measurements is the TimeHarp software (*version 6.1.0.0*). For detailed operation information please refer to the literature available at www.picoquant.com.[59]

Multimode Fiber/CCD Spectrometer/Winspec Software:

Placed above the sample, the multimode fiber collects fluorescence and directs it to the spectrometer, which has a liquid nitrogen cooled/charge coupled device (LN/CCD) detector (Princeton Instruments, Inc.). The CCD has a spectral range of 400-1000 nm over 1340 pixels for a spectral resolution of 0.45 nm per pixel.

4.4 Lab Capabilities

Figure 4.12 summarizes the capabilities of our lab using the set-up described in section 4.3. These capabilities are summarized in the following sections.

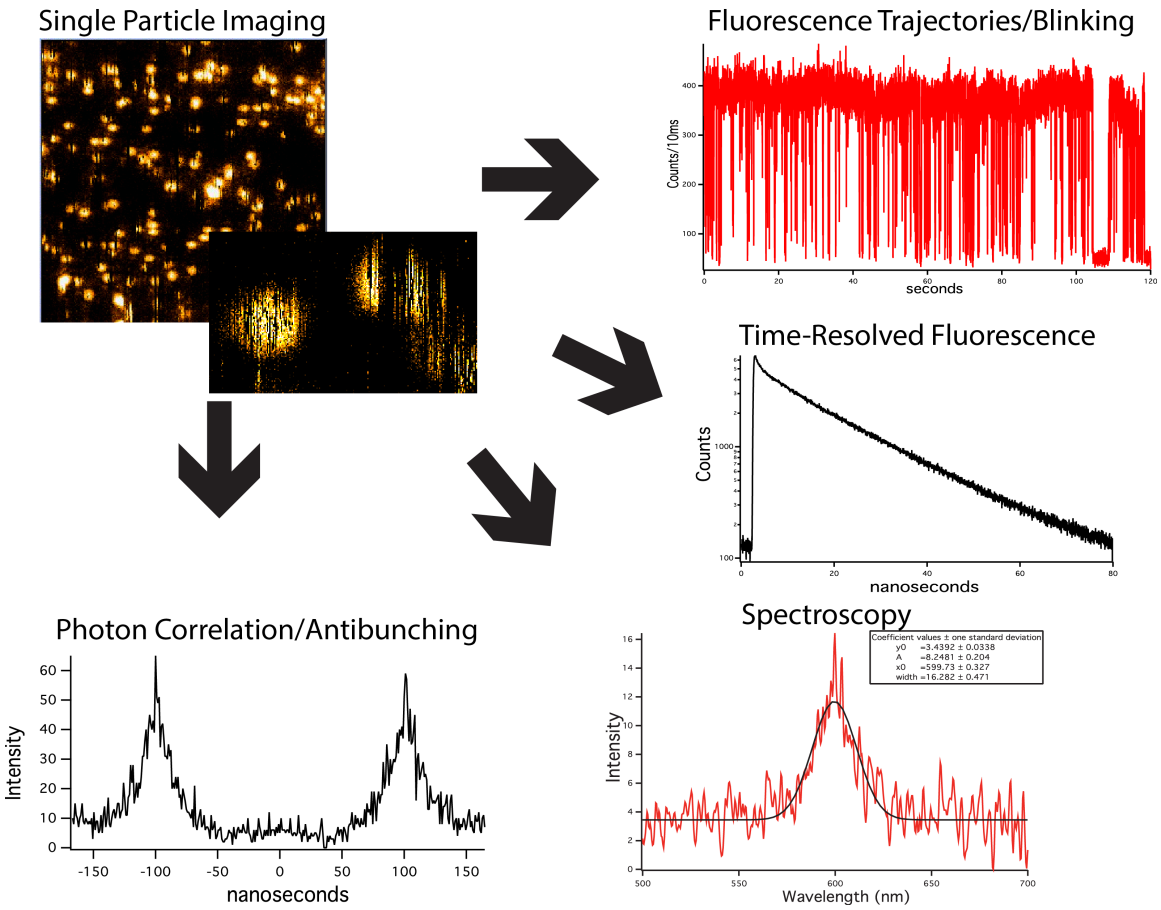

FIGURE 4.12: Capabilities of the Moyer lab for single molecule analysis.

Single Particle Imaging:

The confocal system enables us to image single particles, which opens the door for a range of characterization. The upper left of figure 4.12 shows a typical image of single quantum dots spin-cast in poly-(methyl methacrylate) (PMMA). The main image is a 19.5 x 19.5 μm scan with 256 x 256 pixel resolution. The inset is a zoomed-in image of single quantum dots. The images reflect the blinking nature of quantum dots.

Fluorescence Trajectories/Blinking:

By "parking" on the center of a single dot and collecting fluorescence photons using the SPAD detectors and the TCSPC card, we can generate fluorescence versus time traces, or fluorescence trajectories, from the macrotimes discussed previously as shown in the upper right of figure 4.12. Traces such as these further reflect the blinking nature of quantum dots.

Time-Resolved Fluorescence:

While "parked" on a single quantum dot, we can also collect fluorescence decays from the microtimes, as shown in the middle right of figure 4.12. The time tagged-time-resolved (T3R) mode in the TimeHarp software allows simultaneous collection of macrotimes and microtimes.

Spectroscopy:

Coupling the fluorescence of a single quantum dot from above into the CCD spectrometer enables us to collect the fluorescence of individual quantum dots. The lower left quadrant of figure 4.12 shows a typical spectrum of a single quantum dot. The spectrum was acquired over 10 seconds.

Photon Correlation/Antibunching:

Using a modified set-up shown in figure 4.13, called the Hanbury Brown-Twiss (HBT) geometry,[60] we can correlate the arrival times of photons collected from nanocrystals that are split between two detectors. With this technique we can confirm the presence of multiple nanocrystals or occurrence of multiple exciton emission. The HBT setup is a start-stop technique that enables correlation of time delays between photons emitted from a fluorescent sample. A 50/50 beamsplitter divides the fluorescence signal from the sample into two single photon counting detectors, one of which is designated as the start and the other as the stop. Detection of a photon at one detector starts an internal clock, which stops when a photon registers at the other detector. The time delays (τ) between start and stop photon events are correlated in a histogram, with zero time delay indicating simultaneous detection of photons at both detectors. A representative correlation histogram is shown in the bottom left of figure 4.12. The absence of a peak at zero time delay ($\tau = 0$) denotes photon antibunching behavior. If a peak appears at $\tau = 0$, this indicates either a) there are two or more photon emitters present or b) multiple

excitons are excited and emitted from the same fluorophore during one laser pulse. Side peaks occur at the repetition frequency of the laser, indicating consecutive single photon emission. This method of photon correlation is a powerful technique for characterizing excited state dynamics of single emitters.

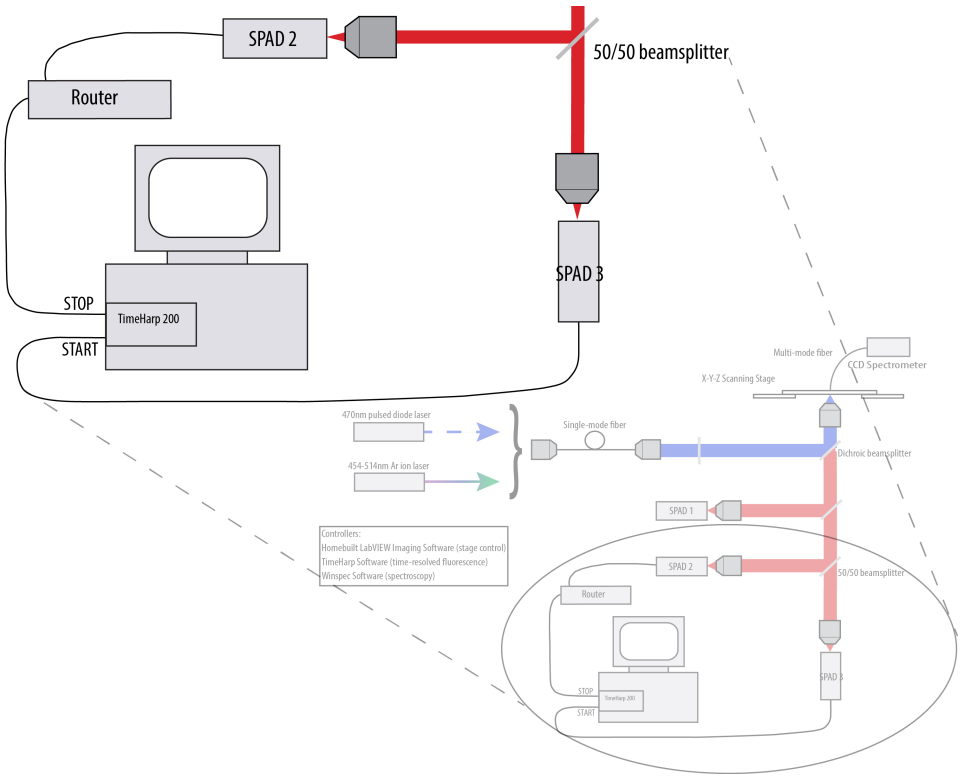

FIGURE 4.13: Schematic of Hanbury Brown-Twiss geometry for photon correlation spectroscopy.

These capabilities enable simultaneous collection of single particle fluorescence dynamics, decays, and spectra. This suite of experimental methods encompasses all data acquired and analyzed in the current dissertation research. An additional electrode device

for electric field characterization was fabricated using the instrumentation outlined in the following section.

4.5 Cleanroom Instrumentation

The following instruments were used in fabrication of electrode devices. Fabrication was carried out in a Class 100 CleanRoom (Grigg Hall). A more detailed description of the fabrication process is given in Appendix B.

1. Brewer Spin Processor

    -Coat substrates with photoresist

2. Quintel Ultraline Q 4000-6 Contact Mask Alignment System

    -Expose photoresist with UV light using photomask to create pattern on substrate

3. Surface Technology System (STS) ASE® Plasma Etch System

    -Remove excess photoresist

4. Kurt J. Lesker PVD-75 Electron Beam Evaporation and AJA International ATC 1800-F Sputter Deposition System

    -Metal deposition

CHAPTER 5: LITERATURE REVIEW OF REVELVANT TOPICS

5.1 Fluorescence Intermittency or "Blinking"

Blinking describes the intermittent behavior of fluorescence observed in single emitters including atoms, molecules, ions, and nanocrystals.[61] It is an important and inevitable topic encountered in the current research of single nanoscale emitters, and thus deserves extensive development of background knowledge. Herein, we discuss blinking as a fundamental phenomenon of single emitters, and present several different models to explain the distributed kinetics involved in blinking dynamics. While there have been many models presented to explain blinking, we highlight a few to show the diversity of thought. It should be noted that at present, it still remains a poorly understood phenomenon.[62]

Blinking can be observed in the fluorescence intensity vs. time trace collected in our lab of a single nanocrystal under continuous excitation by a laser as shown in figure 5.1. The trace consists of abrupt transitions from emitting ("on") to non-emitting ("off") states, all with seemingly arbitrary length.

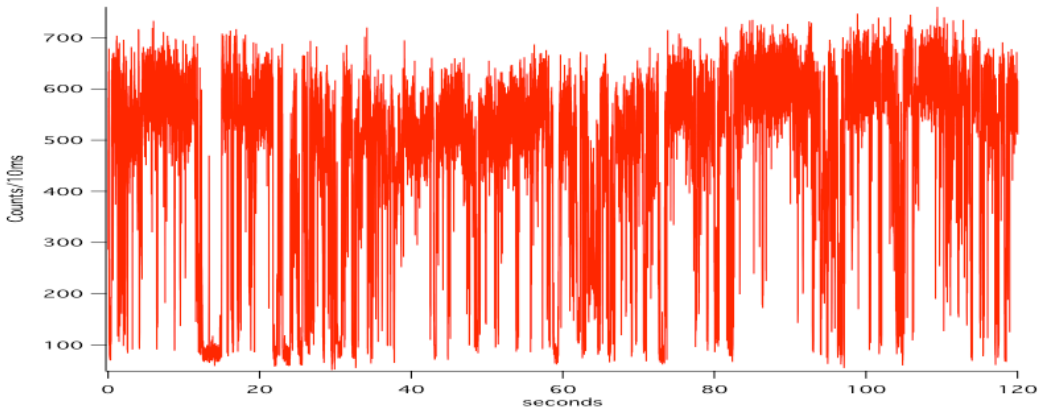

FIGURE 5.1: Fluorescence versus time trace of single CdSe NC collected in our lab.

Quantum jumping is a natural explanation for intermittency in single emitters, which was explored theoretically for a single atom by Cook and Kimble.[63] Therein, quantum jumps are described as an electron transition from a radiative state to a metastable nonradiative state, which turns off the fluorescence. These transitions occur arbitrarily in time, and thus produce fluorescence intensity vs. time traces as shown above. When theory is extended to single molecules, the metastable state is a triplet state. Early studies of single molecule fluorescence revealed a blinking effect in individual organic molecules in molecular crystals.[61] In these systems, blinking was due to intersystem crossing transitions to and from a metastable triplet state and statistical modeling of lengths of on/off times showed single-exponential behavior, consistent with an excursion to and from a single nonradiative state. In later studies, off times up to several minutes were observed for many organic molecules in polymers, which lead to non-exponential on/off distributions.[64] The characteristic long off times observed in these systems do not

coincide with the lifetime of a triplet state and therefore cannot be explained by intersystem crossing events.

More recent work on organic molecules has suggested that photoinduced charge separation and subsequent trapping of a carrier somewhere close to the molecule causes these long off times.[65] The quantum jumping theory predicts recovery from a single trap state, which invokes single exponential behavior. However, a dispersion of trapping-detrapping kinetics from a distribution of states would explain the nonexponential distribution of off times. This could also be extended to complex nanocrystal systems. While atoms and molecules likely transition to a single non-radiative state, there are a manifold states to consider in nancrystals, as they are comprised of thousands of atoms, many of which are in close proximity to the surface.

The first report of fluorescence intermittency in room temperature studies of nanocrystals by Nirmal et al. attributed the "off" state to a photoionized, charged state, and the "on" state to reneutralization of the particle.[6] According to the model of Efros and Rosen,[66] the nanocrystals become charged via an Auger-assisted ionization process involving multiple excitons. A biexciton occurs when two excitons exist in the nanocrystal at the same time. Auger ionization refers to the annihilation of the biexciton when one exciton essentially transfers its energy to the other to relax back to the ground state. The promoted charge may have enough excess energy to escape the nanocrystal core, leaving behind a charged or ionized NC. In these ionized states, charges could be

trapped on or near the surface of the nanocrystal, or in the case of core/shell nanocrystals, at the core/shell interface. Subsequent excitations of electron-hole pairs relax nonradiatively by efficient Auger recombination.[66] The nonradiative Auger recombination rate is many orders of magnitude faster than the radiative rate, thus the quantum yield is small, leading to a "dark" nanocrystal. Fluorescence only recovers when the trapped charge returns back to the nanocrystal core and recombines with the remaining carrier. The off state is said to initiate by charging of the nanocrystal, leading to the conclusion that a charged NC is non-emissive. However, experimental and theoretical evidence suggests that charged nanocrystals are emissive,[67-70] and the charging model of nanocrystal off states remains under scrutiny.[10, 71] The results presented in this dissertation work invoke a model in which charged NCs can be emissive, thus suggesting that multiple charges are responsible for off states.

Statistical modeling of the lengths of on and off times in fluorescence trajectories reveals a virtually universal inverse power law behavior over a large dynamic range from microseconds to seconds with an exponent $m_{on/off} \sim 1.5$.[72] This power law is a signature of distributed kinetics and complex long-range order.[73] The simple three-state model presented above with constant rates of ionization and neutralization does not explain the power law behavior. Alternative models consider exponentially distributed ionization-recombination (electron transfer) rates,[74] resonant electron transfer from a diffusive excited state to a trap state,[73] a diffusion-controlled electron transfer model with a crystal-

induced surface state,[75] three-dimensional electron hopping diffusion,[76] and electron tunneling towards a uniform spatial distribution of traps.[77]

The electron tunneling model of fluorescence intermittency in CdS nanocrystals considers a three-state system which permits PL from a charged state where the charge is trapped far away from the core.[77] This model attributes the charged state to an excited electron tunneling towards a uniform spatial distribution of traps. The charged state then involves two different regimes, one bright and one dark. This model predicts exponential behavior for the neutral on states, which agrees with experimental results on uncapped CdS nanocrystals. Expanding theory to capped nanocrystals in which longer on times persist, extended on periods are explained by considering the location of the residual hole (left behind by a trapped electron) either on the shell or in the core. Having the residual hole trapped on the shell will still permit significant radiative recombination, and therefore PL. As a result, there are three modes of luminescence in which 1) the core is charged, and the NC is off 2) the shell is charged and the NC is on for an extended period if time and 3) the NC is neutral and on for very short periods of time (called "grey" states). It is interesting to note that the location of the hole may lead to several emitting states with various brightnesses, as observed experimentally.[69] These results indicate that a simple on or off picture is not sufficient. We consider a similar model to explain our findings in the current work, which permits emission from charged exciton, or trion, states.

Considering the tunneling model of ionization, barrier height, and thus trapping-detrapping kinetics should be unaffected by changes in temperature. This is confirmed in the case of off-time distributions, which exhibit power law behavior regardless of temperature, excitation intensity, surface morphology, and size in CdSe and CdTe NCs.[73] In these experiments, a truncation of the power law at long on times was also observed, suggesting a secondary photoinduced, thermally activated process. In addition, it is curious that on-times follow an inverse power law at all, and many physical models are inconsistent with power law behavior of on states. In the current work, we also observe a deviation from power law behavor for both on and off states in the presence of metal films.

An alternative diffusion model explains blinking without the long-lived trap hypothesis.[78] Therein, switching between on and off states is caused by large variations in the nonradiative relaxation rate (k_{nr}) of the excited state to the ground state via surface hole traps. The model assumes that hole trap sites due to unpassivated selenium bonds on the NC surface form a band of states with a width of about 200 meV, located ~ 300-400 meV above the highest energy hole state ($1S_{3/2}$). Absorption spectroscopy experiments show that fast hole trapping occurs upon excitation, while the electron remains in the lowest $1S_e$ state with the $1P_e$ state lying ~ 300 meV above (nanocrystal size dependent).[79] In this case, hole trapping is an Auger-assisted process involving the electron. This model suggests a light-induced diffusion of the energy difference between

the $1S_e$-$1P_e$ levels, and thus the energy of the electron, as the cause of distributed kinetics. Considering the set of nuclear coordinates of the combined nanocrystal and ligand layer corresponding to the difference in energy, as in electron transfer theory, small changes in these coordinates could occur when the nanocrystal is photoexcited. That can translate into diffusion in the energy (ε) of the $1S_e$-$1P_e$ transition, leading to large variations in the hole-trapping rate. Fluctuations in ε about a value very close to the lowest trap state energy can lead to pronounced on an off behavior observed in fluorescence intermittency. In our system, we consider electric field induced diffusion of energy levels.

As discussed previously, charged nanocrystals can be emissive and there is likely a distribution of surface trap states, thus the location of surface charges should affect the PL quantum yield.[80] The presence of charge, or electric field, inside a nanocrystal will significantly affect oscillator strengths, charge carrier lifetimes, electron-phonon coupling, and electron transport properties.[81] Direct measurements of electrostatic charge on single CdSe nancrystals at room temperature using electrostatic force microscopy (EFM) revealed that half the the NCs were neutral and the other half were positively charged before photoexcitation and exhibited blinking behavior of the charge signal.[81] After excitation, the positive charge on some nanocrystals increases and the number of nanocrystals showing blinking behavior also increases. Interestingly, photoionization occurs over the course of minutes, and after laser cutoff the positive charge decays over the course of hours. These findings have important implications for the role of surface

charges and electric fields on the carrier dynamics in nanocrystal systems, which are investigated in the current work.

5.2 Spectral Diffusion

Another phenomenon that is also common to single emitters is spectral diffusion. It is a key feature of NC photophysics explored in the current work. Theory predicts discrete molecular-like energy levels in single NCs as described in Chapter 3, giving rise to distinct optical transitions and the size-tunable nature of nanocrystal properties. It follows that the transition line-widths of single nanocrystals should be extremely narrow. Although ultra-narrow linewidths (hundreds of μeV) have been achieved at cryogenic temperatures,[5] room temperature spectroscopies of single nanocrystals yield linewidths (FWHM) of 60-70 meV (~20nm). Experimental evidence suggests that the broad spectrum observed is not due to the intrinsic physics of the particle, but is actually comprised of many instances of spectral diffusion over the course of an acquisition.[4, 7] Instead, changes in the nano-environment of the nanocrystal such as ligands exchanging or fluctuations in the local electric field have been implicated.[8] Low-temperature (25 K), two-photon spectroscopy revealed fluctuations in the spectral shape, intensity, and line positions of CdSe/ZnS nanocrystals over successive two-minute acquisitions.[4] These fluctuations, up to tens of meV, were not related to multiple exciton dynamics or heating of the nanocrystal. Instead, the time evolution of single NC spectra as shown in figure 5.2 was attributed to modification of the NC surface due to photoexcitation. Successive

excitations can lead to bond rearrangements at the NC surface. The creation and subsequent annealing of surface defects could affect the transition dipole of a radiative transition, leading to fluctuations in spectral intensity over time. Studies of single CdSe/ZnS QDs at 10 K revealed a strong dependence of the single QD linewidth on excitation intensity, wavelength, temperature, and integration time due to excess excitation energy and thermal effects.[54] These findings have important implications for the current work, which was conducted at room temperature, in that it leads to thermally broadened spectra for single CdSe/ZnS QDs as we will see in Chapter 7.

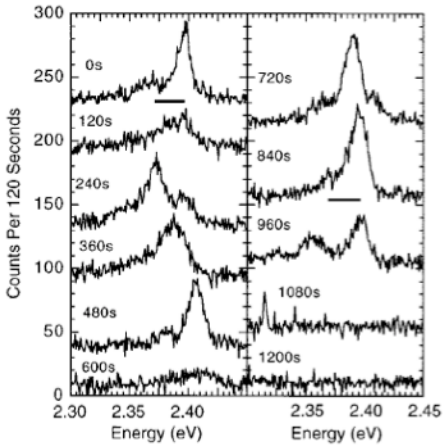

FIGURE 5.2: Time evolution of single nanocrystal spectrum at low temperature. Taken with permission from the literature.[4]

5.3 Applied Electric field Effects

In the current work, we explore the role of electric fields in nanocrystal carrier dynamics, thus a discussion of the Stark effect is warranted. The Stark effect is the shifting and/or splitting of energy levels in atoms and molecules in response to an external electric field. In spectroscopy, this can manifest itself as a spectral shift, narrowing, broadening, or new peaks may even arise. This effect can be observed in nanocrystals because of their discrete energy levels due to quantum confinement, and as such is termed the quantum-confined Stark effect (QCSE). The QCSE shifts the electron and hole both energetically and spatially. With increasing electric field, the electron is shifted to lower energies, while the hole is shifted to higher energies, effectively shrinking the bandgap energy and redshifting the exciton emission. In addition, the electron and hole are forced to opposite sides of the nanocrystal, reducing the overlap and therefore the recombination efficiency (i.e. quantum yield).

Low temperature (10K) Stark spectroscopy of single CdSe core and CdSe/ZnS core-shell nanocrystals has revealed reversible shifts up to tens of meV in the PL spectrum with an applied electric field[7] (figure 5.3a). Figure 5.3b shows a Stark series of spectra at a range of applied fields.

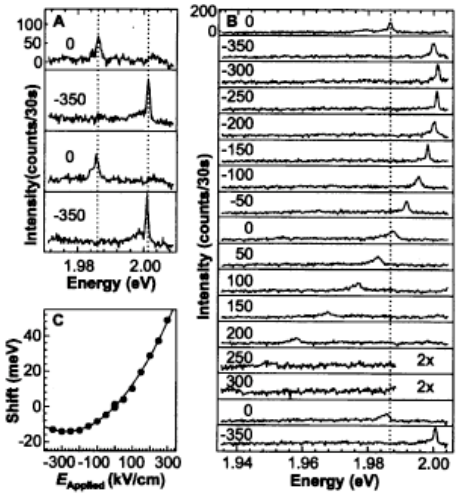

FIGURE 5.3: Stark spectroscopy of single CdSe NCs. Taken with permission from the literature.[7]

A plot of spectral shift versus electric field (figure 5.3c) can be fit to the following function:

$$\Delta E = \Delta\mu\xi + \frac{1}{2}\Delta\alpha\xi^2 \qquad (5\text{-}1)$$

(where E = transition energy, μ = dipole moment,
ξ = applied field, and α = polarizability)

The presence of a linear and quadratic component in ΔE indicates both dipolar and polarizable character in the emitting state. It is important to note that the relevant quantities are changes in the permanent dipole moment (Δμ) and the polarizability (Δα) from the ground state to the excited state. A change in the permanent dipole is not expected, although a dipole in the first excited state for CdSe nanocrystals (Δμ=32 Debye) was suggested in low-temperature (100 K) ensemble absorption spectroscopy.[82]

In addition, a large permanent dipole in the ground state (i.e. structural dipole) has been observed for wurtzite CdSe nanocrystals.[83, 84] Any permanent polarization is expected to be unchanged in the excited state. However, the excited state is expected to be more polarizable due to the delocalized state of the excited electron.

Due to differences in size, shape, and orientation, a range of values for polarizability and excited-state dipole were calculated for individual nanocrystals fit to the above equation. Averaging over the ensemble, the dipolar component goes to zero ($\Delta\mu=0$) as expected for randomly oriented dipoles. This leads to a purely quadratic curve from which the calculated average polarizability, α, is 2.38 x 105 Å3, on the order of the physical volume of the nanocrystal. A surprisingly large average excited-state dipole of 88.3 Debye was also extracted. Observing a single nanocrystal over 50 minutes, the component of the dipole along the direction of the applied field changes over time. The large, changing excited state dipole is attributed to a dipole induced (μ_{int}) by a highly polarizable excited state in the presence of a strong, varying internal electric field (ξ_{int}) such that:

$$\mu_{ind} = \Delta\alpha\xi_{\text{int}} \qquad (5\text{-}2)$$

and $$\Delta E = \alpha(\xi_{\text{int}} + \xi_{applied})^2 \qquad (5\text{-}3)$$

The extracted local electric fields are on the order of 100 kV/cm and may be due to the presence of charge carriers on or near the surface of the nanocrystal. The dynamics of ionization, recombination, and redistribution of external charges can lead to local

electric field fluctuations and may explain spectral shifting and line broadening. We revisit the effects of the permanent dipole and internal electric field of the nanocrystal in Chapter 7.

The shifts induced by the applied electric field in these experiments are strikingly similar to those observed in random spectral diffusion. This suggests that local electric fields could be responsible for spectral diffusion. The origin of these local electric fields is could be due to carrier (electron or hole) trapping on or near the nanocrystal surface via an Auger ionization process, leaving behind a charged core. Similarly, Auger ionization has been implicated as the cause of fluorescence intermittency, or blinking. The charging model invokes a simple two-state picture in which the nanocrystals are neutral during on states, and ionized during off states. This relation suggests a correlation between spectral diffusion and blinking.[8] The question remains: is the electric field due to a single trapped charge enough to explain these dynamic processes?

The effect of an electric field on nanocrystal blinking at room temperature has also been investigated.[85] By applying a modulated electric field, significant periodic changes in the fluorescence trajectory of nanocrystals were observed as shown in figure 5.4. Interestingly, the shapes of intensity versus applied field curves shown in figure 5.5 vary greatly not only from NC to NC, but in different regions of the same trajectory. Some curves show enhancement with the field, while some exhibit quenching. This indicates a constant redistribution of surface states with the applied field.

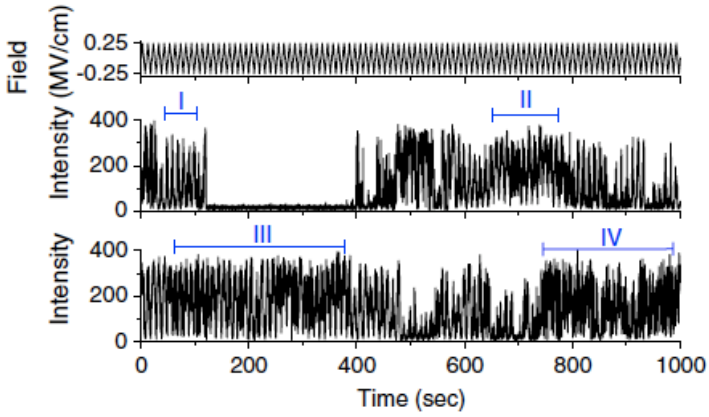

FIGURE 5.4: The Stark effect on fluorescence intensity vs. time traces. Taken with permission from the literature.[85]

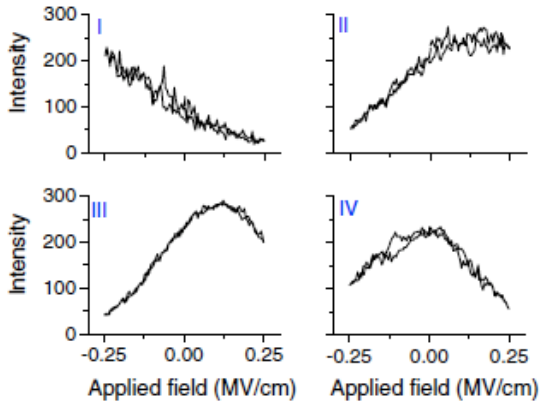

FIGURE 5.5: Intensity versus applied field for various regions shown in figure 5.4. Taken with permission from the literature.[85]

This system was modeled using the three state system in figure 5.6, involving ground, exciton and charge transfer states. In these CdSe/ZnS core-shell NCs, the charge transfer states are presumably located at the core-shell interface and are easily accessible. Once in the charge transfer state, additional deep trap states on the ZnS surface become

accessible. Modulation of these surface trap states relative to the exciton and charge transfer states is thought to be responsible for the observed changes in photoluminescence intensity or quantum yield. Interestingly, no correlation was found between intensity modulation and spectral diffusion.

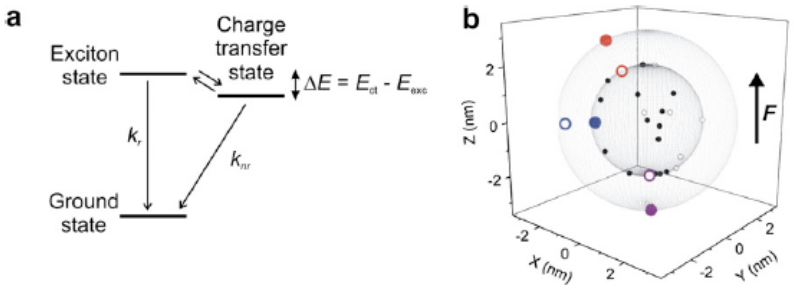

FIGURE 5.6: Simple model for electric field effect on fluorescence trajectories. Taken with permission from the literature.[85]

The effects of applied electric fields on single conjugated polymers have revealed linear Stark effects and spontaneous switching of dipoles.[86, 87] The linear Stark effect involves an interaction of the applied field with some permanent polarization or dipole in the molecule or particle. Linear Stark effects are not expected in molecules which are centrosymmetric and nonpolar, which also describe spherical nanocrystals. Ladder-type poly(para-phenylene) (LPPP) molecules exhibited modulation of the fluorescence spectrum of a single chromophore on the LPPP molecule with the application of a maximum amplitude 625 kV/cm external electric field at 5 K. Figure 5.7a shows a

typical spectrum, which is strongly correlated to the applied triangle electric field (shown below in white). Positive biases induce blue shifts, while negative biases induce red shifts. The maximal shifts are ~1.5 nm, or ~5 meV. While random spectral diffusion, as described previously, is superimposed on the field response, it is clear that there is a field effect. The integrated intensity, shown in figure 5.7b reveals no clear correlation of intensity with applied field, but when averaged over 18 cycles, the intensity decreases by 20%. Spontaneous switching of the dipole is also observed in that the response to the applied field vanishes, and then returns over the course of 30 minutes. This change in response is indicative of a change in the effective dipole that interacts with the field by a rearrangement of local charges. This is evidence that significant reorganization of charge can occur without observing a marked change in intensity as in blinking. Intensity modulations are only expected when the exciton is separated or ionized. However, in a related article, photoluminescence quenching and enhancement was observed under the influence of an applied electric field.[87] These observed dynamics in the permanent polarization in molecules could be related to the complex charging dynamics that cause blinking in single molecules and quantum dots. The implications are important when one considers the effect of an applied electric field on NC emission intensity, as will be discussed in Chapter 7.

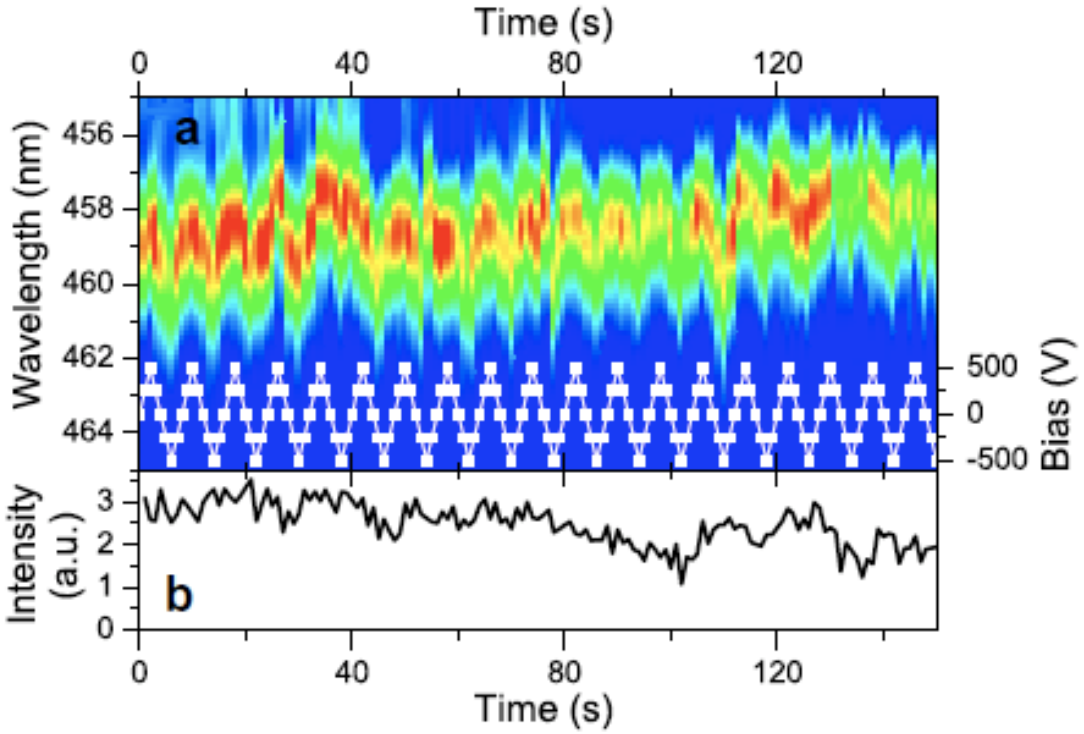

FIGURE 5.7: Modulation of fluorescence spectrum of LPPP molecule with applied field. Taken with permission from the literature.[86]

5.4 Metallic and Plasmonic Interactions

During the course of our experiments, we discovered a strong interation of NC excited states with a rough gold thin film. Thus, a discussion of excition-plasmon interactions is presented here. Metal surfaces and nanoparticles are known to exhibit plasmonic effects, which can have a profound effect on spectroscopy of materials.[88] According to the Drude model, metals possess a large number of free electrons, which are free to move about the conduction band. A surface plasmon (SP) can be thought of as a collective oscillation of this free electron density. This excitation is a resonance

phenomenon that requires a specific frequency of radiation to set the electrons into oscillation. For the metals gold and silver, this frequency lies in the range of visible light ($\sim 10^{14}$ Hertz). The effects of this local electric field can be two-fold: 1) a coupling of the plasmon to the excitation field or 2) a coupling of the plasmon to the quantum dot transition dipole. The ability to easily excite plasmons in these materials has led to their use in a variety of applications.

A rough metal surface can be approximated by ellipsoids, which scatter the incoming light. An emitting dipole near the surface will interact with both the incident electromagnetic field and the scattered field. The coupling of the scattered field to the emitting dipole can become quite large when the transition frequency is near the resonance of the metal surface plasmon. Thus, any emission modulation could be attributed to the interplay of two competing processes: increased absorption and emission by coupling to the metal plasmon and nonradiative energy transfer from the exciton to the metal.[89] These findings are in contrast to interactions of single emitters with flat metal surfaces.[56, 88] On a flat conducting surface, plasmons do not play a role.

Coupling of quantum dot (QD) excited states to nanostructured metals has recently become an area of intense research owing to the distinct, yet complimentary optical properties of both nanomaterials. While quantum dots exhibit tunable absorption and emission for superior light-harvesting capabilities, nanostructured metals are capable of localizing electromagnetic energy, thereby enhancing excitation or emission fields.[90]

Exploiting their combined properties can lead to ultimate control of light-matter interactions at the nanoscale.[91] These types of interactions have been shown to modify the excited state dynamics and emission properties of single emitters. Enhanced absorption cross sections, increased radiative rates, and energy transfer have been observed in the weak coupling regime, which involves interaction of the excited state dipole with an electromagnetic field localized at the metal surface.[89, 92-96] This highly localized optical field is a surface plasmon, generated by resonant oscillations of surface electron density. Nanoparticles of gold and silver readily interact with optical frequencies, leading to strong surface plasmon resonances in the visible spectrum. SPs can also be generated in metallic films at metal/dielectric interfaces. Exciton-plasmon interactions proceed through efficient coupling of the excited state to electronic states within the nearby metal surface. Coupling of single quantum dots to rough metal films and nanoparticles has revealed suppression of blinking dynamics, enhancement and quenching of fluorescence emission, increased spectral shifting, and reduced excited state lifetimes.[70, 97-108] A variety of other platforms for exciton-plasmon coupling have been investigated, including nanocrystal-metallic nanorod/nanowire,[109, 110] and J-aggregate-metal nanoshell constructs.[111] The methods presented in Chapter 7 present a simple architecture for the study of multiple exciton-plasmon interactions.

5.5 Multiple Excitons

Due to the exciton-plasmon coupling described in the previous section, we have observed a strong enhancement in multiple exciton emission of single quantum dots, an overview of which is presented here. As mentioned previously, nanoscale emitters such as semiconductor nanocrystal quantum dots exhibit complex excited state dynamics. Amongst the most intriguing phenomena observed in quantum dots as a result of these dynamics are blinking,[6] spectral diffusion,[4, 5] and multiple exciton behavior.[112] We have already discussed blinking and spectral diffusion, but simultaneous existence of multiple excitons is also an important topic in this work. Existence of multiple excitons in a single quantum dot can be achieved in one of two ways: a) from absorption of a single photon of energy many times the bandgap energy or b) from absorption of more than one lower-energy photon from a single laser pulse. For solar cell applications, the generation of multiple excitons from a single high-energy photon, and subsequent extraction of several carriers would ultimately improve the efficiency of third-generation solar cells.[1, 113, 114] On the contrary, emission from high-order excitons is valuable for lasing or light-emitting diode applications incorporating quantum dots.[115, 116]

Multiple exciton emission from quantum dots has been inferred from ensemble spectroscopic techniques,[117, 118] or observed directly from photon correlation measurements utilizing single molecule techniques.[119-121] Using photon correlations, the ratio of the biexciton (BX) to exciton (X) fluorescence quantum yield can be readily

determined.[120] This method of observing multiexicton emission is distinct from low-temperature single molecule spectroscopic techniques.[122] However, the quantum yield of biexcitons and higher order excitons is typically low or unobserved due to efficient nonradiative Auger recombination.[123] Methods to improve the quantum yield of multiple excitons include growth of thick shells in nanocrystals specifically designed to suppress the Auger rate.[122, 124-127] The findings presented in Chapter 7 are conducted on conventional CdSe/ZnS QDs and support either a change in the Auger rate and/or the radiative rate of the nanocrystal in the presence of a rough gold film.

5.6 Marcus Electron Transfer Theory

A suitable model for understanding the complex dynamic system of a single NC and its surroundings is within the framework of Marcus electron transfer theory, according to the model of Jones *et. al*.[128, 129] The beginnings of a comprehensive model that will account for distributions of trap states, the fine electronic structure of the ground state exciton, and interactions of the exciton with the NC surface and/or local environment is shown in figure 5.8. The lowest exciton states are coupled to the ground state via the radiative rate (k_r) and to a trap state by (k_t). The de-trapping rate, k_{-t}, (not shown) is the rate of transfer from the trap state back to the exciton state. The trap state depicted in the figure is likely a distribution of traps located somewhere on or near the nanocrystal surface. Other parameters, which appear in classical Marcus theory include the Gibb's free energy (ΔG), the reorganization energy (λ), and the electronic coupling

between states (V_{el}). Treating the trapping processes in the same way as electron transfer in molecular systems, we can extract these parameters from time-resolved fluorescence measurements. We revisit some of these parameters in the analysis of our experimental data.

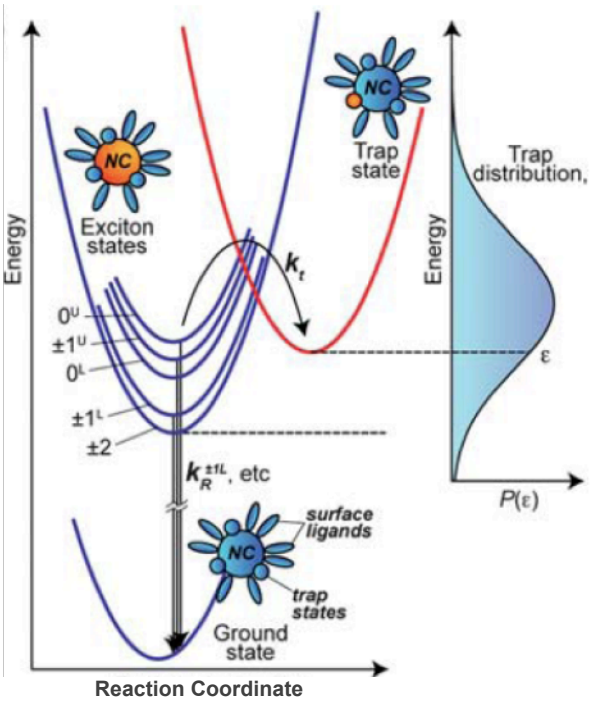

FIGURE 5.8: Scheme of Marcus electron transfer theory applied to nanocrystal systems. Taken with permission from the literature.[129]

Trap states (or other non-radiative states) cannot be directly probed using photoluminescence. However, multiexponential decays obtained in PL measurements contain signatures of carrier dynamics involving both radiative and non-radiative

processes.[130] The photoluminescence quantum yield is the probability for a nanocrystal in the lowest excited state to relax radiatively (by emitting a photon). This probability depends on the rates of radiative (k_r) and non-radiative (k_{nr}) processes as follows:

$$\text{Quantum Yield} = \frac{k_r}{k_r + \sum_m (k_{nr})_m} \qquad (5\text{-}4)$$

In equation 5-4, *m* is an integer number of rates, which reflects the likely distribution of non-radiative pathways described previous. The extracted quantity in photoluminescence experiments is the average lifetime, τ_{avg}, where:

$$\tau_{avg} = \frac{1}{k_{total}} \text{ and } k_{total} = k_r + \sum_m (k_{nr})_m \qquad (5\text{-}5)$$

The nature of the non-radiative states is unknown and likely requires a complex explanation.

Although classical electron transfer (ET) theory is well understood for molecular systems,[131] an extension of this formalism to nanocrystal systems will enable a more in-depth understanding of how excitons interact with their local environment. Classical Marcus theory describes electron-transfer reactions between molecules in solution. In order for electron transfer between two molecules to occur, they must approach each other to enhance electronic coupling and therefore the probability of transfer. In addition to this spatial rearrangement of reactants, the surrounding solvent molecules must also re-orient to accommodate the electron transfer. The potential energy of the reactants and surrounding medium is a function of thousands of different nuclear configurations

(reaction coordinates) of the reactants and solvent molecules, approximated by a parabolic potential-energy surface. After electron transfer occurs, the nuclear configurations of the products represent a different potential-energy surface. This is depicted in figure 5.9, where the left curve is the reactants' surface, and the right curve is the products' surface. In this picture, the excited donor (D*) is weakly interacts with the acceptor (A) through a bridge (B). After electron transfer occurs, the donor is positively charged (D+), and the acceptor is negatively charged (A-).

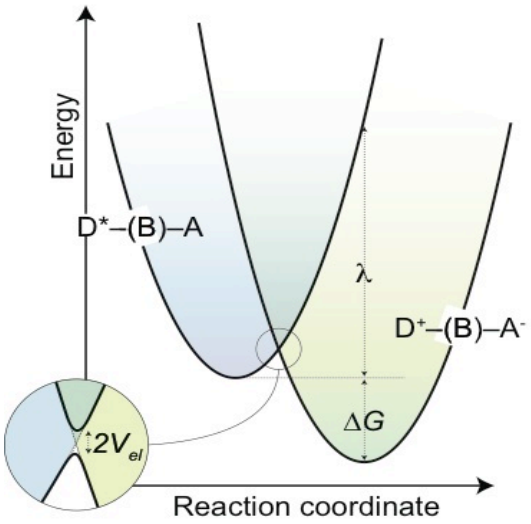

FIGURE 5.9: Electron transfer theory for molecular systems.

Thermal fluctuations can drive the potential energy of the reactants away from equilibrium, up to the crossing point of the potential energy curves shown in the figure. At the intersection, there is some probability of an electron transfer. Considering the

probability of reaching the intersection, the frequency for crossing the intersection region, and transition probability for going from reactants to products, the rate of electron transfer is given by:

$$k_{et} = \kappa \exp\left(-(\Delta G + \lambda)^2 / 4\lambda k_B T\right), \qquad (5\text{-}6)$$

where κ is the average transition probability for electron transfer, proportional to the electronic coupling between initial and final states (V_{el}^2), ΔG is the free energy difference between reactants and products (driving force), k_B is the Boltzmann constant, T is temperature, and λ is the reorganization energy (the amount of reorganization the environment has to undergo to accommodate charge redistribution), which has contributions from the changes in bond lengths of the reactants and changes in the solvent orientation coordinates. Considering the relationship between ΔG and λ, three regimes of electron transfer can be classified as follows: normal ($-\Delta G<\lambda$), activationless ($-\Delta G=\lambda$), and inverted ($-\Delta G>\lambda$). The inverted region is particularly interesting as it predicts a regime in which the electron transfer rate (k_{et}) decreases with increasing negativity of ΔG.

The electron transfer picture for NC systems is decidedly more complex, mainly due to sample inhomogeneity, and complicated surface interactions. In contrast to molecules, as-synthesized NCs consist of a small core and a well-defined surface, which is passivated and stabilized by coordinating ligands introduced during the synthetic process.[14] In most cases a shell of wider bandgap semiconductor material, such as zinc selenide, is grown around the core, which increases the photoluminescence (PL) quantum

yield by passivating surface traps and further confining the electron and hole to the core.[19] Nanocrystals have a large surface area to volume ratio, with many of the atoms lying on or near the surface. For example, in a 3.1-nm CdSe QD with a wurtzite crystal structure, 58% of the atoms are within 0.4 nm of the surface.[132] Many of these atoms are in direct contact with surface ligands and the surrounding solvent or matrix. Some of the outer surface atoms that are not passivated with a coordinating ligand present dangling bonds, which may serve as trap sites for photogenerated charge carriers. As a result, surface states are expected to play an integral role in charge carrier dynamics. High energy carriers excited well above the bandgap may couple with surface states, leading to bond rearrangements at the surface and changes in the electronic states of the NC. A single disrupted bond could lead to local perturbations in the energy levels of the NC such as introducing a mid-bandgap state, effectively quenching radiative recombination.[4]

The complexity in electronic structure of NCs lends itself to the picture shown in figure 5.10. Instead of a single donor state in molecules, one can consider the size-dependent fine structure of the band-edge exciton. Acceptor species may include surface-attached ligands, nearby molecules, surfaces, or other nanoparticles, and can be controlled experimentally. In addition to nearby acceptors, we must also consider trap states within the nanocrystal core/shell structure. Understanding the "simplest" case of a nanocrystal core/shell structure and its coordinating ligands represents the first step in completing the picture of electron transfer for nanocrystals. Considering a distribution of

trap states due to the nanocrystal surface or interface defects, all with different rates of trapping (k_t) and de-trapping (k_{-t}), will clearly complicate the ET picture.

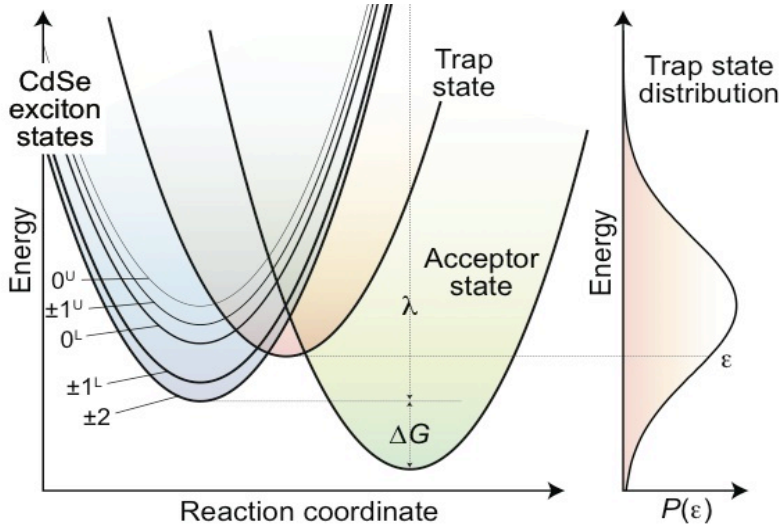

FIGURE 5.10: Marcus electron transfer theory for nanocrystals.

The role of surface traps in NC systems has been studied in the framework of Marcus electron transfer theory.[128] In this study, temperature-dependent time-resolved photoluminescence (TRPL) measurements are used to indirectly probe the effect of trap state distributions on exciton photoluminescence. While trap states cannot be probed directly in PL measurements, analysis of multiexponential decays can reveal the contributions from radiative and non-radiative processes. TRPL decay measurements on a size series of CdSe/CdS/ZnS NCs at 12 temperatures from 77K to 300K were fit to multiexponential functions. A kinetic model incorporating the exciton fine structure and

a radial trap state distribution reveal two distinct traps state distributions: one lying ~130 meV above the mean exciton energy, and the other ~5 meV above the mean exciton energy. The calculated reorganization energies (λ~200meV for high-lying traps, and λ~30meV for low-lying traps) suggest that the high-energy distribution represents surface traps on the outer ZnS shell, which is in close contact with surrounding solvent and ligands. The lower energy distribution may represent interfacial traps, which would require minimal nuclear reorganization of the lattice. In addition, a linear dependence of reorganization energy as a function of molecular polarizability of the solvent is observed which suggests a significant contribution of the reorganization energy is due to the local environment of the nanocrystal. Interestingly, average lifetime values (τ_{avg}) determined in this ensemble study did not agree with calculations for single nanocrystals unless trap states ~100 meV below the exciton energy were considered. Such deeply trapped states were not detected in the ensemble measurements. The presence of deeply trapped states is implicit in most blinking models as discussed previously. Single nanocrystal experimental measurements incorporating the same formalism would be particularly enlightening. In the next chapter we develop the analytical methods utilized to elucidate useful dynamic information from the data presented in this work.

CHAPTER 6: ANALYTICAL METHODS

6.1 Introduction

Using our suite of single molecules techniques, we generate several different types of data, all of which require a different analytical method. This chapter shows representative data collected using each technique, and describes our methods. Some techniques are based on literature methods, which have been discussed and cited in earlier chapters. Others are unique to our group and this dissertation research. All analysis routines used in this work were written in IGOR Pro data analysis software.

6.2 Blinking Analysis

A typical blinking trace is shown in figure 6.1 (top). The trace is generated by binning the macrotimes of sequential photons in bins of a chosen time. Photons are detected within hundreds of nanoseconds of each other. In the present case, and throughout this work, the bin size is set at 10 milliseconds. This means that all of the photons that arrive within the first 10 milliseconds of the start of the experiment are added to the first bin to yield a count level, and so on. Thus, the y-axis is counts per 10 milliseconds, and the x-axis is time. Figure 6.1 (bottom) is a histogram of the count levels. In this case, it is a bimodal distribution with clear on and off emission states of the quantum dot. The shape of this distribution can change considerably from QD to QD.

Analysis of many quantum dots is necessary to build any level of statistical significance for observed effects. For this dissertation work, a program was written to read binary data files, bin photon arrival times, and generate blinking statistics as described in what follows.

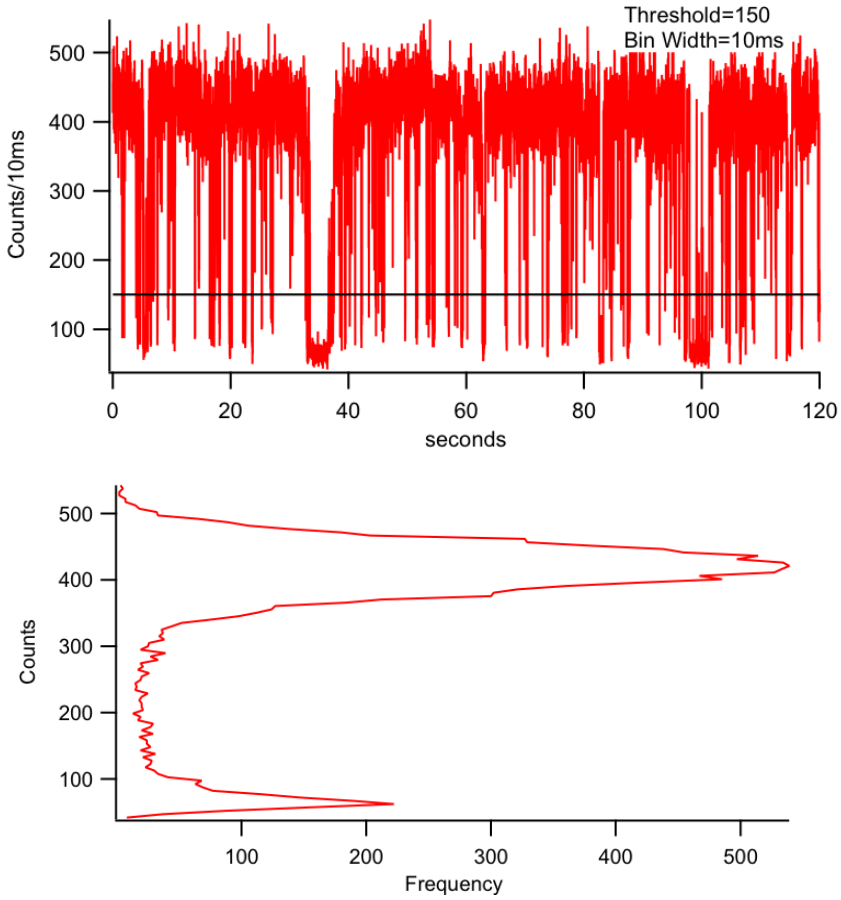

FIGURE 6.1: Representative fluorescence versus time (blinking) trace of a single quantum dot (top), and a histogram of counts (bottom).

Blinking statistics are generated by first selecting a threshold for which the dot is considered on or off. In the present work, a center threshold is chosen from examining the count level histogram. If a bimodal distribution is apparent, a center level between the two peaks is selected as shown in the figure 6.1. From this a binary trace of either on or off (1 or 0) is generated, and the lengths of on and off times are counted. The most common method to characterize blinking is to describe the probability of on/off times of certain lengths occurring. Figure 6.2 shows plots of the probability versus on/off time of the blinking trace in figure 6.1. The data can usually be fit to a power function of the form: $P\left(t_{on/off}\right) \propto t^{-m_{on/off}}$. The fit parameters *y0 (minimum)*, *A (amplitude)*, and *pow (power exponent)* are shown on each graph, where *pow* corresponds to $m_{on/off}$ in the power function. The on/off exponent, *m*, is what is typically reported in the literature. In general, the more gradual the slope of the line (smaller *m*), the more probable longer on/off times are likely to occur.

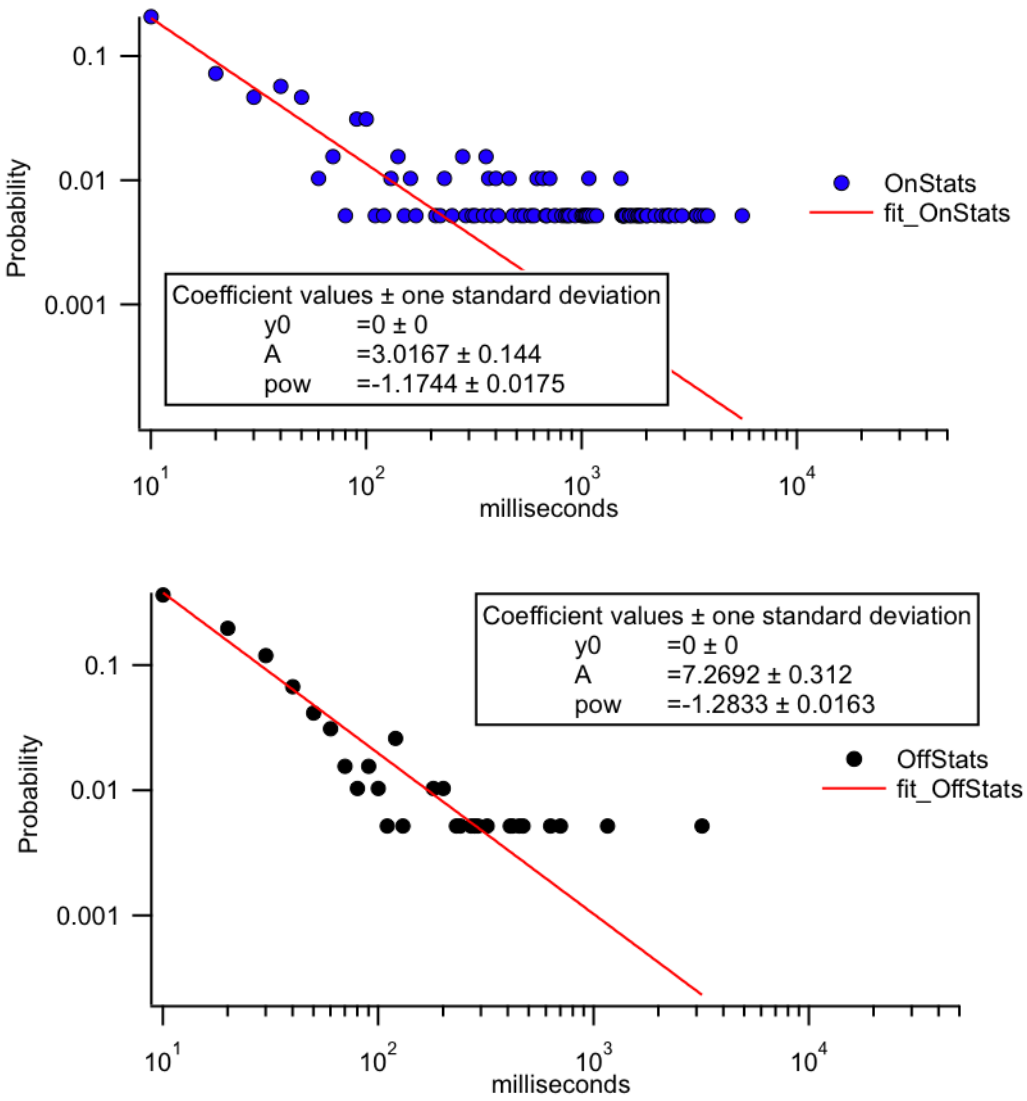

FIGURE 6.2: Probability of on (top) and off (bottom) times for the quantum dot shown in figure 6.1. Each is fit to a power law, where the power exponent (*pow*) is determined and reported as $m_{on/off}$.

6.3. Lifetime Analysis

Lifetime decays are generated from binning the microtimes of detected photons as described in the previous chapter. Existing homebuilt IGOR Pro software was utilized to deconvolve the instrument response function (IRF) from the collected data to extract an average lifetime of the data. All data are fit to a multiexponential function of the form:

$$I(t) = A_1 e^{-t/\tau_1} + A_2 e^{-t/\tau_2} + A_3 e^{-t/\tau_3} \ldots,$$

where I is intensity, A is a pre-exponential factor, t is time, τ is a characteristic lifetime, and the subscripts 1, 2, 3… refer to the number of exponential functions needed to fit the decay. In general, if a decay is single exponential (a straight line on a log-log counts vs. time decay trace), that is indicative of a single radiative relaxation process. More complex multiexponential decays are indicative of multiple radiative and nonradiative processes involved in the decay of the excited state. A typical lifetime decay (red curve) with IRF (blue curve), and decay fit (black curve) is shown in figure 6.3 (top). The residuals above the graph indicate an accurate fit. Average lifetimes, calculated as:

$$\sum_n \left(\frac{\left(A_n \tau_n\right)^2}{\sum_m A_m \tau_m} \right),$$

where n and m represent a number of exponentials, are typically reported in the literature. The table at the bottom of figure 6.3 shows the outcome of a 4-exponential fit, with values for A and τ, and a calculated average lifetime of ~20 ns. We recognize that the average lifetime is often insufficient to describe the underlying carrier dynamics. In the

present work, we employ kinetic modeling to extract useful information from the lifetime decay data. The principles of the kinetic modeling are discussed in section 6.5.

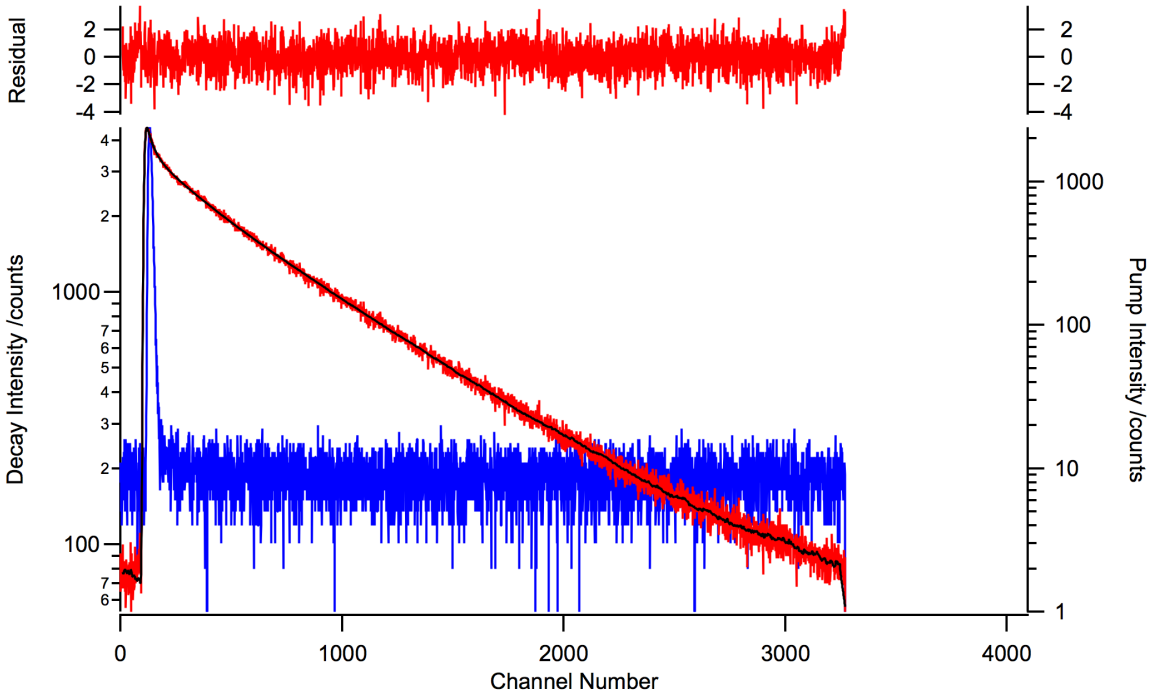

	Fit Coefficients		Fit Yields		Fit Quality	
0	Decay 1 scale:	1	ps/ch :	30	Chisquare:	3612.86
1	Pump 1 bkgd:	9.303	Ramp /ns :	100	Reduced Chisq (1):	1.11199
2	Pump 1 shift:	23.57	Gain :	4096	Durbin-Watson (2):	2.00993
3	Decay 1 bkgd:	75.39			Standard deviation:	1.05229
4	A1:	0.4061	Yield1 /% :	1.0078	RMS:	1.05257
5	Tau1:	1.328	Tau1 /ps :	39.85	Kurtosis (0):	0.0870345
6	A2:	0.02977	Yield2 /% :	1.5737	Skewness (0):	-0.170324
7	Tau2:	28.29	Tau2 /ps :	848.84		
8	A3:	0.01659	Yield3 /% :	6.1371	Average lifetime /ps:	20223.7
9	Tau3:	198.1	Tau3 /ps :	5942		
10	A4:	0.06742	Yield4 /% :	91.281		
11	Tau4:	724.7	Tau4 /ps :	21741		
12						

FIGURE 6.3: Typical lifetime decay fitting (top). The red curve is the raw experimental data, the blue curve is the instrument response function and the black curve is the fit data. This data was fit to 4-exponentials, the results of which are shown in the table (bottom).

6.4 Spectroscopy Analysis

Single particle spectra are collected using a multimode fiber as described in chapter 4. Optimal alignment of the fiber to direct the fluorescence from the sample into the spectrometer is necessary for adequate signal to collect a spectrum, which is achieved over several seconds. Acquisition times are typically 5 to 10 seconds. A single raw spectrum of an individual quantum dot is shown in figure 6.4. Raw spectral data includes a background fluorescence signal as indicated in the figure, which must be subtracted. Figure 6.5 shows the raw spectrum after the background was subtracted. Each spectrum is subsequently fit to a Gaussian function of the form:

$$y_0 + A\exp\left\{-\left(\frac{x - x_0}{width}\right)^2\right\},$$

where y_0 is the function minimum, A is the amplitude, x_0 is the peak position, and *width* is the standard deviation. These values are extracted for further analysis of spectral diffusion.

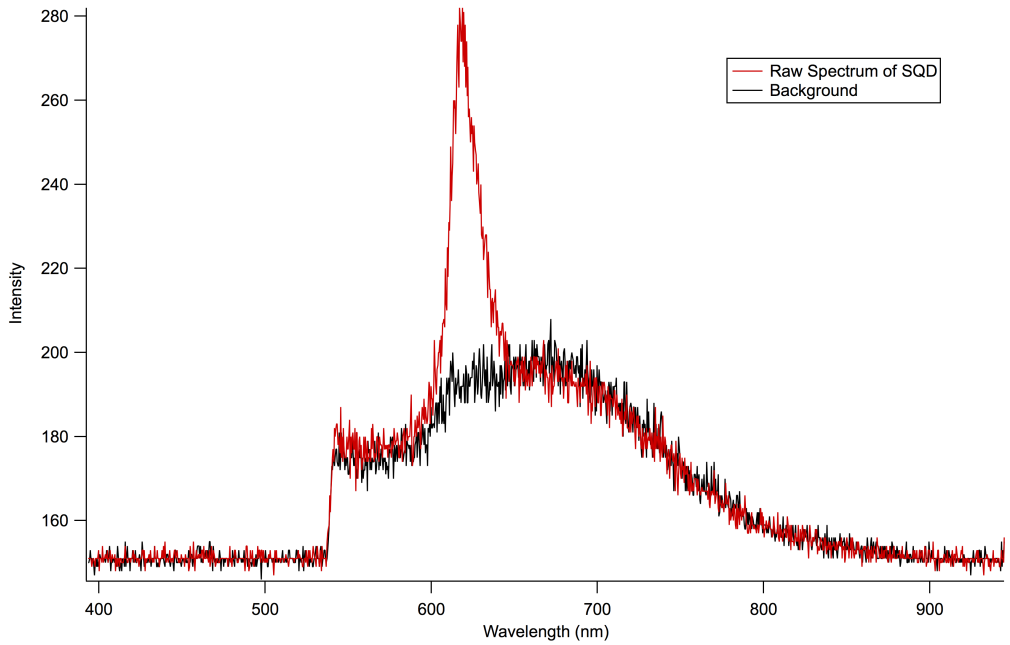

FIGURE 6.4: Typical raw data of single quantum dot (SQD) spectrum acquired for 10 seconds (red). Typical background acquired on a "dark" spot on the sample (black).

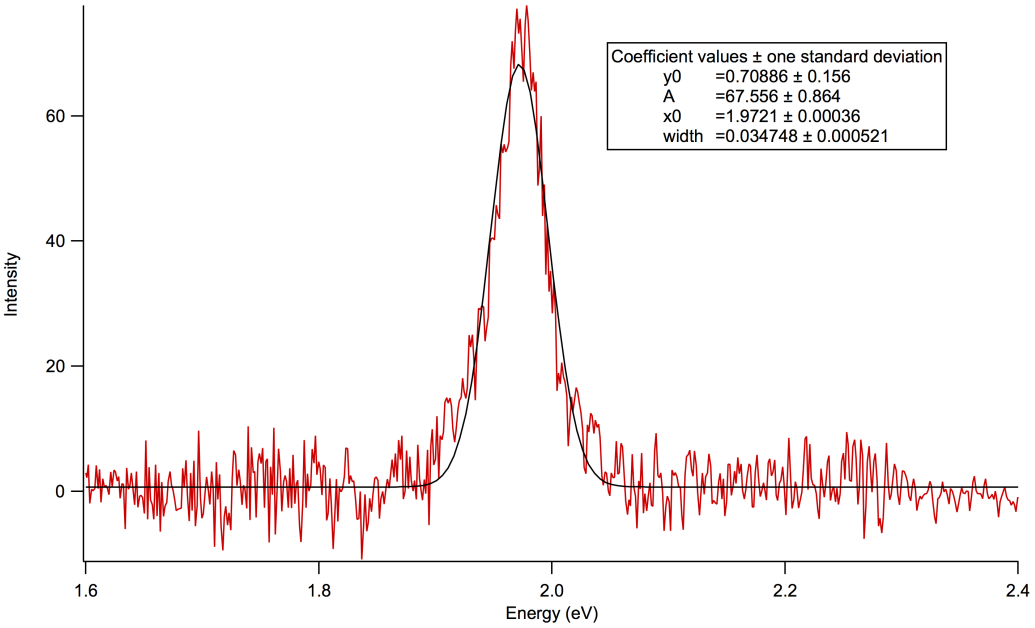

FIGURE 6.5: Spectrum of single quantum dot acquired for 10 seconds. The x-axis has been extrapolated from a wavelength axis to an energy axis. The spectrum is fit to a Gaussian function. The fit parameters described in the text are shown in the textbox.

The Winspec spectroscopy software is capable of collecting successive spectra at chosen time intervals. Figure 6.6 shows three panels that represent the time evolution of the spectrum of an individual QD. The leftmost panel is a 2-dimensional plot of the raw spectrum (with background subtracted). The vertical axis is time, while the horizontal axis is energy and the color scale represents intensity. The middle panel is the fitted data, with a data point at the maximum energy of each spectrum. The rightmost panel is a time evolution of the widths extracted from Gaussian fits, with the horizontal axis in millielectronvolts (meV). A program was written to load spectroscopy data files, subtract the background fluorescence signal from each spectrum, convert to an energy axis, fit each spectrum to a Gaussian function, and generate a 2-dimensional plot as shown below.

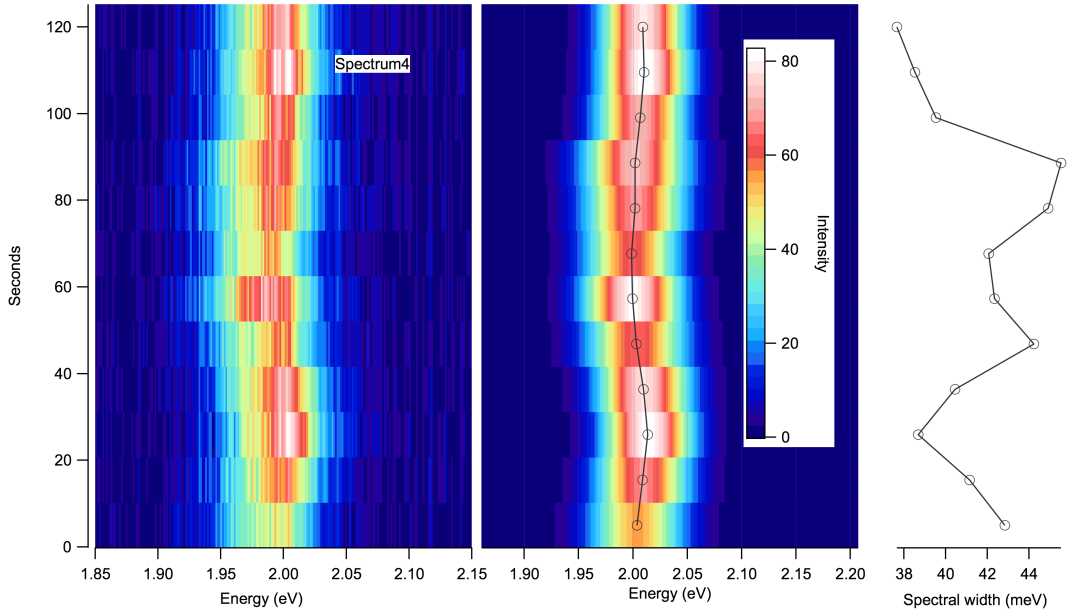

FIGURE 6.6: Time evolution of emission from single quantum dot. Left- Raw data with background subtracted. Middle- Fitted data. Right- time evolution of width extracted from Gaussian fit.

6.5 KINETIC MODELING

Homebuilt kinetic modeling software enables us to extract additional information from lifetime decays beyond average lifetimes. Lifetime decays are fit using the methods described in section 6.3. These decays are loaded into the modeling software, and fit to a user-defined kinetic scheme. Figure 6.7 shows a screenshot of the kinetic modeling software.

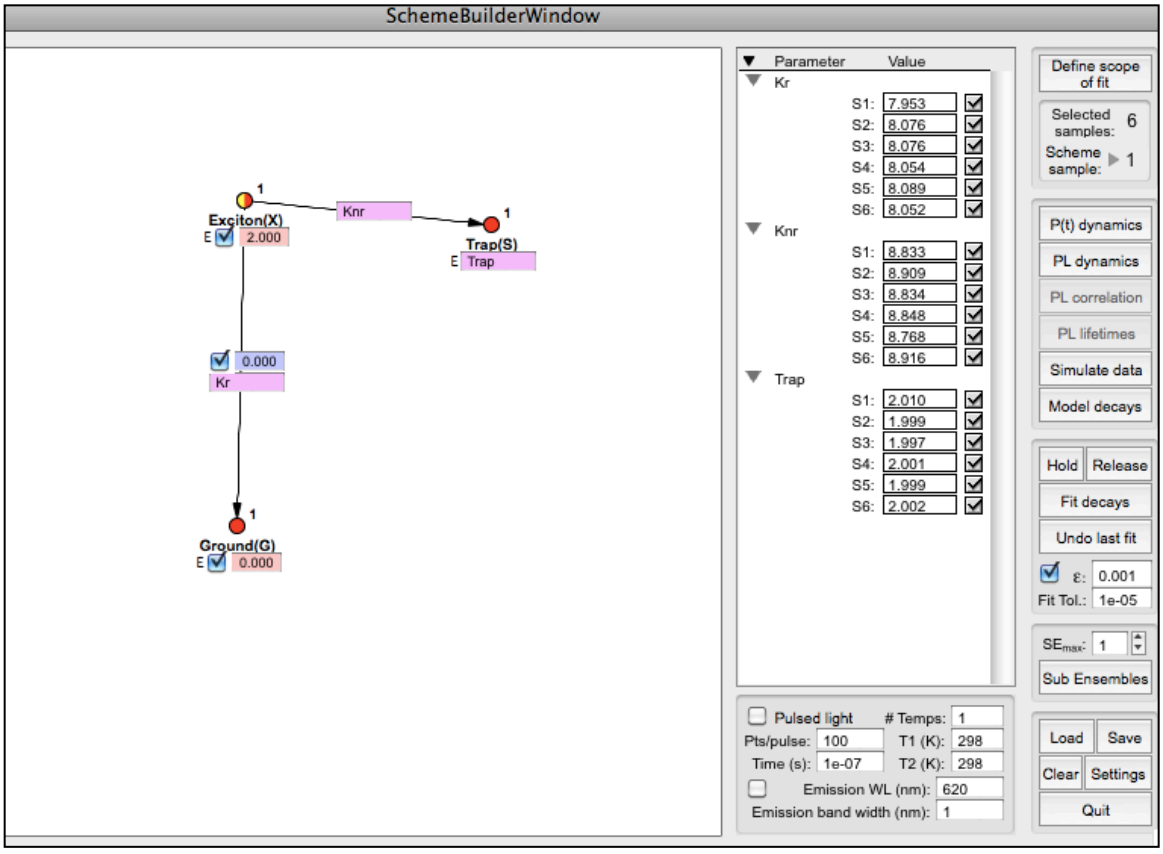

FIGURE 6.7: Screenshot of homebuilt kinetic modeling software.

A simple three state model involving ground (G), exciton (X), and trap (S) states is built in the scheme window on the left. Transitions connecting the states are represented by arrows. The ground state energy is fixed at 0 eV, while the exciton state is fixed at 2.0 eV. A single radiative transition for the path from the exciton state to the ground state is represented by the variable k_R, while a non-radiative transition to the trap state is represented by k_{NR}. This scheme is used for global analysis of six decays. Within this scheme, we can write differential equations for the populations, ρ, of each of the states as follows:[129, 130]

$$\frac{\mathrm{d}\rho_X}{\mathrm{d}t} = \rho_S(t)k_{SX} - \rho_X(t)(k_{XS} + k_R)$$

$$\frac{\mathrm{d}\rho_S}{\mathrm{d}t} = \rho_X(t)k_{XS} - \rho_S(t)k_{SX}$$

$$\frac{\mathrm{d}\rho_G}{\mathrm{d}t} = \rho_X(t)k_R$$

These simultaneous differential equations are solved within the software by finding the eigenvectors and eigenvalues a rate matrix. The result gives an expression for the population of X as a function of time:

$$\rho_X(t) = A_1 \exp(k_1 t) + A_2 \exp(k_2 t)$$

The calculations yield values for A_1, A_2, k_1, and k_2 and are used to fit the data loaded into the scheme builder, extracting values for k_R and k_{NR}. Figure 6.8 shows an example of kinetic fits to a three-state model. This method is utilized in Chapter 7 to elucidate the role of an applied electric field in quantum dot dynamics.

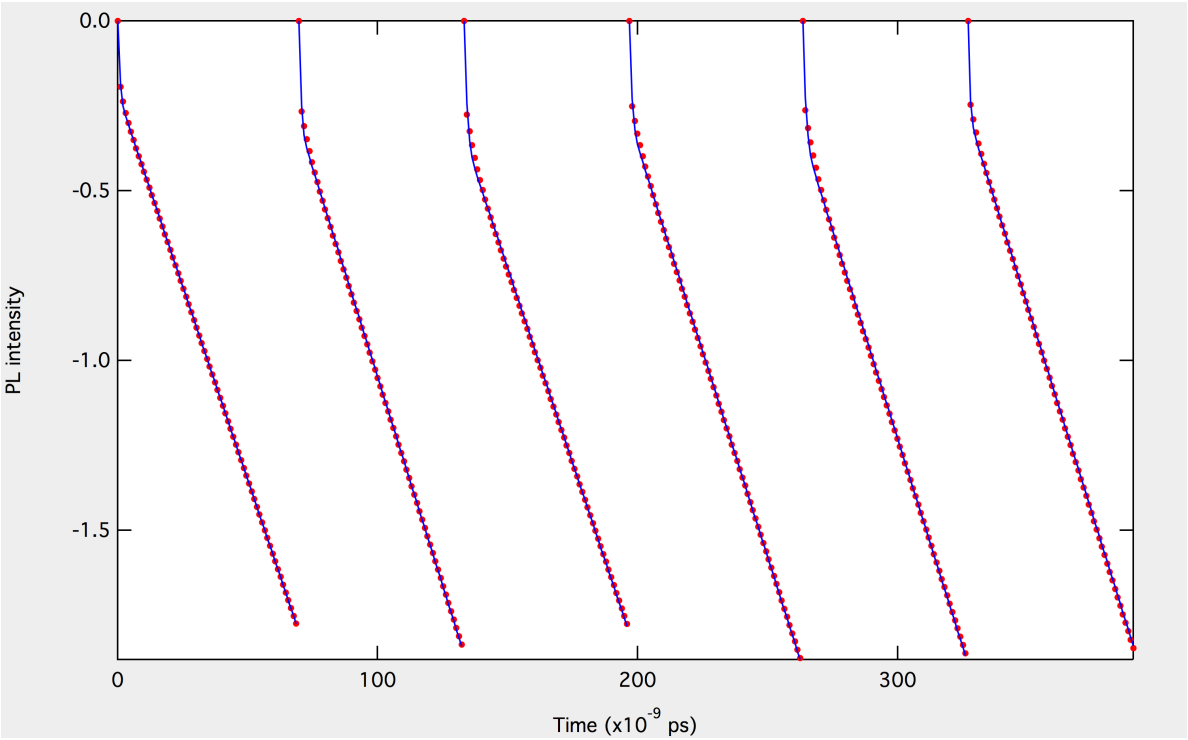

FIGURE 6.8: Example lifetime decays (red) fit to a three state model (blue) using the kinetic modeling software.

CHAPTER 7: RESULTS

7.1 Introduction

Using the experimental and analytical methods described in previous chapters, we have investigated the optical properties of single semiconductor nanocrystal quantum dots under several conditions. Control experiments were conducted without an applied electric field to establish a baseline for comparison to electric field experiments. It was found that spin-casting the nanocrystals within a polymer matrix yields an extremely stable environment for long-term study of single nanocrystals. This semiconductor nanocrystal-polymer system is utilized in all of the work presented here. An electrode device was designed and patterned for use in electric field measurements. Kinetic modeling of electric field data yields valuable information about the effect of electric fields on the nonradiative trapping rate. In exploring alternative electrode designs to achieve higher electric fields, a simple architecture for studying the behavior of multiple excitons in nanocrystals was developed. In this system, a gold film used as an electrode contact also interacts with the excited state of the nanocrystals through plasmonic effects, leading to a pronounced increase in the quantum efficiency of multiphoton emission. By applying an electric field in this system, we can tune the ratio of multiexciton emission to single exciton emission (MX:X).

7.2 Effect of an Electric Field On Single Nanocrystals in a Polymer Matrix

7.2.1 Sample Preparation

The investigation of single particles requires reliable sample preparation, which yields single particles that are spatially separated much farther than the point spread function of the instrument. To achieve an appropriate density of quantum dots on the glass substrate, a dilute (~10^{-11} M) solution of quantum dots is made from the stock solution with toluene solvent. The sample is then drop-cast onto a clean glass substrate, and the excess solvent wicked away. The drop-cast method often yields varied sample densities, and quantum dots are directly exposed to air, leading to single QDs that photobleach quickly. An alternative method of sample preparation, which leads to very photostable single QDs was employed in the current work.

A method of sample preparation was developed to embed the semiconductor nanocrystal quantum dots in a polymer matrix. Spin-casting is utilized, resulting in reproducible samples with repeatable single-particle densities. Using a dilute sample of quantum dots, we ensure that single QDs can be spatially resolved. An additional benefit of the polymer is a stable environment for the quantum dots, protecting the surfaces from degradation and photobleaching. As a result, quantum dots remain photostable under long-term laser excitation for experimental observation, which will be evident throughout these results. For control experiments, CdSe/ZnS quantum dots (Evident Technologies, 617 nm emission) were diluted to 10^{-11} M in a poly-(methyl methacrylate) (PMMA)/toluene (2.5 wt%) solution and spin-cast at 4000 rpm onto a clean glass

coverslip substrate. The thickness of the QD/PMMA layer was measured as ~150 nm using an Alpha-step surface profiler. Figure 7.1 shows confocal images of single quantum dots spin-cast on the glass substrate.

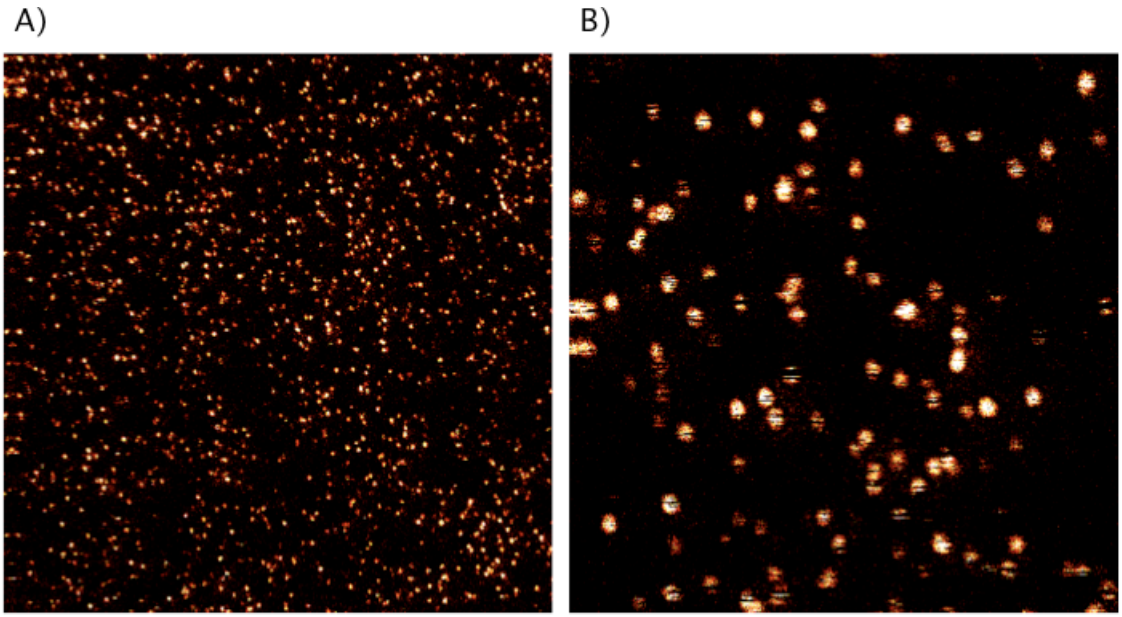

FIGURE 7.1: Images of single nanocrystals spin-cast from a PMMA/toluene solution. Each bright spot is the fluorescence collected from a single quantum dot. A) full 75 x 75 μm confocal scan. B) 20 x 20 μm confocal scan.

7.2.2 Electrode Device Fabrication

Electrode devices were fabricated in a Class 100 Clean Room (Grigg Hall). An interdigitated electrode was patterned on a glass slide using photolithography. The original interdigitated design consists of 2 μm wide gold electrode digits with 2 μm wide spaces in between. Glass slides were cleaned with organic solvents and dried with

nitrogen gas. A positive photoresist (Shipley 1813) was spin coated on the glass slide at 3000 rpm for 30 seconds and baked at 115˚C for 60 seconds. Glass slides were exposed using a contact mask aligner (Quintel Ultraline Q 4000-6). Following exposure, slides were developed in MF-319 developer solution (Microposit®), rinsed with DI water and dried with nitrogen. To remove any excess photoresist, slides were cleaned with oxygen plasma for 10 seconds using Surface Technology System (STS) Advanced Silicon Etch (ASE®) system. A ~100 nm layer of gold was evaporated onto the slides using electron beam evaporation (Kurt J. Lesker PVD 75). Excess photoresist and gold was lifted off using N-Methyl-2-pyrrolidone (NMP) with heat and sonication. Afterward, another oxygen plasma etch was performed for ~2 minutes to remove any excess photoresist. Electrodes were checked for visual defects using an optical microscope and tested for finite resistance using a multimeter. A schematic of the sample architecture is shown in figure 7.2. Details of each step of the photolithography process are outlined in Appendix B. An alternative electrode design was also employed in the current work, which consists of two electrodes with a single 5μm wide space.

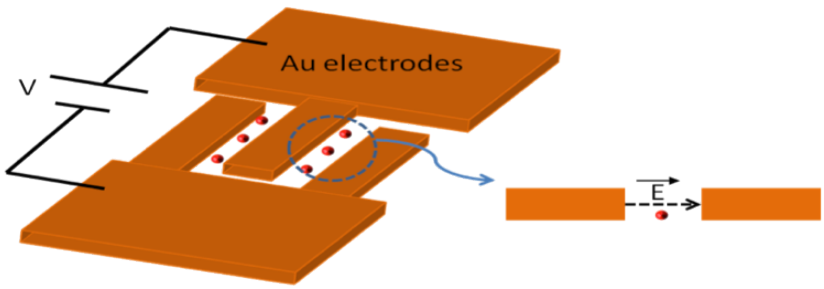

FIGURE 7.2: Schematic of device architecture for electric field experiments.

7.2.3 Electric Field Experiments

Early control samples were prepared by drop-casting on the electrode device. Alternatively, control samples were prepared using the spin-casting method as described in section 7.2.1. Instead of spin-casting onto a glass substrate, the samples were cast onto a glass-mounted gold electrode device described in section 7.2.2. Our homebuilt confocal microscope was utilized to image, and collect time-resolved spectroscopic data from the samples. Figure 7.3 shows an image of the single nanocrystals on the interdigitated electrode device prepared by drop-casting.

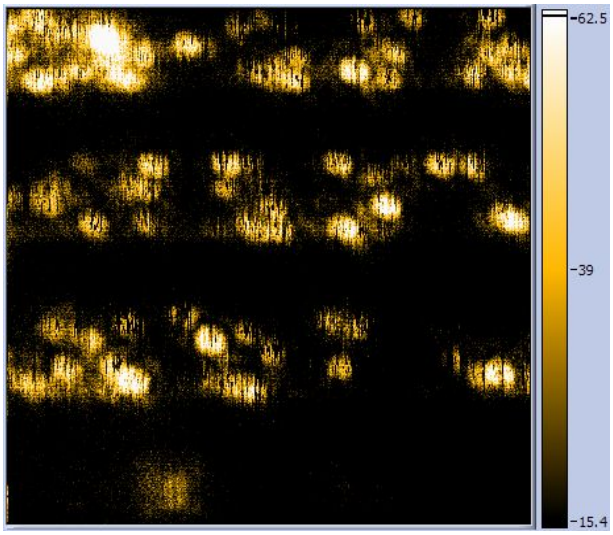

FIGURE 7.3: Image of single nanocrystals on the electrode device prepared by drop-casting method.

Electrode devices were cleaned by sonicating in toluene for 10 minutes, then rinsing with isopropyl alcohol. A fresh sample was prepared as described in section 7.2.1.

Electrical leads were attached to the gold contacts of the electrode device. A voltage was applied using either a dc power supply or function generator. We were able to collect blinking, lifetime decays, and photoluminescence emission spectra of single nanocrystals simultaneously.

7.2.4 Results of Data Analysis and Kinetic Modeling

Data presented in the following sections elucidate the dynamic behavior of 30 control QDs and 29 QDs under the influence of an applied electric field on samples that were prepared as described in sections 7.2.1 and 7.2.3. A 0.05 Hz triangle voltage was applied in all electric field data presented here. Both samples were excited at a laser power of 0.8 kW/cm^2, corresponding to an average number of excitations, $\langle N \rangle$, per pulse of ~0.8 (see Appendix A for calculation). We present the results of blinking, lifetime, spectroscopy, and kinetic modeling analysis of the two sets of QDs. Due to the nature of the three types of data collected, we observe dynamics of the single nanocrystals across three distinct time scales, from nanoseconds to seconds.

For blinking data, photons are binned on a 10-millisecond timescale as described in Chapter 6. A blinking trace representative of the control data set is shown in figure 7.4 (top), and the count rate histogram is shown on the bottom. It is clear that the nanocrystal exhibits bimodal on-off blinking, with some variations in the intensity of the on state. From statistical analysis, the power law exponents are determined as: m_{on}= 1.2, and m_{off}= 1.03. In contrast, the blinking of a nanocrystal in the presence of an applied electric field is shown in figure 7.5. The varying electric field amplitude (± 54 kV/cm) is shown above

the blinking trace. There are no obvious changes in intensity in direct response to the applied field, which has been reported in the literature as discussed in Chapter 5.[85] This may be due to an order of magnitude lower electric field strength compared to those experiments. The power law exponents in the presence of the applied field are: m_{on}= 1.1, and m_{off}= 1.37. This exponent is essentially the gradient of the power law function. Thus, a small exponent (a more shallow gradient) is indicative of a tendency toward longer on/off periods and vice versa. We observe a small decrease in m_{on}, indicative of longer on periods, and an increase in m_{off}, which denotes shorter off periods. Although this may not be immediately apparent upon initial inspection of the blinking traces, further analysis of the count rate histograms reveals the origin of the changes in the power law exponents.

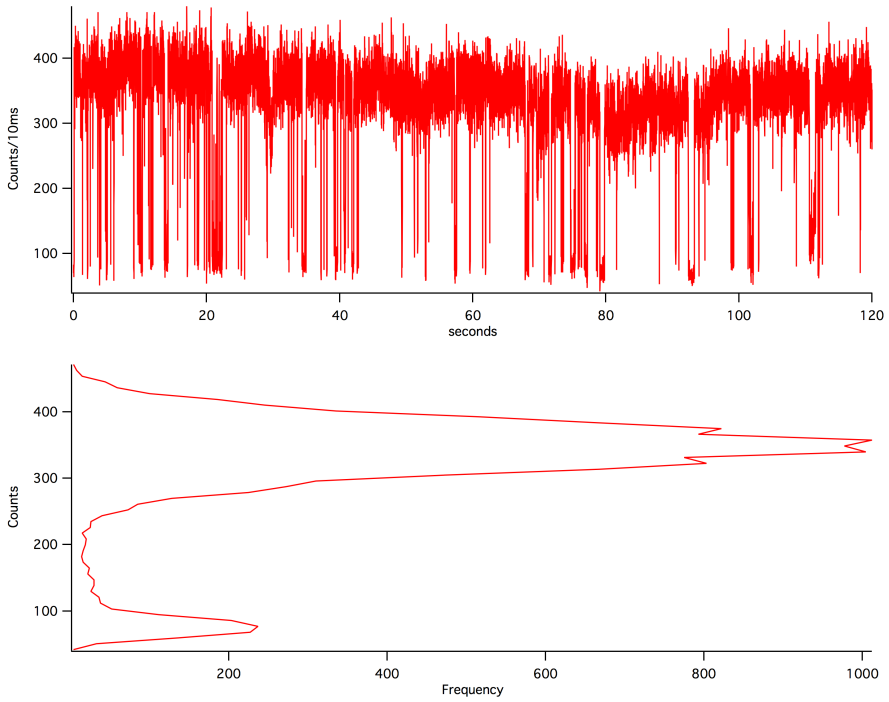

FIGURE 7.4: Blinking trace of control quantum dot on electrode substrate without an applied field.

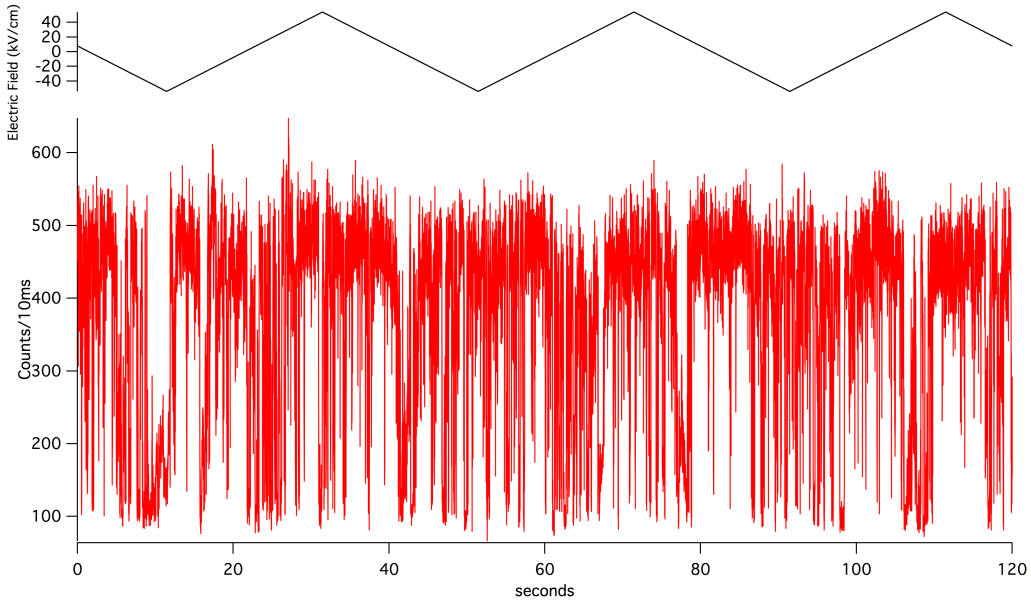

FIGURE 7.5: Blinking trace of single quantum dot under the influence of an applied electric field. The time-dependent electric field amplitude is shown above.

Figure 7.6 shows the count rate histograms of the QDs in figures 7.4 and 7.5, respectively. The histograms are identical to those shown previously for blinking traces, except they have been rotated. Fitting the "on" distribution to a Gaussian function, we extract a width of 52 counts/10ms for the control QD (top), and 60 counts/10ms for the QD under an applied electric field (bottom). The distribution of the control QD is broadened slightly due to a dip in the intensity around 70 seconds. The on state distribution of other control QDs are as narrow as ~30 counts/10ms. In addition to a broader on state distribution, a significant number of counts exist between the two modes in the presence of the applied field, as highlighted in figure 7.6. The broader distribution of on state intensities and existence of intermediate count levels under an applied electric field suggests the existence of "grey" states, in which the QD is neither at maximum quantum yield, nor in an off state. The method frequently employed to determine blinking statistics does not discriminate between on states and grey states. Thus, any grey state is perceived as an "on" state, leading to the observation of longer "on" periods, indicated by a smaller "on" exponent. We suggest that this grey state is comprised of charged excitons, in which a charge is trapped on or near the surface of the nanocrystal, but excited state electrons and holes remain localized in the core, keeping the nanocrystal in an emitting state. Analysis of both data sets reveals clear trends in the blinking statistics and lifetimes, and kinetic modeling supports this model. The results of both data sets are presented in the following sections.

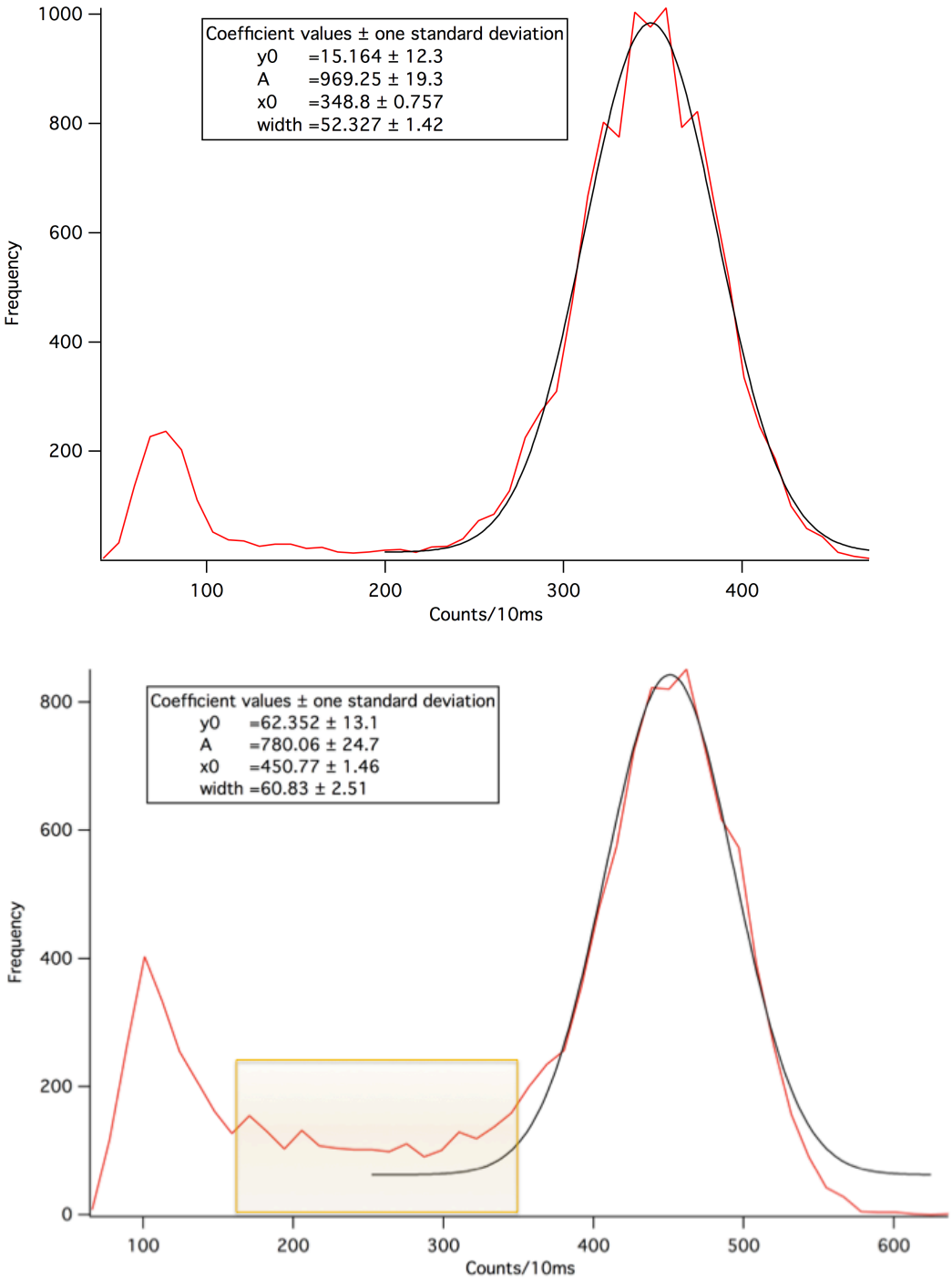

FIGURE 7.6: Count rate histograms of QDs in figures 7.4 (top- control) and 7.5 (bottom- electric field). A Gaussian fit to the on state distribution is shown in black. The presence of a significant number of counts between the modes when the electric field is applied is highlighted.

Blinking traces from each data set were analyzed as described in section 6.2. A histogram of on and off exponents in the absence (black) and presence (red) of an applied electric field is shown in figures 7.7 and 7.8. From the histogram, we observe that in the presence of the electric field the on time distribution shifts to a smaller exponent, m_{on}. The corresponding histogram for the off exponent, m_{off}, shows little change between the two data sets, but the applied field distribution is skewed toward larger exponents, or shorter off times, in the presence of the field. The findings of a distribution centered around longer on times and a tendency toward shorter off times are consistent with one another. The relative insensitivity of the off exponent to environmental changes has been shown in the literature,[73] and is not surprising. Further lifetime analysis allows us to determine a simple scheme to explain these findings.

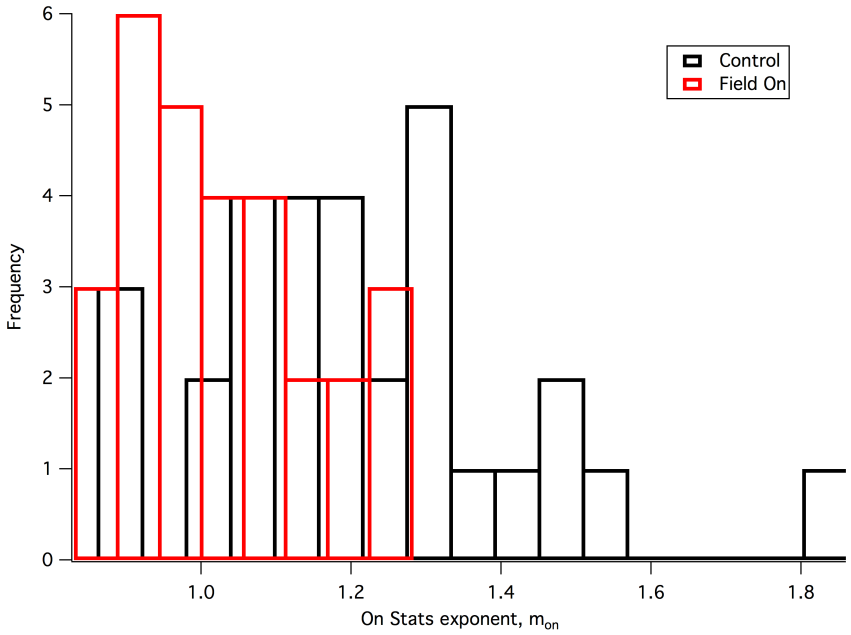

FIGURE 7.7: Histogram of "on" exponent in the absence and presence of an applied electric field.

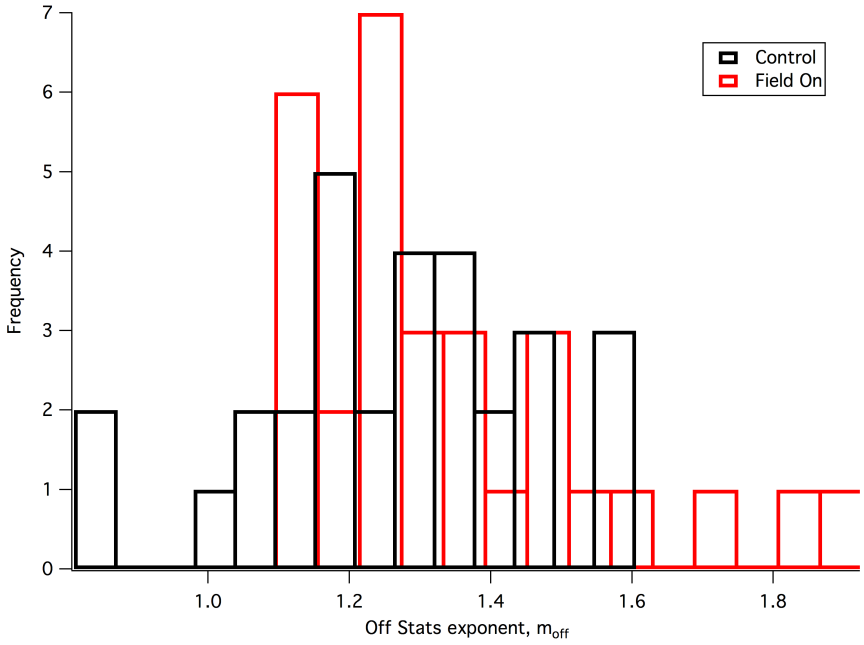

FIGURE 7.8: Histogram of "off" statistics in the absence and presence of an applied electric field.

The excited state lifetime of a single QD at room temperature is observed on the nanosecond timescale. Each single nanocrystal lifetime decay was fit to a sum of three exponential functions as described in section 6.3. Each fit yields an average lifetime, τ_{avg}, of the excited state. This lifetime represents the average time it takes for a photon to be emitted from the fluorescent nanocrystal after an excited state is generated. Photons emitted early in the decay stem from fast radiative processes, while those emitted later result from slower radiative processes. The rates of these collective processes lead to the overall average lifetime of the nanocrystal. Since quantum yields are not typically 100%, decay rates are influenced by non-radiative processes as well, which cannot be directly observed in time-resolved fluorescence measurements. The lifetime decays of the two QDs in figures 7.4 and 7.5 are shown in figure 7.9. Average lifetimes of 22.6 ns and 16.9 ns are calculated for the control QD and QD under the influence of applied field, respectively. It is clear that the shapes of the decays are vastly different, indicating that the electric field is affecting the underlying carrier dynamics. The lifetime of 22.6 nanoseconds is consistent with the ~20 ns room temperature PL lifetime of single nanocrystals reported in the literature for high intensity states.[133-135] Results of fitting the lifetime decays from each set of data are presented in figure 7.10.

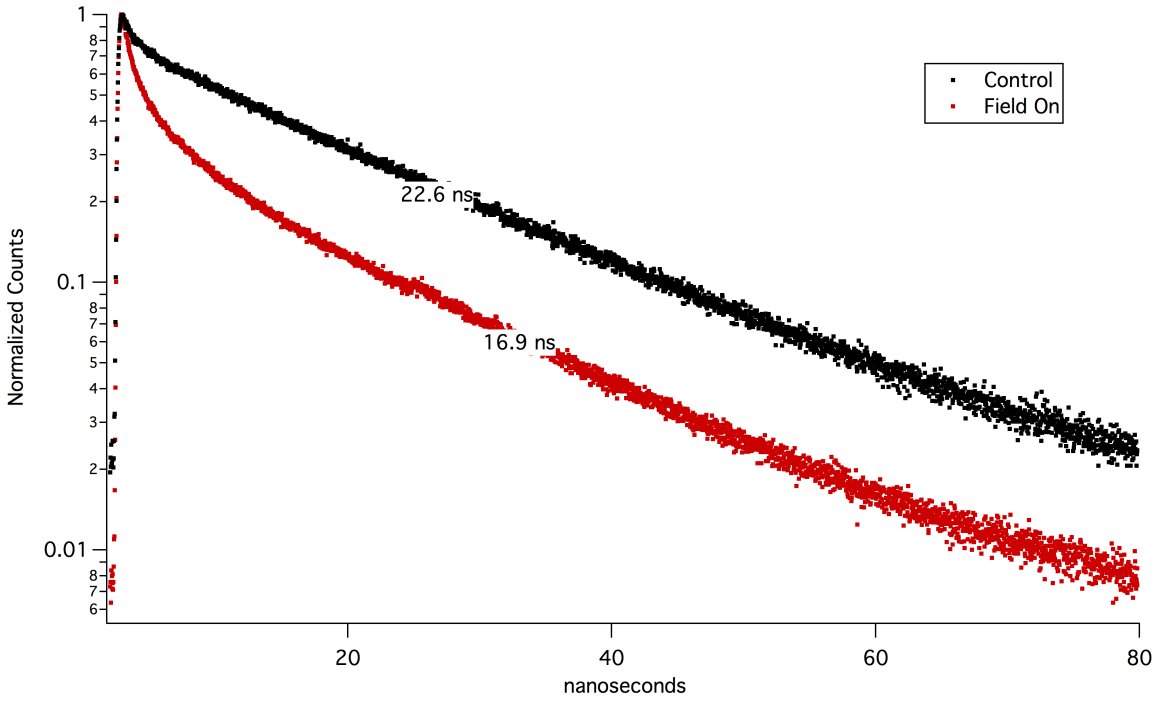

FIGURE 7.9: Fluorescence lifetime decays of single QDs shown in figures 7.4 and 7.5. The calculated average lifetimes from three exponential fits are shown on the graph.

The results of fitting decays of single quantum dots in the absence and presence of an applied electric field are shown in figure 7.10. It is clear that in the presence of the applied electric field, the distribution shifts to shorter average lifetimes. This is consistent with the existence of charged excitons, which relax faster than neutral excitons due to the presence of the excess charge.[9, 80, 136] As discussed previously, the fluctuation of trapped charges on the surface of nanocrystals, and the electric fields due to those charge distributions have been linked to random spectral diffusion of nanocrystals.[7] An investigation of the spectral dynamics of the two sets of data described here is presented in the next section.

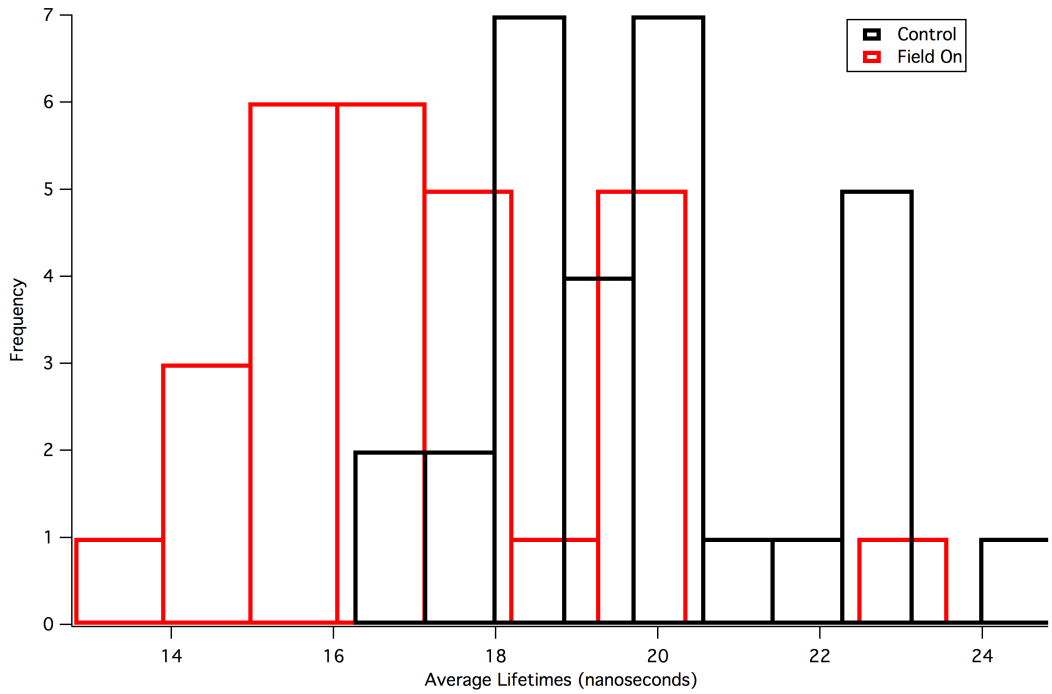

FIGURE 7.10: Histogram of lifetime decays from control and electric field data.

In the current work, single quantum dot spectra are collected over 5 or 10 second acquisitions. While the CCD detector of the spectrometer described in Section 4.3 is cooled to liquid nitrogen temperature (77 K), the nanocrystal sample is held at room temperature (298 K). In this room-temperature set-up, 5-10s acquisition times are necessary to achieve suitable signal-to-noise ratios. Time-resolved spectra are collected by taking successive 5- or 10-second acquisitions of a single quantum dot over 60 or 120 seconds. The time evolution of the control QD in figure 7.4 is shown in figure 7.11. Each spectrum was acquired for 10 seconds over the course of 120 seconds. The raw spectrum is shown in the left panel, while the Gaussian fits are shown in the center panel. The extracted spectral width, σ, from the Gaussian fit shown in the right panel can be

expressed in terms of the full width at half maximum (FWHM) of the spectrum as $FWHM = 2\sqrt{2\ln 2}\sigma$. For the nanocrystal in figure 7.11, we calculate an average FWHM of 86 meV, or 25.6 nm. This linewidth approaches the room temperature linewidth extracted from steady state spectroscopy of CdSe quantum dot ensembles, as shown in Chapter 2. For comparison, spectra of single CdSe QDs at 10 K collected for 10 seconds yield linewidths of ~2 meV.[54] Those experiments, in which spectra were collected on a 0.1 s time scale as a function of excitation intensity, wavelength, temperature and integration time show that a broad room temperature linewidth results from spectral shifting that is fast compared to the acquisition time. Even though rapid spectral shifting leads to the broad single nanocrystal spectra shown in figure 7.11, we do observe additional shifting of the already dynamically and thermally-broadened spectra observed in the time evolution.

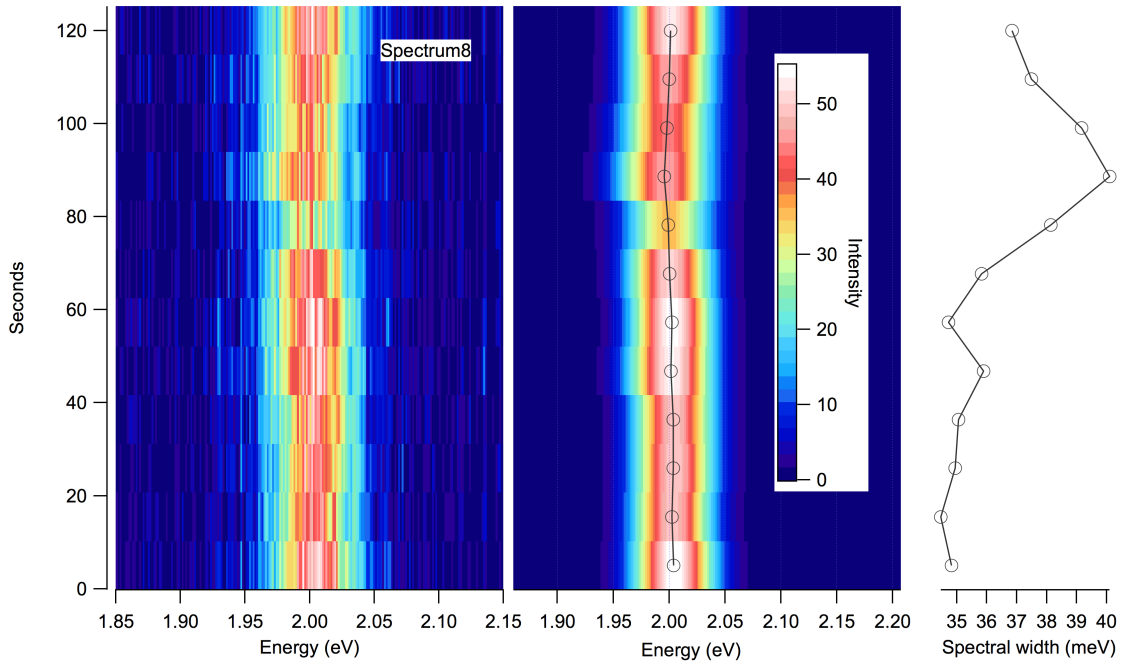

FIGURE 7.11: Time evolution of single quantum dot spectrum.

In addition to shifts in emission energy, we also observe changes in spectral width as a function of time. Figure 7.12 shows the correlation of width versus peak energy. It is clear from the linear regression that more narrow spectra tend to be blue-shifted. In accordance with the quantum-confined Stark effect, higher electric field strengths that stabilize, or red shift, the emission also serve to induce more spectral diffusion, therefore broadening the spectrum.[7] This correlation has been shown in CdSe nanocrystals capped by a CdS rod-like shell.[68] In this system, it was proposed that the surface charge responsible for the local electric field perturbations affecting the exciton was allowed to de-localize along the length of the rod. Thus, the observed quantum-confined Stark effect was a function of the distance of the charge from the exciton localized in the CdSe

core. According to that model, such a correlation is unexpected for spherically symmetric nanocrystals. A correlation between peak position and linewidth has been shown for spherical CdSe/CdS/ZnS NCs in dielectric media,[137] and is clearly observed here. Several of the control QDs either exhibited no width-peak energy correlation, or showed the reverse trend. We revisit the trend later. The results of fitting the time-resolved spectra of both data sets are presented next.

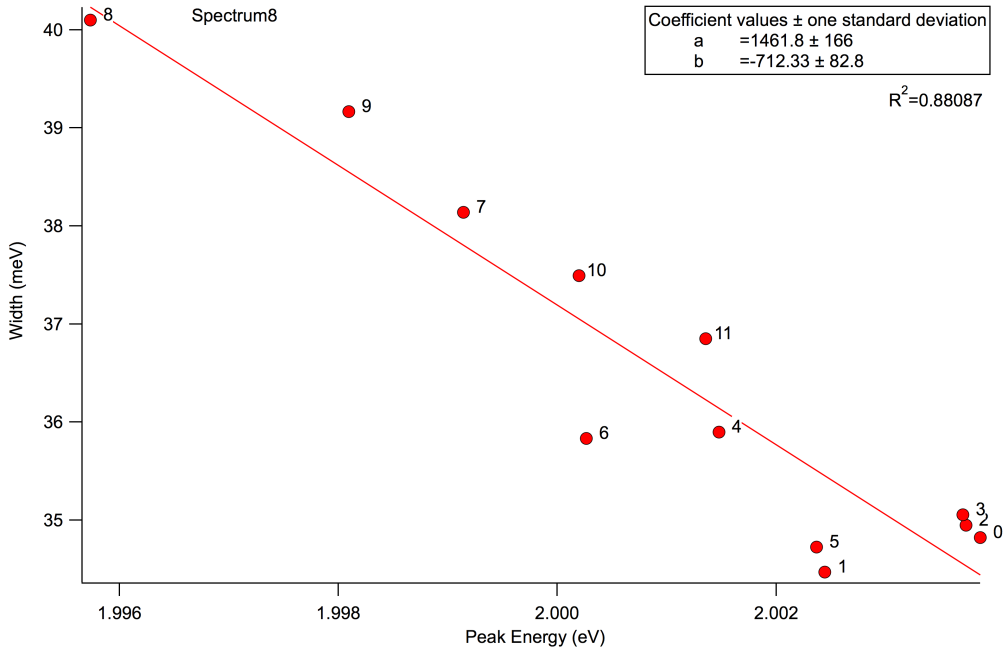

FIGURE 7.12: Correlation of width and peak energy of the single QD spectra in figure 7.11.

Each individual spectrum is fit to a Gaussian function as described in section 6.4, and the peak position and spectral widths are extracted. As discussed in Chapter 5, single

quantum dots exhibit random diffusion of the emission spectrum over time.[4, 5] In addition, Stark spectroscopy of single nanocrystals has revealed reversible switching of the emission energy of single quantum dots at 10 K in response to applied electric fields.[7] It is important to note that low temperature linewidths of single QDs are considerably narrower than room temperature linewidths, as discussed previously. As a result, the signal from an individual quantum dot at low temperature is distributed over a narrower range of pixels, leading to an increased signal-to-noise ratio (SNR). Due to the increase in SNR, single QD spectra can be acquired on millisecond timescales at low temperature. At room temperature, we do not observe clear trends in emission energy in response to the applied electric field. Figure 7.13 shows a histogram of the peak energies of quantum dots in the absence and presence of the applied electric field and exhibits no obvious change in the distribution. The histogram of extracted spectral widths shown in figure 7.14 also shows very similar distributions in control and electric field data.

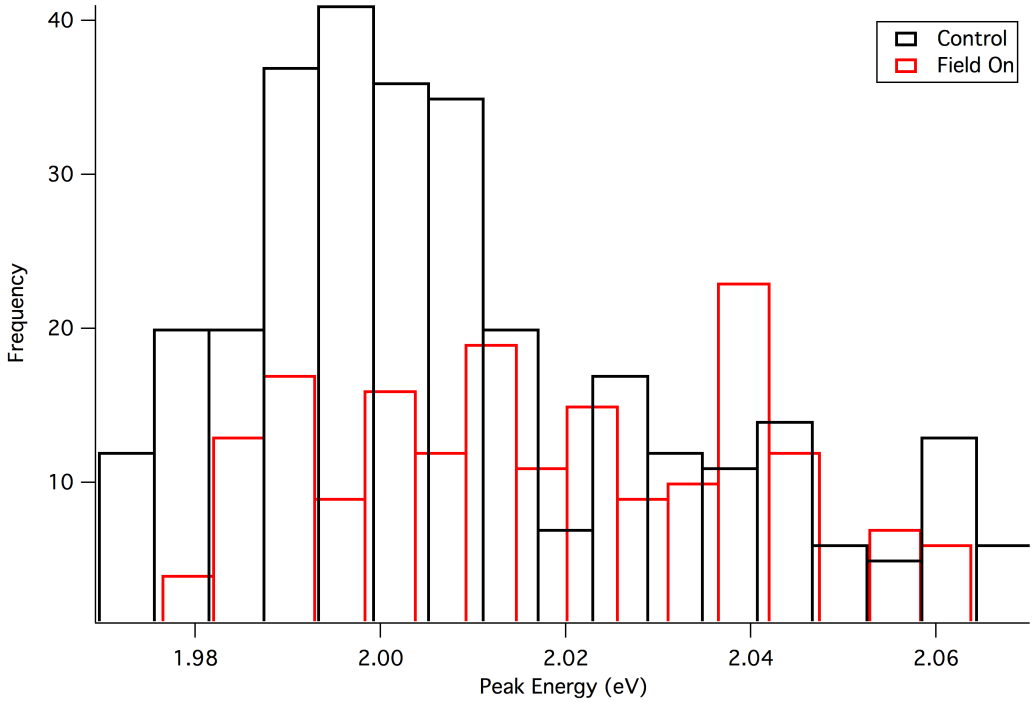

FIGURE 7.13: Histogram of peak energies from Gaussian fits of single nanocrystal spectra in the absence and presence of an applied electric field.

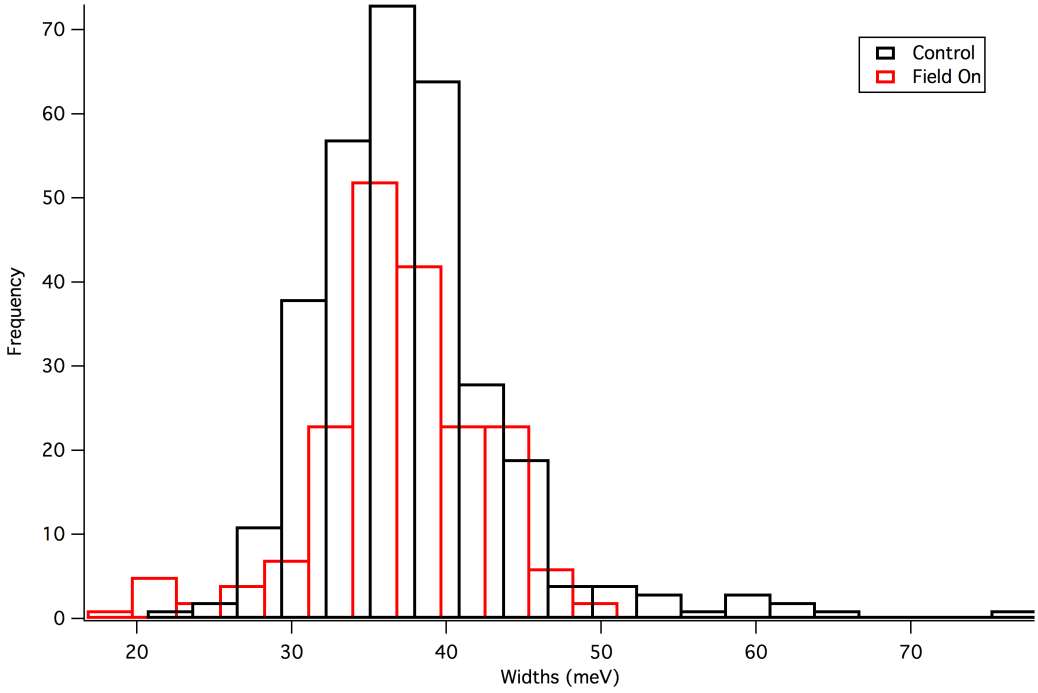

FIGURE 7.14: Histogram of widths, σ, from Gaussian fits of single nanocrystal spectra in the absence and presence of an applied electric field.

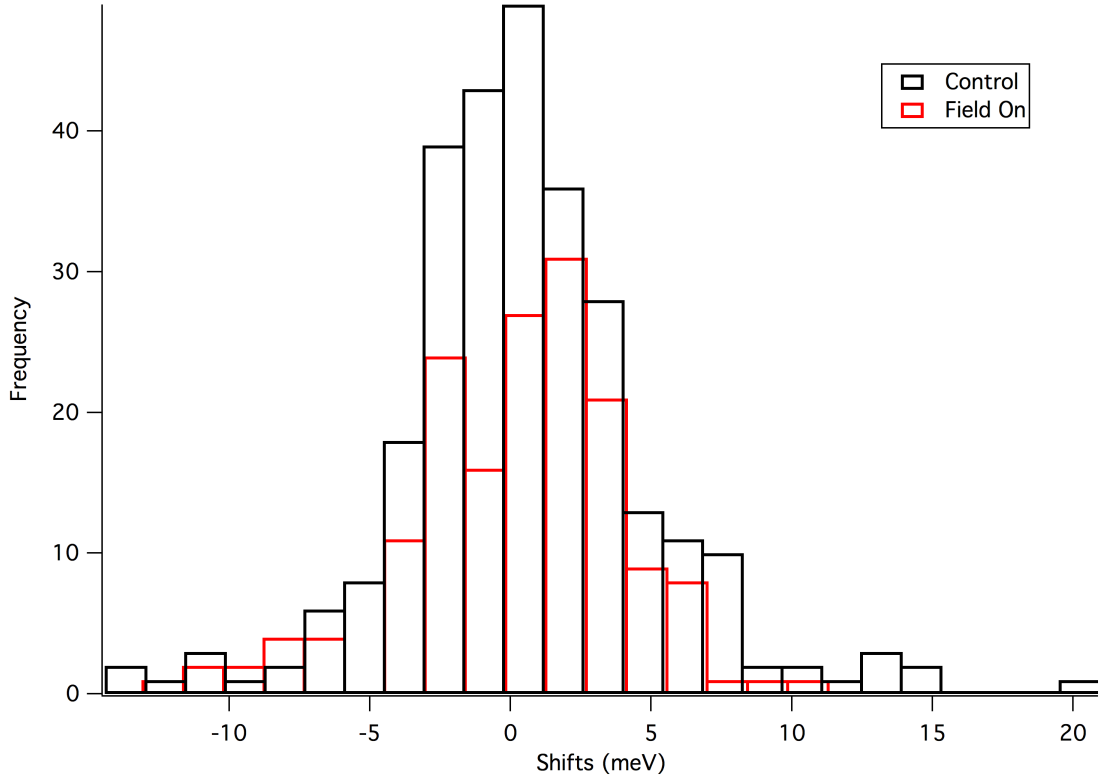

FIGURE 7.15: Histogram of spectral shifts from Gaussian fits of single nanocrystal spectra in the absence and presence of an applied electric field.

Spectral shifts, calculated as the difference in emission energy between consecutive spectra, are shown in the histogram in figure 7.15. Again we show that the histograms are nearly identical. Fitting each shift distribution to a Gaussian function, we can extract a FWHM of 9.8 ± 0.2 meV for the control sample, and 10.9 ± 0.6 meV for the electric field sample. These values, which represent the extent of spectral diffusion, are slightly higher than the values of 4.2 meV at 10K,[8] and 3.7 meV at room temperature,[137] that have been reported in the literature. We attribute the greater extent of spectral diffusion in our experiments to the higher excitation energy of 2.64 eV (470 nm) utilized in our experiments compared to 2.4 eV (514 nm) and 2.54 eV (488 nm) employed in the

previous experiments, and a higher excitation intensity. It was suggested in previous experiments that the reorganization of charge which leads to fluctuations in the local electric field of a nanocrystal is due in part to excess excitation energy released when the exciton relaxes to the emitting state.[54] Thus, an increase in excitation energy and intensity will broaden the spectrum.

Compared to the timescale of blinking (milliseconds) and lifetime (nanoseconds) data, the spectral dynamics can only be monitored over the course of several seconds at room temperature. While we have shown that the presence of the electric field has an effect on the millisecond and nanosecond dynamics, these effects are indistinguishable on a second time scale. Using the kinetic modeling software described in section 6.5, we present a simple model to explain the change in dynamics observed in blinking and lifetime analysis.

We summarize the observations and analysis of blinking, lifetime, and spectroscopy of QDs under an applied electric field compared to the control QDs in Table 7.1. From these observations, we conclude that the electric field must be affecting the charge carrier dynamics. To elucidate the underlying carrier dynamics, lifetime decay fits were modeled using the kinetic modeling methods described in section 6.5.

TABLE 7.1: Summary of observations of QD dynamics under an applied electric field

Observations
Broadened on state distribution and emergence of intermediate state
Decreased m_{on} (longer "on" times)
Unchanged m_{off}
Decreased average lifetime
Unchanged spectral characteristics

A simple three-state model was chosen for global fitting of the decays, a schematic of which is shown in figure 7.16. The exciton state is fixed at 2 eV above the ground state, while a single trap state is used as a parameter in the fitting. A minimum number of parameters are chosen to fit the data, which include a radiative rate, k_R, a nonradiative trapping rate, k_T, and the trap state energy, all highlighted in red in figure 7.16. The Gibb's free energy, ΔG, is calculated as the difference between the trap state energy and the exciton state energy. In the Marcus electron transfer model described in Chapter 5, the Gibb's free energy is a measure of the driving force for electron transfer.

The lifetime decay of each nanocrystal was fit using the outlined parameters. The parameters extracted are presented in the results that follow.

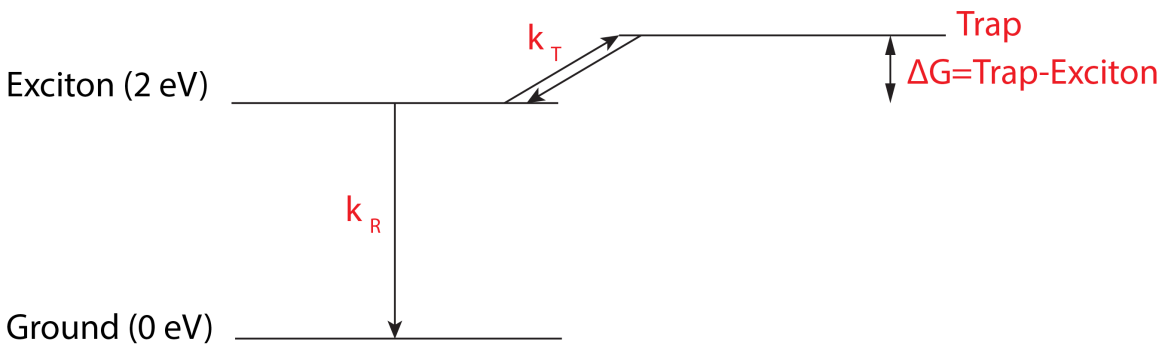

FIGURE 7.16: Three state model used to fit the lifetime decays of single nanocrystals in the absence and presence of an applied electric field.

Figure 7.17 shows a histogram of the Gibb's free energy values extracted for single QDs in the absence and presence of an applied electric field. A shift in the distribution of ΔG to more negative values is clearly shown in the histogram. As discussed previously, a more negative value of ΔG represents an increasingly energetically favorable process. Since the exciton state is fixed in the model, the difference in energy of the exciton and trap states can either reflect a change in the exciton state energy or the trap state energy. Since a stabilization of energy is more likely, we can conclude that the effect of the electric field over the time average of the lifetime acquisition is to lower the energy of the trap state, leading to a higher probability

of trapping. This has important implications for the results of blinking and lifetime data presented herein. As the trap state energy is lowered, the trapping rate increases. Thus, it is more likely that excited carriers will visit the trap state. In earlier experiments, the transition to a trap state was synonymous with a blinking "off" event.[6] However, other models permit emission from a charged nanocrystal,[69] leading to a distribution of emitting states from single nanocrystals. We have induced low-emitting states using an applied electric field, effectively controlling the emission behavior of a single quantum dot. From our earlier observations of the broadened distribution of count rates in the blinking analysis, we can conclude that this is due to emission from charged excitons. Since the trap state is more accessible, the nanocrystal becomes charged more often during successive excitations. When a charge becomes trapped, the weaker emitting grey state persists due to the relatively slow return rate, or de-trapping rate of the trapped charge.

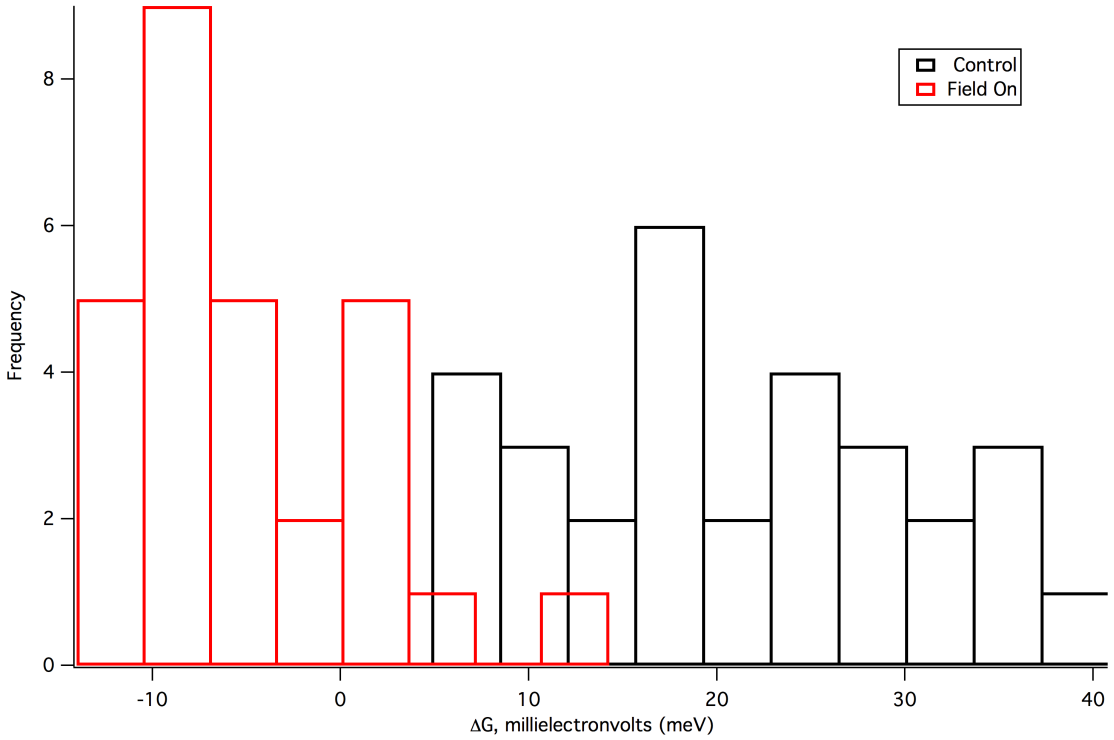

FIGURE 7.17: Histograms of Gibb's free energy, ΔG, extracted from kinetic modeling.

Distributions of the radiative rates in the absence and presence of the applied electric field are shown in figure 7.18. An increase in the radiative rate, consistent with a charged exciton is observed in the distributions. A concomitant increase in the trapping rate is also observed in the distribution of trapping rates shown in figure 7.19. The return rate from the trap state to the exciton states can be described and calculated by Marcus theory.

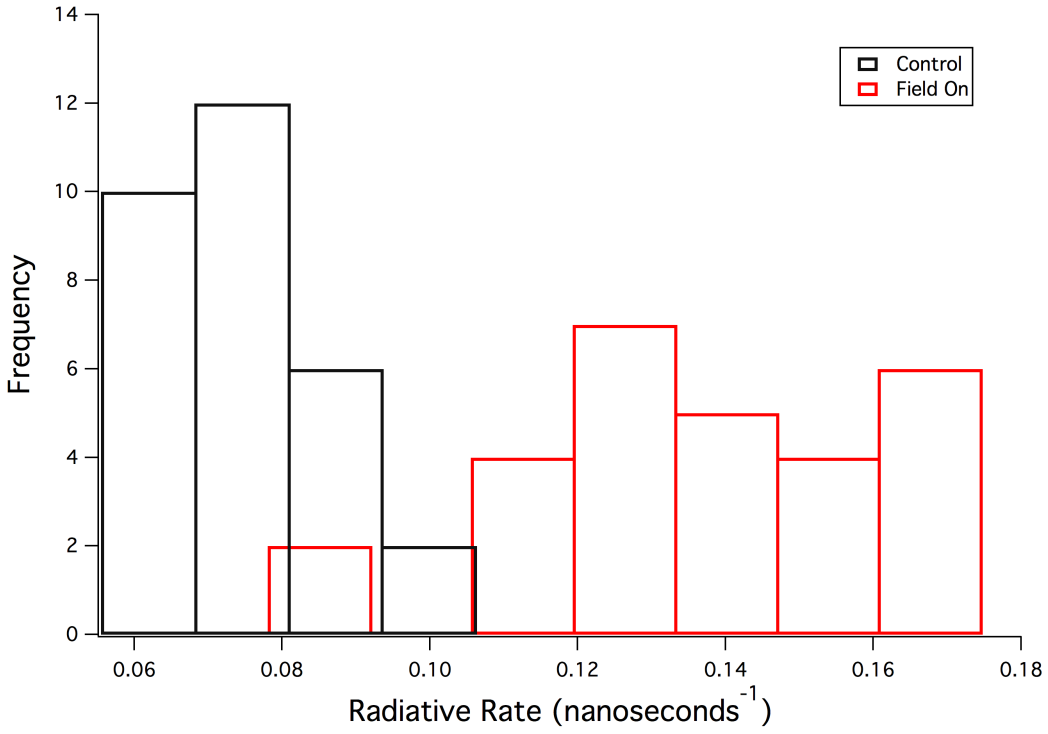

FIGURE 7.18: Histograms of radiative rates extracted from kinetic modeling.

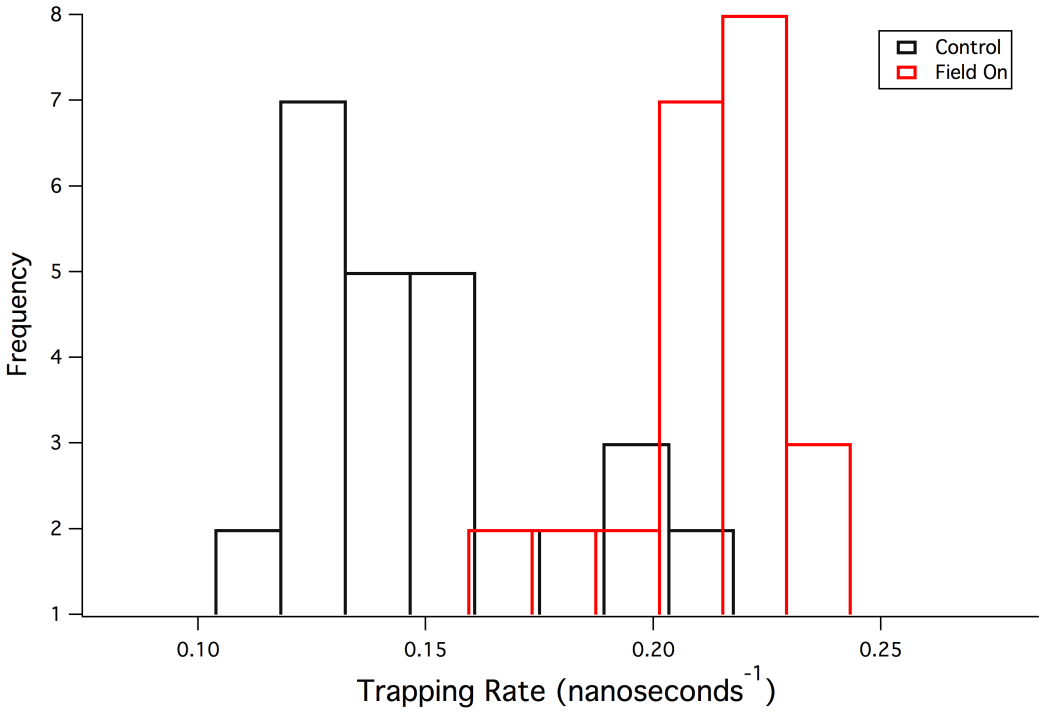

FIGURE 7.19: Histograms of trapping rates extracted from kinetic modeling.

While we do not fully parameterize Marcus electron transfer theory for nanocrystals here, we do extract the very important parameter ΔG, which is a step towards completing the picture of Marcus electron transfer theory for nanocrystals. The extracted values for ΔG are consistent with ensemble measurements incorporating this formalism.[128] The average decrease in ΔG of ~8 meV is consistent with Coulomb interaction energies of charges separated by several nanometers, which suggests multiple surface charging.

The response to switching a dc electric field on and off for several seconds while observing a single QD was also explored. The results indicate a comparable behavior to that observed with the constantly varying triangle applied field. Most notably, the behavior is non-linear with the applied electric field. The dynamics did not respond directly to switching the electric field on and off. In the case of a varying field, the average electric field experienced by the nanocrystal over the course of our experiment is ~27 kV/cm. Our findings suggest that the electric field effect is a small perturbation to the surface charge distribution. Once charges are perturbed, the return to their equilibrium state may take an extended period of time beyond our observation period. This non-linear effect is indicative of electric field-induced charge redistribution, which should exhibit hysteretic behavior. We summarize the interpretation of our observations in Table 7.2.

TABLE 7.2: Summary of interpretation of observations of QD dynamics under an applied electric field

Observations	Interpretation
Broadened on state distribution and emergence of intermediate state	Electric field induced perturbation of surface charge distribution and trap state energies
Decreased m_{on} (longer "on" times)	On states appear longer due to prolonged grey states= emission from charged NC
Unchanged m_{off}	Off states are still induced by multiple charging events
Decreased average lifetime	Increased k_R, consistent with emission from a charged NC
Unchanged spectral characteristics	Insufficient temporal resolution

In addition to a broadening in the distribution of emissive states of the nanocrystal, we occasionally observe discrete transitions between two levels from single quantum dots as shown in figure 7.20. This has been observed previously in CdSe/CdS nanocrystals.[9] What at first glance may appear to be two nanocrystals is actually the transition of one nanocrystal from an intermediate emitting state to a high emitting state. This emissive behavior was previously attributed to transitions to and from a trion, or charged exciton state.[9] The average lifetime extracted from a three-exponential fit is 17.5 ns. We are also able to generate decays using only certain ranges of photons as described in the literature previously.[9, 133, 134] These methods have revealed single exponential decay behavior associated with the high count rate regions of the blinking trace. As photons from lower count ranges are included in the decay, it becomes less single-exponential. This is attributed to dynamic fluctuations in the nonradiative pathways over the course of acquisition.[133] The single decay rate extracted from the top 10% of photons has been attributed to the intrinsic radiative rate of the nanocrystal.[134]

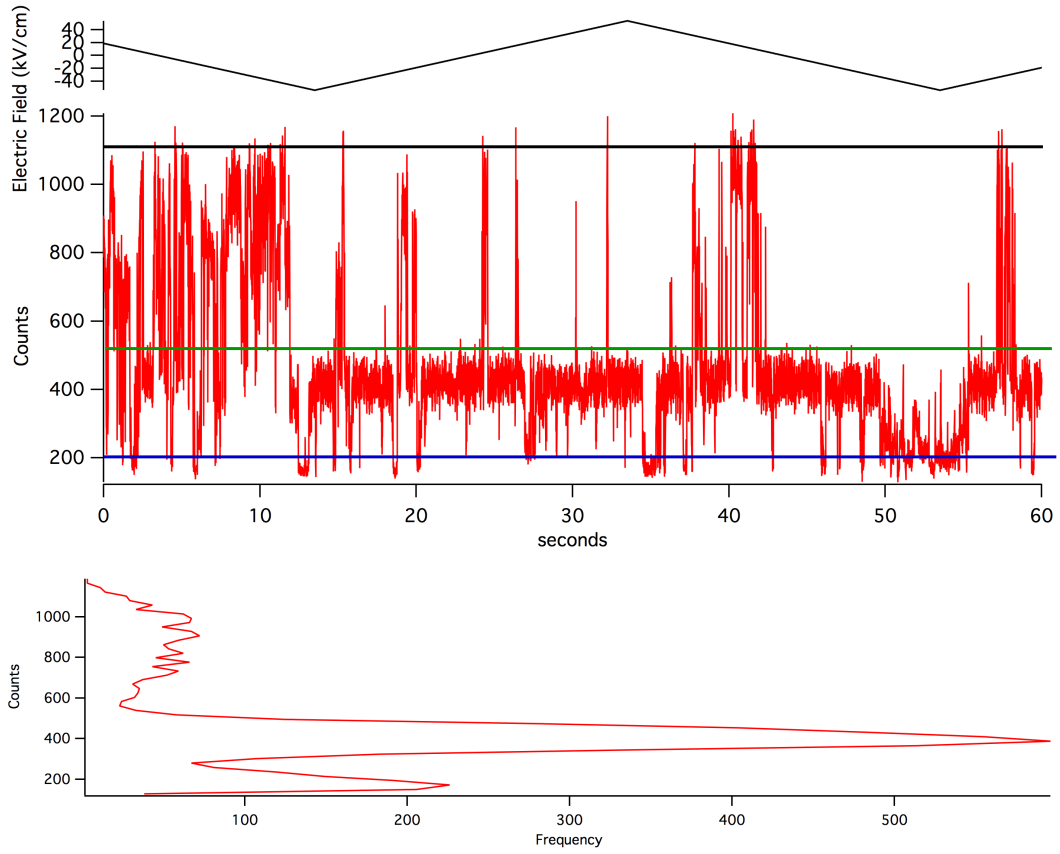

FIGURE 7.20: Two-level blinking in the presence of an applied electric field.

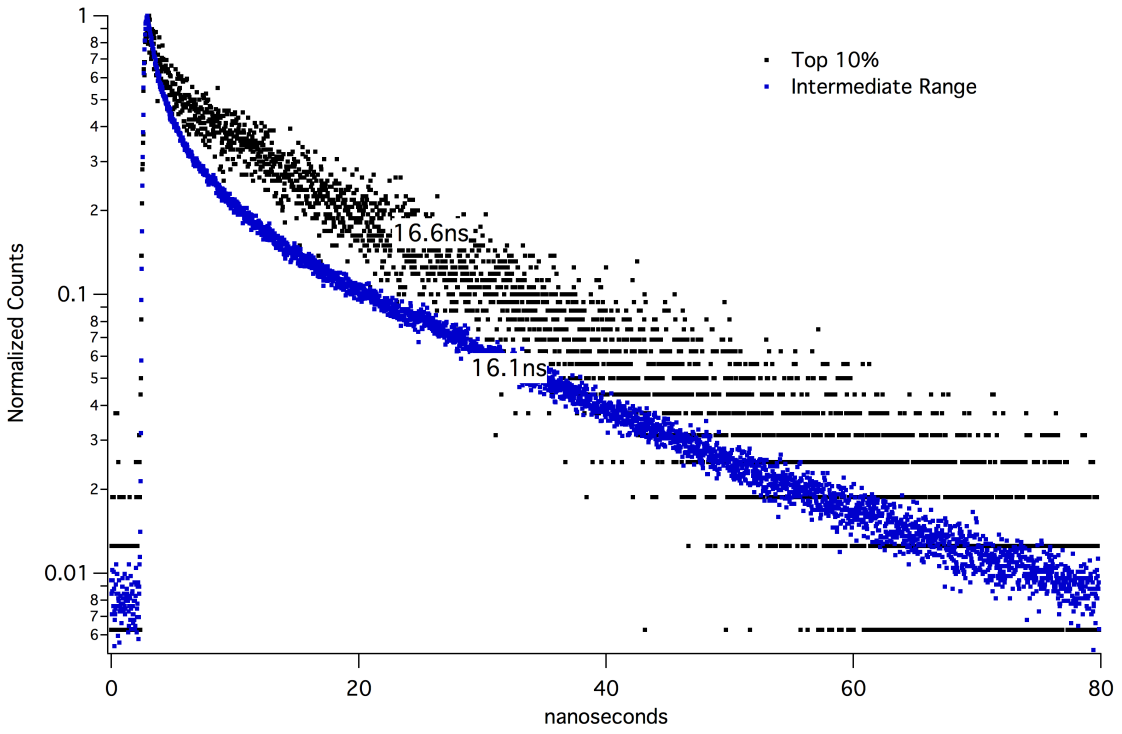

FIGURE 7.21: Lifetime decays of indicated ranges in figure 7.20. The calculated average lifetimes are shown on the graph.

Figure 7.21 shows the decays generated from the top 10% of photons (above black line in figure 7.21), and from the intermediate range (between blue and green lines). It is clear that although the average lifetimes are very similar, the shapes of the decays are very different. The decay of the intermediate range is clearly less single exponential than the top 10% range. As previously described, this is consistent with a distribution of non-radiative pathways. It is clear that the decay of this state involves a significant contribution from a non-radiative trap state that is varying in energy over time. This can also explain the non-exponential behavior of the QD under an applied electric field shown in figure 7.9. The two-level blinking shown in figure 7.20 has not, to our

knowledge been shown for CdSe/ZnS QDs. This may be due to the high conduction band energy of ZnS compared to the conduction band of CdSe, which will reduce the leakage of the electron wavefunction into the shell and surroundings. Since CdSe/CdS is a quasi-type II heterojunction, there is a higher probability of the electron localizing to the surface, and thus a greater trapping probability. In applying an electric field to CdSe/ZnS QDs, we have effectively created a condition in which the electron can trap more easily, thus enabling us to observe this discrete intermediate state, the same effect shown in CdSe/CdS QDs.[9]

Figure 7.22 shows the corresponding time-resolved spectra for the QD in figure 7.20. The integration time for each spectrum is 5 seconds. The spectral widths are consistent with a single nanocrystal. The correlation of width vs peak energy in figure 7.23 shows the reverse trend from that presented earlier on a control QD. We suggest that the variation in this correlation is dependent upon the emitting state of the nanocrystal, and whether or not external charges are present. It is conceivable that the presence of multiple excess charges will affect the local electric field of the nanocrystal, and therefore the spectral dynamics.

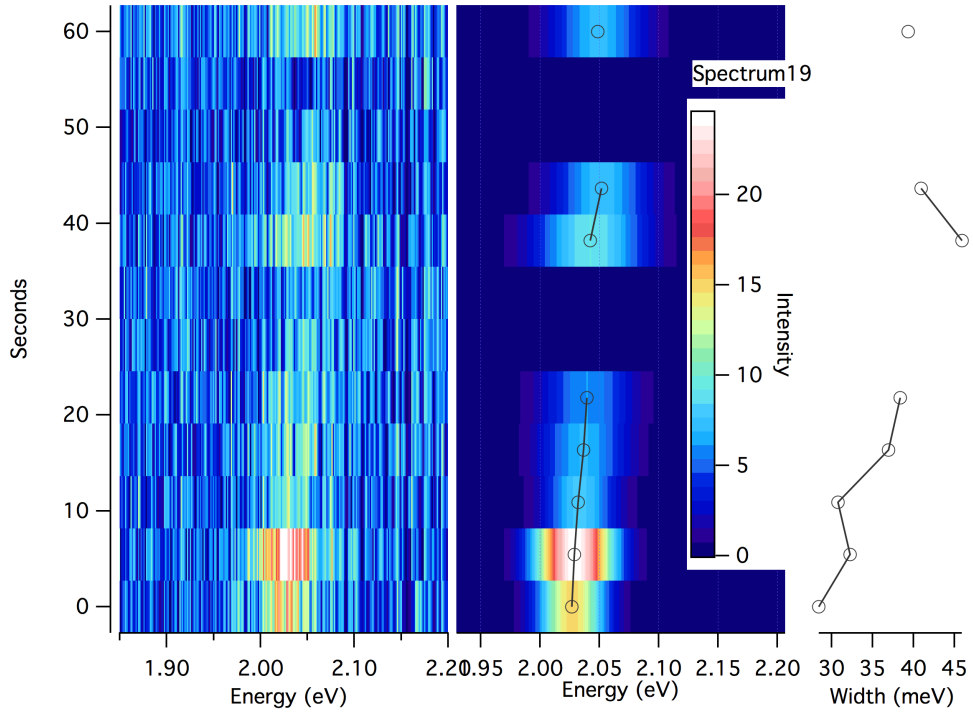

FIGURE 7.22: Time evolution of spectrum for QD shown in figure 7.20. The spectral widths are consistent with that of a single quantum dot.

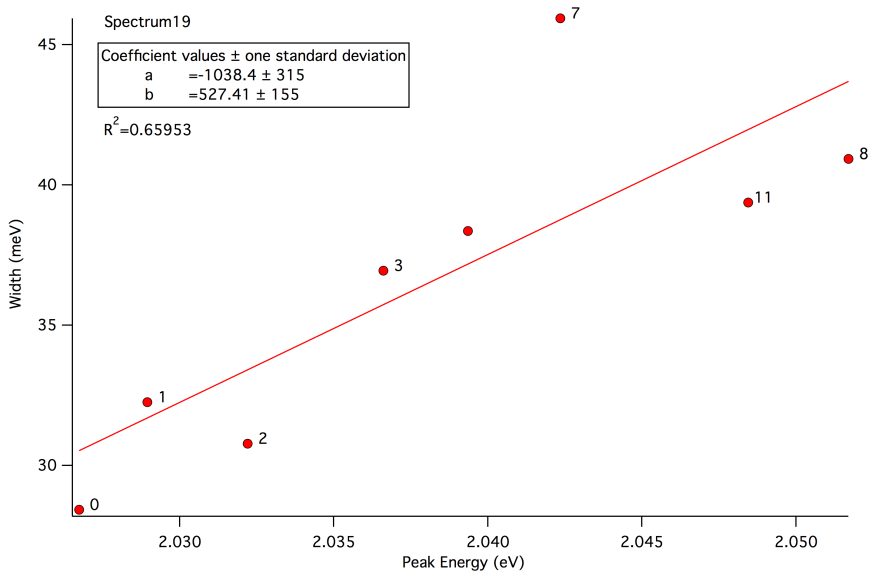

FIGURE 7.23: Correlation of extracted peak width and peak energy for the spectrum shown in figure 7.22.

We have shown that the effect of a modest applied electric field of ~50 kV/cm leads to small fluctuations in intensity of single nanocrystal blinking and changes in PL decay behavior. We attribute the changes in emission behavior to redistribution of surfaces charges, associated with the polarizability of the excited state. This is consistent with our observation of a nonlinear effect. As mentioned in Section 5.3, the electric field effect on a polarizable system is proportional to the square of the applied electric field. Stark spectroscopy of nanocrystals has revealed a strong polarizable character in the excited state.[7] The redistribution of charge by application of electric fields in this experiment leads to an increased trapping rate due to modulation of nonradiative pathways associated with surface charge distributions, as confirmed by modeling of lifetime decays. Kinetic modeling enabled the extraction of important parameters for a Marcus electron transfer-inspired theory of carrier dynamics in nanocrystals. This in-depth analysis clearly demonstrates that surface charges and trapping play an integral role in excited state dynamics. Specifically, emission from charged states is supported, and therefore off states are due to trapping of multiple charges. Additional data from within our group also supports multiple charging of nanocrystals through blinking correlation experiments between neighboring QDs. Small perturbations by an applied electric field show that the redistribution of the surface charges leads to a pronounced change in radiative decay of the exciton, demonstrating a complex role of surface states in the radiative decay of the exciton state.

7.3 Effect of a Strong Localized Electromagnetic Field on Nanocrystal Multiexciton Dynamics

While exploring alternative electrode designs for electric field experiments, we developed a simple method to study multiexciton dynamics in single nanocrystal systems. In this section, we demonstrate strong enhancement of multiphoton emission from CdSe/ZnS core-shell quantum dots localized near a rough gold thin film utilizing single molecule time-resolved fluorescence spectroscopy. By employing the Hanbury Brown-Twiss geometry described in Chapter 4, we were able to correlate time delays between photons emitted from a fluorescent sample to reveal a strong enhancement of multiphoton emission. Analysis of single QD photon correlations, blinking data and fluorescence decays show an increase in radiative recombination rates of multiexcitons that are much higher than previously expected and, perhaps more significantly, are not correlated with concomitant increases in single exciton recombination rates. We believe that these results confirm a stronger coupling of multiexcitons to plasmon modes via a coupling to plasmon multipole modes. The device architecture shown in figure 7.24 represents a simple approach for study of multiexciton-plasmon interactions.

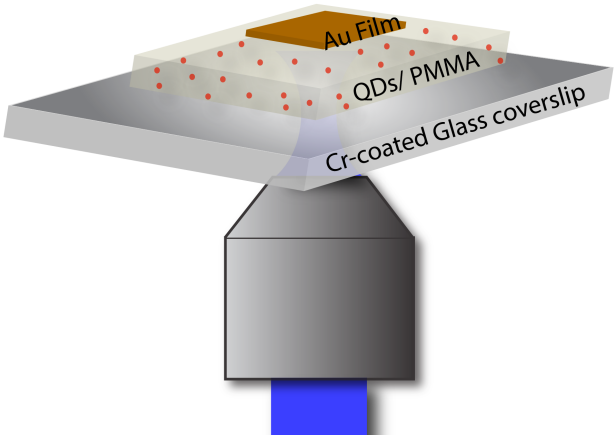

FIGURE 7.24: Schematic diagram of sample architecture for multiexciton-plasmon experiments. A dilute solution of quantum dots in PMMA/toluene is spin-cast on the chromium-coated glass coverslip. A gold film is sputtered directly on top of the QD/PMMA layer.

To prepare the sample, a thin layer of chromium (~10 nm in thickness) was evaporated onto a clean glass substrate using an electron beam evaporator. Commercially available CdSe/ZnS quantum dots (Evident Technologies, 617 nm emission) were diluted to 10^{-11} M in a poly-(methyl methacrylate) (PMMA)/toluene (2.5 wt%) solution and spin-cast onto the chromium-coated glass substrate. The thickness of the QD/PMMA layer was measured as ~150 nm using an Alpha-step surface profiler. Regions of the QD/PMMA layer were masked, and a layer of gold was sputtered on top of the QD/PMMA at 100 W for 10 minutes. Individual quantum dots were imaged using our homebuilt laser scanning confocal microscope. The results of photon correlation spectroscopy, blinking, and time-resolved fluorescence will be presented here.

Representative photon correlation data of quantum dots on the same sample isolated from the gold film (control), and coupled to the gold film are shown in figure 7.25. The sample was excited with a power density of 2.4 kW/cm^2. At this laser power density, the average number of excitons generated per QD per pulse, $\langle N \rangle$, is estimated at 2.5. (See Appendix A for calculation). Control QDs rarely exhibit multiphoton emission, evidenced by the absence of a peak at $\tau = 0$. From the control experiments, we can conclude that the presence of the chromium (Cr) has very little effect on the radiative recombination rate of the multiexcitons, and that Auger recombination still dominates multiexciton behavior. Hence, the absence of a peak at $\tau = 0$. This is in contrast to quantum dots coupled to the gold film, which consistently exhibit multiphoton emission from a multiexciton (MX) state. In addition, the intensity of the side peaks, corresponding to single photon emission (X), is diminished in the presence of the gold film. It is also clear that both single exciton (X) and multiexciton (MX) peaks are much narrower compared to the control samples, indicative of a shortened excited state lifetime. Quantitative analysis consists of dividing the intensity of the peak at $\tau = 0$ by the average intensity of the side peaks. This relative ratio, labeled MX:X, for 85 quantum dots is illustrated in figure 7.25g. The red curve is a Gaussian fit of the data with parameters *y0* (minimum), *A* (amplitude), *x0* (mean), and *width* (standard deviation). The fit indicates a mean ratio of ~0.46, while a few QDs exhibit ratios greater than unity, confirming a widespread effect. While it may be tempting to use this ratio as a measure of the relative quantum yield of emission from a biexciton state (BX) to single photon emission (X), as

has been shown by Nair *et al.*,[120] that is not accurate in this case. Nair was careful to point out that this is valid only in the limit of $\langle N \rangle \rightarrow 0$, a condition which is not met in this case as we pointed out above. Thus, we only use the MX:X ratio as method to demonstrate that enhanced multiphoton emission is observed on many quantum dots when coupled to the rough gold film.

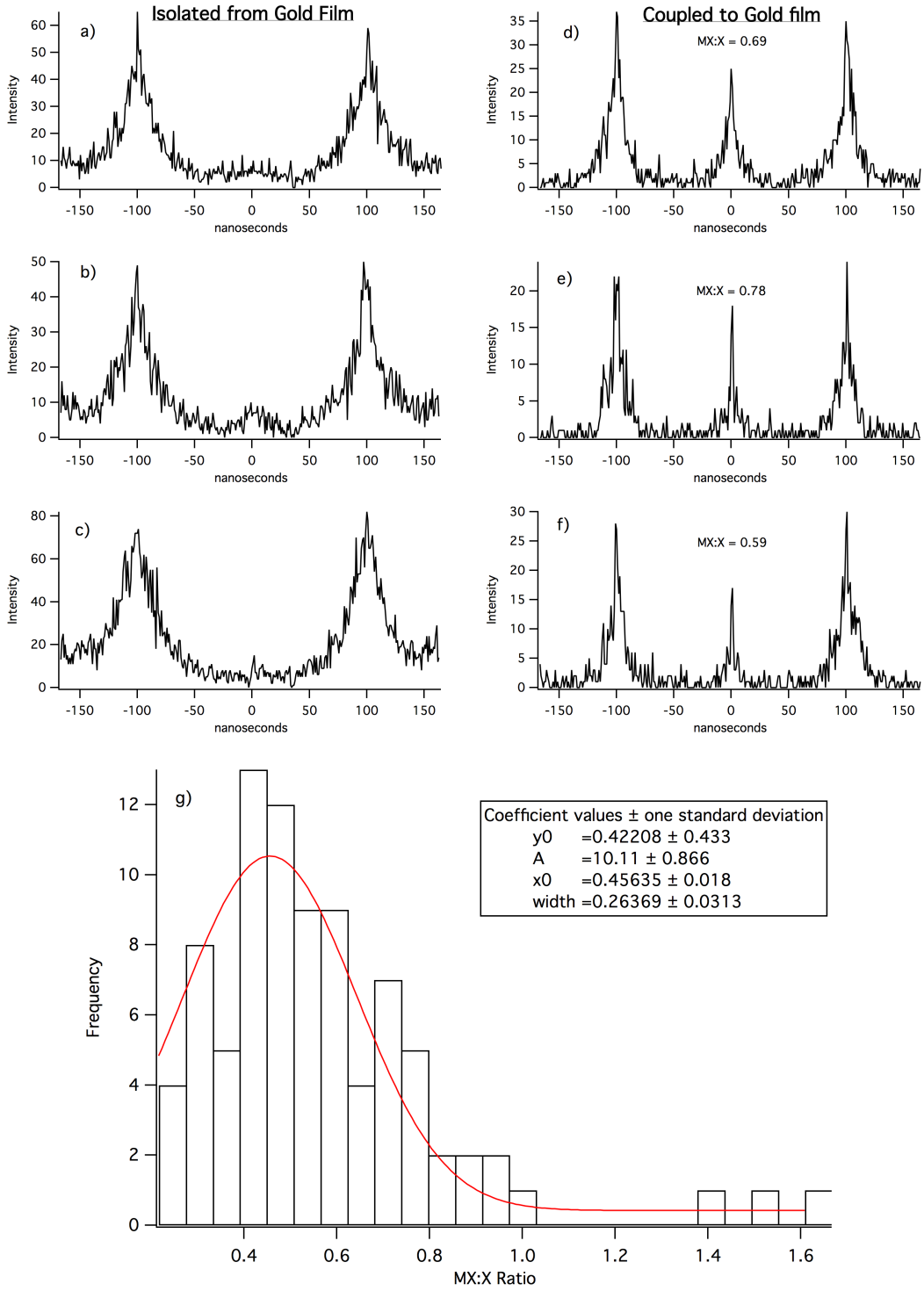

FIGURE 7.25: Photon correlation histograms of three quantum dots isolated from the gold film (a-c) and three quantum dots coupled to the gold film (d-f). Histogram of MX:X ratios for 85 quantum dots (g) and a Gaussian fit (red curve).

What requires specific attention regarding these photon correlation data are (1) the decrease in X fluorescence quantum yield, (2) the increase in MX fluorescence quantum yield, and (3) the narrowing of each of the peaks. We believe that these observations are a result of a coupling to the plasmon modes of the rough gold film, but that the single exciton state interacts significantly differently than the multiple exciton state. Regarding the control data, the absence of a central peak (antibunching), despite a high exciton emission number per QD per pulse (~2.5) is well known to result from strong Auger recombination, which reduces the probability of two-photon emission from the same pulse. In other words, Auger recombination dominates the radiative emission rate. However, our results clearly indicate that the MX fluorescence rate has become very competitive with the Auger rate despite the obvious introduction of the energy transfer pathway introduced by the rough gold film. We will now show, quantitatively, how the radiative rate of the MX must be much stronger than the normal $m^2 k_R^X$ expected for multiexciton states, where m is the number of excitons generated, and k_R^X is the radiative rate of the single exciton. We begin with a lifetime analysis and then revisit the photon correlation data.

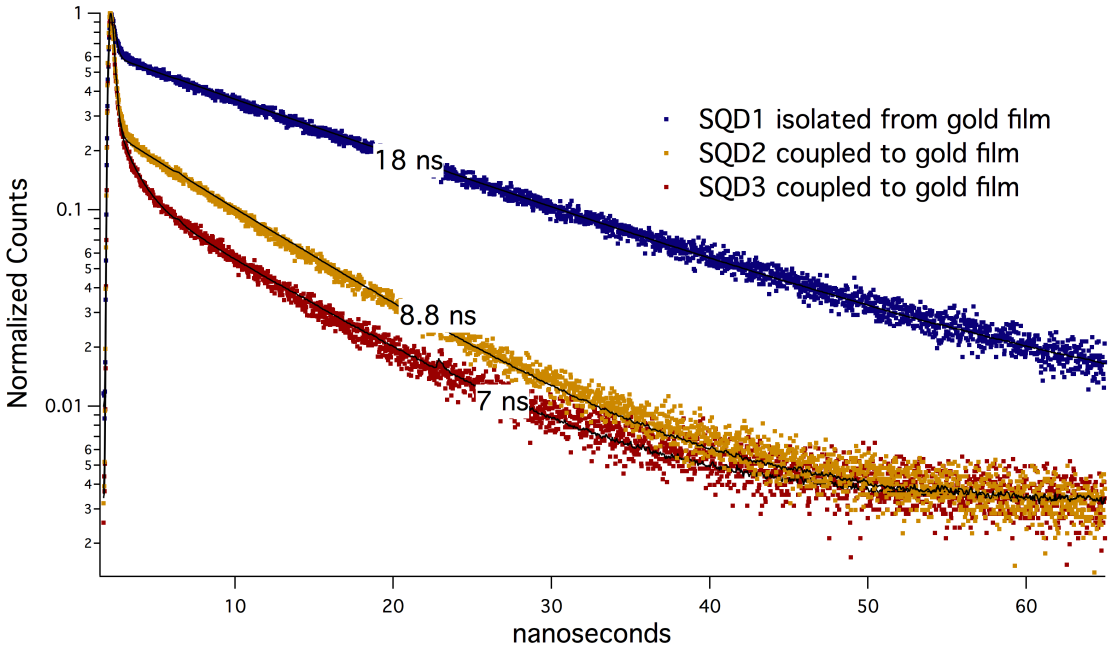

FIGURE 7.26: Lifetime decays of single quantum dots (SQDs) isolated from the gold film (blue- SQD1) and coupled to the gold film (yellow- SQD2, red- SQD3). Average lifetimes calculated from multiexponential fits are shown in the graph. Sample was excited at 2.4 kW/cm^2.

Figure 7.26 shows a quantitative analysis of the lifetimes of control SQD1 (blue curve) and SQD2 and SQD3 coupled to the gold film. The SQD1 and SQD2 decays were each fit to a bi-exponential function, which exhibit a decrease from an average lifetime of 18 ns to 8.8 ns in the presence of the gold film. The SQD3 decay was fit to a tri-exponential function to obtain an average lifetime of 7 ns. The variation in average lifetime from dot to dot near the gold film demonstrates a distribution of coupling to the metal, likely due to the sample preparation method and sample inhomogeneity. We attribute the slow component of the decay to X photon emission and the fast component to MX emission. We justify this assignment later using lifetime decay analysis. The MX

emission is most likely BX emission, but we cannot rule out emission from higher order excitons, such as triexcitons.

Multiphoton emission from single nanocrystal systems is usually unobserved due to fast non-radiative Auger recombination processes, which competes with any radiative processes. Therefore, our observation of multiphoton emission must result from either a decrease in the Auger recombination rate or an increase in the radiative rate. In specially engineered thick-shelled nanocrystals, significant Auger rate reduction has been observed.[122, 124] In these materials, a concomitant reduction in blinking behavior is also observed, leading to non-blinking quantum dots.[126] When thick-shelled nanocrystals are coupled to localized surface plasmon modes, enhanced radiative emission from biexciton states is also observed, along with enhanced fluorescence and a reduction in blinking.[105] For conventional CdSe/ZnS nanocrystals coupled strongly to silver nanoparticles, an increase in multiphoton emission was attributed to an increase in the radiative decay rate due to the enhanced electromagnetic field of the surface plasmon.[104] However, in that study the increase in radiative decay is further supported by fluorescence enhancement near the silver nanoparticles with enhancement factors approaching ~20. We *do not* observe an increase in X radiative emission, but rather we observe the opposite.

To explore the possibility of radiative rate enhancement in our experiments, we calculated a radiative rate enhancement factor based on the blinking traces of 5 control QDs and 5 QDs coupled to the gold film. Figure 7.27 shows the blinking traces of SQD1 and SQD3 from Figure 7.26. We note two observations from these data: 1) a ~ 50 %

decrease in count rate and 2) an increase in the rate of blinking in the presence of the gold film. These findings are distinct from previous observations of fluorescence enhancement and blinking reduction in the presence of nanostructured metals.

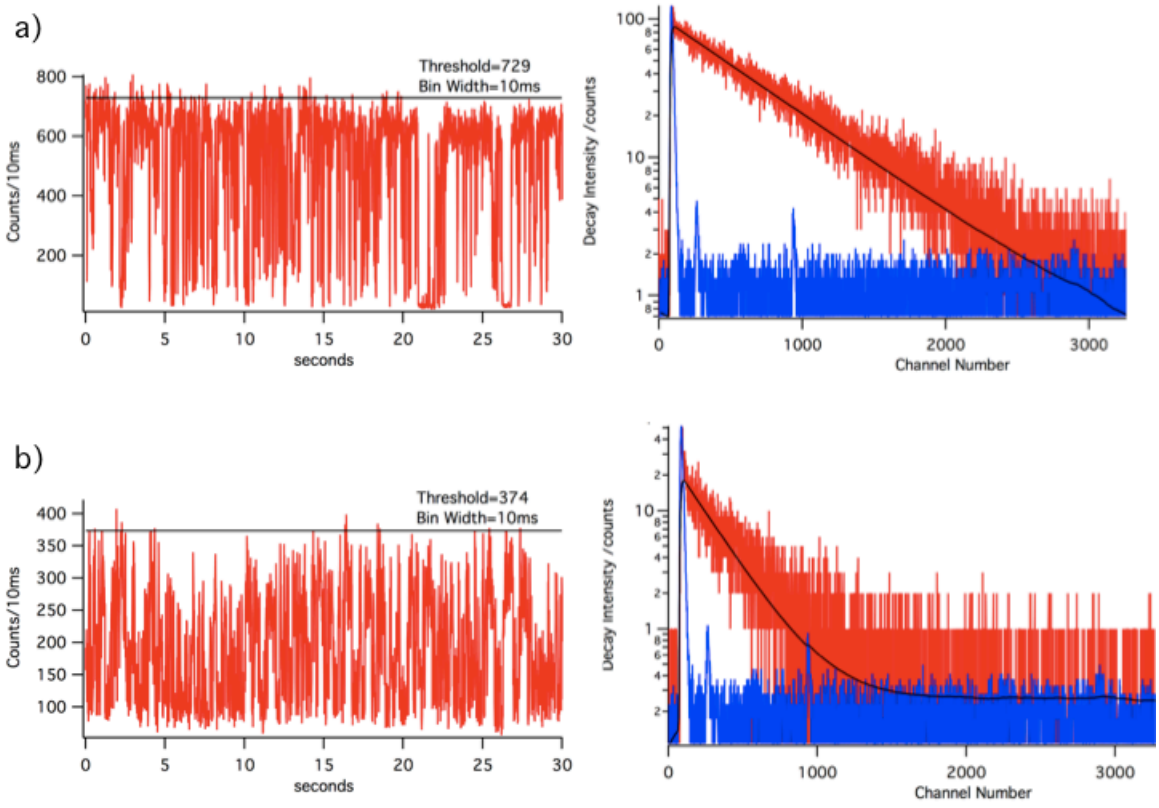

Figure 7.27. Blinking traces of SQD1 (a) and SQD3 (b) from figure 7.26 with threshold of top 10% of photons indicated, and corresponding lifetime decay of those photons.

Following methods utilized in the literature,[133, 134] we generated a lifetime decay using only the top ~10% of binned photons, yielding a single exponential decay, shown to the right of each blinking trace. It is notable that the fast component does not appear in

the top 10% decay. As stated previously, we assign the fast component to multiphoton emission exclusively. Thus, the following analysis corresponds only to single photon emission. Fitting each decay shown in figure 7.27 to a single exponential, we extract lifetimes of 18.1 ns, and 6.7 ns for SQD1 and SQD3, respectively. For the control QDs, we assume that when the QD is at maximum efficiency, $QY = 1$, and the nonradiative rate, k_{NR}, is 0. Thus, we ascribe the extracted rate to the radiative lifetime, τ_R, of single photon emission from the nanocrystal.[134] For control QDs we calculate the average radiative rate:

$$\tau_R = 16.4ns, \text{ so } k_R = 0.061ns^{-1}$$

For QDs in the presence of the metal, we recognize that there must be an additional nonradiative energy transfer pathway to the metal, leading to the observed reduction in quantum yield. To determine the ratio of the quantum yield in the presence of the gold, QY_{Au}, to quantum yield isolated from the gold, QY_0, we take the average count rate (counts/10ms) for 10 QDs, normalized to the percent of time spent in an on state, and obtain:

$$\frac{QY_{Au}}{QY_0} = \frac{185}{299} = 0.62$$

In the presence of the metal, the average lifetime of the top 10% for 5 QDs is 8.87 ns. Considering the additional energy transfer pathway, we can write:

$$QY_{Au} = \frac{k_R'}{k_R' + k_{ET}} \qquad 0.62 = \frac{k_R'}{(1/8.87)}$$

where k_R', and k_{ET} are the radiative rate in the presence of the metal, and the energy transfer rate, respectively. Thus, we calculate an enhancement factor for the radiative rate:

$$k_R' = 0.07 ns^{-1} \qquad \frac{k_R'}{k_R} = \frac{0.07}{0.061} = 1.15$$

We can also calculate an energy transfer rate as follows:

$$k_R' + k_{ET} = (1/8.872)$$

$$k_{ET} = 0.043 ns^{-1};\ \tau_{ET} = 23 ns$$

The calculated energy transfer rate, which is slower than the radiative rate, is plausible since complete quenching is not observed. The small enhancement factor of 1.15 leads to a radiative rate of the single photon emission that is not rapid enough to compete with fast Auger processes in conventional CdSe/ZnS nanocrystals. Therefore, we must consider either 1) a reduction in the Auger rate due to the plasmon field, or 2) a disproportionately large increase in the radiative rate of multiphoton emission (MX) compared to single photon emission (X). We propose that either is possible via a strong coupling of the electronic distribution of the MX wavefunctions with the plasmon modes of the rough gold film. A disproportionately larger increase in radiative rate of the MX

relative to that of the X via resonant coupling of these more complex modes to higher order multipole plasmon modes, which has previously been reported,[138] is more likely. We suggest that this multipole coupling is likely more efficient for multipole electronic distributions as those that occur in multiexciton states.

To demonstrate that our observations are due to a multiexciton effect, we quantified the MX:X ratio as a function of incident laser excitation power for a single quantum dot. Photon correlation of a single quantum dot in the presence of the rough gold film at increasing laser power is shown in figure 7.28a. At 0.6 kW/cm^2, the multiexciton emission is negligible, and increases with laser power to a ratio of 0.72. Each side peak was fit to a two-sided exponential function as demonstrated in figure 7.28a, and the average integrated area under the curves was plotted versus laser power as shown in figure 7.28b. The relationship of this slow component exhibits linear behavior illustrated by the fit to a linear regression with parameters *a* (y-intercept) and *b* (gradient), consistent with single photon emission from a single exciton state.

It is clear in figure 7.28a that at high laser power a fast component grows in rapidly, which is not well-fit by the two-sided exponential, yet accounts for significant peak area. We note the narrowness of these side peaks, which appear strongest at high intensity, and are roughly one pixel wide. The resolution of our photon correlation data is about 900 ps and we will show below that this fast component is about 200 ps or less as determined by the fluorescence lifetime measurement with a resolution of 30 ps. Taking the difference between the fitted peak intensity (black) and the total peak intensity

(various colors) as a measure of the excess area, and plotting the average versus laser power, we obtain the nonlinear curve shown in figure 7.28c. This curve is fit to a polynomial function of the form $f(x) = K_0 + K_1x + K_2x^2$, where K_1 is set to zero so as to eliminate the single exciton contribution which we have already taken into account with the slower photon correlation component. This quadratic behavior is expected for emission from a biexciton state, and is confirmed by comparison to a plot of the intensity of the central peak versus laser power shown in figure 7.28d, which by definition originates from a multiexciton state. At the highest laser powers of 2.4 and 3.6 kW/cm^2, both side and central peaks exhibit extremely narrow features, approaching the resolution limit of the experimental set-up. Thus, comparing the control data to data in the presence of the gold film under the same illumination conditions and therefore $\langle N \rangle$, we have shown that MX emission is strongly enhanced and that a concomitant increase in X emission is *not* also observed.

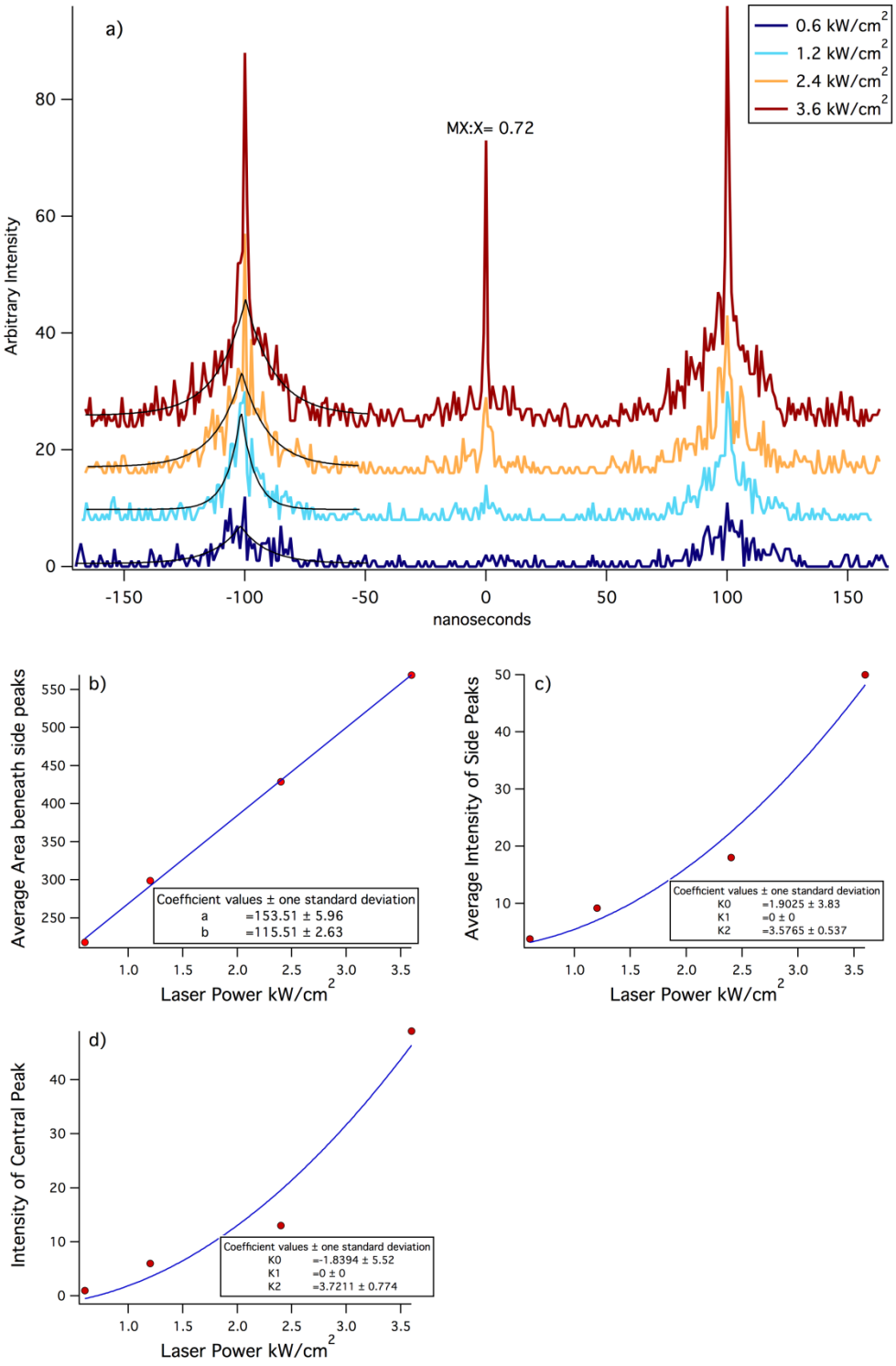

FIGURE 7.28: Photon correlation histogram of a single quantum dot at increasing laser power (a). Plots of average area of slow component of side peaks (b), average intensity of fast component of side peaks (c), and central peak (d) versus laser power.

The extreme narrowing of both side and central peaks in the presence of the gold film is a fascinating observation, which deserves some discussion. Our analysis supports a fast (subnanosecond) radiative rate for the multiexciton state, which we justify with lifetime data in our discussion of figure 7.29. Thus, a photon emitted from a single exciton state will have the normal X radiative rate enhanced by a factor of 1.15 as calculated previously (slow photon). The intial photon(s) emitted from a biexciton state or higher will exhibit a subnanosecond MX radiative rate (fast photons), with the last having the slow X radiative rate. In correlating photons, we must consider the possible combinations of slow and fast photons. The side peaks correspond to the correlation of photons emitted in successive laser pulses. Regarding the side peaks in figure 7.28, the appearance of both a slow component and a fast component, which grows in rapidly at high powers and therefore higher $\langle N \rangle$, is indicative of a high probability of biexciton generation in successive pulses, which is more probable when $\langle N \rangle$ is large. The fast component observed in the side peaks of figure 7.28 must correspond to the correlation of fast photons emitted from a biexciton state or higher order generated in successive pulses. We also observe the slow component in the side peaks, which can result from the correlation of either 1) X from a single exciton state or 2) X from a biexciton state in successive pulses. Regarding the central peak in figure 7.28 at 3.6 kW/cm^2 ($\langle N \rangle = 3.7$), the appearance of solely a fast component is indicative of either 1) emission from high order exciton states (above biexciton), or 2) simultaneous biexciton emission. Emission from triexcitons is not inconceivable since $\langle N \rangle = 3.7$. A narrow central peak must

correspond to the correlation of photons emitted from an MX state within the same laser pulse. We note that in figure 7.25, where $\langle N \rangle = 2.5$, the representative photon correlation data of QDs coupled to the gold film exhibit a non-negligible slow component in the central peak. This can only occur if a fast and slow photon are correlated within the same laser pulse, a condition which can only be met if we consider the generation of a triexciton state, which emits in a cascading fashion.

We show complimentary data from fluorescence decays of a single QD at increasing laser power. The purpose of this data is to confirm that the fast component in the photon correlation data is quantifiable using high temporal resolution lifetime data with 30 ps resolution. The fluorescence decays of a different, but structurally and environmentally similar quantum dot at increasing laser power is shown in figure 7.29. Each decay was fit to a 2-exponenital function of the form $I(t) = A_1 e^{-t/\tau_1} + A_2 e^{-t/\tau_2}$, comprised of a fast ($\tau_1$) and slow ($\tau_2$) component. We show that as the laser power increases (blue curve to red curve), the average lifetime decreases from 11.3 ns to 9 ns, and the contribution of the fast component increases. The inset of figure 7.29 shows a plot of the contribution of the fast component ($A_1\tau_1$) divided by the contribution of the slow component ($A_2\tau_2$). This relationship exhibits clear saturation behavior, observed previously in experiments with conventional CdSe/ZnS QDs,[117] and represents an upper limit to the quantum efficiency of high order excitons. Interestingly, the blinking traces that accompany the lifetime decays in figure 7.29 exhibit an obvious transition from pronounced long on and off states to rapid transitions between on and off as shown in

figure 7.27. This is in contrast to previous reports of blinking suppression in the presence of metal films.[70, 98, 105] These additional blinking traces are presented in Appendix C. Hence, we have shown by two methods that multiphoton emission, which results from multiple exciton occupancy in single QDs is strongly enhanced in the presence of a rough gold film.

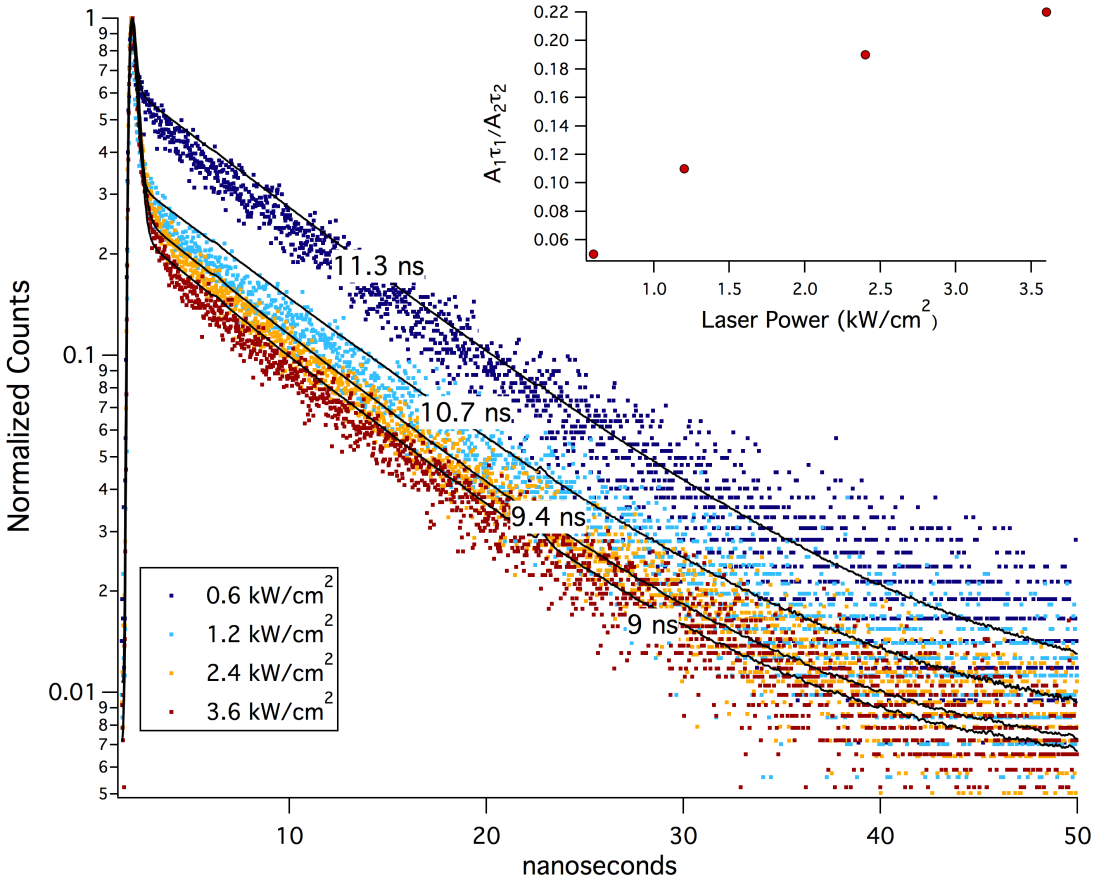

FIGURE 7.29: Lifetime decays of a single quantum dot at increasing laser power. Each decay was fit to a 2-exponential function composed of a fast (τ_1) and slow (τ_2) component. The relative contribution of fast and slow components is shown in the inset as a function of laser power density.

The proposed strong enhancement of the MX radiative rate can be derived mathematically using lifetime decay data. The fast component, τ_1, extracted from fits of the decays varies from 35 ps to 197 ps, accounting for 3 to 15% of the decay. We assign this component to two-photon emission from a biexciton state, τ_{BX}. Then, the slow component, τ_2, corresponds to single photon emission from a single exciton state, τ_X. We can derive the following expression for the quantum yield of two-photon emission from a biexciton state, Y_{BX}, from the yield of the biexciton component using Poission statistics as outlined in Appendix D:

$$Y_{BX} = \frac{A_{BX}\tau_{BX}}{A_{BX}\tau_{BX} + A_X\tau_X} = \frac{\Phi\sigma\tau_{BX}\left(k_R^{BX} + k_R^X\eta\right)}{\Phi\sigma\tau_{BX}\left(k_R^{BX} + k_R^X\eta\right) + \tau_X k_R^X\left(2 - \Phi\sigma\eta\right)},$$

where $\eta = \frac{k_{BX}}{\left(k_X - k_{BX}\right)}$, k_{BX} and k_X are $1/\tau_1$ and $1/\tau_2$, respectively and $\langle N\rangle = \Phi\sigma$.

From this, we can derive an expression for the ratio, *R*, between biexciton and exciton radiative rates:

$$R = \frac{k_R^{BX}}{k_R^X} = \frac{k_{BX}\left(2 - \Phi\sigma\eta\right)}{\Phi\sigma k_X\left(1 - Y\right)} - \eta$$

Since k_{BX} and k_X are $1/\tau_1$ and $1/\tau_2$, respectively and $\langle N\rangle = \Phi\sigma$, we can write:

$$R = \frac{k_R^{BX}}{k_R^X} = \frac{\tau_2\left(2 - \langle N\rangle\eta\right)}{\langle N\rangle\tau_1\left(1 - Y\right)} - \eta$$

Plotting R versus $\langle N\rangle$ for values of $1/\tau_1$, $1/\tau_2$, and Y_{BX} we obtain figure 7.30.

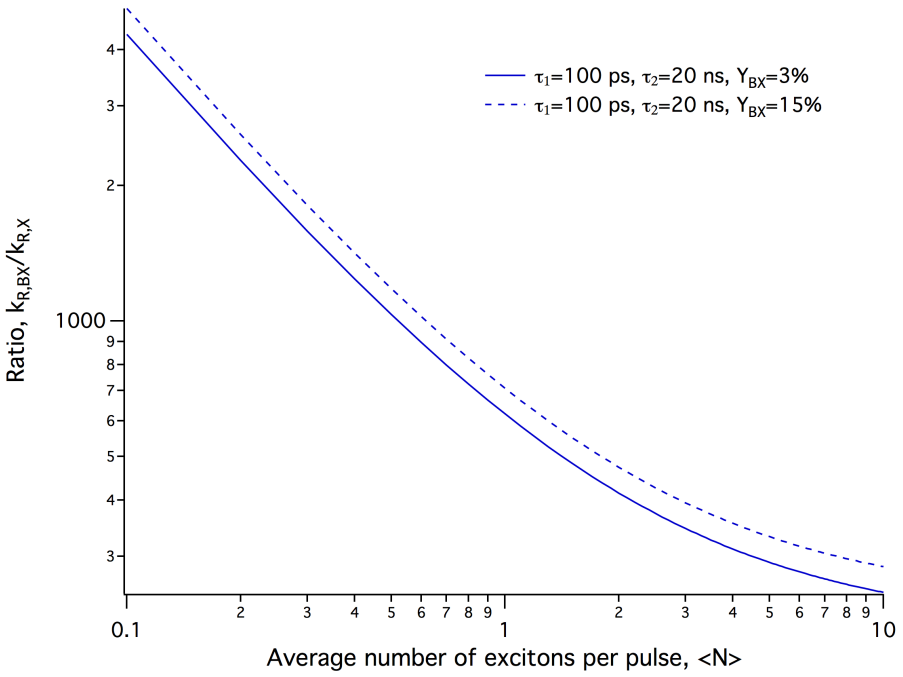

FIGURE 7.30: Calculated ratio of biexciton radiative rate to single exciton radiative rate versus average number of excitons per pulse.

The values of τ_1, τ_2, and Y_{BX} used in the calculation are realistic based on fits to the decays in figure 7.29. Based on this analysis, we can estimate an enhancement factor of the radiative rate of the biexciton in the high power limit as ~350. This two orders of

magnitude larger than the enhancement factor of the single exciton state, and supports our assertion of strong coupling of multiexciton states with the multipole plasmon modes of the rough gold film, leading to a disproportionately larger increase in radiative rate of the MX relative to that of the X. This enhancement factor is significantly larger than expected, but strongly supported by the experimental evidence that has been presented. As we have outlined, the only other possible explanation for the observed increase in MX emission and decrease in X emission is a decrease in the Auger recombination rate, of which there is no evidence in the literature for conventional CdSe/ZnS nanocrystals.

We have demonstrated the enhancement of multiphoton emission in conventional CdSe/ZnS quantum dots coupled to a rough gold film and a simultaneous decrease in the quantum yield of the single exciton state which results from non-radiative energy transfer to the metal. We have distinguished unequivocally by rigorous analysis the temporal emission behavior of single excitons versus multiexcitons (most likely, biexcitons). The result is a marked increase in the multiphoton emission probability of a single QD via plasmonic coupling to the metal. We suggest a stronger radiative enhancement of the MX mode compared to the X mode via coupling to higher order multipole modes of the plasmon.

7.4 Effect of an Applied Electric Field on Nanocrystal Multiexciton Dynamics

Using the sample architecture described in section 7.3, we explored the effect of an electric field on the mulitexciton emission of single QDs. A dc electric field is applied to the sample by attaching electrical leads to both electrodes using conductive carbon tape. A schematic is shown in figure 7.31. Using the same method to determine the MX:X ratio as described in section 7.3, we determine the change in that ratio in the presence of an applied electric field. The change is calculated by subtracting the MX:X ratio in the presence of the field from the ratio in the absence of field for each individual QD. A summary of the results is presented in the histogram in figure 7.32. Based on our convention, a negative change in MX:X denotes an increase in the MX:X ratio, and vice versa. Data from 76 quantum dots reveals a distribution centered on zero, indicating that most QDs exhibit little to no change in the ratio as an electric field of ~100 kV/cm is applied. The electric field is calculated by measuring the potential across the electrodes, then dividing by the PMMA thickness (~150 nm). The resulting electric field strength is then divided by the dielectric constant of PMMA (3.7). The distribution in figure 7.32 is roughly symmetric about zero, indicating an equal probability of increasing or decreasing the MX:X ratio in the presence of the applied electric field. Examples of each case are presented in the following sections.

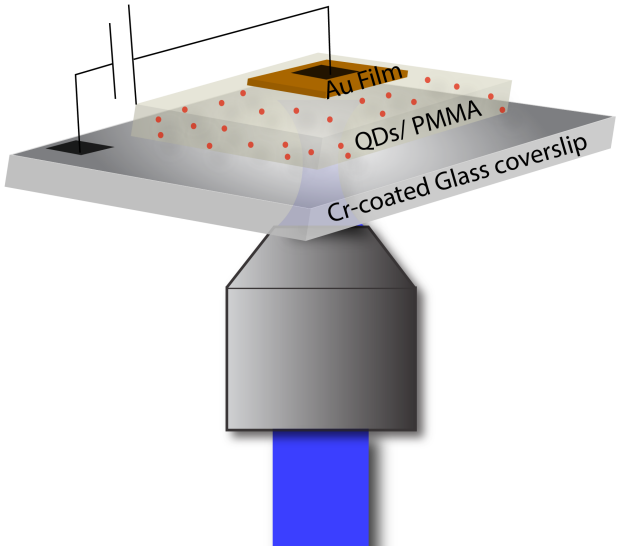

FIGURE 7.31: Schematic of architecture for electric field dependent study of multiexciton dynamics.

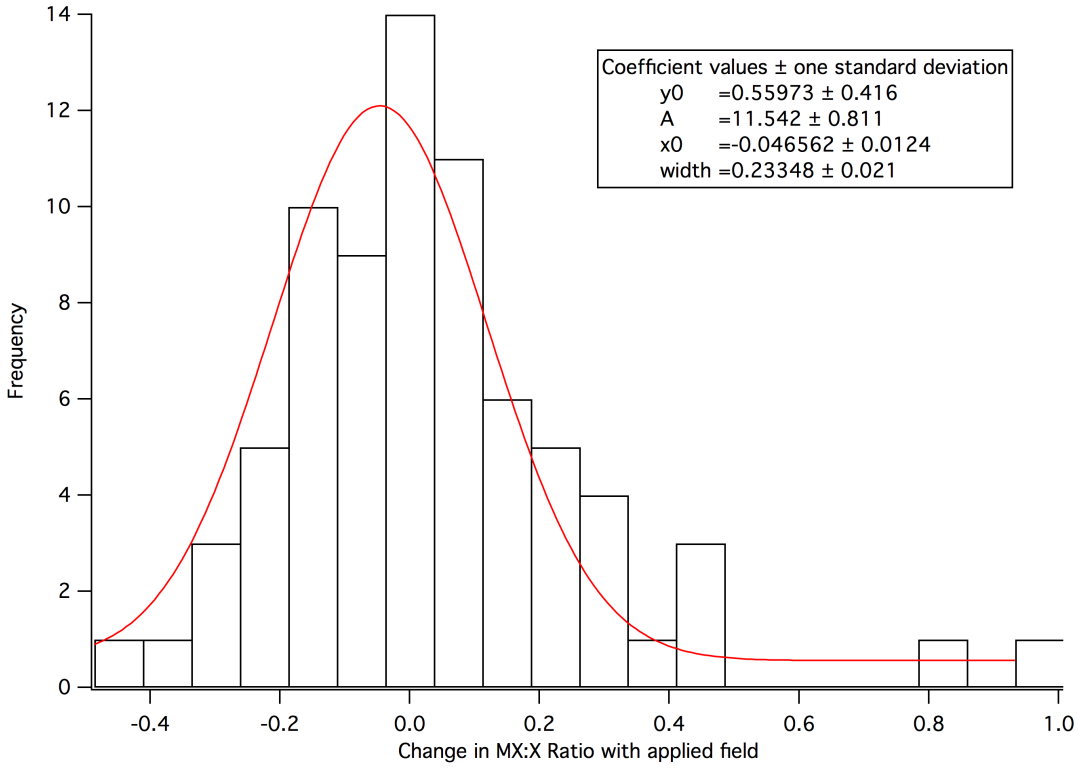

FIGURE 7.32: Histogram of the change in MX:X ratio under the influence of an applied electric field.

We collect successive photon correlation traces on single quantum dots to investigate the normal dynamics of the multiexciton in the absence of an applied electric field. Representative traces collected at 0.6 kW/cm^2 (top) and 2.4 kW/cm^2 (bottom) are shown in figure 7.33. These laser power densities correspond to an average number of excitons per laser pulse as follows: $\langle N \rangle = 0.6$ and $\langle N \rangle = 1.2$, respectively. (See Appendix A for calculation) In each graph, Trace1 and Trace2 are collected on a single quantum dot successively for 30 seconds each. At 0.6 kW/cm^2, both traces show little dynamic fluctuations from trace to trace. At 2.4 kW/cm^2, we demonstrate a case in which there is essentially no change in the MX:X ratio, and a separate case in which there is a ~30% change in the MX:X ratio. Dynamic behavior in the ratio can be caused by changes in either the single photon emission (side peaks) or multiphoton emission (central peak). We explore the effect of the electric field on single photon and multiphoton emission. We distinguish between normal dynamic behavior and an electric field effect by demonstrating that the electric field effect is switchable. In what follows, we present examples of various cases of no electric field effect, and marked changes in the ratio with an applied electric field.

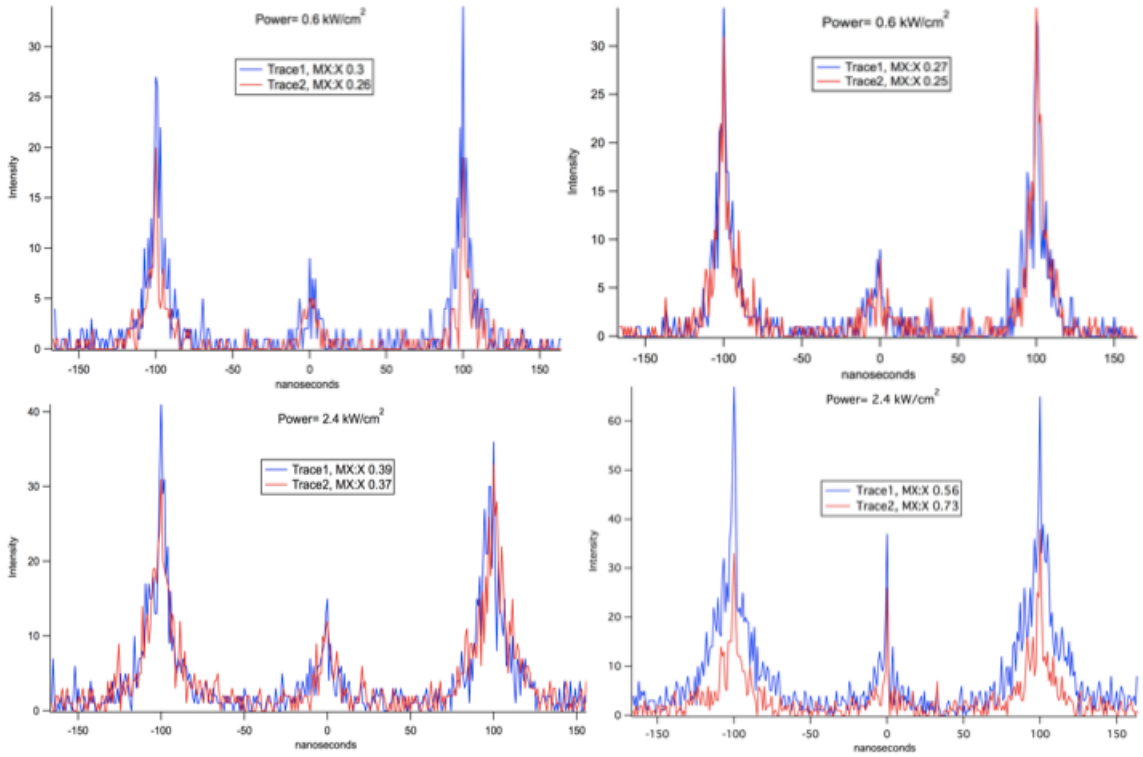

FIGURE 7.33: Representative photon correlations of typical multiexciton dynamics. Top samples were excited at 0.6 kW/cm^2, and the bottom excited at 2.4 kW/cm^2.

Figure 7.34 demonstrates a case in which the electric field does not affect the MX:X ratio. In this particular case, the first trace was collected with the electric field switched on, and then the field was turned off. Figure 7.35 shows a case in which the MX:X ratio increases by more than 100% when the electric field is switched off. Upon further inspection, it is clear that the ratio is influenced mainly by an increase in the single photon emission whereas the multiple photon emission is relatively unchanged.

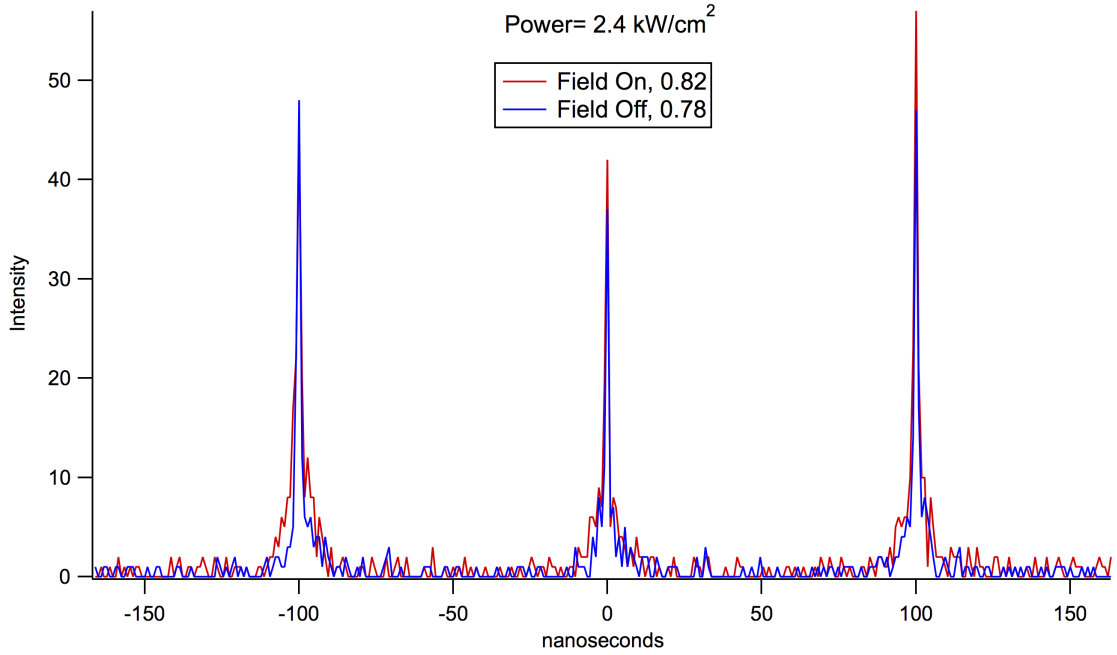

FIGURE 7.34: A representative photon correlation which shows no change in MX:X ratio under the influence of an applied electric field.

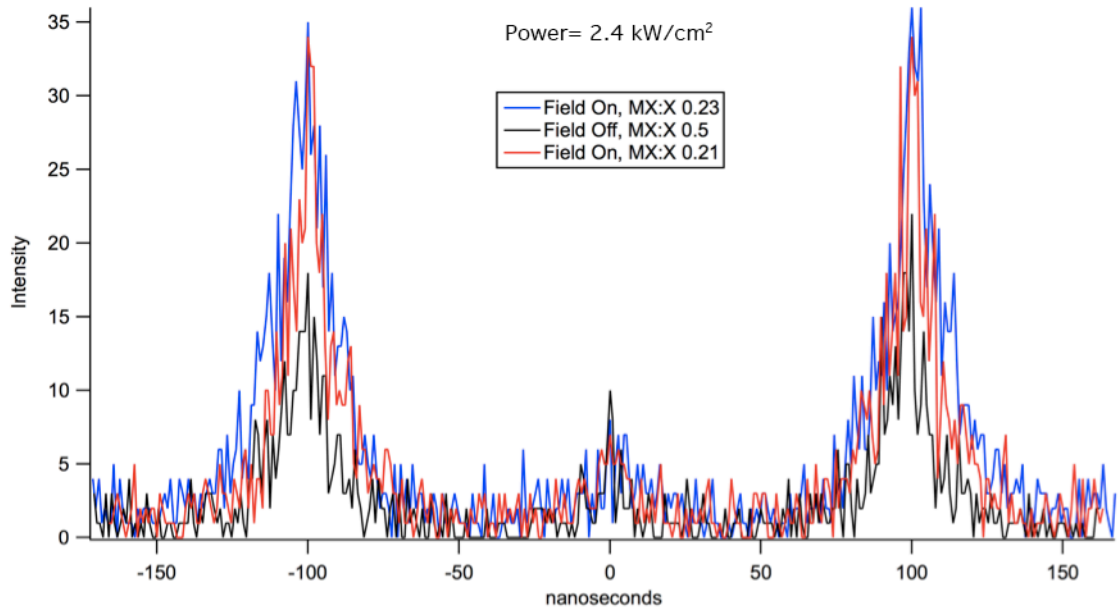

FIGURE 7.35: A representative photon correlation which shows an increase in MX:X ratio when the applied electric field is switched off.

A third case in which the ratio decreases by 13% is shown in figure 7.36 when the field is switched off. We can conclude in this case that the single photon emission is enhanced in the presence of the electric field. Figure 7.37 shows a greater than 100% increase in the MX:X ratio when the electric field is switched off. It is clear that while the multiple photon emission is relatively unchanged when the electric field is switched off, the single exciton emission decreases drastically, leading to the observed increase in MX:X.

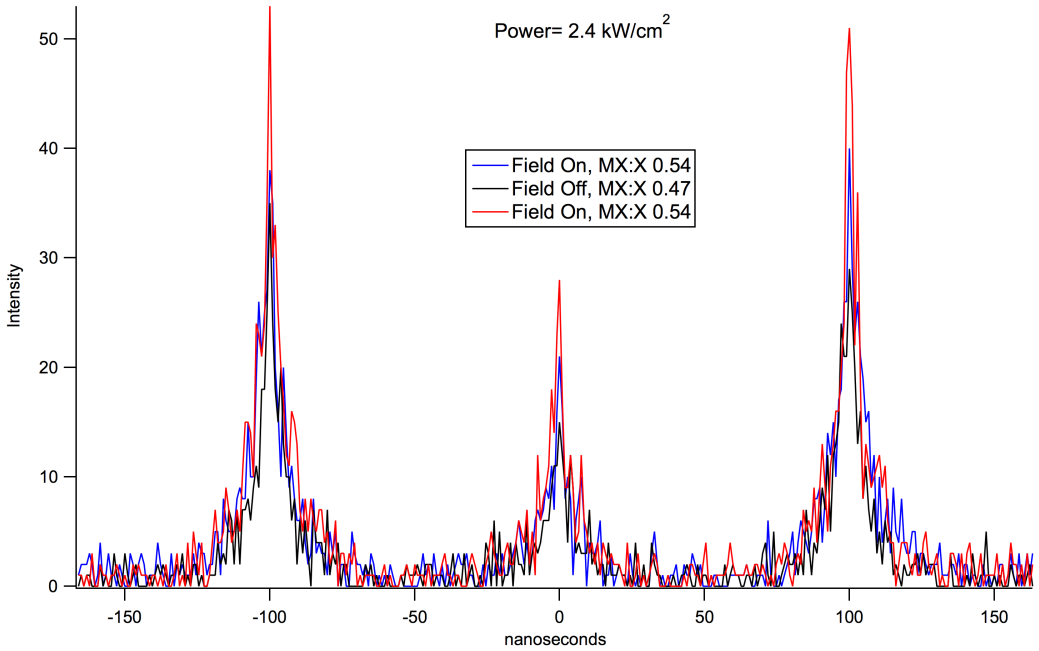

FIGURE 7.36: A representative photon correlation which shows a decrease in MX:X ratio by 13% when the applied electric field is switched off.

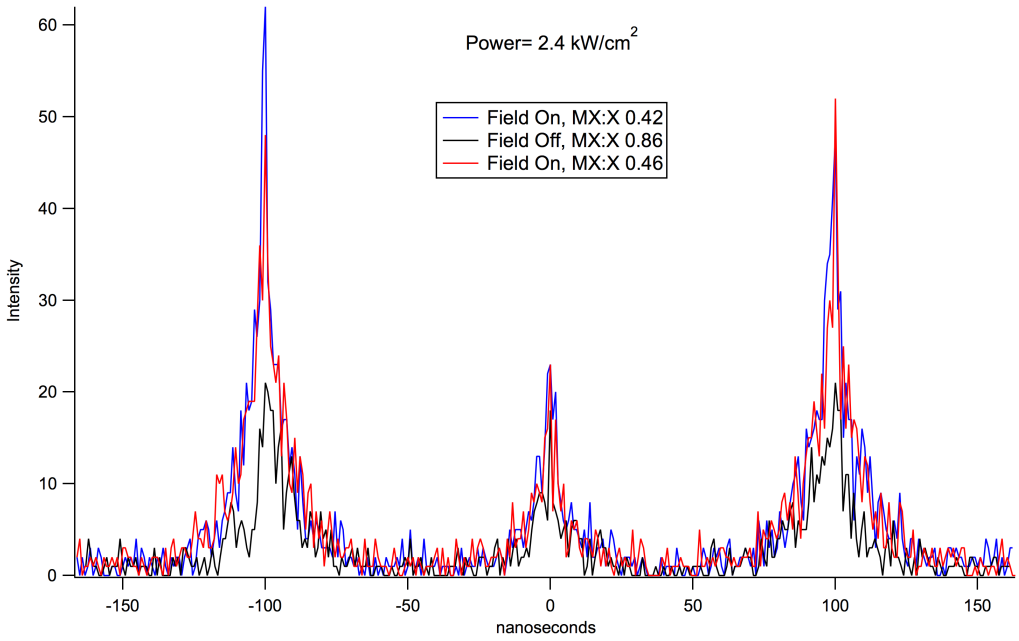

FIGURE 7.37: A representative photon correlation which shows a greater than 100% increase in the MX:X ratio when the electric field is switched off.

In figure 7.38, there is no electric field present for the first trace, and then it is switched on for the second trace. A 53% increase in the MX:X ratio occurs when the field is switched on. Here, we observe that the single photon emission is quenched in the presence of the applied field, while multiple photon emission is relatively unchanged. To summarize, we observe both an increase and decease in the MX:X ratio with applied electric field, which result mainly from changes the single photon emission. This variation in the effect of an electric field shown in these 5 cases is exemplified in the histogram shown in figure 7.32. A suitable model must account for this range of effects.

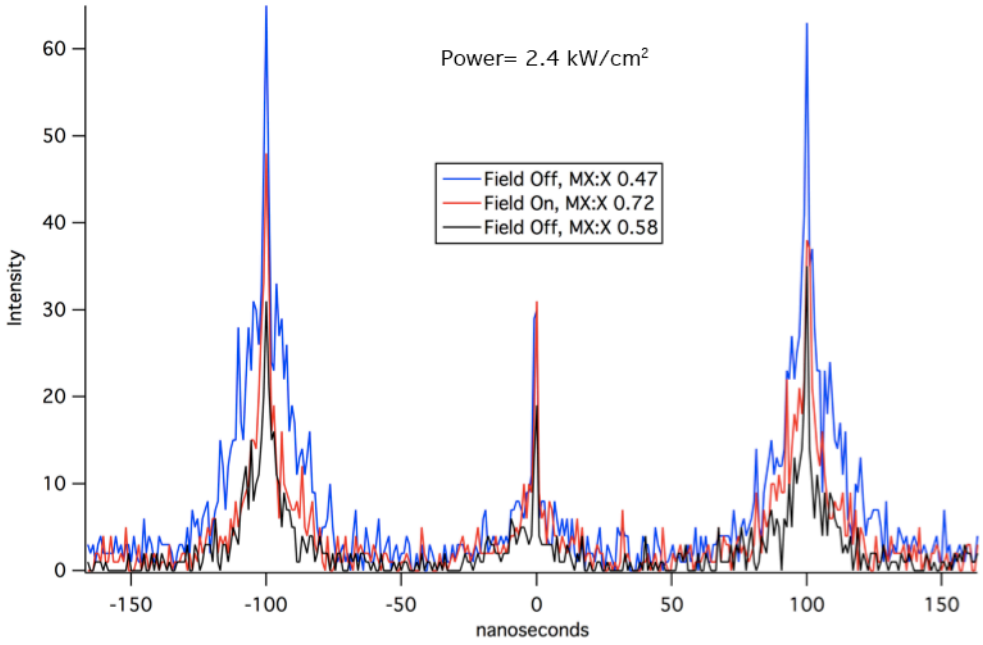

FIGURE 7.38: A representative photon correlation which shows a 53% increase in the MX:X ratio when the field is switched on.

When we consider the electric field effects on photon emission in these experiments, it is clear that the field can lead to either a decrease or increase in single photon emission, and has virtually no effect on the multiphoton emission. This is a linear effect and can be explained by changes in either the non-radiative or radiative rates. We have shown in section 7.2 that the effect of a modest applied electric field of ~50 kV/cm leads to small fluctuations in the intensity of single nanocrystal blinking and changes in PL decay behavior. We attributed this to redistribution of surfaces charges, associated with the polarizability of the excited state. This lead to an increased trapping rate due to modulation of nonradiative pathways associated with surface charge distributions. In

direct contrast, the effects observed in this experiment are due to the effect of the applied electric field on the single and multiple exciton states rather than surface charges.

For a single exciton in the absence of an applied electric field, the electron and hole may align with the permanent dipole, **μ**, of the nanocrystal, as shown in figure 7.39.[82-84] This permanent dipole can stem from an intrinsically polar wurtzite crystal structure[83] or, more likely, oppositely charged crystal facets since permanent dipoles are also observed in non-polar zinc-blende nanocrystals.[84] These permanent dipoles correspond to internal electric fields in the nanocrystal on the order of 100 kV/cm.[7] In our experiment, the orientation of this permanent dipole is randomly distributed from QD to QD that is spin-cast on the sample surface. When a single exciton, which is aligned with the internal electric field, couples to the rough gold film as shown in figure 7.39, we additionally expect that coupling to be random. This is due to the fact that plasmon wavevectors, indicated by the small black arrows in the figure, are randomly oriented at the metal-dielectric (PMMA) interface. The rough nature of this interface is directly responsible for strong coupling of the excited state to a broad distribution of plasmon wavevectors, and would not occur on a smooth gold surface. We now explore how applying an electric field affects coupling with the surface plasmons and how it leads to the observed effects in photon correlation data presented above.

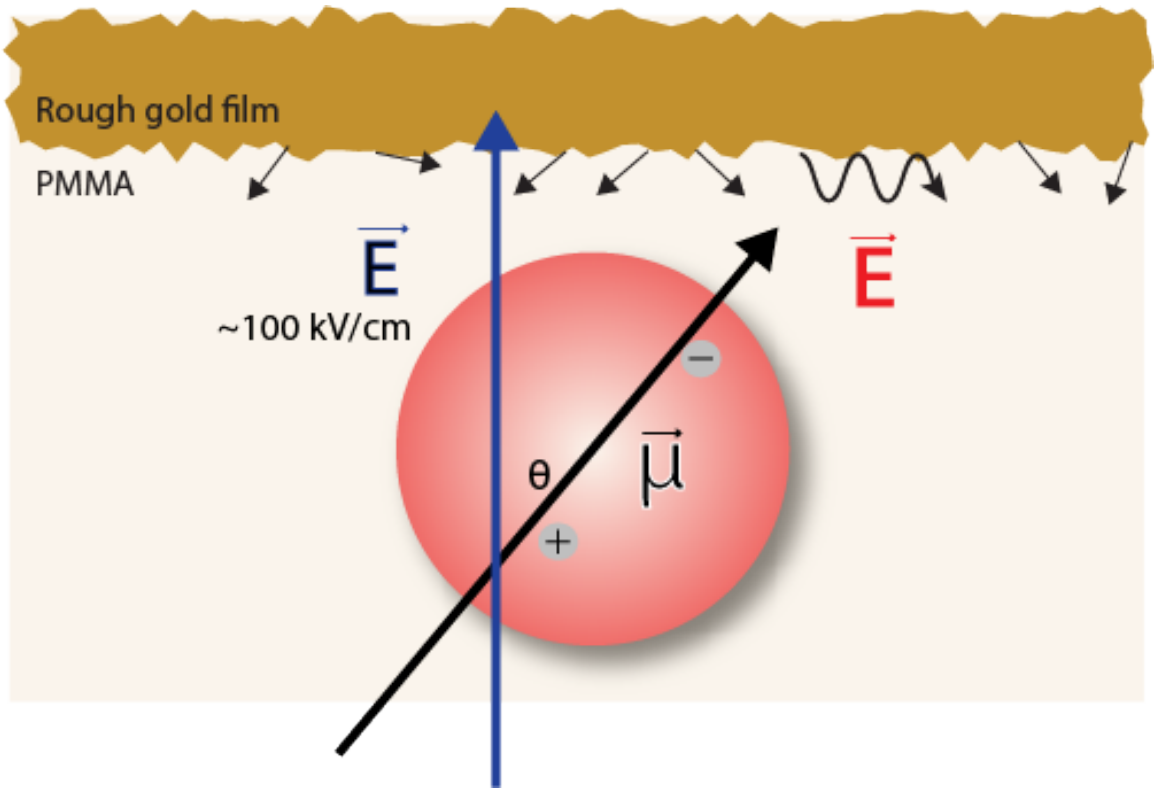

FIGURE 7.39: Schematic of single exciton coupling to plasmon modes of a rough gold film. The nanocrystal internal electric field,μ, is represented by the large black arrow. The applied electric field is represented by the vertical blue arrow, and the plasmon field vectors are represented by small black arrows.

As stated previously, the electric fields applied in this experiment are on the order of nanocrystal internal electric fields (~100 kV/cm). Since the electric field is applied in the same direction each time, and the exciton is aligned with the permanent dipole, we expect a distribution of interaction of the electric field with the exciton transition dipole. We represent the magnitude of this interaction by the dot product of the applied electric field vector, **E**, and the transition dipole moment **μ**: $\boldsymbol{E \cdot \mu}$. Note that since the transition dipole and the permanent dipole are in the same direction, we use the same symbol. By

applying an external electric field on the order of the permanent dipole, we re-orient the exciton, thereby changing the coupling of the excited state to the surface plasmon wavevector distribution. Depending on the degree of the re-orientation, we may expect to observe either PL enhancement or quenching of the excited state. It has previously been shown that coupling to a random gold surface can lead to PL enhancement or quenching depending upon the plasmon local electric field vector.[100] If the exciton is re-oriented such that non-radiative energy transfer via the surface plasmon is favored, then we expect to observe PL quenching. The applied electric field may also alter the exciton-plasmon coupling such that an electric field enhancement, and therefore PL enhancement occurs. This justification is clearly supported by the histogram data, which demonstrates an equal probability of quenching or enhancement.

As discussed extensively in section 7.3, emission of multiphotons is enhanced in the presence of the rough gold film. We attributed this to a large enhancement of the radiative rate of a multiexciton state compared to the radiative rate of a single exciton state (~350-fold). This is facilitated by a strong coupling of multiexcitons to multipole plasmon modes.[138] We observe in these electric field experiments that the multiphoton emission is relatively unaffected by the applied electric field. This observation supports the conclusion of coupling to multipole plasmon modes, which would be minimally affected by a dipolar electric field.

CHAPTER 8: CONCLUSIONS

We have explored the synthesis, characterization, biological applications, and photophysics of single nanocrystal systems. For biological applications of single nanocrystals to be successfully implemented, high-quality bright and robust fluorophores are necessary. This is especially true in the case of tracking single biomolecules within intracellular environments. An in-depth understanding of the functionality of most subcellular components remains vastly unknown. If we are able to observe the function of single biomolecules in their native environments using materials such as quantum dots as nanoscale reporters, we will change the future of how we detect and treat diseases. As referenced in the introduction, we may realize the ability to detect a single copy of a protein or gene that is indicative of disease. Several challenges still remain for nanocrystals, however. These include proper surface functionalization of nanocrystals for specific targeting of subcellular components, the potential cytotoxicity of cadmium-based materials, and the unstable nature of single quantum dot emission. The instability in quantum dot emission is reflected in the blinking and spectral diffusion that are observed in the emission behavior of quantum dots. These observed effects are due to the sensitivity of quantum dots to their local environment, and can be exploited in biological applications for use as nanoscale reporters of their local environment. We can

only fully understand and appreciate these materials if we have a fundamental understanding of their physical properties, specifically their interaction with light. We know that if we excite these materials with enough energy, they will emit light that can be utilized to track single biomolecules, or as active materials in light-emitting diode devices, for example. What is lacking is a fundamental understanding and control of these emission properties. The results of the experiments outlined in Chapter 7 demonstrate how we are able to exercise control over single quantum dot emission properties with applied electric fields and strong localized plasmon electromagnetic fields. This sort of control of single quantum dot emission properties also implies control over carrier dynamics, which has broad implications for many applications. Specifically, if we are able to control carrier dynamics, we can realize electro-optic devices and solar cell devices. To summarize our experiments, we have shown:

1) The influence of moderate applied electric fields on single quantum dot fluorescence intensity and PL decays, and quantitative modeling of a set of SQD data.
2) Controlled multiexciton emission through coupling with a plasmon field
3) Controlled MX:X emission ratio with applied electric field

The novel contributions within the field of single quantum dot photophysics are stated above. By implementing a suite of single molecule spectroscopic techniques, we were able to elucidate the complex photophysics of single nanocrystal systems. Techniques of confocal microscopy, time resolved fluorescence, time-correlated single photon counting, single quantum dot spectroscopy, and photon correlation spectroscopy

have been utilized extensively to characterize the nature of carrier dynamics in nanocrystals. By applying a moderate electric field to nanocrystals embedded in a polymer matrix in section 7.2, we were able to connect changes in fluorescence intensity and statistics to an electric field induced re-distribution of surface charges, and therefore modification of non-radiative pathways. The re-distribution of surface charge is supported by the fact that the electric field effect is non-linear, indicating an interaction with a polarizable excited state. The multiexponential behavior of the lifetime decays in the presence of the electric field are indicative of a strong influence of surface trap states on radiative emission of the exciton and support a dynamically varying nonradiative trapping rate. This is further confirmed by kinetic modeling, which indicates a more energetically favorable trapping process in the presence of the applied electric field. Although the nature of the trap state remains unclear, we can associate charge trapping with a change in the intensity distribution of on states, which is evidence for emission from charged exciton states. This further suggests that a single trapped charge cannot be the cause of an off state. The role of surface trapping in nanocrystal excited state dynamics is complex, but our experiments show that the distribution of surface charges plays a significant role. These findings have important implications on our current understanding of both the emitting states and dark state of single quantum dots. Demonstrating the influence of applied electric fields on the emission behavior of single exciton states is important for a complete understanding of carrier dynamics in nanocrystals. Completing the picture of electron transfer theory for nanocrystals will aid

in this process and require further experimentation for extraction of other paramaters such as reorganization energy. Adding temperature control to our single molecule system will enable temperature-dependent studies, and high-resolution single molecule spectroscopy. This will lead to better temporal resolution of single nanocrystal spectra and the observation of electric field effects on energetic behavior. Ultimately, the link between spectral diffusion, blinking, and PL dynamics can be explored by simultaneous collection of data.

We have also explored the emission behavior of multiexciton states generated in single nanocrystal systems. In section 7.3, we presented a simple architecture for achieving strong enhancement of multiphoton emission from single nanocrystals mediated by coupling of the excited state of the nanocrystals to a rough gold film. Rigorous analysis of blinking, lifetime decay, and photon correlation data lead to strong evidence of radiative rate enhancement of a biexciton state where the same enhancement is not observed for the single exciton state. The coupling of the biexciton state to multipole plasmon modes in the metal is much stronger than that of a single exciton state, leading to the observed enhancement factor in the biexciton radiative rate of ~350, confirmed by laser power dependent lifetime decay data. This enhancement factor is much larger than has previously been demonstrated, and has important implications for lasing and light emitting diode applications. In addition, we have an opportunity to observe excited state dynamics of multiexciton states that are rarely observed. Using this architecture, we have observed the effect of an applied electric field on the multiexciton

state. One can also conduct further experiments under conditions other than applied electric fields to observe their effect on multiexciton states.

In section 7.4, we have shown that we can modulate the ratio of multiple photon (MX) to single photon (X) emission in single nanocrystals by applying an electric field. An electric field of ~100 kV/cm is on the order of the internal electric field of the nanocrystal, and can now affect the exciton directly in a linear interaction. We observe an equal probability of enhancement and quenching when an electric field is applied, which we can attribute to a modification of single exciton coupling with the rough gold film. The change in MX:X ratio is mainly controlled by the X emission, with the electric field having little effect on the multiphoton emission. This is further evidence of coupling of a multiexciton state to higher order plasmon modes. Electric field control also represents a method to control X emission, but not MX emission, which could be utilized for tailoring emission in electro-optic devices. Electric field dependent experiments on the lifetime decays were not conducted, but it would be particularly enlightening to see if the same effect is observed. This may be further confirmation of the fast and slow component assignments in lifetime decays.

This dissertation research has broad implications relating to applications of biological imaging, solar energy, and devices such as electro-optic modulators, light-emitting diodes, and lasers. Electric fields persist and are important in all of those applications. Relating back to biological systems, the sensitivity of quantum dot emission to local electric fields can be used as a modality of reporting intracellular

information on the nanoscale. If we are to use nanocrystals to advance technological applications such as this, knowing how these materials respond to local electric fields is of paramount importance. The continued pursuit of a fundamental understanding and control of charge carrier dynamics will ultimately advance the use of nanomaterials in technology.

REFERENCES

1. Kamat, P. V., Quantum Dot Solar Cells. Semiconductor Nanocrystals as Light Harvesters. Journal of Physical Chemistry C 2008, 112, 18737-18753.

2. Smith, A. M.; Duan, H.; Mohs, A. M.; Nie, S., Bioconjugated quantum dots for in vivo molecular and cellular imaging. Advanced Drug Delivery Reviews 2008, 60, 1226-1240.

3. Pinaud, F.; Michalet, X.; Bentolila, L. A.; Tsay, J. M.; Doose, S.; Li, J. J.; Iyer, G.; Weiss, S., Advances in fluorescence imaging with quantum dot bio-probes. Biomaterials 2006, 27, 1679-1687.

4. Blanton, S. A.; Hines, M. A.; GuyotSionnest, P., Photoluminescence wandering in single CdSe nanocrystals. Applied Physics Letters 1996, 69, 3905-3907.

5. Empedocles, S. A.; Norris, D. J.; Bawendi, M. G., Photoluminescence spectroscopy of single CdSe nanocrystallite quantum dots. Physical Review Letters 1996, 77, 3873-3876.

6. Nirmal, M.; Dabbousi, B. O.; Bawendi, M. G.; Macklin, J. J.; Trautman, J. K.; Harris, T. D.; Brus, L. E., Fluorescence intermittency in single cadmium selenide nanocrystals. Nature 1996, 383, 802-804.

7. Empedocles, S. A.; Bawendi, M. G., Quantum-confined stark effect in single CdSe nanocrystallite quantum dots. Science 1997, 278, 2114-2117.

8. Neuhauser, R. G.; Shimizu, K. T.; Woo, W. K.; Empedocles, S. A.; Bawendi, M. G., Correlation between fluorescence intermittency and spectral diffusion in single semiconductor quantum dots. Physical Review Letters 2000, 85, 3301-3304.

9. Gomez, D. E.; van Embden, J.; Mulvaney, P.; Fernee, M. J.; Rubinsztein-Dunlop, H., Exciton-Trion Transitions in Single CdSe-CdS Core-Shell Nanocrystals. Acs Nano 2009, 3, 2281-2287.

10. Zhao, J.; Nair, G.; Fisher, B. R.; Bawendi, M. G., Challenge to the Charging Model of Semiconductor-Nanocrystal Fluorescence Intermittency from Off-State Quantum Yields and Multiexciton Blinking. Physical Review Letters 2010, 104.

11. Kalyanasundaram, K.; Borgarello, E.; Duonghong, D.; Gratzel, M., Cleavage of Water by Visible-light Irradiation of Colloidal CdS Solutions- Inhibition of Photocorrosion by RuO2. Angewandte Chemie-International Edition in English 1981, 20, 987-988.

12. Henglein, A., Photo-Degradation and Fluorescence of Colloidal Cadmium Sulfide in Aqueous Solution. Berichte Der Bunsen-Gesellschaft-Physical Chemistry Chemical Physics 1982, 86, 301-305.

13. Matijevic, E.; Wilhelmy, D. M., Preparation and Properties of Monodispersed Spherical Colloidal Particles of Cadmium-Sulfide. Journal of Colloid and Interface Science 1982, 86, 476-484.

14. Murray, C. B.; Norris, D. J.; Bawendi, M. G., Synthesis and Characterization of Nearly Monodisperse CdE (E= S, Se, Te) Semiconductor Nanocrystallites. Journal of the American Chemical Society 1993, 115, 8706-8715.

15. Peng, Z. A.; Peng, X., Formation of High-Quality CdTe, CdSe, and CdS Nanocrystals Using CdO as a Precursor. J. Am. Chem. Soc. 2001, 123, 183-184.

16. Qu, L.; Peng, A.; Peng, X., Alternative Routes toward High Quality CdSe Nanocrystals. Nano Letters 2001, 1, 333-337.

17. Talapin, D. V.; Rogach, A. L.; Kornowski, A.; Haase, M.; Weller, H., Highly Luminescent Monodisperse CdSe and CdSe/ZnS Nanocrystals Synthesized in a Hexadecylamine-Trioctylphosphine Oxide-Trioctylphosphine Mixture. Nano Letters 2001, 1, 207-211.

18. Mekis, I.; Talapin, D. V.; Kornowski, A.; Haase, M.; Weller, H., One-Pot Synthesis of Highly Luminescent CdSe/CdS Core-Shell Nanocrystals via Organometallic and "Greener" Chemical Approaches. Journal of Physical Chemistry B 2003, 107, 7454-7462.

19. Hines, M. A.; Guyot-Sionnest, P., Synthesis and Characterization of Strongly Luminescent ZnS-capped CdSe Nanocrystals. Journal of Physical Chemistry 1996, 100, 468-471.

20. Barnard, T. Synthesis of Quantum Dots With Tunable Fluorescence Lifetimes. University of North Carolina at Charlotte, Charlotte, 2004.

21. Mikulec, F. V. Semiconductor Nanocrystal Colloids: Manganese Doped Cadmium Selenide, (Core)Shell Composites for Biological Labeling, and Highly Fluorescent Cadmium Telluride. Massachusetts Institute of Technology, Cambridge, 1999.

22. Yu, W. W.; Qu, L.; Guo, W.; Peng, X., Experimental Determination of the Extinction Coefficient of CdTe, CdSe, and CdS Nanocrystals. Chemistry of Materials 2003, 15, 2854-2860.

23. Bruchez, M.; Moronne, M.; Gin, P.; Weiss, S.; Alivisatos, A. P., Semiconductor nanocrystals as fluorescent biological labels. Science 1998, 281, 2013-2016.

24. Chan, W. C. W.; Nie, S. M., Quantum dot bioconjugates for ultrasensitive nonisotopic detection. Science 1998, 281, 2016-2018.

25. Chan, W.; Maxwell, D.; Gao, X.; Bailey, R.; Han, M.; Nie, S., Luminescent quantum dots for multiplexed biological detection and imaging. Current Opinion in Biotechnology 2002, 13, 40-46.

26. Jaiswal, J. K.; Goldman, E. R.; Mattoussi, H.; Simon, S. M., Use of quantum dots for live cell imaging. Nature Methods 2004, 1, 73-78.

27. Jamieson, T.; Bakhshi, R.; Petrova, D.; Pocock, R.; Imani, M.; Seifalian, A. M., Biological applications of quantum dots. Biomaterials 2007, 28, 4717-4732.

28. Pons, T.; Mattoussi, H., Investigating Biological Processes at the Single Molecule Level Using Luminescent Quantum Dots. Annals of Biomedical Engineering 2009, 37, 1934-1959.

29. Chan, W. C. W.; Nie, S., Quantum Dot Bioconjugates for Ultrasensitive Nonisotopic Detection. Science 1998, 281, 2016-2018.

30. Mattoussi, H.; Mauro, J. M.; Goldman, E. R.; Anderson, G. P.; Sundar, V. C.; Mikulec, F. V.; Bawendi, M. G., Self-Assembly of CdSe-ZnS Quantum Dot Bioconjugates Using and Engineered Recombinant Protein. Journal of the American Chemical Society 2000, 122, 12142-21250.

31. Tran, P. T.; Goldman, E. R.; Anderson, G. P.; Mauro, J. M.; Mattoussi, H., Use of Luminescent CdSe-ZnS Nanocrystal Bioconjugates in Quantum-Dot Based Nanosensors. Phys. Stat. Sol. B 2002, 229, 427-432.

32. Dahan, M.; Levi, S.; Luccardini, C.; Rostaing, P.; Riveau, B.; Triller, A., Diffusion Dynamics of Glycine Receptors Revealed by Single-Quantum Dot Tracking. Science 2003, 302, 442-445.

33. Lidke, D. S.; Nagy, P.; Heintzmann, R.; Arndt-Jovin, D. J.; Post, J. N.; Grecco, H. E.; Jares-Erijman, E. A.; Jovin, T. M., Quantum dot ligands provide new insights into erbB/HER receptor-mediated signal transduction. Nature Biotechnology 2004, 22, 198-203.

34. Howarth, M.; Takao, K.; Hayashi, Y.; Ting, A. Y., Targeting quantum dots to surface proteins in living cells with biotin ligase. Proceedings of the National Academy of Sciences of the United States of America 2005, 102, 7583-7588.

35. Bonasio, R.; Carman, C. V.; Kim, E.; Sage, P. T.; Love, K. R.; Mempel, T. R.; Springer, T. A.; von Andrian, U. H., Specific and covalent labeling of a membrane protein with organic fluorochromes and quantum dots. Proceedings of the National Academy of Sciences of the United States of America 2007, 104, 14753-14758.

36. Derfus, A. M.; Chan, W. C. W.; Bhatia, S. N., Intracellular Delivery of Quantum Dots for Live Cell Labeling and Organelle Tracking. Advanced Materials 2004, 16, 961-966.

37. Medintz, I. L.; Clapp, A. R.; Mattoussi, H.; Goldman, E. R.; Fisher, B.; Mauro, J. M., Self-assembled nanoscale biosensors based on quantum dot FRET donors. Nature Materials 2003, 2, 630-638.

38. Pons, T.; Medintz, I. L.; Wang, X.; English, D. S.; Mattoussi, H., Solution-phase single quantum dot fluorescence resonance energy transfer. Journal of the American Chemical Society 2006, 128, 15324-15331.

39. Sugawa, M.; Nishikawa, S.; Iwane, A. H.; Biju, V.; Yanagida, T., Single-Molecule FRET Imaging for Enzymatic Reactions at High Ligand Concentrations. Small 2010, 6, 346-350.

40. Clapp, A. R.; Medintz, I. L.; Mattoussi, H., Forster Resonance Energy Transfer Investigations Using Quantum-Dot Fluorophores. ChemPhysChem 2006, 7, 47-57.

41. Warshaw, D. M.; Kennedy, G. G.; Work, S. S.; Krementsova, E. B.; Beck, S.; Trybus, K. M., Differential Labeling of myosin V heads with quantum dots allows direct visualization of hand-over-hand processivity. Biophysical Journal 2005, 88, L30-L32.

42. Courty, S.; Luccardini, C.; Bellaiche, Y.; Cappello, G.; Dahan, M., Tracking individual kinesin motors in living cells using single quantum-dot imaging. Nano Letters 2006, 6, 1491-1495.

43. Seitz, A.; Surrey, T., Processive movement of single kinesins on crowded microtubules visualized using quantum dots. The European Molecular Biology Organization Journal 2006, 25, 267-277.

44. Aldana, J.; Wang, Y. A.; Peng, X. G., Photochemical instability of CdSe nanocrystals coated by hydrophilic thiols. Journal of the American Chemical Society 2001, 123, 8844-8850.

45. Katari, J. E. B.; Colvin, V. L.; Alivisatos, A. P., X-ray Photoelectron Spectroscopy of CdSe Nanocrystals with Applications to Studies of the Nanocrystal Surface. Journal of Physical Chemistry 1994, 98, 4109-4117.

46. Clapp, A. R.; Goldman, E. R.; Mattoussi, H., Capping of CdSe-ZnS quantum dots with DHLA and subsequent conjugation with proteins. Nature Protocols 2006, 1, 1258-1266.

47. Uyeda, H. T.; Medintz, I. L.; Jaiswal, J. K.; Simon, S. M.; Mattoussi, H., Synthesis of Compact Multidentate Ligands to Prepare Stable Hydrophilic Quantum dot Fluorophores. Journal of the American Chemical Society 2005, 127, 3870-3878.

48. Mei, B. C.; Susumu, K.; Medintz, I. L.; Delehanty, J. B.; Mountziaris, T. J.; Mattoussi, H., Modular poly(ethylene glycol) ligands for biocompatible semiconductor and gold nanocrystals with extended pH and ionic stability. Journal of Materials Chemistry 2008, 18, 4949-4958.

49. Tekle, C.; van Deurs, B.; Sandvig, K.; Iversen, T.-G., Cellular Trafficking of Quantum-Dot Ligand Bioconjugates and Their Induction of Changes in Normal Routing of Unconjugated Ligand. Nano Letters 2008, 8, 1858-1865.

50. Dubertret, B.; Skourides, P.; Norris, D. J.; Noireaux, V.; Brivanlou, A. H.; Libchaber, A., In vivo imaging of quantum dots encapsulated in phospholipid micelles. Science 2002, 298, 1759-1762.

51. Efros, A. L.; Rosen, M., The electronic structure of semiconductor nanocrystals. Annu. Rev. Mater. Sci. 2000, 30, 475-521.

52. Nirmal, M.; Norris, D. J.; Kuno, M.; Bawendi, M. G.; Efros, A. L.; Rosen, M., Observation of the Dark Exciton in CdSe Quantum Dots. Physical Review Letters 1995, 75, 3728-3731.

53. Norris, D. J.; Efros, A. L.; Rosen, M.; Bawendi, M. G., Size dependence of exciton fine structure in CdSe quantum dots. Phys. Rev. B 1996, 53, 16347-16354.

54. Empedocles, S. A.; Bawendi, M. G., Influence of spectral diffusion on the line shapes of single CdSe nanocrystallite quantum dots. Journal of Physical Chemistry B 1999, 103, 1826-1830.

55. Paesler, M. A.; Moyer, P. J., Near-field optics: theory, instrumentation, and applications. John Wiley & Sons, Inc.: New York, 1996.

56. Novotny, L.; Hecht, B., Principles of Nano-Optics. Cambridge University Press: New York, 2006; p 539.

57. Becker, W., Advanced Time-Correlated Single Photon Counting Techniques. Springer-Verlag: Berlin, Germany, 2005; p 401.

58. Wahl, M., Technote for TCSPC. PicoQuant: 2009.

59. PicoQuant., TimeHarp 200 User's Manual and Technical Data, Software Version 6.1.

60. Hanbury Brown, R.; Twiss, R. Q., Correlation between Photons in two Coherent Beams of Light. Nature 1956, 177, 27-29.

61. Cichos, F.; von Borczyskowski, C.; Orrit, M., Power-law intermittency of single emitters. Current Opinion in Colloid & Interface Science 2007, 12, 272-284.

62. Frantsuzov, P.; Kuno, M.; Janko, B.; Marcus, R. A., Universal emission intermittency in quantum dots, nanorods and nanowires. Nature Physics 2008, 4, 519-522.

63. Cook, R. J.; Kimble, H. J., Possibility of direct observation of quantum jumps. Physical Review Letters 1985, 54, 1023-1026.

64. Vargas, F.; Hollricher, O.; Marti, O.; de Schaetzen, G.; Tarrach, G., Influence of protective layers on the blinking of fluorescent single molecules observed by confocal microscopy and scanning near field optical microscopy. Journal of Chemical Physics 2002, 117, 866-871.

65. Zondervan, R.; Kulzer, F.; Orlinskii, S. B.; Orrit, M., Photoblinking of rhodamine 6G in poly(vinyl alcohol): Radical dark state formed through the triplet. Journal of Physical Chemistry A 2003, 107, 6770-6776.

66. Efros, A. L.; Rosen, M., Random telegraph signal in the photoluminescence intensity of a single quantum dot. Physical Review Letters 1997, 78, 1110-1113.

67. Wang, C. J.; Wehrenberg, B. L.; Woo, C. Y.; Guyot-Sionnest, P., Light emission and amplification in charged CdSe quantum dots. Journal of Physical Chemistry B 2004, 108, 9027-9031.

68. Muller, J.; Lupton, J. M.; Rogach, A. L.; Feldmann, J.; Talapin, D. V.; Weller, H., Monitoring surface charge migration in the spectral dynamics of single CdSe/CdS nanodot/nanorod heterostructures. Phys. Rev. B 2005, 72.

69. Zhang, K.; Chang, H. Y.; Fu, A. H.; Alivisatos, A. P.; Yang, H., Continuous distribution of emission states from single CdSe/ZnS quantum dots. Nano Letters 2006, 6, 843-847.

70. Shimizu, K. T.; Woo, W. K.; Fisher, B. R.; Eisler, H. J.; Bawendi, M. G., Surface-enhanced emission from single semiconductor nanocrystals. Physical Review Letters 2002, 89.

71. Rosen, S.; Schwartz, O.; Oron, D., Transient Fluorescence of the Off State in Blinking CdSe/CdS/ZnS Semiconductor Nanocrystals Is Not Governed by Auger Recombination. Physical Review Letters 2010, 104.

72. Kuno, M. K.; Fromm, D. P.; Hamann, H. F.; Gallager, A.; Nesbitt, D. J., Nonexponential "blinking" kinetics of single CdSe quantum dots: A universal power law behavior. Journal of Chemical Physics 2000, 112, 3117-3120.

73. Shimizu, K. T.; Neuhauser, R. G.; Leatherdale, C. A.; Empedocles, S. A.; Woo, W. K.; Bawendi, M. G., Blinking statistics in single semiconductor nanocrystal quantum dots. Phys. Rev. B 2001, 63.

74. Kuno, M.; Fromm, D. P.; Johnson, S. T.; Gallagher, A.; Nesbitt, D. J., Modeling distributed kinetics in isolated semiconductor quantum dots. Phys. Rev. B 2003, 67.

75. Tang, J.; Marcus, R. A., Mechanisms of fluorescence blinking in semiconductor nanocrystal quantum dots. Journal of Chemical Physics 2005, 123.

76. Barkai, E.; Margolin, G., Aging, non-ergodicity, and levy statistics for blinking nanocrystals. Israel Journal of Chemistry 2004, 44, 353-362.

77. Verberk, R.; van Oijen, A. M.; Orrit, M., Simple model for the power-law blinking of single semiconductor nanocrystals. Phys. Rev. B 2002, 66.

78. Frantsuzov, P. A.; Marcus, R. A., Explanation of quantum dot blinking without the long-lived trap hypothesis. Phys. Rev. B 2005, 72.

79. Guyot-Sionnest, P.; Hines, M. A., Intraband transitions in semiconductor nanocrystals. Applied Physics Letters 1998, 72, 686-688.

80. Franceschetti, A.; Zunger, A., Optical transitions in charged CdSe quantum dots. Phys. Rev. B 2000, 62, R16287-R16290.

81. Krauss, T. D.; Brus, L. E., Charge, polarizability, and photoionization of single semiconductor nanocrystals. Physical Review Letters 1999, 83, 4840-4843.

82. Colvin, V. L.; Alivisatos, A. P., CdSe nanocrystals with a dipole moment in the first excited state. Journal of Chemical Physics 1992, 97, 730-733.

83. Blanton, S. A.; Leheny, R. L.; Hines, M. A.; GuyotSionnest, P., Dielectric dispersion measurements of CdSe nanocrystal colloids: Observation of a permanent dipole moment. Physical Review Letters 1997, 79, 865-868.

84. Shim, M.; Guyot-Sionnest, P., Permanent dipole moment and charges in colloidal semiconductor quantum dots. Journal of Chemical Physics 1999, 111, 6955-6964.

85. Park, S. J.; Link, S.; Miller, W. L.; Gesquiere, A.; Barbara, P. F., Effect of electric field on the photoluminescence intensity of single CdSe nanocrystals. Chemical Physics 2007, 341, 169-174.

86. Schindler, F.; Lupton, J. M.; Feldmann, J., Spontaneous switching of permanent dipoles in single conjugated polymer molecules. Chemical Physics Letters 2006, 428, 405-410.

87. Schindler, F.; Lupton, J. M.; Muller, J.; Feldmann, J.; Scherf, U., How single conjugated polymer molecules respond to electric fields. Nature Materials 2006, 5, 141-146.

88. Moskovits, M., Surface-enhanced Spectroscopy. Reviews of Modern Physics 1985, 57, 783-826.

89. Glass, A. M.; Liao, P. F.; Bergman, J. G.; Olson, D. H., Interaction of metal particles with absorbed dye molecules- Absorption and luminescence. Optics Letters 1980, 5, 368-370.

90. Achermann, M., Exciton-Plasmon Interactions in Metal-Semiconductor Nanostructures. Journal of Physical Chemistry Letters 2010, 1, 2837-2843.

91. Maier, S. A.; Atwater, H. A., Plasmonics: Localization and guiding of electromagnetic energy in metal/dielectric structures. Journal of Applied Physics 2005, 98.

92. Purcell, E. M., Spontaneous Emission Probabilities at Radio Frequencies. Physical Review 1946, 69, 681-681.

93. Drexhage, K. H., Influence of a dielectric interface on fluorescence decay time. J. Lumines. 1970, 1-2, 693-701.

94. Persson, B. N. J., Theory of damping of excited molecules located above a metal surface. Journal of Physics C-Solid State Physics 1978, 11, 4251-4269.

95. Ford, G. W.; Weber, W. H., Electromagnetic Interactions of Molecules with Metal Surfaces. Physics Reports-Review Section of Physics Letters 1984, 113, 195-287.

96. Fu, Y.; Lakowicz, J. R., Modification of single molecule fluorescence near metallic nanostructures. Laser & Photonics Reviews 2009, 3, 221-232.

97. Anger, P.; Bharadwaj, P.; Novotny, L., Enhancement and quenching of single-molecule fluorescence. Physical Review Letters 2006, 96.

98. Fu, Y.; Zhang, J.; Lakowicz, J. R., Suppressed blinking in single quantum dots (QDs) immobilized near silver island films (SIFs). Chemical Physics Letters 2007, 447, 96-100.

99. Ito, Y.; Matsuda, K.; Kanemitsu, Y., Mechanism of photoluminescence enhancement in single semiconductor nanocrystals on metal surfaces. Phys. Rev. B 2007, 75.

100. Matsuda, K.; Ito, Y.; Kanemitsu, Y., Photoluminescence enhancement and quenching of single CdSe/ZnS nanocrystals on metal surfaces dominated by plasmon resonant energy transfer. Applied Physics Letters 2008, 92.

101. Fu, Y.; Zhang, J.; Lakowicz, J. R., Silver-enhanced fluorescence emission of single quantum dot nanocomposites. Chemical Communications 2009, 313-315.

102. Ma, X. D.; Tan, H.; Kipp, T.; Mews, A., Fluorescence Enhancement, Blinking Suppression, and Gray States of Individual Semiconductor Nanocrystals Close to Gold Nanoparticles. Nano Letters 2010, 10, 4166-4174.

103. Ratchford, D.; Shafiei, F.; Kim, S.; Gray, S. K.; Li, X., Manipulating Coupling between a Single Semiconductor Quantum Dot and Single Gold Nanoparticle. Nano Letters 2011, 11, 1049-1054.

104. Naiki, H.; Masuo, S.; Machida, S.; Itaya, A., Single-Photon Emission Behavior of Isolated CdSe/ZnS Quantum Dots Interacting with the Localized Surface Plasmon Resonance of Silver Nanoparticles. Journal of Physical Chemistry C 2011, 115, 23299-23304.

105. Canneson, D.; Mallek-Zouari, I.; Buil, S.; Quelin, X.; Javaux, C.; Mahler, B.; Dubertret, B.; Hermier, J. P., Strong Purcell effect observed in single thick-shell CdSe/CdS nanocrystals coupled to localized surface plasmons. Phys. Rev. B 2011, 84.

106. Gueroui, Z.; Libchaber, A., Single-molecule measurements of gold-quenched quantum dots. Physical Review Letters 2004, 93.

107. Govorov, A. O.; Bryant, G. W.; Zhang, W.; Skeini, T.; Lee, J.; Kotov, N. A.; Slocik, J. M.; Naik, R. R., Exciton-plasmon interaction and hybrid excitons in semiconductor-metal nanoparticle assemblies. Nano Letters 2006, 6, 984-994.

108. Pons, T.; Medintz, I. L.; Sapsford, K. E.; Higashiya, S.; Grimes, A. F.; English, D. S.; Mattoussi, H., On the quenching of semiconductor quantum dot photoluminescence by proximal gold nanoparticles. Nano Letters 2007, 7, 3157-3164.

109. Fedutik, Y.; Temnov, V. V.; Schoeps, O.; Woggon, U.; Artemyev, M. V., Exciton-plasmon-photon conversion in plasmonic nanostructures. Physical Review Letters 2007, 99.

110. Akimov, A. V.; Mukherjee, A.; Yu, C. L.; Chang, D. E.; Zibrov, A. S.; Hemmer, P. R.; Park, H.; Lukin, M. D., Generation of single optical plasmons in metallic nanowires coupled to quantum dots. Nature 2007, 450, 402-406.

111. Fofang, N. T.; Grady, N. K.; Fan, Z. Y.; Govorov, A. O.; Halas, N. J., Plexciton Dynamics: Exciton-Plasmon Coupling in a J-Aggregate-Au Nanoshell Complex Provides a Mechanism for Nonllinearity. Nano Letters 2011, 11, 1556-1560.

112. Klimov, V. I., Spectral and dynamical properties of multilexcitons in semiconductor nanocrystals. Annual Review of Physical Chemistry 2007, 58, 635-673.

113. Ellingson, R. J.; Beard, M. C.; Johnson, J. C.; Yu, P. R.; Micic, O. I.; Nozik, A. J.; Shabaev, A.; Efros, A. L., Highly efficient multiple exciton generation in colloidal PbSe and PbS quantum dots. Nano Letters 2005, 5, 865-871.

114. Schaller, R. D.; Sykora, M.; Jeong, S.; Klimov, V. I., High-efficiency carrier multiplication and ultrafast charge separation in semiconductor nanocrystals studied via time-resolved photoluminescence. Journal of Physical Chemistry B 2006, 110, 25332-25338.

115. Klimov, V. I.; Mikhailovsky, A. A.; Xu, S.; Malko, A.; Hollingsworth, J. A.; Leatherdale, C. A.; Eisler, H. J.; Bawendi, M. G., Optical gain and stimulated emission in nanocrystal quantum dots. Science 2000, 290, 314-317.

116. Stevenson, R. M.; Young, R. J.; Atkinson, P.; Cooper, K.; Ritchie, D. A.; Shields, A. J., A semiconductor source of triggered entangled photon pairs. Nature 2006, 439, 179-182.

117. Achermann, M.; Hollingsworth, J. A.; Klimov, V. I., Multiexcitons confined within a subexcitonic volume: Spectroscopic and dynamical signatures of neutral and charged biexcitons in ultrasmall semiconductor nanocrystals. Phys. Rev. B 2003, 68.

118. Caruge, J. M.; Chan, Y. T.; Sundar, V.; Eisler, H. J.; Bawendi, M. G., Transient photoluminescence and simultaneous amplified spontaneous emission from multiexciton states in CdSe quantum dots. Phys. Rev. B 2004, 70.

119. Fisher, B.; Caruge, J. M.; Zehnder, D.; Bawendi, M., Room-temperature ordered photon emission from multiexciton states in single CdSe core-shell nanocrystals. Physical Review Letters 2005, 94.

120. Nair, G.; Zhao, J.; Bawendi, M. G., Biexciton Quantum Yield of Single Semiconductor Nanocrystals from Photon Statistics. Nano Letters 2011, 11, 1136-1140.

121. Park, Y. S.; Malko, A. V.; Vela, J.; Chen, Y.; Ghosh, Y.; Garcia-Santamaria, F.; Hollingsworth, J. A.; Klimov, V. I.; Htoon, H., Near-Unity Quantum Yields of Biexciton Emission from CdSe/CdS Nanocrystals Measured Using Single-Particle Spectroscopy. Physical Review Letters 2011, 106.

122. Htoon, H.; Malko, A. V.; Bussian, D.; Vela, J.; Chen, Y.; Hollingsworth, J. A.; Klimov, V. I., Highly Emissive Multiexcitons in Steady-State Photoluminescence of Individual "Giant" CdSe/CdS Core/Shell Nanocrystals. Nano Letters 2010, 10, 2401-2407.

123. Klimov, V. I.; Mikhailovsky, A. A.; McBranch, D. W.; Leatherdale, C. A.; Bawendi, M. G., Quantization of multiparticle Auger rates in semiconductor quantum dots. Science 2000, 287, 1011-1013.

124. Spinicelli, P.; Buil, S.; Quelin, X.; Mahler, B.; Dubertret, B.; Hermier, J. P., Bright and Grey States in CdSe-CdS Nanocrystals Exhibiting Strongly Reduced Blinking. Physical Review Letters 2009, 102.

125. Osovsky, R.; Cheskis, D.; Kloper, V.; Sashchiuk, A.; Kroner, M.; Lifshitz, E., Continuous-Wave Pumping of Multiexciton Bands in the Photoluminescence Spectrum

of a Single CdTe-CdSe Core-Shell Colloidal Quantum Dot. Physical Review Letters 2009, 102.

126. Wang, X. Y.; Ren, X. F.; Kahen, K.; Hahn, M. A.; Rajeswaran, M.; Maccagnano-Zacher, S.; Silcox, J.; Cragg, G. E.; Efros, A. L.; Krauss, T. D., Non-blinking semiconductor nanocrystals. Nature 2009, 459, 686-689.

127. Garcia-Santamaria, F.; Chen, Y. F.; Vela, J.; Schaller, R. D.; Hollingsworth, J. A.; Klimov, V. I., Suppressed Auger Recombination in "Giant" Nanocrystals Boosts Optical Gain Performance. Nano Letters 2009, 9, 3482-3488.

128. Jones, M.; Lo, S. S.; Scholes, G. D., Quantitative modeling of the role of surface traps in CdSe/CdS/ZnS nanocrystal photoluminescence decay dynamics. Proceedings of the National Academy of Sciences of the United States of America 2009, 106, 3011-3016.

129. Jones, M.; Scholes, G. D., On the use of time-resolved photoluminescence as a probe of nanocrystal photoexcitation dynamics. Journal of Materials Chemistry 2010, 20, 3533-3538.

130. Jones, M.; Lo, S. S.; Scholes, G. D., Signatures of Exciton Dynamics and Carrier Trapping in the Time-Resolved Photoluminescence of Colloidal CdSe Nanocrystals. J. Phys. Chem. C 2009, 113, 18632-18642.

131. Marcus, R. A.; Sutin, N., Electron Transfers in Chemistry and Biology. Biochimica Et Biophysica Acta 1985, 811, 265-322.

132. Morris-Cohen, A. J.; Donakowski, M. D.; Knowles, K. E.; Weiss, E. A., The Effect of a Common Purification Procedure on the Chemical Composition of the Surfaces of CdSe Quantum Dots Synthesized with Trioctylphosphine Oxide. J. Phys. Chem. C 2010, 114, 897-906.

133. Schlegel, G.; Bohnenberger, J.; Potapova, I.; Mews, A., Fluorescence decay time of single semiconductor nanocrystals. Physical Review Letters 2002, 88.

134. Fisher, B. R.; Eisler, H. J.; Stott, N. E.; Bawendi, M. G., Emission intensity dependence and single-exponential behavior in single colloidal quantum dot fluorescence lifetimes. Journal of Physical Chemistry B 2004, 108, 143-148.

135. Crooker, S. A.; Barrick, T.; Hollingsworth, J. A.; Klimov, V. I., Multiple temperature regimes of radiative decay in CdSe nanocrystal quantum dots: Intrinsic limits to the dark-exciton lifetime. Applied Physics Letters 2003, 82, 2793-2795.

136. Califano, M.; Franceschetti, A.; Zunger, A., Lifetime and polarization of the radiative decay of excitons, biexcitons, and trions in CdSe nanocrystal quantum dots. Phys. Rev. B 2007, 75.

137. Gomez, D. E.; van Embden, J.; Mulvaney, P., Spectral diffusion of single semiconductor nanocrystals: The influence of the dielectric environment. Applied Physics Letters 2006, 88.

138. Toropov, A. A.; Shubina, T. V.; Belyaev, K. G.; Ivanov, S. V.; Kop'ev, P. S.; Ogawa, Y.; Minami, F., Enhancement of excitonic emission in semiconductor heterostructures due to resonant coupling to multipole plasmon modes in a gold particle. Phys. Rev. B 2011, 84.

139. Leatherdale, C. A.; Woo, W. K.; Mikulec, F. V.; Bawendi, M. G., On the absorption cross section of CdSe nanocrystal quantum dots. Journal of Physical Chemistry B 2002, 106, 7619-7622.

140. Peterson, J. J.; Nesbitt, D. J., Modified Power Law Behavior in Quantum Dot Blinking: A Novel Role for Biexcitons and Auger Ionization. Nano Letters 2009, 9, 338-345.

141. Xu, X. S.; Yamada, T.; Yokoyama, S., Correlations between antibunching and blinking of photoluminescence from a single CdSe quantum dot. European Physical Journal D 2009, 55, 691-697.

APPENDIX A: CALCULATION OF SAMPLE EXCITATION

It is useful for experiments to identify how much power is exciting the sample. The laser power per unit area, in units of W/cm^2, is typically reported in the literature. It is calculated by considering the spot size of the laser at the sample. As mentioned previously, the laser beam has nearly a Gaussian intensity distribution. By taking a transverse slice along the focal plane, we can approximate this as a circular excitation spot, whose area is calculated as A= πr^2, where r is the radius. The diameter of the spot is taken as the full width at half maximum (FWHM) of the point spread function, which in our case is ~300 nm. Thus the radius is ~150 nm. So, for a power of 3 μW at the sample,

$$A = \pi(1.5\times10^{-5})^2 = 7.1\times10^{-10}\,cm^2$$

$$Power = \frac{3\times10^{-6}W}{7.1\times10^{-10}\,cm^2} = 4.2\times10^{3}W/cm^2 = 4kW/cm^2$$

For photon antibunching experiments, we also must confirm that this excitation is capable of exciting multiple excitons in a sample from a single laser pulse. At the same excitation power of 3 μW at the sample from above, we calculate the maximum number of photons that a quantum dot can absorb from a single laser pulse.

First, convert μW to units of Joules per second:

$$3\times10^{-6}W = 3\times10^{-6}J/s$$

Convert the energy of a single photon of 470 nm light to Joules:

$$E_{photon} = \frac{hc}{\lambda} = \left(\frac{1240nm \cdot eV}{470nm}\right)\left(\frac{1.6\times10^{-19}\,J}{1eV}\right) = \frac{4.2\times10^{-19}\,J}{photon}$$

Convert Joules per second to photons per second:

$$\left(\frac{3\times10^{-6}\,J}{s}\right)\left(\frac{photon}{4.2\times10^{-19}\,J}\right) = \frac{7.1\times10^{12}\,photons}{s}$$

Considering the pulse repetition rate of 10 MHz, which is equal to 10^7 pulses/s, now convert from photons per second to photons per pulse:

$$\left(\frac{7.1\times10^{12}\,photons}{s}\right)\left(\frac{s}{10^{7}\,pulses}\right) = \frac{7.1\times10^{5}\,photons}{pulse}$$

Now consider the photons from a single pulse that can be absorbed by a single quantum dot. A ratio of the absorption cross-section (σ) of the quantum dot, and the laser spot size is found. The absorption cross-section accounts for the size of the quantum dot and the probability of an absorption process occurring. The area of the laser spot was found to be $7.1\text{x}10^{-10}$ cm^2= $7.1\text{x}10^{4}$ nm^2. The absorption cross-section (σ) can be found using the following relationship[139], where *r* represents the nanocrystal radius, taken to be 2 nm:

$$\sigma = \frac{0.055r^3}{nm} = \frac{0.055(2)^3}{nm} = 0.44nm^2$$

Taking the ratio of σ to the laser spot size, now calculate the maximum number of absorbed photons from the calculated photons per pulse:

$$\left(\frac{0.44nm^2}{7.1\times10^4\,nm^2}\right)\left(7.1\times10^5\,photons/pulse\right)=4\,photons/pulse$$

Calculation of average number of excitations per NC, $\langle N\rangle$, at 0.6 kW/cm^2:

Example calculation of fluence, Φ:

$$E_{photon}=\frac{hc}{\lambda}=\left(\frac{1240\cdot eV}{470nm}\right)\left(\frac{1.6\times10^{-19}\,J}{1eV}\right)=\frac{4.2\times10^{-19}\,J}{photon}$$

$$\left(\frac{607\,J}{s\cdot cm^2}\right)\left(\frac{photon}{4.2\times10^{-19}\,J}\right)\left(\frac{1}{10^7\,s^{-1}}\right)=1.45\times10^{14}\,photons/cm^2$$

*607 J/s•cm^2 corresponds to the a power density of 0.607 kW/cm^2

Example calculation of absorption cross section, σ:[139]

*NOTE: σ is slightly over-estimated here due to the experiments in the above referenced paper being conducted at 350 nm, compared to 470 nm in our setup, thus we divide by a factor of 2 to account for the difference in absorption at the two wavelengths.

$$\sigma=\frac{0.055r^3}{nm}=\frac{0.055(2.5)^3}{nm}=0.86nm^2$$

$$\sigma=\frac{(5.501\times10^5)r^3}{cm}=\frac{5.501\times10^5(2.5\times10^{-7})^3}{cm}=8.6\times10^{-15}cm^2$$

$\langle N\rangle=\Phi\sigma=1.2\ /2^*=0.6$ excitations per pulse

APPENDIX B: FABRICATION OF ELECTRODE DEVICE

TABLE A.1: Steps for Fabrication of electrode devices.

Fabrication Step	Instrumentation/Parameters
1. Clean substrate	Scrub gently with Acetone, Methanol, followed by wash with Isopropyl Alcohol and drying with nitrogen gun
2. Spin coat Photoresist	Brewer: Shipley 1813 positive resist; 30 seconds at 3000 rpm; post bake on 150°C hotplate 60 s
3. Exposure	Quintel: Secure mask on contact aligner, expose for 8 seconds
4. Develop	Gently swirl in MF-319 developer solution 30 s, then 30 s in DI water
5. Plasma Etch	STS-ASE: Descum recipe, 10 s
6. Electron Beam Evaporation	Lesker: Evaporate 10 nm layer of cobalt, then 150 nm layer of gold
7. Lift-Off etch	Sonicate in N-methyl pyrrollidone until all excess metal is lifted off, clean with isopropyl alcohol, dry with nitrogen
8. Plasma Etch	STS-ASE: Descum recipe, 2 min

APPENDIX C: SUPPLEMENTARY BLINKING DATA

The corresponding blinking traces for the lifetime decays shown in figure 7.30 are shown below. It is clear that between 0.6 and 1.2 kW/cm^2, the blinking transitions from clear binary on-off behavior with long on and off times to rapid transitions between on and off states. This is distinct from previous studies, which report suppression of blinking near metal films. Each blinking trace is accompanied by a count rate histogram, and a probability distribution of on (blue circles) and off (black circles) statistics. At 0.6 and 1.2 kW/cm^2, the distributions are fairly well fit to a power law.[72] The poor fit is due to a high number of single occurrences because of the short acquisition period. At higher intensities, the power law is clearly insufficient to fit the distribution as an exponential tail-off appears.[73]

The role of biexcitons in quantum dot blinking has been shown to produce a truncated power law of on-time distributions.[140] Direct observation of biexciton emission as a function of excitation intensity has revealed clear changes in blinking behavior, which was attributed to an Auger-assisted tunneling model.[141] We observe an exponential tail-off of the probability distribution in both on and off times at high excitation intensities in the blinking traces below, which is distinct from previous reports. This blinking behavior further confirms the competition between radiative processes and nonradiative Auger processes as the QD transitions rapidly between radiative and nonradiative states.

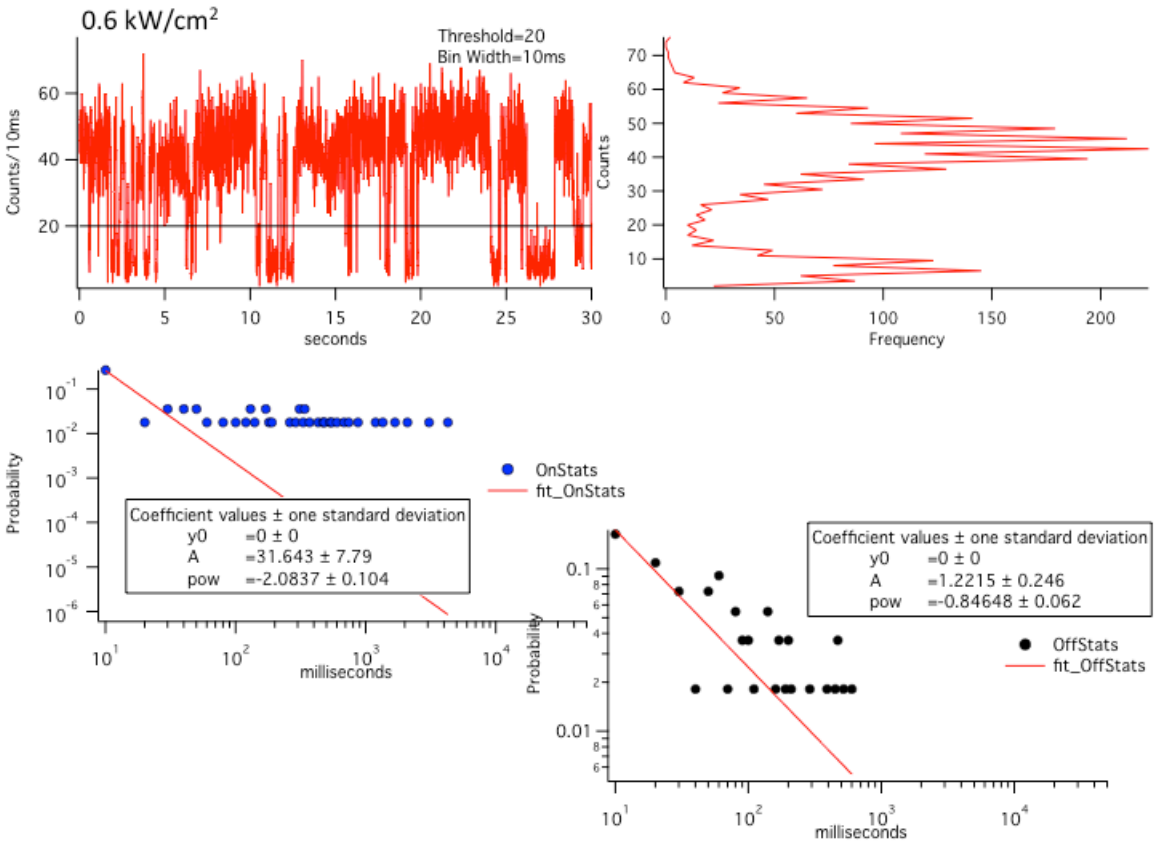
0.6 kW/cm2
Threshold=20
Bin Width=10ms
Counts/10ms
seconds
Counts
Frequency
Probability
OnStats
fit_OnStats
Coefficient values ± one standard deviation
y0 =0 ± 0
A =31.643 ± 7.79
pow =-2.0837 ± 0.104
milliseconds
Coefficient values ± one standard deviation
y0 =0 ± 0
A =1.2215 ± 0.246
pow =-0.84648 ± 0.062
OffStats
fit_OffStats

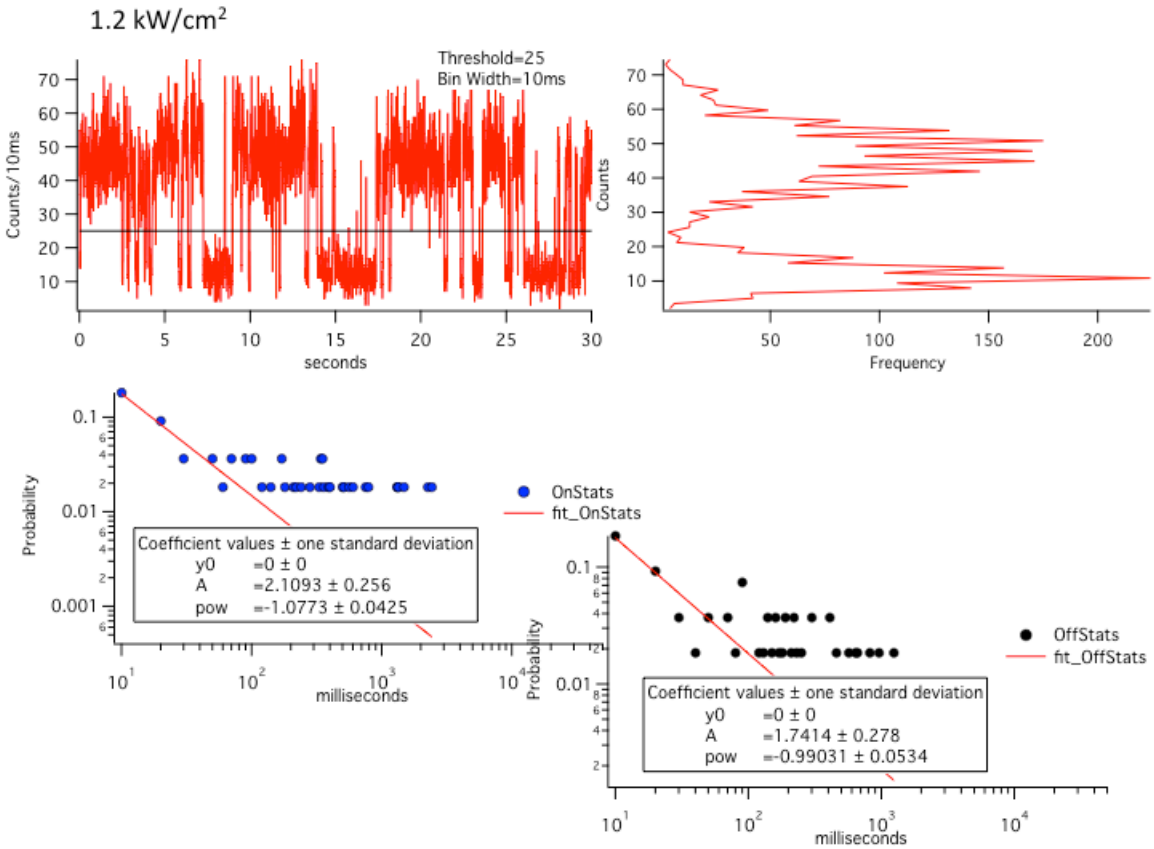
1.2 kW/cm2
Threshold=25
Bin Width=10ms
Counts/10ms
seconds
Counts
Frequency
Probability
OnStats
fit_OnStats
Coefficient values ± one standard deviation
y0 =0 ± 0
A =2.1093 ± 0.256
pow =-1.0773 ± 0.0425
milliseconds
Coefficient values ± one standard deviation
y0 =0 ± 0
A =1.7414 ± 0.278
pow =-0.99031 ± 0.0534
OffStats
fit_OffStats

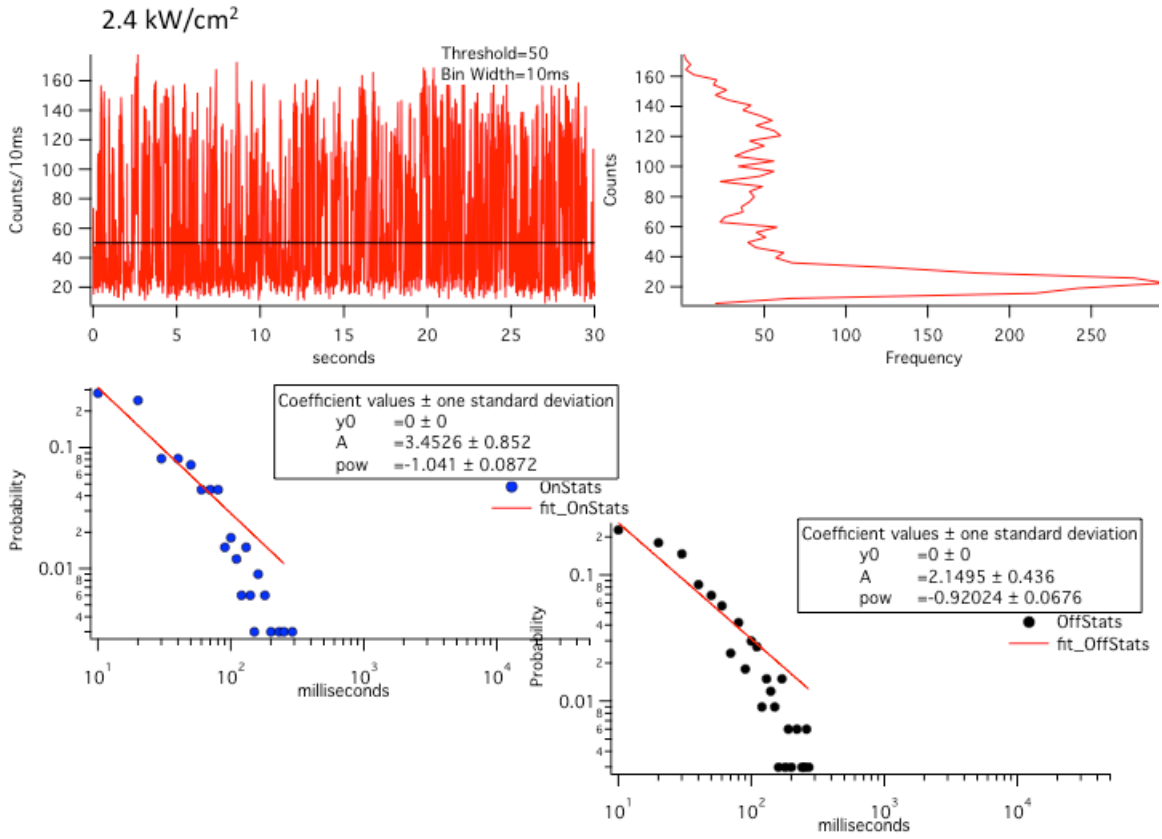
2.4 kW/cm2
Threshold=50
Bin Width=10ms
Counts/10ms
seconds
Counts
Frequency
Coefficient values ± one standard deviation
y0 =0 ± 0
A =3.4526 ± 0.852
pow =-1.041 ± 0.0872
OnStats
fit_OnStats
Probability
milliseconds
Coefficient values ± one standard deviation
y0 =0 ± 0
A =2.1495 ± 0.436
pow =-0.92024 ± 0.0676
OffStats
fit_OffStats

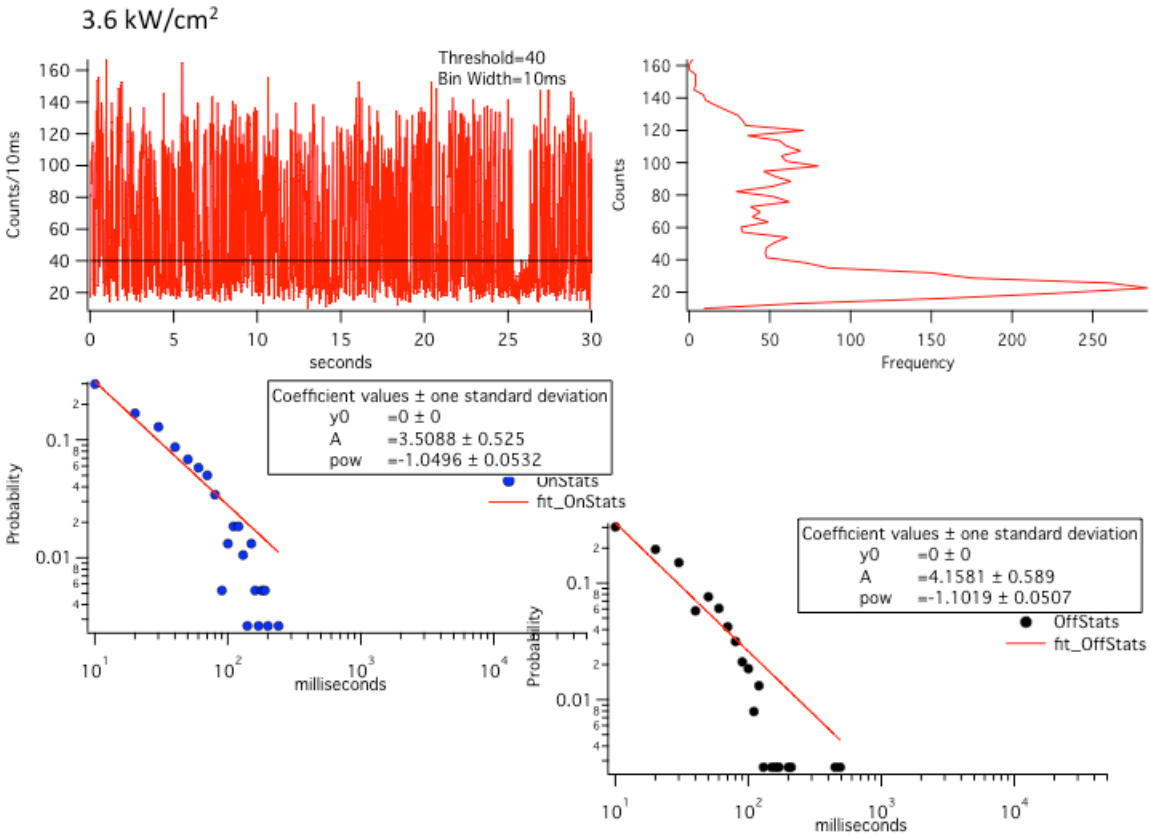
3.6 kW/cm2
Threshold=40
Bin Width=10ms
Counts/10ms
seconds
Counts
Frequency
Coefficient values ± one standard deviation
y0 =0 ± 0
A =3.5088 ± 0.525
pow =-1.0496 ± 0.0532
OnStats
fit_OnStats
Probability
milliseconds
Coefficient values ± one standard deviation
y0 =0 ± 0
A =4.1581 ± 0.589
pow =-1.1019 ± 0.0507
OffStats
fit_OffStats
Probability
milliseconds

APPENDIX D: SUPPLEMENTARY DATA FOR SECTION 7.3

TABLE A.2: Parameters from blinking traces used to calculate enhancement factor.

Control Samples	**Lifetime of top 10%**	**On:Off Ratio**	**Avg Counts**	
_002	18.096	0.82	408.36	
_003	14.4	0.804	172.538	
_004	17.4	0.578667	199.524	
_005	14.2	0.769333	212.798	
_006	18.028	0.869	503.499	
	16.42 ± 1.96		299.3438	Average
Gold Samples				
_017	6.744		82.5571	
_016	7.887		170.417	
_011	9.504		253.946	
_012	9.6		269.007	
_014	10.626		152.224	
	8.87 ± 1.54		185.63022	Average

Derivation of expression for biexciton quantum yield:

Consider the following kinetic scheme:

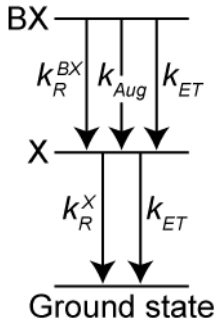

We can write down the differential equations governing the population of the *BX* and *X* states:

$$\frac{d\rho_{BX}}{dt} = -\left(k_R^{BX} + k_{Aug} + k_{ET}\right)\rho_{BX}(t)$$
$$\frac{d\rho_X}{dt} = \left(k_R^{BX} + k_{Aug}\right)\rho_{BX}(t) - \left(k_R^X + k_{ET}\right)\rho_X(t)$$

Where, ρ_{BX}, and ρ_X are the probabilities of finding *BX* or *X* populated. These can be solved to give:

$$\rho_{BX}(t) = \rho_{BX}(0)e^{-k_{BX}t}$$
$$\rho_X(t) = \frac{\rho_{BX}(0)k_{BX}}{k_X - k_{BX}}\left[e^{-k_{BX}t} - e^{-k_X t}\right] + \rho(0)e^{-k_X t}$$

Where $k_{BX} = k_R^{BX} + k_{Aug} + k_{ET}$, and $k_X = k_R^X + k_{ET}$. The initial populations can be estimated from Poisson statistics:

$$\rho_X(0) = \Phi\sigma e^{-\Phi\sigma}$$
$$\rho_{BX}(0) = \frac{(\Phi\sigma)^2 e^{-\Phi\sigma}}{2}$$

Where $\Phi$is the photon fluence and σ is the absorption cross-section. The intensity of fluorescence at time, *t*, is therefore given by:

$$I(t) = \Phi\sigma e^{-\Phi\sigma}\left[\frac{1}{2}k_R^{BX}\Phi\sigma e^{-k_{BX}t} + \frac{\Phi\sigma k_R^X k_{BX}}{2(k_X - k_{BX})}\left[e^{-k_{BX}t} - e^{-k_x t}\right] + k_R^X e^{-k_X t}\right]$$

This can be separated into two exponential components:

$$A_1 e^{-k_1 t} = \frac{1}{2}\left(\Phi\sigma\right)^2 e^{-\Phi\sigma}\left[k_R^{BX} + \frac{k_R^X k_{BX}}{k_X - k_{BX}}\right]e^{-k_{BX}t}$$

$$A_1 e^{-k_2 t} = \frac{1}{2}\Phi\sigma e^{-\Phi\sigma}\left[2k_R^X - \frac{\Phi\sigma k_R^X k_{BX}}{k_X - k_{BX}}\right]e^{-k_X t}$$

The yield of the fast component is given by, $A_1\tau_1 / \left(A_1\tau_1 + A_2\tau_2\right)$, which can be written:

$$Y_{BX} = \frac{A_{BX}\tau_{BX}}{A_{BX}\tau_{BX} + A_X\tau_X} = \frac{\Phi\sigma\tau_{BX}\left(k_R^{BX} + k_R^X\eta\right)}{\Phi\sigma\tau_{BX}\left(k_R^{BX} + k_R^X\eta\right) + \tau_X k_R^X\left(2 - \Phi\sigma\eta\right)}, \text{ where}$$

$$\eta = \frac{k_{BX}}{\left(k_X - k_{BX}\right)}$$